

Material Screening by means of Low-level Gamma Ray Spectrometry with the Dortmund Low Background HPGe Facility

Dissertation
zur Erlangung des akademischen Grades
eines Doktors der Naturwissenschaften
der Fakultät Physik
an der Technischen Universität Dortmund



vorgelegt von
DIPL. PHYS. TILL NEDDERMANN

Lehrstuhl für Experimentelle Physik IV
Fakultät Physik



Dortmund, Februar 2014

Material Screening by means of Low-level Gamma Ray Spectrometry with the Dortmund Low Background HPGe Facility

Dissertation
zur Erlangung des akademischen Grades
eines Doktors der Naturwissenschaften
der Fakultät Physik
an der Technischen Universität Dortmund

vorgelegt von
DIPL. PHYS. TILL NEDDERMANN
Lehrstuhl für Experimentelle Physik IV
Fakultät für Physik
TU Dortmund

Dortmund, Februar 2014

Vorsitzender der Prüfungskommission:	Prof. Dr. C. Westphal, TU Dortmund
Erstgutachter:	Prof. Dr. C. Gößling, TU Dortmund
Zweitgutachter:	Prof. Dr. K. Zuber, TU Dresden
Beisitzer:	Dr. B. Siegmann, TU Dortmund
Termin der mündlichen Prüfung:	28. März 2014

Contents

1. Introduction	9
2. Background knowledge about low level radioactivity measurements	13
2.1. Radioassaying techniques	13
2.2. Radionuclides of interest of low background material assaying . . .	15
2.2.1. Primordial radionuclides	16
2.2.2. Natural decay chains	16
2.2.3. Cosmogenic radionuclides	17
2.2.4. Anthropogenic radionuclides	18
2.3. Special aspects of γ ray spectrometry	18
2.3.1. Efficiency	19
2.3.2. Summing	19
3. Detector system	23
3.1. Shielding	24
3.1.1. Outer shielding	24
3.1.2. Inner shielding	26
3.2. Cosmics veto	30
3.3. Germanium detector	34
3.3.1. Front window sensitivity	35
3.4. Data acquisition electronics	39
3.5. Background spectrum	43
3.5.1. Peaks in the DLB background spectrum	46
Activation products	52
Neutron induced γ lines	53
4. Software for data processing and analysis	57
4.1. Data conversion tool ge-multi-convertintool	57
4.2. Calibration software GeCal	58
4.3. Spectrum evaluation standards	59
4.3.1. Standard DIN 25482-5:1993	62
4.3.2. Standard DIN ISO 11929:2011	65
Application to spectroscopic measurements	69
4.4. Analysis software GeAna	74
4.5. Simulation program VENOM	81

Contents

5. Monte Carlo simulation for full energy peak efficiency determination	85
5.1. Geometry model	87
5.2. Geometry optimisation	88
5.2.1. Dead layer thickness	91
5.2.2. Crystal to endcap distance	97
5.2.3. Sensitive detector volume	101
5.2.4. Discussion of results	106
5.3. Emission probabilities of γ rays in Geant4	109
6. Radioassay of samples	113
6.1. IAEA proficiency tests	113
6.1.1. IAEA-CU-2010-03 World-wide open proficiency test	114
6.1.2. IAEA-TEL-2011-03 World-wide open proficiency test	115
6.2. Material samples for COBRA	119
6.2.1. Conductive silver Ferro LS200	119
6.2.2. OPERA lead sheets	121
6.2.3. Pixel detector readout chips	123
7. Shielding design for the COBRA R&D set-up	127
7.1. Neutron shielding	127
7.2. EMI shielding	129
7.3. Shielding against environmental background	132
8. Summary and outlook	135
Acknowledgements / Danksagung	139
A. Natural decay chains	141
B. CAD drawings	145
C. Exemplary data evaluation report	147
D. MC geometry optimisation	149
E. Dose distribution in HPGe detector	153
F. GRDM γ ray emission probabilities	157
Publications	159
Bibliography	161
List of Figures	177

Contents

List of Tables	179
Acronyms	181

Contents

1. Introduction

For many years a variety of experiments have been performed to probe different aspects of the standard model of particle physics to very high precision. Some phenomena like the matter-antimatter asymmetry can not be explained by the standard model. Experiments probing theories of physics beyond the standard model did, for example, confirm the proposed neutrino oscillations.

Two fields deal especially with phenomena in the low energy region. The first category of experiments tries to investigate the nature of dark matter. XENON100 [AAA⁺12], CRESST [ABB⁺09] and EDELWEISS [BDA⁺09], to name but a few, are searching for rare interactions of hypothetical WIMPs manifesting in a nuclear recoil. The second group of experiments examines the nature of the neutrino – whether it is a Majorana particle or not – and in this case its mass by searching for the neutrinoless double beta decay ($0\nu\beta\beta$ decay). Currently several experiments like EXO [AAB⁺12] or GERDA [AAA⁺13] are taking data to probe the controversially discussed claim [KKDHK01, KKK06] for the observation of the $0\nu\beta\beta$ decay in ^{76}Ge . Other experiments, for example COBRA [EFG⁺13], are still in the Research and Development (R&D) phase and belong to a second generation of projects.

The expected signals stemming from the phenomena described above lie in the range of approximately 1 keV to 5 MeV, which is the same as the decay energies of radioactive nuclides and other nuclear reactions. Therefore, any energy deposition in the used detectors by particles emitted in a radioactive decay causes inevitably background covering the signals of the investigated ultra-rare effects. To lower the background level of the detector systems as much as possible and to maximise their sensitivity, different elaborate measures have to be taken. To minimize the amount of signals induced by cosmic rays, especially muons, the experiments for the search for ultra-rare effects have to be set-up in underground laboratories with a high overburden. Around the world different underground facilities exist in former or active mines or next to road tunnels, for example the Laboratori Nazionali del Gran Sasso (LNGS) in Italy, providing excellent research conditions (see [Pan11, Bet11]). In some of these laboratories the muon flux is suppressed by more than six orders of magnitude to less than 1 muon/(m² h). To shield a detector set-up from the particles emitted by environmental radioactivity multi-layered shieldings usually consisting of copper and lead are used. Furthermore, it can be necessary to suppress electromagnetic or acoustic influences on the highly sensitive experiments. Since many materials contain traces of radioactive nuclides the most difficult task is to minimize background intrinsic

1. Introduction

to the detector systems. Many materials contain radioactive impurities to some extent since often the raw materials already are not radiopure or get in contact with radioimpurities in the production process. On the other hand, some materials like copper are very radiopure due to the production process, but they contain radioimpurities after an exposure to cosmic rays. The different categories of radioactive nuclides occurring in materials are discussed in Section 2.2.

To achieve a very low background level, consequently all construction and shielding materials necessary to set-up the detector system of an experiment are screened for traces of radioactivity by at least one of the different radioassaying techniques described in Section 2.1. Although being very elaborate, the method applied most commonly is low background γ ray spectrometry with high purity germanium (HPGe) detectors. In this method the detection of characteristic γ rays emitted by the daughter nuclide of a radioactive decay is used to detect the decay itself. By measuring a material sample for a certain time and determining the detection efficiency for the γ ray of interest, it is possible to calculate the specific activity of a certain nuclide contained in the sample.

Since the amount of radioimpurities usually found in material samples is very low, a γ ray spectrometry system with an in turn as low as possible background is necessary. By this means, one is able to make a precise prediction for the achievable background of the actual experiment. Because of this requirement, which is in many aspects identical to the ones of the above mentioned experiments, very sophisticated low background γ ray spectrometry systems have been constructed (see e.g. [HLN06]). Consequently, in nearly every underground laboratory around the world several low background γ ray spectrometry systems are operated to assist the construction of experiments for ultra-rare event searches (see [LHG⁺04]). Often these systems were even set-up to support the development of a certain experiment. In addition, some γ ray spectrometry laboratories exist that are located in underground facilities solely set-up for this purpose. Often they have a smaller overburden like the Felsenkeller, VKTA, Dresden, Germany or the Low Level Lab at the Max-Planck-Institut für Kernphysik (MPI-K) in Heidelberg, Germany. Like in the case of the Felsenkeller often the main task of the laboratories is the activity determination in environmental or food samples and material assaying is only a subsidiary task.

The Dortmund Low Background Facility (DLB), a γ ray spectrometry system located above ground but with an artificial overburden, was designed and constructed as a cooperation of the diploma theses by H. Gastrich [Gas09] and the author [Ned09] to support the development of the COBRA experiment. A description of different components of the detector system, a discussion of the achieved background suppression as well as the analysis of the remaining background γ ray peaks are given in Chapter 3. Since only the active veto system against cosmics (see Section 3.2) was completely commissioned in the construction phase, the commissioning of the whole detector system and the development of a data

analysis framework has been the main aim of the present thesis.

In Chapter 2 an overview of the different methods of material assaying is given. Furthermore, the nuclides of interest of low background material screening as well as two special aspects of γ ray spectrometry are discussed. To analyse the spectra acquired with the detector system described in Chapter 3 and determine sample activities from these, different software tools are necessary. A program to convert the raw data to the ROOT [BR97] file format as well as a ROOT class for spectrum calibration are described in Chapter 4. After an explanation of the evaluation standards used in γ ray spectrometry the functionality and usage of the developed ROOT class for spectrum evaluation are explained. To determine the detection efficiency for a γ line of interest, the evaluation tool relies on Monte Carlo (MC) simulations done with the VENOM framework, which is based on the Geant4 [AAA⁺03] tool kit and is developed by the COBRA collaboration. The contributions to VENOM by the author are briefly described in Chapter 2 as well.

The implemented virtual model of the DLB detector set-up that is necessary to determine the detection efficiency by MC simulation is explained in Chapter 5. Since effects like weak electrical fields in some regions of the germanium detector are not implemented in the MC model and only the simple energy deposition within the detector without drifting the charges is simulated, the MC simulation usually can not completely reproduce the measured γ ray spectra. Furthermore, often the properties of the detector crystal like the thickness of the outer contact or its position within the endcap do not exactly match the specification of the manufacturer so that discrepancies between measurement and simulation are inevitable. To reproduce the detection characteristics of the HPGe detector, the MC model is optimised in three steps, which is discussed in Section 5.2. In addition, the simulated emission characteristics of the nuclides most relevant for γ ray spectrometry were validated against the data provided by the Decay Data Evaluation Project (DDEP) [Lab13]. The found discrepancies and the consequences for the MC simulation are discussed in Section 5.3.

The optimised MC model as well as the developed analysis software are used to analyse different material samples. To test the evaluation procedure the author participated in two proficiency test organised by the International Atomic Energy Agency (IAEA). The results as well as the found deviations are discussed in Chapter 6. Furthermore, the spectra of four samples of materials required by the COBRA experiment are analysed and the specific activities contained in the materials are determined.

In addition to the commissioning of the DLB detector system indirectly supporting the COBRA experiment, the author contributed also directly in different tasks to the development of the experiment. Besides the software development for VENOM, the author was also responsible for the redesign of the complete COBRA R&D set-up at LNGS. Due to a relocation of the experiment within the

1. Introduction

Italian underground laboratory in 2011, the different components of the shielding were modified to take advantage of the infrastructure and the increased space. The relocation and the necessary modifications were planned by the author and are described in Chapter 7.

Finally the results of the work are summarised in Chapter 8 and a brief outlook to possible further topics to be worked on is given.

2. Background knowledge about low level radioactivity measurements

2.1. Radioassaying techniques

As discussed in Chapter 1 many experiments rely on very radiopure materials for the construction of their detector systems to create environments that are, as far as possible, background free. Depending on the type of decay products and the aggregate state of impurities as well as the matrix of the materials and the necessary detection sensitivities different radioassaying techniques can be applied. These techniques have individual advantages and disadvantages so that the most suitable method for the problem at hand has to be chosen carefully.

One method to analyse the constituents of a material is mass spectrometry, especially accelerator or inductively coupled plasma mass spectrometry (ICP-MS). Mass spectrometry requires a careful sample preparation to separate elements of interest from the sample matrix and enable the analysis of traces in the first place. Due to this, the method has a high risk for sample contamination and additionally the yield of the preparation has to be determined by spiked samples. Due to the usage of argon gas in ICP-MS, whose most abundant isotope is ^{40}Ar , it is not possible to determine the ^{40}K content in a sample directly, but it has to be calculated from the other potassium isotopes by assuming the natural abundance.

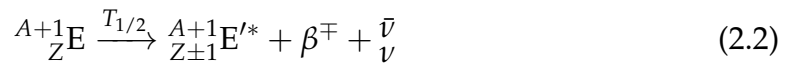
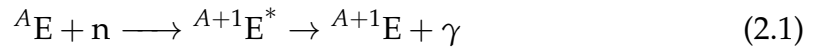
Liquid scintillator counting can be used to determine the activities of α and β decaying nuclides, especially in liquid or soluble materials. Due to the poor energy resolution of liquid scintillators it is difficult to resolve the resulting spectrum into different components in case several nuclides emit particles with similar energies. On the other hand, the counting efficiency is high and the background usually low so that high sensitivities can be reached.

In γ ray spectrometry the characteristic γ radiation emitted in the de-excitation of nuclides is used to detect and characterise a radioactive decay or other nuclear reactions. Especially the high resolution variant using HPGe detectors is often applied to determine the amount of different radioactive nuclides in samples of various kinds. By using very radiopure materials – itself characterised by radioassaying techniques – for the construction of such a detector system, a very low intrinsic background can be reached. If such a system is combined with a sophisticated shielding consisting of different active and passive components, very high sensitivities for radioactive nuclides up to $1\ \mu\text{Bq}/\text{kg}$ can be achieved. This is only possible in case large amounts of sample are used. Although such sensitivi-

2. Background knowledge about low level radioactivity measurements

ties furthermore require data acquisition times of several weeks or even months, this assaying technique is the only one that is able to detect the possible disequilibrium in the natural occurring decay chains of ^{232}Th , ^{238}U and ^{235}U . Because of the high energy resolution of HPGe detectors it is possible to analyse samples containing a large number of radioactive nuclides. Nevertheless, in some cases it is necessary to unfold the recorded spectrum to determine the contained nuclides. In contrast to mass spectrometry γ ray spectrometry is a non-destructive method so that it is possible to use the material that was assayed by γ ray spectrometry in a later application. For details about practical aspects of γ ray spectrometry see the explanations in Section 4.3 as well as Chapters 5 and 6.

The sensitivity of γ ray spectrometry for some nuclides can be increased by irradiating the samples with thermal neutrons, for example inside a nuclear reactor. For some nuclides like ^{238}U or ^{232}Th neutron activation analysis (NAA) makes the direct detection possible in the first place. By neutron activation (NA) many radioactive nuclides can be converted to ones with a shorter half life and thus higher activity. During the sample irradiation in most cases one neutron is captured by a nucleus. The created nucleus has a mass number that is increased by one and is in an excited state, which promptly de-excites by emitting a γ ray (Equation (2.1)).



The produced nuclide decays with a half life $T_{1/2}$, for example by β decay (compare Equation (2.2)). This decay often leaves the daughter nucleus in an excited state so that the β particle is accompanied by the emission of characteristic γ rays (compare Equation (2.3)). These γ rays are used to detect the decay by γ ray spectrometry so that the amount of the target nuclide ${}^A\text{E}$ contained in the sample can be determined. The applicability of this method depends in a complex manner on the elemental composition of the sample as well as the ratio of the half lifes of the different produced nuclides. If the sample matrix is activated by irradiation with neutrons to a large extend, trace elements are only detectable with a high sensitivity in case the half life of the matrix nuclides is much shorter than the one of interest or the produced radionuclide of interest can be chemically separated from the sample matrix. The first is the case for light elements like H, C, N, O, F and Si, which are often contained in sample matrices [ABB⁺02]. If NAA is applicable for the detection of a certain nuclide in the first place is determined by the neutron capture cross-section of it.

The decay of some radionuclides of interest like ^{238}U , ^{232}Th or ^{210}Po is not accompanied by a γ ray emission of significant intensity. Therefore, their activities can not directly be determined by γ ray spectrometry. As an alternative it is

possible to use α spectrometry instead. In contrast to γ ray spectrometry α spectrometry uses very thin samples of low mass, since the range of α particles is very short. Because of this, measurements have to be carried out in an evacuated chamber so that the energy loss of the α particles before hitting the detector can be minimised. The used detectors are usually based on silicon with a flat and very thin shape, since the range of α particles in the detector material is very low. Due to the very low detector volume the interaction probability of γ rays within the detector is very low as well. In combination with the relatively high energy of α particles of approximately 4 MeV to 9 MeV (α particle emissions in the natural decay chains) very low background count rates in the order of 10 cts/d, depending on the detector size, can be reached without the necessity to apply thick shielding.

All three natural occurring decay chains of ^{232}Th , ^{238}U and ^{235}U contain at one stage different isotopes of the radioactive noble gas radon (Rn). Due to its high ability to diffuse out of materials the radioactive equilibrium of the decay chains can therefore be disturbed. This has a major influence on the activity determination by γ ray spectrometry so that samples should be stored in sealed containers for a certain time to allow for a re-establishment of the equilibrium. For many applications of the assayed detector materials radon emanation is one of the limiting aspects. Due to this, several experiments have developed very complex apparatuses to be able to directly measure the radon emanation of materials or radon content of liquids and gases respectively. Due to the short half lives of the radon isotopes ^{219}Rn and ^{220}Rn of less than 60 s only ^{222}Rn can be evaluated in these measurements. Large amounts of the sample or the sample flushing gas are filtered by very radiopure charcoal so that the radon gets enriched in the filter. Afterwards special techniques are used to purify the sample, which is then filled with a counting gas into a proportional counter. A detailed discussion of the procedure and its requirements to the used equipment can be found in [ABB⁺02]. Remarkable sensitivities of 50 μBq for a single sample are quoted there.

Further methods exist but are not widely used. A detailed discussion of the techniques applied by the BOREXINO [AAB⁺09] collaboration to investigate radioimpurities in the detector materials at a remarkable sensitivity level can be found in [ABB⁺02].

2.2. Radionuclides of interest of low background material assaying

As discussed above, low background γ ray spectrometry is used to characterise any kind of material necessary for the construction of experiments for ultra rare event searches with respect to their radionuclide content. Usually all kinds of radioactive nuclides inducing background signals in the detector set-up are undesirable. Due to this, material samples are screened for any kind of γ ray emitting

2. Background knowledge about low level radioactivity measurements

nuclides, but the primordial radioactive nuclides (see Section 2.2.1) and the natural decay chains (see Section 2.2.2) are the ones that can often be detected. Nevertheless, also cosmogenic and anthropogenic nuclides, discussed in Section 2.2.3 and Section 2.2.4, can be found in material samples, but less frequently than the primordial ones. Materials that contain the three natural occurring decay chains as well as ^{40}K are within the scope of γ ray spectrometry sometimes referred to as natural occurring radioactive material (NORM), although in the exact meaning materials containing any of the primordial as well as the cosmogenic nuclides can be referred to as NORM.

2.2.1. Primordial radionuclides

All nuclides that exist since the stellar nucleosynthesis are referred to as primordial. Besides ^{232}Th , ^{235}U and ^{238}U , which are the starting nuclides of the three naturally occurring decay chains (see Section 2.2.2), also ^{40}K belongs to the primordial radionuclides often detected in material samples. In addition to these four nuclides usually identified in γ ray spectra, a lot more elements have primordial radioactive isotopes. ^{113}Cd for example is a β^- emitter with a half life of $(8.00 \pm 0.11(\text{stat}) \pm 0.24(\text{sys})) \times 10^{15}$ a [DRW⁺09] and a relatively high natural abundance of 12.22 % [BLB⁺05]. Due to this, its decay by far dominates the low energy region of the background spectrum acquired by the COBRA low background detector set-up. Other primordials like ^{190}Pt ($t_{1/2} = 6.5 \times 10^{11}$ a) or ^{144}Nd are very long-lived α emitters. ^{176}Lu and ^{138}La emit a significant amount of γ radiation in their decay. Consequently, lanthanum bromide crystals used as scintillation detectors see a significant intrinsic background, which rules out their usage in low background applications. Beside from these examples all nuclides undergoing double β decay like ^{116}Cd , ^{76}Ge , ^{130}Te , ^{136}Xe and ^{150}Nd belong to the group of primordial radionuclides.

2.2.2. Natural decay chains

The primordial parent nuclides ^{232}Th , ^{235}U and ^{238}U of the three (still existent) natural decay chains can be found in many of the natural occurring mineral materials, since the average elemental abundance in the earth's crust is with 9.6 mg/kg (Th) and 2.7 mg/kg (U) [Lid05] respectively relatively high. With the mother nuclides the whole decay chains are inevitably contained in these materials as well, unless any chemical separation did occur. Because of this, for example metals can contain traces of the decay chain nuclides, the amount depending on the exact production process and radionuclide content in the mined ore.

A graphical representation of the three natural decay chains can be found in Appendix A. Each of the chains ends with an isotope of lead, which are the stable nuclides with the highest mass number. All natural decay chains also contain one isotope of the noble gas radon, which can easily diffuse out of many materials. As

a consequence it is possible that the activity of the starting nuclide of each decay chain calculated from the activity of the daughter nuclides of radon is lower than the one calculated from the nuclides in the first part of the chain. In this case the chain is said not to be in equilibrium.

Many nuclide activities in the three decay chains can not directly be determined by γ ray spectrometry, since no or only γ rays with very low emission probabilities are emitted. This is for example the case for ^{232}Th and ^{238}U . Other nuclides like ^{228}Ac or ^{214}Bi have very complex decay schemes, which often lead to unusable peaks in the γ ray spectra due to true coincidence summing (TCS) (compare Section 2.3.2). In addition, many γ rays of the decay chains interfere with others so that an evaluation of these would be very complex. Because of this, only some γ ray peaks of each decay chain are used to determine the activities. Both uranium decay chains contain at least one long-living nuclide in addition to the starting nuclide itself. In the case of ^{238}U this is problematic, since activity of the first part is usually determined via a γ ray of very low emission probability and therefore a dis-equilibrium of the chain can not be detected reliably.

The 2614.5 keV γ line emitted in the decay of ^{208}Tl found in many spectra is usually referred to as the energetically highest natural occurring γ line. Actually this is not correct since it is only the energetically highest γ line with a significant emission probability. In the decay of ^{214}Bi γ rays with energies up to 3183.6 keV are emitted but the emission probabilities of the ones with energy higher than 2614.5 keV are lower than 0.04 %.

2.2.3. Cosmogenic radionuclides

In addition to the above mentioned NORM nuclides cosmogenic produced ^7Be can be included within the scope of γ ray spectrometry in the group of NORM nuclides as well. It is produced by spallation reactions of heavy cosmic particles with oxygen and nitrogen in the atmosphere [Gil08]. Due to the same mechanisms ^{14}C is produced, which is a pure β emitter. Due to its approximately constant concentration in the atmosphere and uptake by living animals and plants, this nuclide is the basis for radiocarbon dating. Besides these nuclides, a lot more are produced for example by capture of secondary neutrons induced by cosmic radiation in the atmosphere. In materials containing silver that are exposed to these neutrons significant amounts of ^{108m}Ag ($t_{1/2} = 438$ a) and ^{110m}Ag ($t_{1/2} = 249.78$ d) are produced. The analysis of such a sample and the consequences of the decay of these nuclides for the COBRA experiment are discussed in Section 6.2.1.

If copper and germanium are not stored underground to shield them against cosmic radiation, different short- and long-living radionuclides are produced in these materials. The activation of copper for example leads to ^{57}Co , ^{58}Co and ^{60}Co . Except from the latter these cobalt isotopes are produced in germanium

2. Background knowledge about low level radioactivity measurements

as well. Additionally ^{54}Mn and ^{65}Zn can be found in activated germanium. For further discussion of these cosmogenic radionuclides see Section 3.5.1 and the references therein.

2.2.4. Anthropogenic radionuclides

The third group of radionuclides are man-made and can partly be found in environmental samples or detector construction materials. Due to the industrial application of ^{60}Co for example in “refractory lining of blast furnace to monitor the lining thickness and abrasion of these sealed vessels” [MLB⁺08] steel samples can contain significant amounts of this nuclide. By recycling of contaminated metals or accidental melting of not properly disposed radioactive sources, iron based materials can contain also other artificial radionuclides (compare [MLB⁺08]). The long-living nuclide ^{137}Cs and several other nuclides with different half lifes are and were released into the environment in accidents of nuclear (power) plants as well as tests or usage of nuclear weapons. At some sites, where it was or is worked on nuclear material in industrial scale, large amounts of radioactivity have been intentionally released into the environment, often aggravated by even larger accidental releases. Examples are the industrial complexes at Mayak, Russia, or Sellafield, England.

2.3. Special aspects of γ ray spectrometry

The spectrometry of γ radiation bases on the interaction of γ rays with the detector material by photo effect and Compton effect as well as pair creation and the subsequent spectrometry of the recoil electrons. It will be waived to explain the different kinds of γ ray interaction as well as the mode of operation of HPGe diodes and electron spectrometry, since this can be found in common physics books. A very thorough discussion can be found in [Gil08]. In the following, several important aspects of γ ray spectrometry are discussed instead.

As it was already explained in the discussion of neutron activation analysis in Section 2.1, a γ ray emitted after the decay of a radioactive nuclide can be used as a signature for the preceding decay. After the decay of the mother nuclide for example by the emission of a β or α particle the daughter nucleus often remains in a very short-living excited state (compare Equation (2.2), page 14). As one possibility the excitation energy can be released by the emission of a characteristic γ ray (compare Equation (2.3), page 14). Since in γ ray spectrometry usually the activity of the mother nuclide with a significant half life is of interest, the promptly emitted γ ray is often assigned to the decay of the mother nucleus what, strictly speaking, is wrong. That the de-excitation belongs to the daughter nuclide is usually of low relevance, although exceptions because of possible summing with X-rays emitted by the daughter nucleus exist.

The '356.01 keV γ ray of ^{133}Ba ' actually means the 356.01 keV γ ray emitted after the decay of ^{133}Ba by its daughter nuclide ^{133}Cs (compare Figure 2.1). This common notation is used in this work.

2.3.1. Efficiency

In γ ray spectrometry with HPGe detectors several different terms with respect to efficiency are used. The relative efficiency is a measure for the detection capability of an HPGe detector for ^{60}Co in comparison to a standard 3 in \times 3 in sodium iodine (NaI(Tl)) detector, measured in a configuration according to the IEEE Std 325-1996 standard test procedure [IEE97].

The intrinsic efficiency describes the absorption characteristics of the detector for a γ ray impinging on it. It depends on the geometry of the detector (crystal) and the absorption coefficient of germanium. Due to the energy dependency of the latter the intrinsic efficiency is energy-dependent as well. This measure can be used with the additions 'total' or 'full energy peak (FEP)' to describe the intrinsic detection efficiency of an impinging γ ray anywhere in the spectrum or in the peak corresponding to the γ ray energy.

The most relevant measure in γ ray spectrometry regarding efficiency is the (absolute) FEP efficiency. In addition to the intrinsic efficiency it also includes the geometry between source and detector. The geometry in turn contains not only the plain spatial arrangement but also the self absorption of γ rays in the sample matrix. The self absorption depends on the elemental composition and the density of the sample and leads to a fast decrease of the sensitivity for energies lower than approximately 80 keV. The FEP efficiency is necessary to determine the activity of a certain nuclide within the sample. The determination is based on the counts registered in the peak that corresponds to the full energy deposition of the γ ray within the sensitive detector volume. The two fundamentally different approaches to determine the FEP efficiency are explained at the beginning of Chapter 5 and the detailed Monte Carlo (MC) simulation studies conducted to improve the determination of this measure are described in the following of that chapter.

2.3.2. Summing

To increase the sensitivity of a given detector set-up for a nuclide of interest it is essential to position the sample in such a way that a maximal FEP efficiency is achieved. By placing the sample directly on the detector endcap, the solid angle that is covered by the detector can be maximised. In many cases the detector shielding is constructed in such a way that the germanium detector can even be surrounded by the sample. In case of liquids, gases and bulk material special Marinelli beakers can be used to surround the detector at its side and the front window with the sample.

2. Background knowledge about low level radioactivity measurements

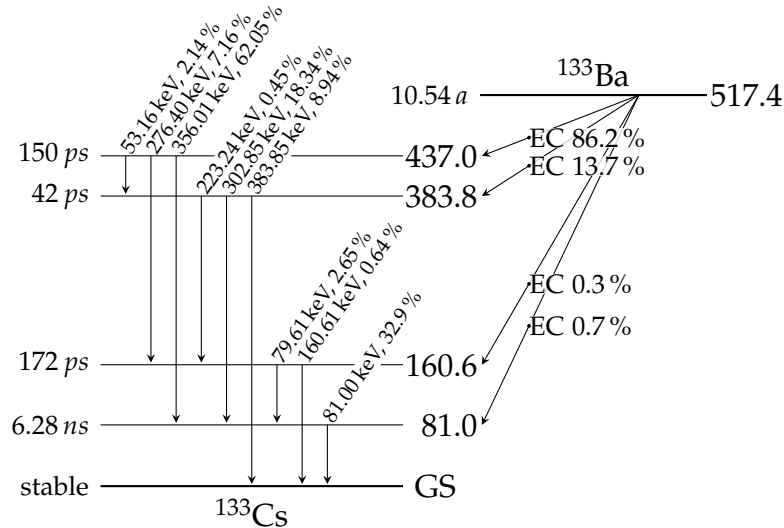


Figure 2.1.: Decay scheme of ^{133}Ba . Emission probabilities per decay of parent nuclide. Decay data taken as ENSDF from [Lab13].

As a consequence of the close geometry of the sample to the detector, problems due to summing do occur. Charge carriers induced by an γ ray interaction in the depletion zone of a semiconductor detector need a certain time to drift within the applied electrical field. Because of the consequently necessary charge collection time Δt , which is usually in the range of 1 μs to 10 μs in HPGe crystals, the interaction of two γ rays with the detector during this period can usually not be distinguished from a single interaction of a γ ray with the summed energy (see discussion below). This effect, called summing, can occur due to two different processes.

The first is called random coincidence summing (RCS) and describes the summing of γ rays emitted during the randomly coincident decay of two or more nuclei. On the one hand the probability for this effect strongly increases with the activity contained in a sample, since the probability for two or more decays during a time window Δt varies with the probability for the single decay and is Poisson distributed. On the other hand the probability for RCS varies with the geometry between sample and detector. The larger the solid angle that is covered by the detector, the more likely it is that more than one γ ray interacts with the detector crystal at the same time. Due to this, RCS can be reduced by placing the sample at a larger distance and is not of relevance for the measurement of already nearly radiopure samples.

The second effect is called true coincidence summing (TCS). It describes the interaction of more than one γ ray with the detector, which were – within several picoseconds – truly coincident emitted in a decay of a single nucleus. Thus, this effect can only be observed in case the excited daughter nucleus de-excites not directly to the ground state but via further energy levels. One example for this

situation is the decay scheme of ^{133}Ba (Figure 2.1). In case the sum of two γ transitions exists also as a single transition the resulting full energy peak contains both processes. Due to their lower energy the single γ rays of the sum have a higher interaction probability, which adds further complexity to the determination of the FEP efficiency. This effect depends only on the chosen geometry during data taking and therefore is also a problem for low count rate γ ray spectrometry. In case the determination of the sample activity is done by comparing the measurement with a standard of known activity containing the nuclides of interest the matrix of the sample and the standard should be as similar as possible since especially the self absorption of low energetic γ rays within the sample and with it the summing probability varies with the matrix parameters. If the FEP efficiency is determined by MC simulation, it is essential to model the emission characteristics of the nuclide of interest as good as possible to take the effect of TCS correctly into account. Further discussion regarding TCS and MC simulation can be found in Section 5.3.

2. Background knowledge about low level radioactivity measurements

3. Detector system

In contrast to ultra low background γ ray spectrometry systems that are operated in special underground laboratories the set-up of the DLB is located above ground in the experimental hall of the Faculty of Physics, TU Dortmund. As it can be seen in Figure 3.1 it consists of four major components. The artificial overburden, also referred to as outer shielding, provides a certain attenuation of cosmic rays and houses all other components. Inside of the overburden the multilayer shielding against environmental radioactivity and neutrons is placed, which is sometimes referred to as lead castle or inner shielding and which in turn encloses the HPGe detector. An active veto detector consisting of plastic scintillator sheets read out by photomultiplier tubes (PMTs) is installed (partly) around the lead shielding to detect cosmic particles that penetrate the outer and hit the lead shielding. It is used to suppress signals induced by cosmic rays in the HPGe detector.

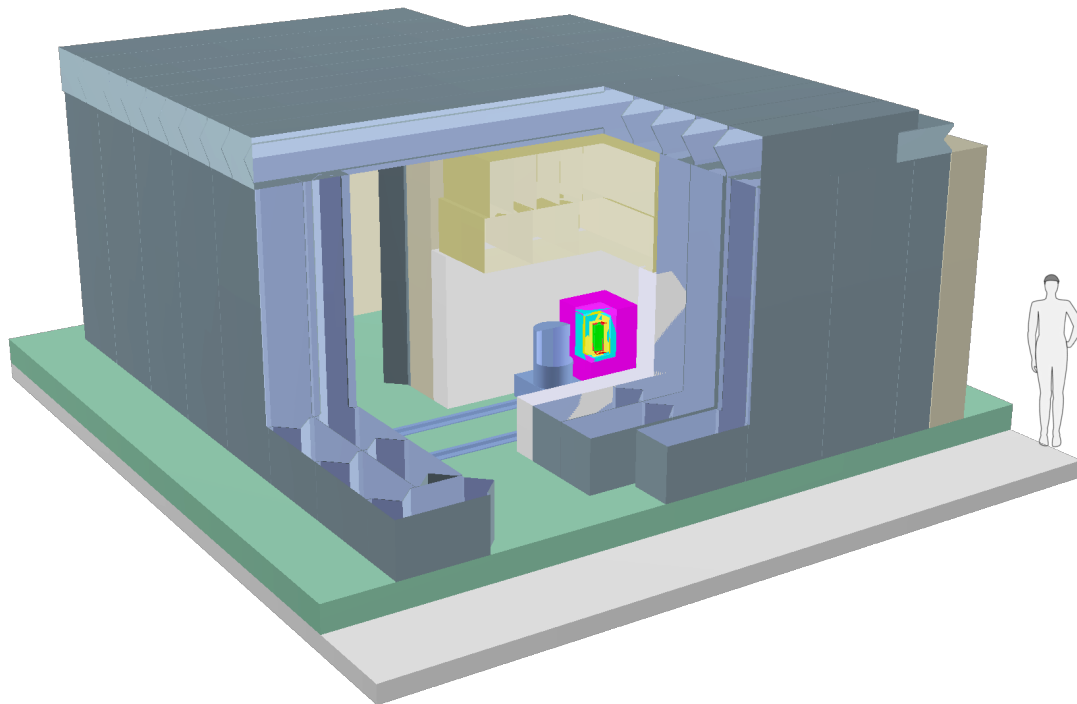


Figure 3.1.: The set-up of the DLB as a (simplified) digital model, implemented in GDML. The outer shielding consist of iron (ochre colour) and concrete blocks (grey and light brown). The inner shielding is shown in magenta. The veto detector is not shown.

3. Detector system

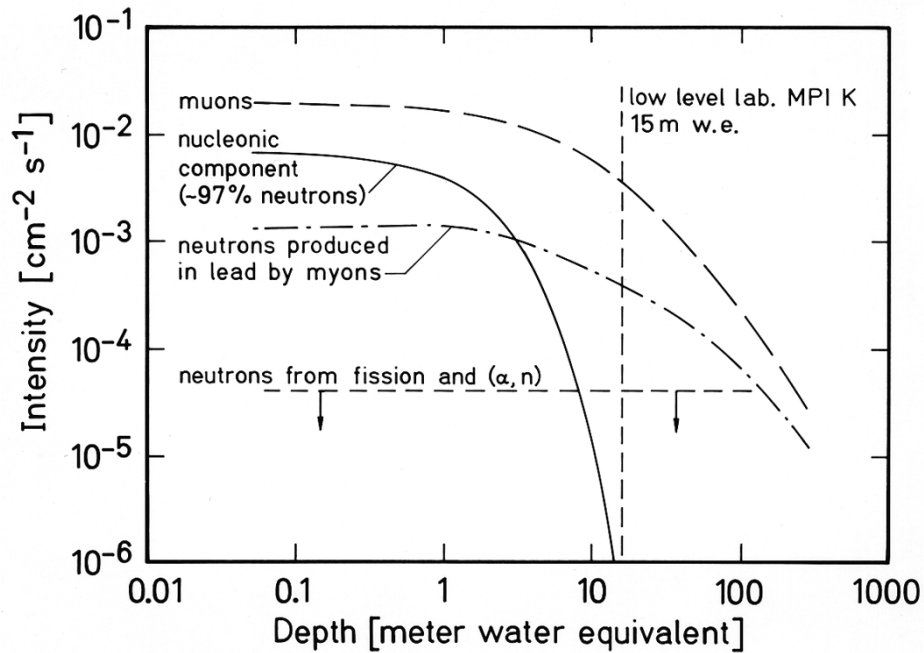


Figure 3.2.: Flux of primary and secondary cosmic rays in dependence of overburden in mwe. Reprinted from [Heu93] with permission from Elsevier.

3.1. Shielding

3.1.1. Outer shielding

γ ray spectrometry systems based on germanium detectors used for material assaying are usually operated under an overburden between hundred and several thousand meters of water equivalent (mwe) to suppress the flux of cosmic rays and its contribution to the background level. However, as can be seen in Figure 3.2, the soft component of cosmic rays can already be shielded by a few meters of water equivalent. Nevertheless, only some detector systems exist with a shallow overburden.

Since some options of setting up the DLB at a shallow underground location were discarded due to different disadvantages, the DLB was erected inside the university campus above ground with a special outer shielding providing an overburden of 10 mwe. The author has planned, optimised and build the outer shielding as part of his diploma thesis [Ned09]. It consists of approximately 319 t (mostly) barite concrete steles and 43 t cast iron blocks assembled to an enclosure of roughly 7 m \times 7.5 m \times 3.5 m outer dimensions. The cast iron blocks are placed with their edges on two 1.7 m high stone walls surrounded with concrete steles so that a low measuring room in form of a tunnel of 3 m length, 1.4 m width and 1.7 m height results. It was constructed as low as possible to maximise the overburden, since the maximum height of the whole outer shield was fixed. Into this

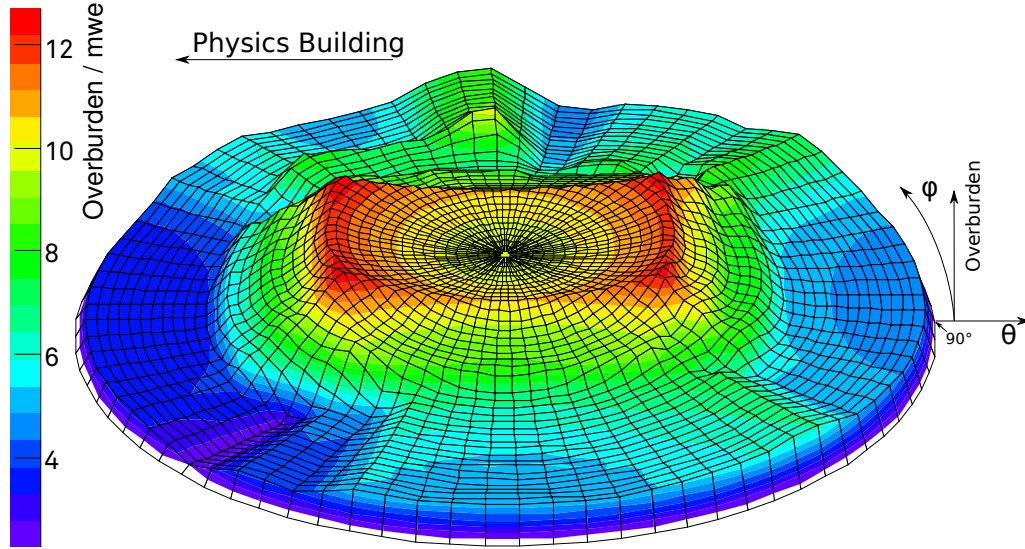


Figure 3.3.: Angular distribution of the overburden. The zenith angle θ corresponds to the radius, the height z and the additional colour coding to the overburden in mwe [Ned09]

tunnel the inner shielding, described in Section 3.1.2, together with the HPGe detector is driven to the measuring position.

This assembly of the outer shielding (see Figure 3.1) results in an angular distribution of overburden at the measuring position, which can be seen in Figure 3.3. The influence of the cuboid-shaped iron block and the corners of the placed concrete steles are clearly visible. Only above a zenith angle θ of more than 45° the overburden drops below 8 mwe. Since the flux of muons decreases approximately with $\cos^2 \theta$ for muons with $\sim 3 \text{ GeV}$ energy [PDG12], less overburden is needed at high angles θ . A detailed description can be found in [Ned09].

The whole outer shielding was sealed and is kept under a slight overpressure by ventilating with filtered air to avoid dust diffusion into the laboratory. As a positive side effect the already relative low radon concentration of $(32.1 \pm 1.0(\text{stat.})) \text{ Bq/m}^3$ in the air is further lowered. When using fresh air from outside of the experimental hall, a mean radon concentration of $(12.9 \pm 0.3(\text{stat.})) \text{ Bq/m}^3$ can be achieved. Since the large temperature range of the outside air can lead to large variations of the temperature in the laboratory as well, which again has an influence on the data acquisition (DAQ) electronics, the ventilation with air from the experimental hall was tested as well for the influence on the radon concentration. In this case the air surrounding the outer shielding acts as a thermal buffer and a radon activity of $(20.9 \pm 0.5(\text{stat.})) \text{ Bq/m}^3$ can be measured. This value is somewhat higher than the value obtained using fresh air from outside since the building materials of the experimental hall emanate radon as well. On the other hand it is lower than the concentration without ventilation since the air volume in the hall is larger than the one in the DLB. The data

3. Detector system

were taken end of February 2010 with a radon measuring device *Alpha Guard*¹ in pumping mode by Saphymo (formerly Genitron). The device was kindly provided by the Laboratory for Isotopes at the University of Bochum (Zentrales Isotopenlabor ZIL, RUBION, Universität Bochum).

3.1.2. Inner shielding

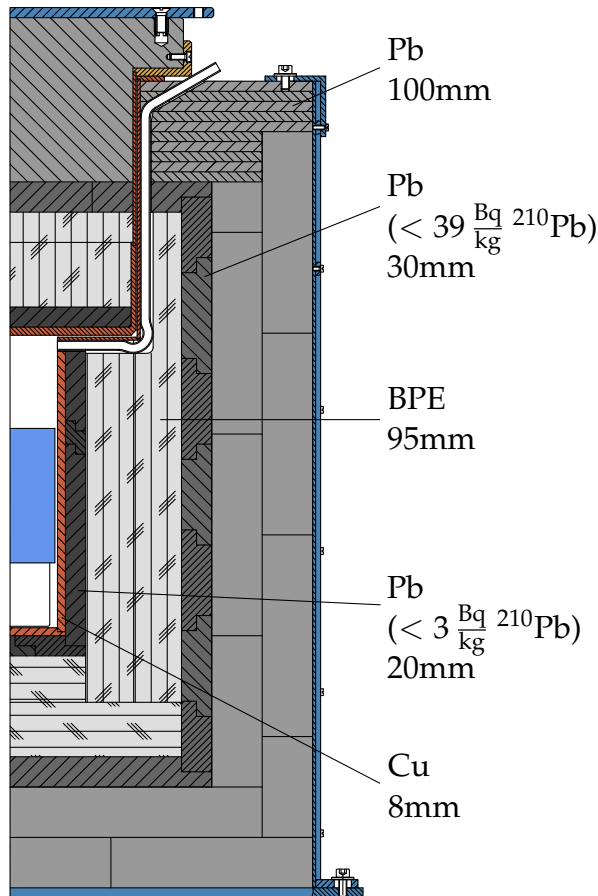


Figure 3.4.: Schematic drawing of the different layers of the inner shielding.

inside the lead shielding by cosmic protons and muons (compare Figure 3.2). The integration of the neutron moderator and absorber into the inner shielding demands a high radiopurity of this material, otherwise the background of the detector is in turn increased by the impurities.

The inner shielding was designed as a part of the diploma thesis of H. Gastrich [Gas09] and bases on the shielding concept developed by W. Wahl, ISuS [Wah08]. As one can see in Figure 3.4 it consist in total of five different layers. From the

The inner shielding against environmental radiation, radioactivity and neutrons has a multilayer layout optimised for a set-up location above ground. In contrast to deep underground locations where the shielding usually consists only of lead and a thick copper layer next to the detector, the design for non underground locations has to be completely different to minimise for example the effect of neutron interactions with copper and accompanied activation.

Also the neutron shielding component has to be designed differently. In underground locations it is placed outside of the lead shielding since neutrons here originate almost exclusively from the surrounding environment, e.g. the rock. In contrast, in above ground set-ups the neutron shield should be integrated into the inner shielding due to the fact that a significant part of the neutrons impinging on the detector are produced

¹http://www.genitron.de/products/alpha_features.html

outermost to the innermost these are

- 100 mm standard lead in form of bricks of size 200 mm × 100 mm × 50 mm, placed in two layers to avoid gaps, with an unknown activity of ^{210}Pb ,
- 30 mm lead with an activity of less than 39 Bq/kg ^{210}Pb ,
- 95 mm boron loaded polyethylene (BPE) as a neutron moderator and absorber,
- 20 mm lead with an activity of less than 3 Bq/kg ^{210}Pb and
- 8 mm electrolytically produced copper.

A part of the standard lead was purchased from Metall-Technik-Halsbrücke, Germany (bricks) and JL Goslar, Germany (plates) and is not hardened with antimony. The other part of the lead bricks was already available in the laboratory and is of unknown origin and quality. The low activity lead layers with $< 39 \text{ Bq/kg}$ and $< 3 \text{ Bq/kg}$ ^{210}Pb were purchased in form of standard lead bricks from Plombum, Poland, and cut and machined to their final shape by the mechanical workshop belonging to the Faculty of Physics. The upper solid lead part of the shielding plug was produced by Von Gahlen, Germany.

A detailed description of the design of the shielding as well as the purpose of the different shielding layers and their arrangement can be found in [Gas09].

The structure of the removable plug is the same as the remaining part of the shield, except for the thickness of the outermost lead layer and the copper pot enclosing the layers and attaching them to the uppermost lead part. The plug can be removed with a small crane to allow access to the sample chamber of approximately $(94 \times 94 \times 93) \text{ mm}^3$ size above the HPGe detector.

The inner shielding together with the HPGe detector is mounted on a vibration damped heavy load wagon, which was manufactured as well as all parts of the inner shielding by the mechanical workshop. By this, it is possible to drive the detector system, which has a mass of approximately 2.8 t, under the iron block of the outer shielding to the measuring position. Due to the low height of the tunnel, necessary for large solid angle of the outer shielding's iron block, the detector system has to be driven out of the tunnel to introduce or change a sample.

The BPE used as a neutron moderator and absorber is the same material as the one used at the set-up of the COBRA experiment at LNGS. According to the diploma thesis by S. Oehl [Oeh04], the material was provided by the Forschungszentrum Karlsruhe (FZK), nowadays known as Karlsruhe Institute of Technology (KIT). The material consists mainly of polyethylene (PE) (chemical formula $(\text{C}_2\text{H}_4)_n$) containing about 14.4 wt% hydrogen [WB09] and is therefore a good neutron moderator. By mixing a compound containing boron into the PE, the material is as well able to absorb the moderated neutrons since ^{10}B , with a natural abundance of 19.9(7) % [BLB⁺05], has a large thermal ($kT \simeq 25 \text{ meV}$)

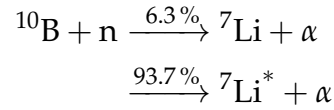
3. Detector system

Table 3.1.: Radiopurity data of BPE (sample mass 249.9 g), measured at LNGS (Detector GePaolo, live-time 340 512 s). Uncertainties with 68.3 % ($k = 1$) and upper limits with 95 % CL ($k = 1.645$).

Chain	Nuclide	Activity / mBq/kg
^{232}Th	^{228}Ra	< 3.0
	^{228}Th	7.0 ± 2.7
^{238}U	^{226}Ra	12 ± 3
	^{234}Th	< 75
	^{234m}Pa	< 230
	^{235}U	< 9.8
	^{40}K	< 64
	^{137}Cs	< 4

neutron cross section of 3850(80) b [CHO⁺11]. The used BPE contains 8.7 wt% diboron trioxide (chemical formula B₂O₃) [Oeh04], which corresponds to a boron content of 2.7 wt%.

The reaction of the neutron capture is of the type (n, α). In detail the following reactions are possible:



The branching ratios were calculated from the ratio of cross sections for the reactions (n, α_0) and (n, α_1) ((n, α) to ground and first excited state) [CHO⁺11]. In case of the reaction to the excited state ${}^7\text{Li}^*$ the energy is released by the emission of a 477.6 keV γ ray with an intensity of 100 % [Fir96]. As an alternative one could use a material containing lithium since the (n, α) reaction of ${}^6\text{Li}$ ends always directly in the ground state of ${}^3\text{H}$, but the reaction has only a cross section of 940.1 b for thermal neutrons [GZX⁺11] and ${}^6\text{Li}$ in addition only a natural abundance of 7.6 % [BLB⁺05].

Because of the 477.6 keV γ ray emitted in 93.7 % of all ${}^{10}\text{B}$ (n, α) ${}^7\text{Li}$ reactions, the placement of the BPE is crucial. Due to the neutron production by cosmic particles most of the high Z shielding material should be located outside of the neutron moderating layer, but the γ ray also has to be absorbed again. Because of this, more than 98 % of the ~ 2650 kg lead used in the DLB inner shielding is located outside of the neutron moderating and absorbing BPE layer. The 20 mm low background lead between the BPE layer and the HPGe detector attenuate the intensity of the emitted 477.6 keV γ rays to 1.9 % [BHS⁺10, Lid98].

This close positioning near the detector is only possible since the BPE is fairly radiopure. The results of the radiopurity measurement of this material, done by

M. Laubenstein at LNGS, are given in the diploma thesis of H. Gastrich [Gas09]. The data can be found in Table 3.1 and are included here since they are necessary for the analysis of the background spectrum in Section 3.5.1.

Due to the many different parts of the inner shielding the machining of these was not finished during the diploma thesis of H. Gastrich. He described the planned cleaning procedures for the different parts already in his thesis [Gas09]. Since some of the applied procedures did differ from the planned ones, these are described here shortly.

After the heavy load wagon was assembled on the spot due to its large mass, the cleaning of the lead bricks belonging to the outer layer was started. The outermost lead bricks were scrubbed with a special cleaning fleece, rinsed off with bi-distilled water and wiped with tissues soaked with acetone and with isopropyl alcohol afterwards. The parts of the < 39 Bq/kg and < 3 Bq/kg lead layers were wiped once with isopropyl alcohol soaked tissues, cleaned in an ultrasonic bath with acetone and isopropyl alcohol for 5 min each and wiped again. After the ultrasonic baths the innermost copper parts were in addition put into a 5 wt% citric acid bath for 30 min and rinsed off with bi-distilled water. The parts of the BPE layer were only wiped with tissues soaked each with acetone and with isopropyl alcohol since they were too large for cleaning in the ultrasonic bath. Since some parts had to be adjusted or individually machined during the assembling, the assembly of the inner shielding took some time. The HPGe detector (see Section 3.3) was mounted on a support platform on the heavy load wagon, its position fine adjusted and the cooling finger electrically insulated from the lead shielding with a thin PE foil to avoid ground loops. Details of the cleaning and assembly procedure is described in an internal note.

The whole arrangement of the size $600 \text{ mm} \times 600 \text{ mm} \times 800 \text{ mm}$ is surrounded by thin steel sheets in order to ensure the mechanical stability of the shield. This enclosure provides in combination with a sealing the encapsulation of the system against airborne radioactive radon. The latter diffuses out of the surrounding materials like concrete containing the primordial radioactive decay chains of ^{238}U , ^{232}Th and ^{235}U . To displace radon from the measuring chamber around the HPGe detector, a copper tube was included into the lead shielding, which allows the flushing of the chamber with gaseous nitrogen constantly evaporating from the detector dewar. Approximately 0.65 l/min of nitrogen are piped into the measuring chamber so that its volume is exchanged in less than 3 min. Another pipe next to the plug of the shielding (see Figure 3.4) allows optional electrical access to the chamber for coincidence measurements with a small detector, e.g. a CdZnTe detector.

3.2. Cosmics veto

The DLB is equipped with an active anti cosmics veto detector, in publications like [TH91] also referred to as an external guard counter, surrounding the inner shielding to suppress the background induced by cosmics penetrating the outer shielding. Since electrons and hadrons should be nearly completely blocked by the overburden, the main remaining cosmic rays inducing background in the detector system are muons. Muons can interact directly with the germanium detector or produce secondary particles within the inner shielding.

Due to the enormous efforts to suppress the background with the applied passive shielding measures, a major part of the remaining background is induced by interactions of cosmic rays. Because of this, the author designed and constructed an active veto detector during his diploma thesis [Ned09]. The veto detector consists of plastic scintillators read out by PMTs. According to [Maß01] all components were used before as parts of the forward trigger plane (FTP) of the former HARP² experiment at CERN. The constructed veto detector is mounted below the iron block of the outer shielding. It consists of a top plane and two side planes mounted parallel to the walls of the tunnel and hanging below the top. Since the top is wider than the distance between the sides, the veto detector has a Π -shaped cross section so that the detector and the inner shielding can be driven on the wagon into the tunnel and under the veto.

The used scintillators have a size of approximately $122 \text{ cm} \times 20 \text{ cm}$. At the short ends so-called fishtail PMMA light guides transform the rectangular cross section of the panels to the round front window of the used Hamamatsu *R2490-05* PMTs. For the application at HARP the scintillator thickness of 5 mm was sufficient, since the energies of the particles of interest were rather high. For minimal ionising particles like muons an average ionisation energy loss of 2 MeV/cm in plastic scintillator for particle energies above 100 MeV [Pau71] can be assumed. Therefore, an average energy deposition of 1 MeV for a vertical traversing muon can be expected. The variation of the energy loss in thin absorbers is usually described by a Landau distribution [Leo94].

The Landau distribution can not be neglected if nearly all muons traversing the scintillators have to be detected. Therefore, triggered spectra were taken and the thresholds of the used NIM discriminators accordingly adjusted. With the chosen thresholds the event rate of a single scintillator outside of the outer DLB shielding was found to be nearly twice as high as the rate of $180 \text{ m}^{-2} \text{ s}^{-1}$ one can roughly expect at sea level [PDG12, Booklet]. To reduce this rate the top of the veto was equipped with two layers of scintillators measuring in coincidence so that only particles passing both layers contribute to the overall veto signal. Although the source of the increased rate remained unclear within the framework of the authors diploma thesis – for detailed discussion see [Ned09] – it became

²hadron production

clear shortly afterwards that the increased background rate can be attributed to the interaction of environmental γ radiation.

To suppress this contribution usually scintillators with a thickness of 4 cm to 5 cm [PLBA96, SSK04] are applied and the discriminator thresholds for the PMTs increased accordingly. This is possible since the energy deposited by muons increases linear with the thickness of the scintillator, whereas environmental γ radiation deposits less than 2.7 MeV due to the highest natural (significantly) occurring γ line with 2614 keV (compare Section 2.2.2). Because of the fast response of organic scintillators, summing is negligible.

In [Ned09] the muon rate inside the outer shielding was measured to be $82.2 \text{ m}^{-2} \text{ s}^{-1}$ at a position $\sim 25 \text{ cm}$ below the iron blocks, assuming that the soft component of the cosmic rays is completely suppressed. This corresponds to a muon attenuation of 38.4 %. Using the densities of the cast iron blocks 6.95 g/cm^3 and the concrete shielding elements 3.31 g/cm^3 measured in [Ned09], their vertical thickness of 1.17 m and 0.5 m respectively and the continuous-slowing-down-approximation (CSDA) ranges given in [GMS01] for different materials, the minimal energy of muons passing vertically through the overburden can be calculated to $\sim 1.56 \text{ GeV}$ (with linear interpolation between given data points).

As discussed in Section 3.5, the background of the detector system is already reduced significantly by the veto build in the authors diploma thesis. The weak points of it are the single scintillator layers mounted at the two sides of the inner shielding, the fact that these do not extend to the lower edge of the shielding (only approximately to the height of the lower edge of the detector crystal) and the missing scintillators at the remaining two sides of the shielding facing the detector dewar and the opposite side. The single scintillator layers contribute to a large amount of veto rate (since the discriminator thresholds were set to detect all cosmic particles) and increase the dead time of the detector system. The cosmic radiation impinging on the areas of the shielding not covered by scintillators contribute to the background rate by direct and indirect interaction with the detector crystal. Because neutrons scatter very often, also the coverage of the shielding with scintillators below the height of the detector crystal is important. The rate of cosmic particles impinging from the two uncovered sides is lowered already since the used scintillators at the installed sides and the top are twice as long as the shielding and are therefore narrowing down the uncovered solid angle. Additionally, the length of the iron block above the detector is much higher than its width. Consequently, the influence of the completely uncovered sides is further suppressed. Even though several enhancements are still possible, a test with two scintillators crossed at the usual measuring position of the HPGe detector, which was not yet installed at that point, revealed that approximately 89 % of the cosmic particles directly hitting the 'detector' are detected by the active veto [Ned09].

To improve the active veto and suppress the remaining background further, Th. Quante planned in his master's thesis [Qua12] the upgrade of the veto system.

3. Detector system

The side walls of the veto detector will be reworked and improved by adding a second scintillator layer. The new veto walls will extend to the lower edge of the lead shielding. At the time of writing the supporting structures for the scintillators were produced in the mechanical workshop of the Faculty of Physics. The side opposite to the dewar will be covered by vertically mounted scintillators read out at their lower end. The coverage of the side towards the dewar is rather difficult due to the limited space available. Due to this, Chr. Nitsch tested several read out options for scintillators with and without light guides within his bachelor's thesis [Nit12]. The scintillators will be mounted with the light guides perpendicular to it and a chamfer of 45° at the wide end of the light guide so that light coming from the scintillator will be reflected towards the PMT. Although the light guide and scintillators are wrapped in reflecting foil, some light is lost with this read out method so that the discriminator thresholds have to be chosen really low and two layers have to be installed to suppress the increased counting rate from γ ray interactions, as mentioned above.

Since cosmic particles can induce signals in the germanium detector by prompt and delayed processes, the optimal time window for the rejection of signals induced in the germanium detector after each detected veto signal is controversially discussed in different publications. Values of $2\ \mu\text{s}$ up to "a few hundred microseconds" [LBPA96] can be found for example in [LPL⁺08, Heu91, SSK04, RA88], in parts depending on the used approach of applying the veto. In some publications only in case of a coincident signal of both the veto and the germanium detector the germanium event is discarded and the veto time is subtracted from the live-time. If the veto triggers without a coincident signal from the germanium detector, the veto trigger is ignored and the veto time for this trigger is not subtracted from the live-time. This approach can lead to an overestimation of the live-time of the system. The quoted veto times are most of the time based on measurements with a time to amplitude converter (TAC) started by the veto and stopped by the germanium signal. In these cases a spectrum representing the amplitude distribution of the output signal, proportional to the time difference, was used to obtain the optimal veto time.

Based on a recommendation by W. Wahl, who uses the approach to detect only coincidences between veto and germanium detector, a rejection time of $\sim 765\ \mu\text{s}$ per veto event was applied by triggering an adjustable monostable flip-flop. The chosen value is a trade-off to the value used by W. Wahl, since our group decided to stop the counting and with it the live-time of the detector system for each veto event detected (compare also Figure 3.9). With a total veto rate of $\sim 400\ \text{s}^{-1}$ for the set-up as described in [Ned09] a significant fraction of all veto events does overlap. Unfortunately, the multi channel analyzer (MCA) used to read out the germanium detector (described in Section 3.4) does not stop counting the live-time during an applied veto signal, although possible pulses from the germanium detector are rejected. Therefore, the veto time has to be measured externally. The

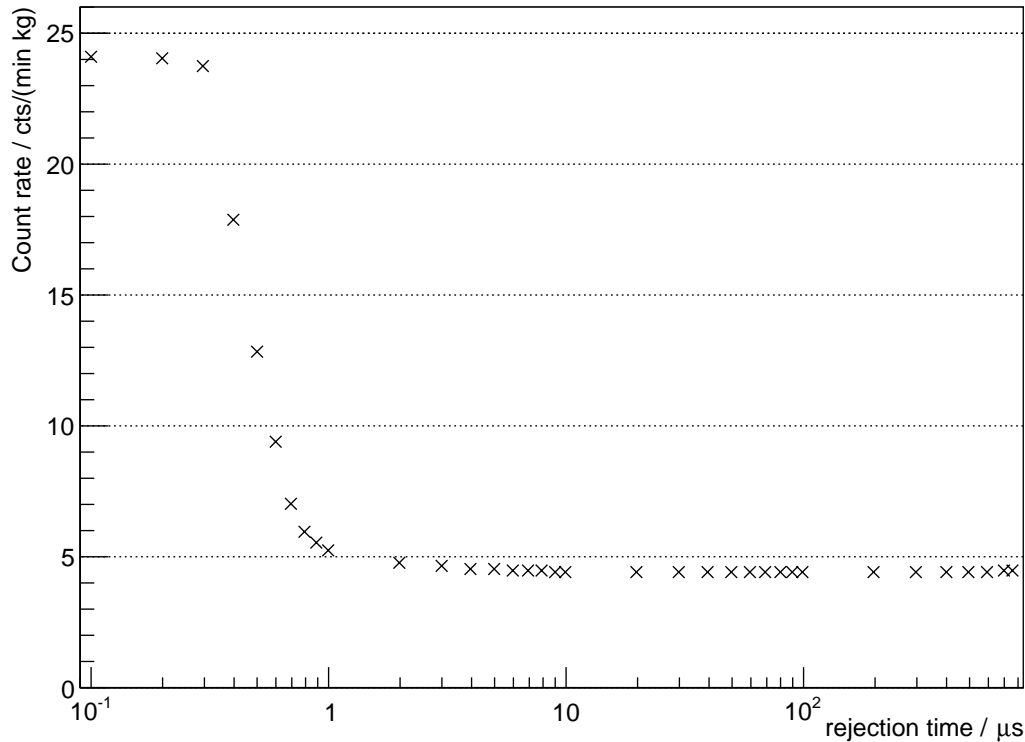


Figure 3.5.: Resulting background count rate in dependence of applied rejection time. [Qua12]

relative veto time is determined by gating a counter counting pulses from a pulser with the veto signal and dividing the number by the total number of applied pulses (compare also Section 3.4). With the above mentioned settings the total veto time sums up to approximately 16.7% of the real time of a data acquisition period.

The major drawback of the used read out by the MCA, which acquires a pulse height spectrum for a certain time, is that the resulting background spectrum for a certain applied veto time can only be obtained by taking data for some time. Due to the achieved low background a measuring time of approximately four weeks is necessary to collect enough statistics. To change the DAQ to an event based read out system (for details see Section 3.4), a VME single board computer was purchased. It allows the read out of the DLB detector system with one of the COBRA flash analogue to digital converters (FADCs), which were kindly provided by the AMANDA collaboration. This system allows to record the timestamps of the veto signals independently from the germanium detector signals. With this DAQ system it became possible to record the background data once and apply a certain rejection time during the offline analysis. In this manner the influence on the resulting background count rate and the possible suppression of peaks in the spectrum resulting from delayed processes can be investigated.

With this FADC based DAQ system Th. Quante investigated the effect of differ-

3. Detector system

ent rejection time lengths on the resulting background count rate in his master's thesis. He found out that the rate is decreasing significantly for times longer than $0.3\ \mu\text{s}$ (see Figure 3.5), reaching a minimal rate for a $200\ \mu\text{s}$ time window. For longer rejection times the rate increases slightly again, probably due to the increasing rejection time leading to a smaller life-time. Nevertheless, the rate does not change much for rejection times longer than $10\ \mu\text{s}$. Consequently, he recommended to use a pulse length of $50\ \mu\text{s}$ [Qua12]. This reduced rejection time per event leads to a total veto time of approximately 1.05 % [Qua12] for the current veto or 0.4 % for the veto top plane, measured with the pulser method explained above.

3.3. Germanium detector

The heart of the DLB is the HPGe detector, produced by Canberra Semiconductor NV in Olen, Belgium. It has a standard electrode (p-type) (semi-)coaxial diode with a relative efficiency (compare Section 2.3.1) of 60 % and a mass of approximately 1.247 kg. p-Type detector crystals have a lithium diffused outer n^+ contact with a typical thickness between $500\ \mu\text{m}$ and $700\ \mu\text{m}$ and an inner ion-implanted boron p^+ contact of $0.3\ \mu\text{m}$ thickness [Can09, Gil08]. Since the electrodes do not belong to the sensitive volume of the crystal, the thickness of the outer contact, often referred to as the dead layer, is crucial for the sensitivity to low energetic γ rays. Therefore, the effective thickness of the dead layer is experimentally determined in Section 5.2.1. Due to the usual thickness of the outer contact and the necessary detector endcap (see below), typical p-type detectors have an energy threshold of 35 keV to 40 keV and a very low sensitivity to energies slightly above.

The crystal has a diameter of 71 mm and a length of 60 mm. The inner contact, which is drilled from the bottom of the cylindrical crystal upwards along the z-axis, has a depth of 42 mm and a diameter of 10 mm [Can10].

The aim of construction of the DLB was to achieve a very low background level to reach the lowest possible detection limits (DLs) for different radioactive nuclides. Therefore, an ultra low background (ULB) cryostat was purchased together with the detector crystal, which is especially designed to avoid background contributions from the components needed to operate and read out the detector crystal. Because of this, the crystal is mounted inside a holder made of 99.99 % pure copper within an endcap made of a very radiopure type of aluminium with a guaranteed thorium and uranium content of less than 1 parts per billion (ppb) [Can08a], sometimes referred to as Kryal. In addition, the preamplifier is shifted from its normal position close to the crystal to the dewar so that the detector diode is shielded by the thickness of the full shielding from the often not very radiopure electronic parts like printed circuit boards (PCBs). In contrast to dipstick cryostats, the U-style integral type of the cryostat prevents any di-

rect paths for radiation to the germanium diode, which improves the achievable background level significantly.

During operation the detector has to be permanently cooled with LN₂ to 77 K to keep thermally generated leakage currents to a minimum. Although it is possible to store the detector at room temperature, this would support the slow diffusion of the lithium atoms of the outer contact into the crystal, which corresponds to a thicker contact and lower sensitivity for low energy γ rays. Therefore, the detector was kept permanently cooled since its delivery in 2008, except for one thermal cycle (warming up and cooling down again) of approximately 48 h duration. The level of LN₂ is permanently controlled with a level monitor developed by M. Alex and O. Schulz in [Ale09, Sch11] using the change of the capacitance of a cylindrical pipe with the LN₂ level.

3.3.1. Front window sensitivity

Several measurements to characterise the germanium detector were performed in the not installed state by H. Gastrich in [Gas09]. The subsequently ascertained demand for an extended characterisation with different uncollimated and collimated sources to determine the detector's response precisely was impeded by the assembled state in the inner shielding.

Other experiments, for example, did scanning measurements from different directions to determine the exact position of the germanium crystal and its supporting structures like the cup within the detector endcap [Key04, CLPBC⁺10]. Depending on the γ ray energy of the used radioactive sources, different features of the detector crystal can be verified. Cabal et al. used the 356 keV γ line of a collimated ¹³³Ba source to measure the (effective) diameter of the inner detector contact by doing a radial scan [CLPBC⁺10]. This energy is high enough to penetrate germanium up to the typical thickness of the closed end side of the crystal but on the other hand is low enough to be deposited to a large extend locally by single side interactions. Ashrafi et al. did characterise their detector by measuring many radioactive sources at many positions within the (r, z) -plane of the crystal and obtained a sensitivity map for the surrounding area of the detector (see [ALV99] and references therein). Budjás et al. even took an X-ray image of their detector to validate the manufacturers specifications [BHMS09].

Due to the limited space within the shielding, it is very complicated to do the scanning measurements with the detector surrounded by the shielding elements. Especially scans using γ lines with higher energies are difficult due to the necessary collimator dimensions. In addition, scans to determine the vertical position of the germanium crystal within the detector endcap are nearly impossible due to the very limited space between endcap and shielding. Furthermore, it would be very difficult to measure the vertical position relative to the upper edge of the detectors endcap.

3. Detector system

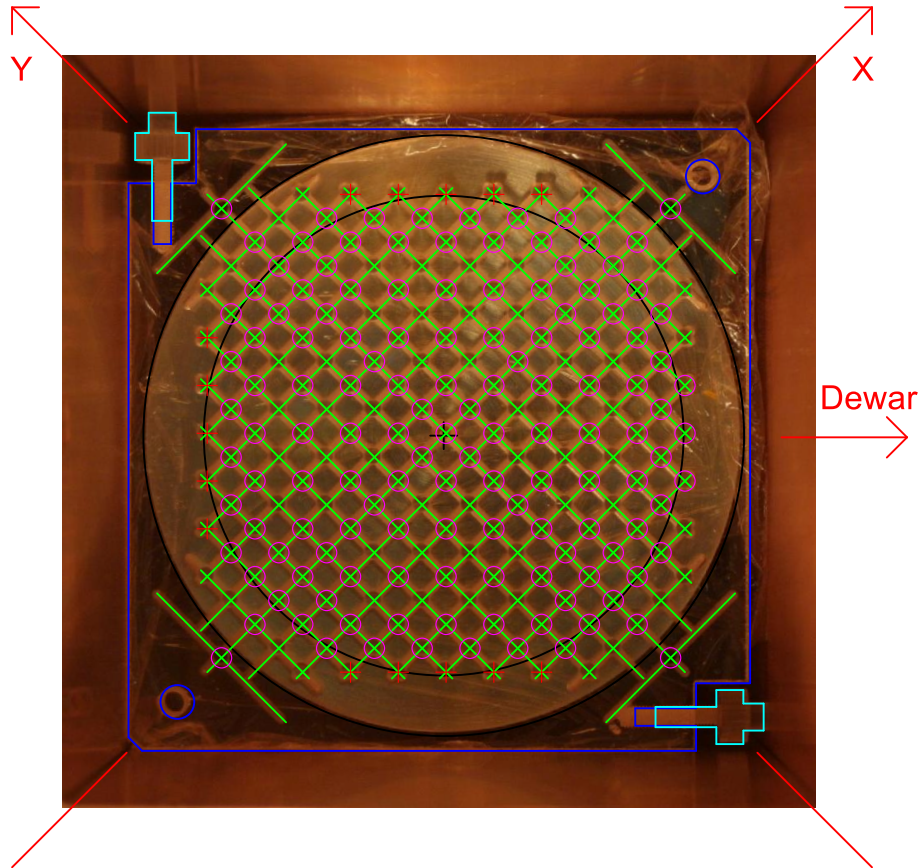


Figure 3.6.: Top view of the detector with positioning plate overlaid with the scanning grid (-) and used coordinate system. Measured positions (○), unreachable positions (+) and nominal crystal position (-) are marked.

Because of its thickness of approximately $700\ \mu\text{m}$ (compare also Section 3.3 and Section 5.2.1) the variation of the outer dead layer can be determined by using collimated low energy ($< 100\ \text{keV}$) γ rays. Therefore, a positioning plate with a grid of V-shaped grooves was designed, which can be fixed by two screws on top of the detector endcap. In Figure 3.6 a picture of the positioning plate, which was manufactured by the mechanical workshop, placed within the sample chamber and the CAD layout are superimposed. The displacement between the planned and the real position of the grid plate and with it also the position of the scanning points relative to the nominal crystal position was measured by the use of *QCAD*, a 2D CAD application available for Linux [Rib08], within the superimposed picture.

Furthermore, a collimator was constructed and build by the mechanical workshop (for details see Figure B.1). Since the used ^{241}Am source of type Bebig Am1.K17 has an activity of $40\ \text{MBq}$ and ^{241}Am besides the main emission of $59.54\ \text{keV}$ also emits higher energetic γ lines, a suitable material had to be used for the collimator. Due to this, the source with outer dimensions of $\varnothing 4.8\ \text{mm}$ and

16.25 mm length is surrounded by a lead tube with a wall thickness of 7.65 mm. The upper end is closed with a lid of 9.5 mm thickness and to the lower end a copper cylinder of 42.5 mm height and 20.5 mm diameter is attached. Copper was chosen since the K-shells X-rays have energies of ~ 8.0 keV and ~ 8.9 keV. In contrast to the X-rays of lead with energies of 72.8 keV, 75.0 keV and 84.9 keV, these lie well below the lower energy threshold of 40 keV, where p-type germanium crystals are sensitive. Due to the choice of applying copper the emitted X-rays are irrelevant in the measurement. The huge thickness of the copper cylinder was chosen to be able to collimate also the used γ lines with 98.97 keV and 102.98 keV energy and attenuate their intensity at every off-z-axis position at the collimator to a negligible level.

In addition to the undesirable emission of X-rays in lead, it is very difficult to produce a thin collimator hole in lead. The required method of electro erosion is not available at the workshops belonging to the TU Dortmund. The needed borehole in copper of more than 40 mm depth and only 1 mm diameter was kindly provided by M. Heilmann, Institute of Machining Technology at TU Dortmund (Institut für spanende Fertigung, TU Dortmund). To suppress also high energetic γ rays a thin lead plate of 2 mm thickness and a borehole of 1.5 mm diameter was added between the radioactive source and the collimator (compare page 145). Loaded with the ^{241}Am source the whole collimator was fixed by placing it inside a tube made from PMMA with a closed end having two tongues fitting into the grid of the positioning plate ensuring an automatic centring of the collimated γ ray beam at the desired measuring positions.

By using this scanning system, an extensive study to determine the homogeneity of the detector front dead layer was conducted. Since the acquisition times at the different position were chosen in that way to gather enough statistics in the two ^{241}Am peaks at ~ 100 keV, the total scan was very time-consuming. It is possible to determine the dead layer thickness locally at each scanning position by the measured ratio of peak areas at 100 keV and 59 keV due to the energy dependence of the absorption coefficient.

Figure 3.7 shows the peak count rate in dependence of the (x, y) scanning position. Omitting data points less than 2.5 mm away from the crystal edge a mean count rate of approximately 27.2 cts/s can be calculated. The rate varies by more than +11 % and -20 % around the mean and is especially dropping significantly along the negative y axis for $x = 0$. This can also clearly be seen in Figure 3.8, representing a cross section trough Figure 3.7. Taking the absorption coefficient for 59.54 keV γ rays in germanium from [BHS⁺10], the ratio of the minimal and maximal value of the rate and assuming the dead layer thickness to be the only source for this variation, one can calculate a thickness variation of approximately 290 μm . Since the variation of the count rate appears to be quite large, it was checked whether the possible slight movements of the source within its shielding above the collimator could be responsible for this. The latter can be excluded,

3. Detector system

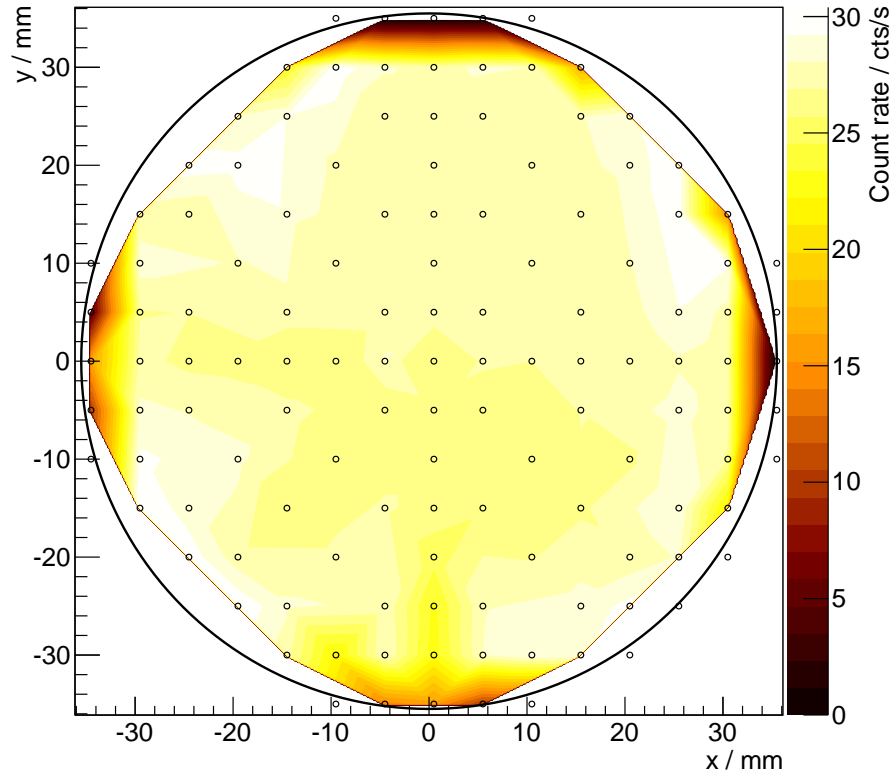


Figure 3.7.: Position dependent detector front-side sensitivity. Measured count rates of the ^{241}Am 59.54 keV peak. Data points (\circ) are marked. Compare Figure 3.6 for the positioning. The colour coding can only be taken as valid between crystal centre and data points within the detector edge.

since the radius of radioactive material within the source is larger than the possible displacement of the source above the collimator assuming a homogeneous distribution of the radioactive nuclei within the source.

Comparing the data in [CLPBC⁺10] with the obtained results, the variations seem to be plausible. Cabal et al. measured the count rate along the front face of an n-type germanium detector, which have a dead layer of less than $1\ \mu\text{m}$ compared to $\sim 700\ \mu\text{m}$ for p-type detector crystals (see also Section 3.3). They found even for such a highly sensitive detector type a count rate variation of approximately 15%. Nevertheless, it can not be completely excluded that the count rate variation is in part caused by any unnoticed movement of the collimator parts so that already the rate of impinging γ rays may have varied.

The more general characterisation measurements are included in Section 5.2 where they are used to minimise the deviations between the full energy peak efficiency determined by measurement and computer simulations. Up to now the described detailed front face scanning is not used for the optimisation of the Monte Carlo (MC) model of the detector system described in Chapter 5.

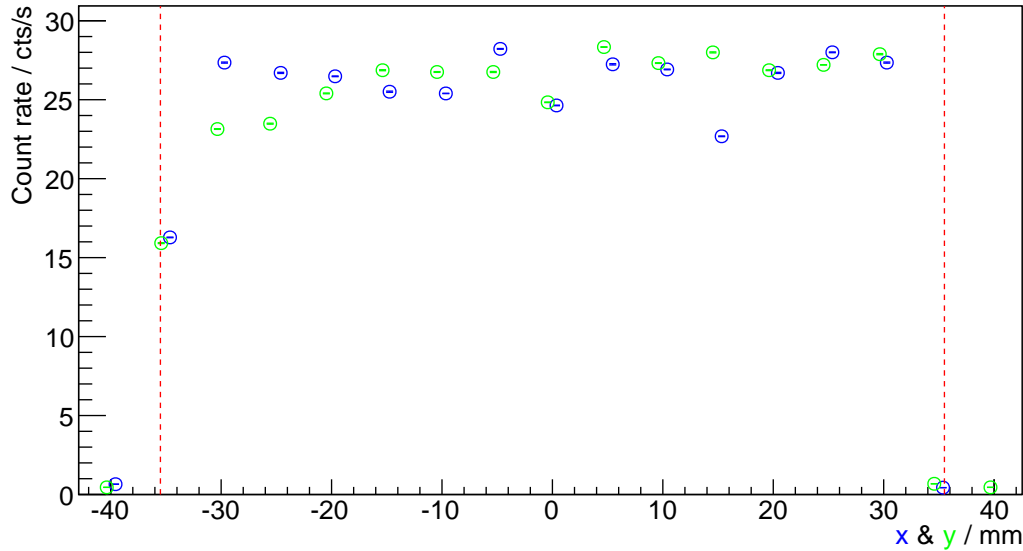


Figure 3.8.: Cross section through the detector front-side sensitivity in Figure 3.7. Measured count rates of the ^{241}Am 59.54 keV peak for $y = 0$ and $x = 0$ respectively. The crystal edge is indicated by the dashed, red lines. The statistical uncertainties of the data points are barely visible.

3.4. Data acquisition electronics

Most of the DAQ electronics described in the following are modules in the NIM format, placed in several NIM bins inside a standard 19" rack.

The positive high voltage (HV) bias of 3500 V to 4000 V that is required to operate the HPGe detector is provided by an Ortec *459 Bias Supply* and is applied via the preamplifier to the outer contact of the germanium crystal [Gil08]. A temperature monitoring circuit inside the preamplifier assures that the bias can only be applied to the crystal if it is in cold state.

The HPGe crystal is read out by a Canberra *Model 2002C Spectroscopy Preamplifier*, a charge sensitive resistive feedback preamplifier, which is mounted on the cryostat's detector arm next to the dewar. The input stage of this device is cooled by LN_2 for noise reduction [Can04]. The preamplifier mainly consist of a low noise field effect transistor (FET) fed back by a resistor parallel to the charge integrating capacitor, which ensures the discharge of the latter with an approximate time constant of 50 μs . The input of the preamplifier is connected to the inner contact (-) of the crystal and therefore collects the signal induced by the holes (the electrons drift to the outer contact (+)). This results in an output pulse of positive polarity with a steep rising edge of several 100 nanoseconds duration depending on the charge collection characteristics of the crystal. The main purpose of the preamplifier is to collect the charge induced by an interaction in the crystal and provide a high impedance input for the detector and a low impedance output for the main amplifier [Gil08]. Depending on the setting of an internal jumper, the

3. Detector system

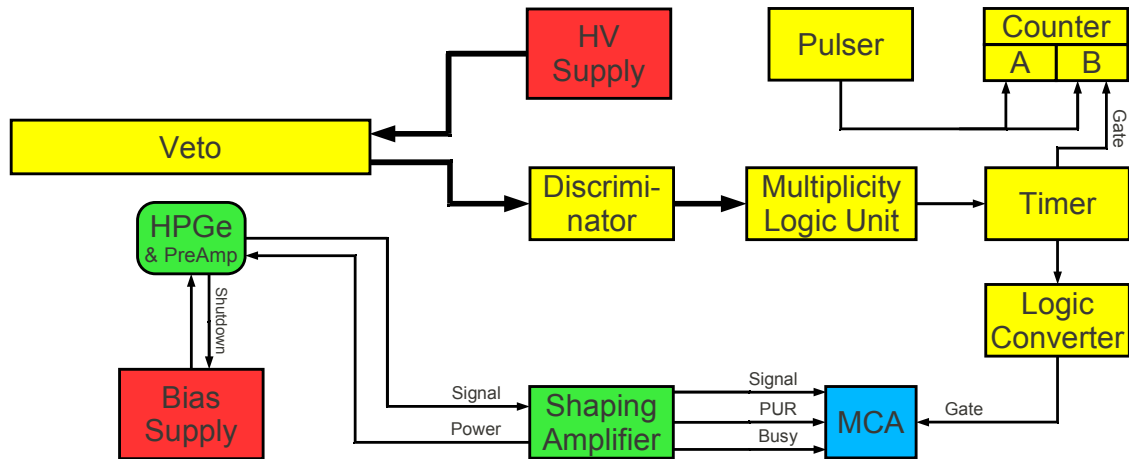


Figure 3.9.: DAQ system with conventional read out. Multiple connections are shown by bold arrows. The multiplicity logic unit consists actually of two identical devices operated in slightly different modes. The signals are combined afterwards by a simple OR unit, which was left out for simplicity.

output amplitude is 100 mV or 500 mV per MeV deposited energy [Can04]. The latter setting is used for standard measurements with the DLB.

The main amplifier is an Ortec *Model 672 Spectroscopy Amplifier* that amplifies and shapes the signal. The device has several possible settings, but is usually used for standard measurements of the DLB with a shaping time of 6 μ s and a triangular shaped, unipolar output pulse. The standard amplification used is 9.1, which provides an input range of approximately 0 keV to 2750 keV based on the range of natural occurring γ lines (compare 2.2.2). Furthermore, it is operated in automatic mode for pole-zero (PZ) cancellation and baseline restorer (BLR) rate. The main amplifier powers the preamplifier via a 9-pin Sub D cable. In the opposite direction the output signal of the preamplifier is transmitted by a single ended (SE) connection to the main amplifier. In addition to the output signal in the range of 0 V to 10 V, the main amplifier provides two logic signals. The pile-up rejection (PUR) signal is provided in case a pile-up of two preamplifier pulses is detected. Another signal is provided during shaping (BUSY), which allows a live-time correction at the pulse analysing system [Per01].

The PMTs of the veto detector are powered via a custom made 48-channel distributor by a Heinzinger *HN 2500-025* power supply. The PMT signals are discriminated by different models of LeCroy discriminators with thresholds adjusted per channel or module (depending on the model) according to the individual amplification characteristics of the PMTs. The fast (negative) NIM logic output signal is combined by two LeCroy *380A Multiplicity Logic Unit*, what allows for the detection of an adjustable number of coincident input signals. After the final combination of the logic signals by a Borer *OR 320* module, the veto output is represented by a single signal. To apply a certain rejection time per veto event

(compare discussion in Section 3.2), the signal is extended from its approximate length of 50 ns by a CERN *N2255 Timer*. The fast NIM logic signal of a certain length is converted by a NIM to TTL converter to create a compatible signal for the following pulse analysing system. For details see [Ned09].

Up to now the output, PUR and BUSY signals of the main amplifier are transmitted to an Ortec *TRUMP®-PCI-8K* multi channel buffer (MCB) in form of a PCI card plugged into a standard PC operated under Microsoft Windows XP. In the range of 0 V to 10 V the card increases per detected signal one of up to 8192 bins (13 bit resolution) corresponding to the height of the incoming pulse unless a PUR or signal from the veto, applied to the Gate input of the card, was detected as well. The MCB card is only able to acquire spectra for a certain adjustable time period. Unfortunately, an usually list mode called acquisition mode is not available with this hardware. In this DAQ mode each signal is analysed regarding its pulse height and stored together with a timestamp to an event list.

The MCB is read out by the Ortec *Maestro®-32 MCA Emulation* software, version 6.06. With this software several settings like lower and upper level discriminators of the card and the acquisition state regarding the Gate input (off/coincidence/anti-coincidence) can be set. Since the software allows the execution of batch jobs, this feature is used to overcome the weak point of the non existent list mode. With the DLB usually single spectra of 15 min or 1 h are automatically acquired, saved and the measurement restarted so that it is possible afterwards to check, for example, the count rate near the peaks of the radon daughter products especially at the beginning of a measurement period (due to flushing of the measurement chamber with nitrogen, radon is slowly expelled, but it can also be emanated from the sample itself) or monitor the decrease of counts in peaks of short lived nuclides produced during NA. The software also allows rudimentary calibration of the acquired data according to peak position and width, but is usually only used for data acquisition. The spectra of the single runs are stored to the hard disk of the DAQ PC and afterwards processed by the software described in Chapter 4.

According to the manual of the MCB [Per00] it should in principle be possible to acquire the correct live-time (without the in total applied rejection time, compare discussion in Section 3.2) by applying the Gate signal also to the BUSY input of the MCB card. As a draw back the BUSY signal provided by the main amplifier can not be used simultaneously and the MCB has to be switched to simple live-time correction mode, which can not handle losses caused by pulse pile-up. Because of this, the in total applied rejection time is measured by counting the ~ 50 ns lasting pulses from a standard pulser. Depending on the applied rejection time per event, a pulsing frequency of 10 Hz to 20 Hz is used. One counter counts the total number of applied pulses, the other one is gated by the same veto signal also applied to the Gate input of the MCB and therefore counts only during this time. By dividing both numbers, the applied relative rejection time

3. Detector system

can directly be calculated. This method does only determine the mean fraction of the time, since not every single veto signal is sampled and the result is only for a large number of counts equal to the real applied fraction. The determined relative rejection time is automatically subtracted by the software described in Section 4.1, unless the user does switch this off or no measured relative value is found in the corresponding data directory. This method does not account for the case where already a non negligible dead time occurs during the conversion of the signals by the HPGe detector (the total rejection time and the dead time of the MCB then overlap in parts). But this overlap does only occur in high count rate situations, for example during calibration runs. For these measurements the veto detector can be switched off (in the MCA software) anyway, since the background contribution is then negligible, so the effect described above is not of relevance for low background measurements.

To overcome the drawbacks of the used MCB and to enable an event by event data recording, the DAQ system will be replaced by an FADC based system in the near future. Therefore, the input ranges of a Struck *SIS3300* 12 bit 100 MHz 8 channel VME based FADC, kindly provided by the AMANDA collaboration to the COBRA experiment, were modified by the electronics workshop of the Faculty of Physics to match different input ranges, which were up to now provided by the adjustable amplification of the main amplifier. It is intended to directly read out the preamplifier of the HPGe detector to get rid of the slight temperature dependence of the main amplifier gain and calculate optimal shaping parameters during the offline data analysis. The FADC is read out by a Concurrent Technologies *VX 511/063-23* VME Single Board Computer with an Ubuntu Linux operating system. A small program that runs on the single board computer communicates with the VME bus and acts as a VME to TCP bridge. The Data-Acquisition and Control Environment (DAQCorE), developed by O. Schulz [Sch11] for the COBRA experiment using the SCALA programming language, communicates via TCP/IP with the VME bus server. DAQCorE can be executed on any platform, since it runs in a Java Virtual Machine (JVM). It stores the pulse shape data acquired by the FADC together with time information and corresponding settings in so called TTree structures of the file format belonging to the ROOT data analysis framework. After the data acquisition the recorded pulses are processed by MAnTiCORE, an analysis tool kit based on the ROOT framework and also developed by O. Schulz [Sch11]. With this piece of software it is possible to calculate the optimal pulse processing parameters and do sophisticated analyses.

In addition to the Windows based DAQ PC a workstation operated with Ubuntu Linux is available in the laboratory. It is used to manage the data storage of the spectra to the cell of the distributed network file system AFS operated by the working group. Furthermore, it allows the simple usage of the software described in Chapter 4 and will be used to read out the FADC based DAQ system. The power supply of both DAQ PCs and the whole DAQ rack is backed up by

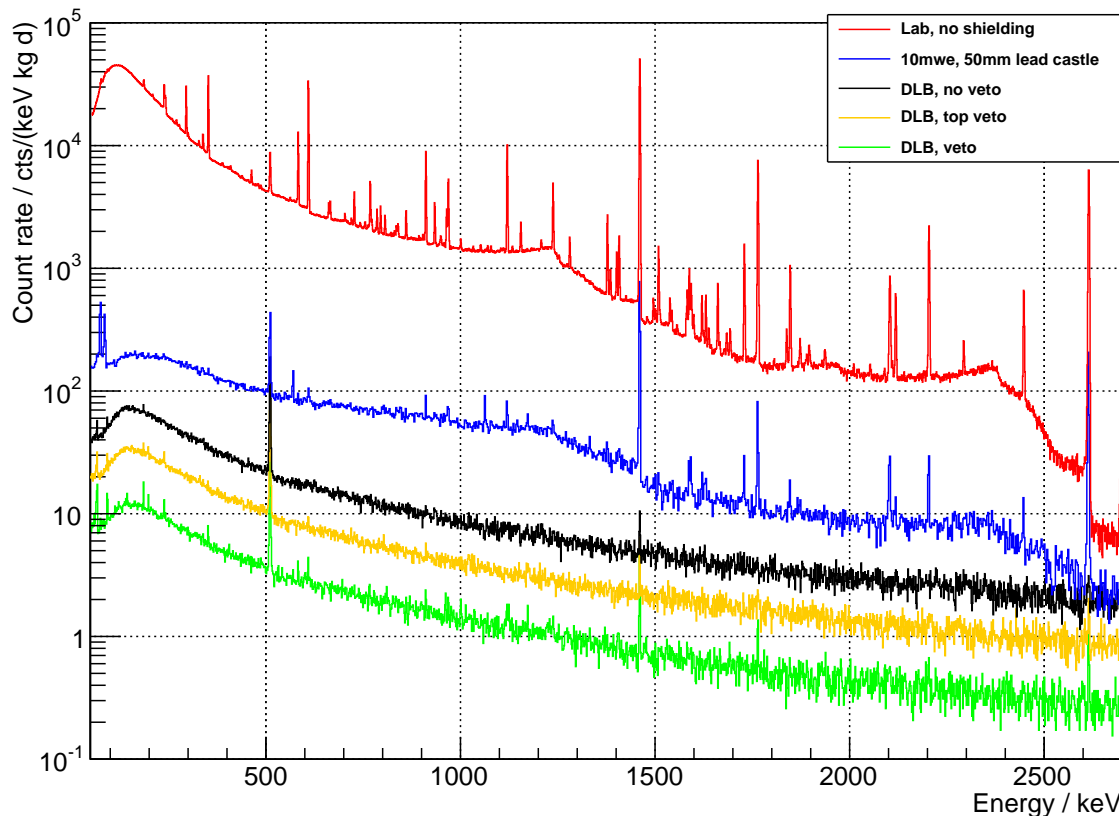


Figure 3.10.: Background spectrum of the detector system, taken at different stages of completion.

an uninterruptible power supply (UPS) to protect the electronics and prevent the loss of the calibration in case of a short power interruption.

3.5. Background spectrum

During the construction of the DLB the HPGe detector was used to take several spectra at different stages of completion. The achieved background suppression is enormous and reflects the great efforts made to build a HPGe γ ray spectrometry system with an – under the given circumstances such as the location and limited budget – as low as possible background index.

After the delivery of the HPGe detector a spectrum was taken by H. Gastrich in a lab of the working group [Gas09]. The spectrum (see Figure 3.10, red curve) shows a high number of intense peaks representing the full energy deposition of γ rays emitted by the many nuclides belonging to the natural decay chains and ^{40}K contained in many standard building materials (see Section 2.2). The spectrum is dominated by the Compton continua belonging to the γ lines at 2614.5 keV and 1460.8 keV of the decays of ^{208}Tl (^{232}Th chain) and ^{40}K respectively. The Compton edges are clearly visible at 2382 keV and 1243 keV.

3. Detector system

As a next step a spectrum (see Figure 3.10, blue curve) was taken inside the constructed outer shielding (see Section 3.1.1) with the detector placed within a provisional lead shielding of 50 mm thickness. The background continuum and low intensity γ lines are already suppressed to a large extent. The spectrum is still dominated by the Compton continua of the above mentioned γ lines of ^{208}Tl and ^{40}K . In addition to the two peaks of the aforementioned γ lines also the single escape (SE) peak at 2103.5 keV belonging to the 2614.5 keV γ line of ^{208}Tl is clearly visible. Furthermore, peaks belonging to ^{228}Ac (911.2 keV) and ^{214}Bi (609.3 keV, 1120.3 keV, 1729.6 keV, 1764.5 keV, 2204.2 keV and 2447.9 keV) can be identified. The 511 keV peak, caused by annihilation radiation following pair production of high energy γ rays in the vicinity of the detector or interaction of cosmic muons with the shielding, is already the most intense peak found in the spectrum below 1400 keV.

After the assembly of the inner shielding with its different components (see Section 3.1.2) another spectrum (see Figure 3.10, black curve) was acquired. To acquire the above described two spectra relatively short time periods were sufficient. In contrast, the spectrum inside of the shielding had already to be taken for nearly ten days. Nevertheless, the fluctuations in the spectrum are still quite large so that re-binning is necessary. The two clearly visible peaks remaining in the spectrum are the 511 keV annihilation peak and the γ line emitted in the decay of primordial ^{40}K . In addition, some small peaks can be found in the region below 200 keV.

The background levels discussed above have been achieved by applying only passive shielding techniques. To improve the background level further, the active veto (described in Section 3.2) is used to suppress signals induced by interactions of cosmic radiation. In preparation of the upgrade of the veto system (see Section 3.2 and [Qua12]), its side planes were dismantled. Already by using only the top plane of the veto detector, the background level can be lowered significantly (see Figure 3.10, yellow curve). In Table 3.2, it is visible that the integral counting rate is already lowered by more than 50 % only by using the top veto plane.

Before the dismantling of the side planes of the veto detector, the DLB was operated for three years with the veto system as it was constructed and build in the authors diploma thesis [Ned09]. Although the veto side planes have only been operated in single layer configuration (see Section 3.2) and will therefore be upgraded, the background was significantly suppressed by their usage (compare Figure 3.10, green curve). Comparing the integral count rates in Table 3.2 it is clearly visible that the overall background is suppressed again by nearly 64 %. In total the background rate is lowered approximately to 17 % of the value without applying the veto detector. Theodórsson quotes in [The96] the achievable background reduction to be a factor of 6 for systems with small overburden and up to 15 for an overburden of 10 mwe to 20 mwe. In comparison to the low level laboratory at the Max-Planck-Institut für Kernphysik (MPI-K) in Heidelberg, Ger-

Table 3.2.: Background characteristics at different stages of completion of the DLB. Integrals normalised to the germanium crystal mass.

Stage	Integral		Integral		511 keV peak /cts/d
	40 keV-2700 keV /10 ³ cts/(kg d)	/ cts/(kg min)	100 keV-500 keV /10 ³ cts/(kg d)	/ cts/(kg min)	
Lab, no shielding	11 061.2(18)	7681.4(13)	7253.3(15)	5037.0(10)	19 900(160)
10 mwe, 50 mm Pb	146.80(26)	101.95(18)	61.59(17)	42.77(12)	1675(38)
DLB without veto	34.399(57)	23.888(40)	18.208(39)	12.644(27)	699(11)
DLB with top veto	16.224(25)	11.267(18)	8.483(18)	5.891(12)	318.1(61)
DLB with veto	5.846(13)	4.0599(87)	3.0486(91)	2.1171(63)	107.4(22)

3. Detector system

many, with an overburden of 15 mwe where an integral background index of 1.75 cts/min (40 keV to 2680 keV) [TH91] is achieved, the resulting background count rate of the constructed non underground low background γ ray spectrometry system of (4.0599 ± 0.0087) cts/(kg min) is already quite low.

Taking the inhomogeneous distribution of the overburden (see Section 3.1.1) into account, a further improvement of the background count rate by a factor of approximately two by upgrading the veto side planes can be expected. This assumption is supported by comparing the so far achieved suppression factor of ~ 6.5 of the 511 keV annihilation peak to the reduction of this peak of 20 and the suppression factor of the integral rate of 12 quoted in [TH91] by applying external guard counters.

Due to the large background suppression already achieved with this imperfect veto detector, compared to the spectrum without applying the veto, more peaks become visible in the spectrum again. By lowering the overall background level, these peaks can be separated from the continuum in shorter time periods, although their count rate is still very low. To gather this statistics more than 5 weeks of data taking have been necessary. One should note that the background continuum above 1250 keV drops below 1 cts/(keV kg d). The peaks that can be found in the remaining background spectrum will be discussed in detail in Section 3.5.1.

3.5.1. Peaks in the DLB background spectrum

Due to the huge reduction of the background continuum (see Section 3.5) by applying different measures, very small peaks become visible in the spectrum if it is acquired for a long time (compare Figure 3.11). In the following, the identified peaks are discussed that stem from various radioimpurities, activation products and particle interactions in the materials of the detector and the surrounding shielding.

Taking a look at the peaks found in the background spectrum (see Table 3.3), roughly 50 % belong to γ lines emitted during the decay of nuclides of the natural decay chains ^{232}Th , ^{238}U and ^{235}U . In the region below 100 keV several peaks of ^{210}Pb and ^{234}Th , both belonging to the decay chain of ^{238}U , are visible. Due the short range of low energetic γ rays, the position of these nuclides can be localised to the materials of the detector or the innermost shielding layer made of copper. On the other hand, the absence of the bismuth X-ray peaks (except for the combined peak of lead and bismuth X-rays at 74.9 keV) does not support the vicinity of ^{214}Bi to the detector crystal, although ^{214}Bi belongs to the ^{238}U chain as well. Using the MC model developed in Chapter 5 with VENOM (see Section 4.5) and assuming the detector endcap as the location of the ^{210}Pb and ^{234}Th impurities, it is possible to determine specific activities for the aluminium of the endcap of approximately 4.19(44) Bq/kg and 515(56) mBq/kg respectively. The vast differ-

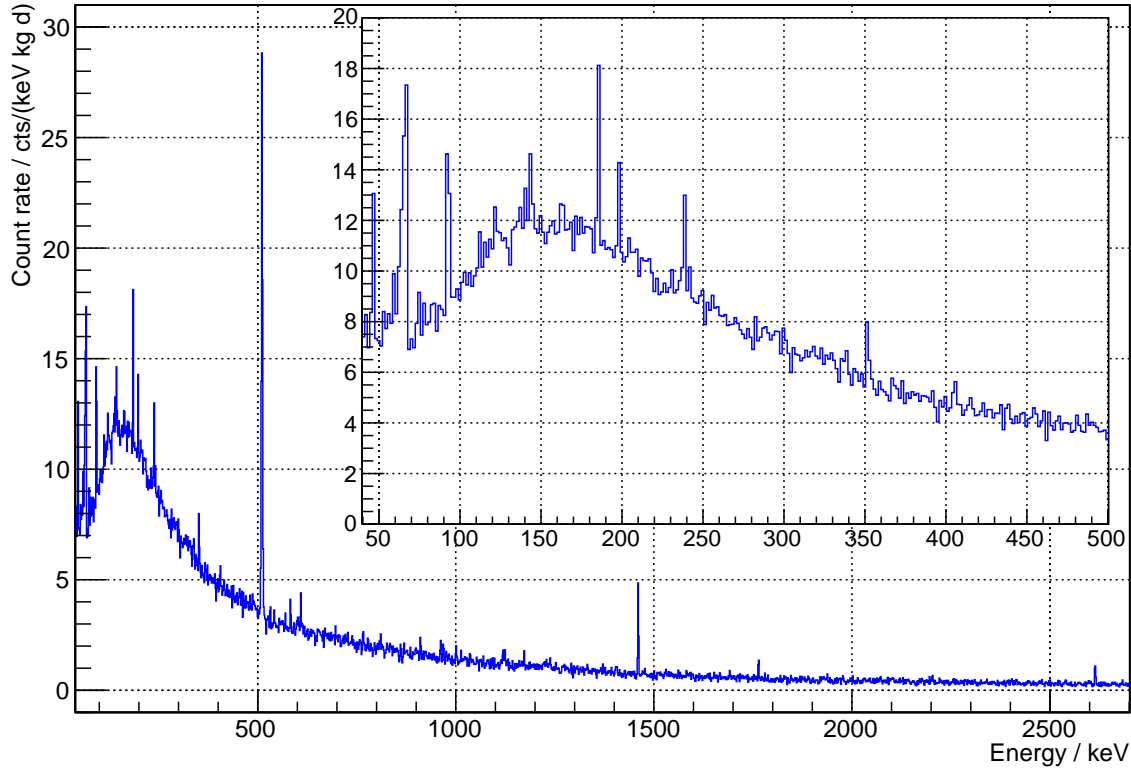


Figure 3.11.: Background spectrum of the complete detector system, acquired with the active veto detector in operation. Acquisition live-time 30 d. Bin width 1.56 keV, spectrum rebinned by factor 4.

Table 3.3.: Peaks found in the background spectrum in counts per day (cpd). Upper limits for asymmetric peaks of $(n, n'\gamma)$ reactions in germanium not calculated. 'BE' denotes binding energy. Uncertainties given with $k = 1$. Upper limits with 95 % coverage probability are given in case the value did not exceed the decision threshold (see Section 4.3). Energy and emission probability data of decays taken from [Lab13], of reactions and their half lives from the updated online version of [Fir96]. Reactions taken from the specified literature (see column 'Source') and references therein.

Energy / keV	Peak / cts/d	Nuclide / Reaction	Source	Remarks
46.54	12.5(12)	^{210}Pb		
53.44	2.05(78)	$^{72}\text{Ge}(n, \gamma)^{73m}\text{Ge}$	[Heu96]	$T_{1/2} = 0.499\text{ s}$
59.3	3.5(12)	Unidentified		
63.30	11.7(11)	^{234}Th		
66.72	30.1(16)	$^{72}\text{Ge}(n, \gamma)^{73m}\text{Ge}$	[Heu96]	$\Sigma, T_{1/2} = 0.499\text{ s}$
68.75	-	$^{73}\text{Ge}(n, n'\gamma)^{73}\text{Ge}$	[Heu93]	
72.81	< 1.80	$\text{Pb } K_{\alpha 2}$	[BMLA94]	
74.82	1.95(77)	$\text{Bi } K_{\alpha 2}$	[Wah07]	$^{212}\text{Pb}, ^{214}\text{Pb}$
74.97		$\text{Pb } K_{\alpha 1}$	[Heu93]	

Continued on next page.

3. Detector system

Table 3.3.: (Continued.)

Energy / keV	Peak / cts/d	Nuclide / Reaction	Source	Remarks
77.11	< 2.17	Bi K $_{\alpha 1}$	[Wah07]	^{212}Pb , ^{214}Pb
84.95	< 1.78	Pb K $_{\beta 1}$	[Heu93]	
87.35	} < 2.98	Bi K $_{\beta 1}$	[Wah07]	^{212}Pb , ^{214}Pb
87.58		Pb K $_{\beta 2}$	[Heu93]	
92.38	} 19.0(14)	^{234}Th		$p = 2.18\%$
92.80		^{234}Th		$p = 2.15\%$
112.1	1.90(85)	^{234}Th (?)		$p = 0.215\%$
122.06	3.50(98)	^{57}Co	[Heu93]	Cu activation
136.47	< 1.86	^{57}Co	[Heu93]	Cu activation
139.68	2.3(11)	$^{74}\text{Ge}(n, \gamma)^{75m}\text{Ge}$	[Heu93]	$T_{1/2} = 47.7\text{ s}$
143.59	} 7.5(13)	$^{57}\text{Co} + \text{Fe BE}$	[Heu93]	Ge activation
143.77		^{235}U		$p = 10.94\%$
159.70	< 1.32	$^{76}\text{Ge}(n, \gamma)^{77m}\text{Ge}$	[Heu93]	$T_{1/2} = 52.9\text{ s}$
163.36	2.16(95)	^{235}U		$p = 5.08\%$
174.95	< 2.99	$^{70}\text{Ge}(n, \gamma)^{71m}\text{Ge}$	[Heu93]	$T_{1/2} = 79\text{ ns}$
185.72	} 14.2(12)	^{235}U		$p = 57.0\%$, fit
186.01		$^{65}\text{Cu}(n, \gamma)^{66}\text{Cu}$	[Heu93]	185.6(1) keV
186.21		^{226}Ra		$p = 3.56\%$
198.4	7.1(12)	$^{70}\text{Ge}(n, \gamma)^{71m}\text{Ge}$	[Heu93]	$T_{1/2} = 20.4\text{ ms}$
205.32	< 2.95	^{235}U		$p = 5.02\%$
237.82	} 10.5(11)	$^{65}\text{Cu}(n, \gamma)^{66}\text{Cu}$	[Heu93]	
238.63		^{212}Pb		
242.00	3.2(12)	^{214}Pb		
295.22	1.59(78)	^{214}Pb		
338.32	1.39(70)	^{228}Ac		
351.93	6.33(91)	^{214}Pb		
477.60	< 0.79	$^{10}\text{B}(n, \alpha)^7\text{Li}$		
510.74	} 107.4(22)	^{208}Tl		$p = 22.5\%$
511		annihilation		μ induced
562.93	-	$^{76}\text{Ge}(n, n'\gamma)^{76}\text{Ge}$	[Heu93]	
569.70	1.15(55)	$^{207}\text{Pb}(n, n'\gamma)^{207}\text{Pb}$	[BMLA94]	
583.19	3.04(69)	^{208}Tl		$p = 85.0\%$
595.85	-	$^{74}\text{Ge}(n, n'\gamma)^{74}\text{Ge}$	[Heu93]	
609.31	4.53(74)	^{214}Bi		$p = 45.5\%$
661.6	< 0.77	^{137}Cs		
669.62	< 1.77	$^{63}\text{Cu}(n, n'\gamma)^{63}\text{Cu}$	[Heu93]	
691.4	-	$^{72}\text{Ge}(n, n'\gamma)^{72}\text{Ge}$	[Heu93]	
727.33	1.01(49)	^{212}Bi		$p = 6.65\%$
810.76	1.47(52)	^{58}Co	[Heu93]	Cu activation
817.87	< 0.66	$^{58}\text{Co} + \text{Fe BE}$	[Heu93]	Ge activation

Continued on next page.

Table 3.3.: (Continued.)

Energy / keV	Peak / cts/d	Nuclide / Reaction	Source	Remarks
834.01	} < 1.41	$^{72}\text{Ge}(n, n'\gamma)^{72}\text{Ge}$	[Heu93]	
834.85		^{54}Mn	[Heu93]	Fe activation
840.84	< 0.84	$^{54}\text{Mn} + \text{Cr BE}$	[Heu93]	Ge activation
860.53	2.57(69)	^{208}Tl		$p = 12.4\%$
869.5	1.46(52)	Unidentified		
898.6	1.12(48)	Unidentified		
911.20	2.05(53)	^{228}Ac		$p = 26.2\%$
962.06	} 2.56(68)	$^{63}\text{Cu}(n, n'\gamma)^{63}\text{Cu}$	[Heu93]	
964.79		^{228}Ac		$p = 4.99\%$
968.96	2.06(50)	^{228}Ac		$p = 15.9\%$
1001.03	2.01(50)	^{234m}Pa		
1013.7	0.89(43)	Unidentified		
1063.66	< 1.16	$^{207}\text{Pb}(n, n'\gamma)^{207}\text{Pb}$	[Heu93]	
1115.55	< 0.63	$^{65}\text{Cu}(n, n'\gamma)^{65}\text{Cu}$	[Heu93]	
1120.29	1.26(48)	^{214}Bi		$p = 14.9\%$
1124.53	2.42(85)	$^{65}\text{Zn} + \text{Cu BE}$	[Wah07]	Ge activation
1173.23	1.46(45)	^{60}Co		Cu activation
1238.11	1.18(43)	^{214}Bi		$p = 5.83\%$
1332.49	1.10(41)	^{60}Co		Cu activation
1377.67	< 0.90	^{214}Bi		$p = 3.97\%$
1460.82	12.73(78)	^{40}K		
1630.62	< 0.52	^{228}Ac		$p = 1.52\%$
1764.49	2.80(49)	^{214}Bi		$p = 15.3\%$
1847.42	0.58(29)	^{214}Bi		$p = 2.03\%$
2204.21	1.11(45)	^{214}Bi		$p = 4.91\%$
2614.51	4.05(50)	^{208}Tl		$p = 99.8\%$

ence of both values belonging to the same decay chain (unless the equilibrium of the chain is very disturbed) and the magnitude of the values disfavors the detector endcap as the location of these radioimpurities. The guaranteed uranium content (see [Can08a]) of less than 1 ppb (10^{-9} g of the element per gram sample) can be converted using the factors for example given in [Köt12, Tab. 2.11] to an upper limit of 12.3 mBq/kg for ^{238}U , disfavouring the assumed location as well. Assuming the upper limit of 3 Bq/kg for ^{210}Pb in the innermost lead layer as an actual value, one can calculate that about 5.5×10^5 decays of ^{210}Pb emitting the 46.54 keV γ line occur in this shielding layer every day. The innermost shielding layer made of 8 mm copper attenuates these γ rays by several orders of magnitude and keeping in mind that the detection efficiency at this energy is very low (see Chapter 5), this source can be neglected completely. Since electrolytic copper is fairly clean regarding radioimpurities due to its manufacturing process, a location of the ^{210}Pb impurity within the detector housing, for example some

3. Detector system

soldering lead, is highly probable.

With increasing energy of the γ rays and the decrease of the absorption coefficient in all materials, the possible locations of the decaying nuclides extend further to the outer shielding layers. Taking a closer look at the four γ lines of ^{235}U , some discrepancies become obvious. The proximity of nearly all lines to other γ lines gives rise to the complexity of the problem. The 163 keV peak, which is usually used as the reference line for the presence of ^{235}U (see [Wah07]), is a hint that traces of uranium can be found somewhere near the detector. A fit to the peak found at approximately 186 keV reveals a mean of 185.6(1) keV. This slightly supports ^{235}U as the peaks origin instead of the alternative neutron interaction or ^{226}Ra decay, although it has to be kept in mind that the energy resolution at 186 keV is approximately 1 keV and the definite assignment of the origin is impossible. The ^{235}U origin of the 186 keV peak favours again the ^{235}U assumption for the 163 keV peak. On the other hand, for the γ line at 205 keV only an upper limit was calculated although it has nearly exactly the same emission probability as the 163 keV γ line. Using the MC simulation (see Chapter 5) one can determine the efficiency at the energies of the four ^{235}U γ lines. Assuming that ^{235}U is contained in the aluminium endcap of the detector, the efficiencies at these energies differ by maximum 5% relative to each other, so that this can be assumed as nearly constant. With a ratio of 11.2 of the emission probabilities of the 163 keV and 185 keV lines, one would roughly expect the same ratio for the net peak count rates in the spectrum. Instead, the ratio is approximately 6.6(30) disfavouring ^{235}U as the origin of this peak. In addition, the absorption coefficients for these two γ lines do not differ that much that a higher amount of shielding material between the emitting nuclide and the detector can be responsible for this deviating ratio. For example after 8 mm of copper the ratio of the photon intensities of these energies is changed from 1 to ~ 0.82 but reducing the absolute intensity to about $\sim 20\%$ as well (calculated with data from [BHS⁺10]). Assuming the detector endcap as the location of the radioimpurity and using the first three γ lines of ^{235}U (see Table 3.3), one can calculate specific activities for the aluminium of the endcap in the range of 19 mBq/kg to 52 mBq/kg. Assuming the ratio of the natural abundance of ^{235}U to ^{238}U , the upper limit for the activity of ^{235}U given by [Can08a] is approximately a factor of 21 lower than the limit of 12.3 mBq/kg for ^{238}U , highly disfavouring the assumption that the peaks stem from uranium contained in the detector endcap.

In addition to the already mentioned nuclides belonging to the decay chain of ^{238}U seven peaks emitted in the decay of ^{214}Bi and three in the decay of ^{214}Pb can be identified (see Table 3.3). Among these are the γ lines recommended for the activity determination of the ^{226}Ra sub-chain. Furthermore, several γ lines of ^{228}Ac , ^{212}Pb and ^{208}Tl – all part of the ^{232}Th chain – can be identified as well. As G. Heusser states in [Heu91] it is possible to locate the thorium contamination by the three strongest γ lines 238.6 keV, 583.2 keV and 2614.5 keV of the ^{232}Th decay

chain by acquiring several spectra using different radiopure materials of varying thickness as absorbers. This is only possible since the relative decay rate of the two mother nuclides can not be influenced by disequilibrium of the thorium decay chain. The same holds true for the γ lines belonging to ^{214}Pb and ^{214}Bi of the lower part of the ^{238}U decay chain. Since both aforementioned nuclides are daughters of ^{226}Ra , which has a long half life of 1600 a, only the location of this part of the full chain can be deduced. Nevertheless, due to the higher energies of the γ rays it becomes more and more complex to locate these nuclides within the shielding by MC simulation and a detailed analysis is not the aim of this work.

The most prominent peak above 511 keV is the 1460.8 keV γ line emitted in the decay of primordial ^{40}K (see Figure 3.11) limiting the detection capabilities for ^{40}K impurities in samples. Using the MC simulation (for details on the procedure see Section 4.5 and Section 5.3) and the analysis tool described in Section 4.4 it can again be tried to locate the source of the radioimpurity. Due to the large mass of 54.5 kg of the BPE used as a neutron moderator and absorber within the inner shielding (see Section 3.1.2) it was assumed that this material is the location of the ^{40}K radioimpurity. Using the efficiency obtained from the MC simulation the specific BPE activity corresponding to the observed background peak is 180(22) mBq/kg. Using the radiopurity data for the used BPE given in Table 3.1, which were determined by M. Laubenstein at LNGS before the construction of the shielding, it becomes obvious that the neutron moderator can not be the location of the ^{40}K radioimpurity, since the determined value is nearly three times higher than the given upper limit of 64 mBq/kg (95 % CL). Since the inner shielding is placed within a counting room having walls made of very huge masses of concrete and sand lime brick, the background peak at 1460.8 keV can be caused by ^{40}K contained in these materials as well. Although 15 cm of lead are placed between detector and the walls, there is a certain chance ($< 2 \times 10^{-4}$ using absorption data from [BHS⁺10]) that a 1460.8 keV γ ray reaches the detector crystal without prior interaction. It was tried to determine by MC simulation the efficiency for ^{40}K decaying in the sand lime brick walls supporting the iron block above the measurement position (compare Section 3.1.1). For this, the MC simulation was vastly optimised (stopping immediately any electrons ‘produced’ within the outer lead layers, walls etc.), so that it was possible to simulate four million decays on a single PC within a few minutes. Using the computing cluster operated by the working group (see Section 4.5) 20×10^9 decays were simulated within five hours, corresponding to approximately 230 kBq ^{40}K contained in the walls. Normalising this activity to the mass of the walls, this corresponds to a specific activity of ~ 39 Bq/kg, which is presumably lower than the actual value. Since only in 12 of all simulated decays some energy was deposited in the detector, this method to determine the contribution of the surroundings is not applicable without using variance reduction techniques (scoring, etc.) in the MC simulation and is therefore not further investigated. Another possible location of ^{40}K

3. Detector system

Table 3.4.: Activities of activation products in the germanium detector derived from the background spectrum acquired end of 2009. Efficiencies determined by MC simulation. Saturation activities $A_{\text{spec, sat.}}$ converted from production rates given in the references. The theoretical predictions depend on the spectra of the cosmic rays. Activities found in different detectors are directly comparable only if the history of exposure to cosmic rays is identical.

Nuclide	$A_{\text{spec}} / \mu\text{Bq/kg}$		$A_{\text{spec, sat.}} / \mu\text{Bq/kg}$	
	measured	experimental [ABC ⁺ 92]	theoretical [CGL ⁺ 10]	
⁵⁷ Co	77(16)	34(5)	88 - 112	
⁵⁸ Co	< 45	41(11)	126 - 160	
⁵⁴ Mn	< 49	38(10)	60 - 83	
⁶⁵ Zn	332(91)	440(70)	729 - 891	

could be the surfaces of the copper parts installed around the detector. Since the parts were not electro-polished after machining but only cleaned, ⁴⁰K, probably contained in the citric acid used for cleaning, could stick to the surfaces. Nevertheless, the location of the different background sources is beyond the scope of this work and is due to this not further investigated.

Activation products

In addition to the peaks that can be associated to decays of natural occurring radioactive nuclides, several peaks can be identified that belong to nuclides produced by activation by cosmic ray particles. The peaks that can be found in the spectrum can be separated into two groups, those of nuclides produced in germanium and those created in the surroundings of the detector (nearly all in copper). Although in the case of ⁵⁷Co and ⁵⁸Co the same nuclides can be produced in germanium as well as copper, their decay is visible in different peaks in the spectrum, since in decays intrinsic to the detector also the binding energy of the daughter nuclide is deposited in the detector crystal, therefore appearing as a peak with a higher energy.

In germanium the activation products ⁵⁷Co, ⁵⁸Co, ⁵⁴Mn and ⁶⁵Zn can be produced, all having an half life of less than one year. The intrinsic decays of these nuclides can be seen as peaks in the spectrum at 143.59 keV, 817.9 keV, 840.84 keV and 1124.53 keV. The measured net count rates (see Table 3.3) were converted to activities by determining the efficiency again with the MC simulation discussed in Chapter 5. As it can be seen in Table 3.4 the observed activities do not differ much from the experimental data found in literature, but deviate from the theoretical ones. Since the peak at ~ 143.7 keV may contain a small contribution of ²³⁵U (see discussion above) the measured activity is possibly overestimated. Keeping in mind that the discussed background spectrum was acquired at the

end of 2009, it is of interest to analyse these peaks in a background spectrum acquired after the completion of the anti cosmic veto (see Section 3.2). The detector was permanently surrounded by its shielding containing an integrated thick neutron moderator (see Section 3.1.2) and the flux of fast neutrons created by muon interactions in high Z shielding materials is therefore vastly reduced. Consequently, the ^{57}Co and ^{65}Zn peaks in a new spectrum should be much smaller due to their half lives of 271.8 d and 244.3 d. Therefore, it could be possible to clarify the source of the 143.7 keV peak by the acquisition of a new background spectrum.

^{57}Co and ^{58}Co are produced in copper as well and are visible as peaks at the energies of the emitted γ rays of 122 keV, 136.5 keV and 810.8 keV (^{58}Co). In addition to these nuclides also ^{60}Co is produced in copper. Since the innermost shielding layer as well as the detector cup holding the crystal are made of copper, the location of the produced nuclides can not easily be found out, but the shielding layer is more likely due to its much higher mass. Since the detector has an arm made of stainless steel and iron as well as steel are contaminated with ^{60}Co due to their production process (see [MLB⁺08] and references therein) this detector part could be responsible for the ^{60}Co seen in the spectrum as well. Nevertheless, all net peak count rates belonging to these nuclides (see Table 3.3) are fairly low. As a continuation of this work the peak count rates could be converted to activities using the MC simulation assuming the different locations and compared to the theoretical production rates in copper given in [CGL⁺10] or experimental ones determined in [LH09].

For a detailed discussion of production mechanisms of intrinsic radioimpurities by neutron activation see [Heu96].

Neutron induced γ lines

In addition to the peaks caused by the decays of natural occurring radioactive nuclides and activation products, several peaks can be found in the spectrum that are caused by capture of (thermal) neutrons (reaction $^A\text{X}(n, \gamma)^{A+1}\text{X}$) or inelastic scattering (reaction $^A\text{X}(n, n'\gamma)^A\text{X}$) (compare [Heu96]). Depending on the target isotopes the neutron capture reaction produces a metastable nuclide or one in its excited state.

Especially all capture reactions at isotopes of germanium produce metastable states. As one can see in Table 3.3 nearly all γ lines can be found in the spectrum that are emitted in the de-excitation of metastable states of germanium isotopes with half lives longer than the applied rejection time of the anti cosmic veto (see Section 3.2) and are therefore not suppressible by this active reduction technique. The height of the peaks is only influenced by the effectiveness of the neutron shielding. Since most of the high Z lead shielding elements are located outside of the neutron moderator (see Section 3.1.2), most of the muon induced neutrons are produced outside of the neutron shield as well. If these neutrons are moderated

3. Detector system

by the BPE and absorbed by the boron doping, they can not cause the induction of the aforementioned γ peaks. Only the γ ray peak at 174.9 keV caused by the de-excitation of the lower metastable state of ^{71}Ge can be suppressed due to its short half life of 79 ns (compare discussion in [BCK⁺03]). The de-excitation of the 66.7 keV metastable state of ^{73}Ge does occur by the sequential emission of two γ rays with 53.4 keV and 13.3 keV. Since the 13.3 keV level has a half life of 2.95 μs [Fir96] it is likely that the second transition occurs during the used shaping time of the main amplifier of 6 μs . Therefore, the peak at 66.7 keV, representing the sum of both γ rays, is much higher than the 53.4 keV and is the by far most intense line below 500 keV (see Figure 3.11). Nevertheless, the ratio is more than twice as high one would expect from the half life and the shaping time. Bunting and Kraushaar [BK74] see the opposite case – a much higher 53.4 keV peak – since they use only a shaping time of 1 μs .

Škoro et al. use the 139.7 keV peak induced by the $^{74}\text{Ge}(n, \gamma)^{75m}\text{Ge}$ reaction to deduce the thermal neutron flux within the detector shielding. According to [ŠAK⁺92] the flux can be calculated with the formula

$$\Phi_{\text{th}} \left(\frac{\text{n}}{\text{cm}^2 \text{ s}} \right) = \frac{R_{\text{n}, 139.6 \text{ keV}}}{N(^{74}\text{Ge}) \sigma(^{74}\text{Ge}) \frac{\varepsilon_{139.6 \text{ keV}} + \alpha_{\text{tot}}}{1 + \alpha_{\text{tot}}}} \quad , \quad (3.1)$$

where $R_{\text{n}, 139.6 \text{ keV}}$ is the net count rate of the 139.7 keV peak per second and $N(^{74}\text{Ge})$ the number of ^{74}Ge isotopes in the detector, which can be calculated from the detector mass of 1.247(2) kg and the natural abundance of ^{74}Ge of 36.729(85) % [BLB⁺05]. $\varepsilon_{139.6 \text{ keV}}$ is the FEP efficiency for the 139.6 keV γ ray, which has a certain chance to escape the detector. The de-excitation of ^{75m}Ge can alternatively occur by internal conversion, where the energy of the nucleus is transferred to an electron of the lower shell, which is then emitted from the atom. This effect is taken into account by adding the total conversion coefficient α_{tot} . Since these electrons can nearly never escape the detector crystal, the fraction in the denominator of Equation (3.1) is simply the efficiency that the energy released in the de-excitation of ^{74}Ge is deposited in the detector. $\sigma(^{74}\text{Ge})$ is the partial neutron capture cross section for the production of the metastable state of ^{75}Ge . By MC simulation, the efficiency was determined to be approximately 77.9(39) %. The value of the total conversion coefficient α_{tot} of 1.54 has been taken from [FS99], accessed via [NuD], and the value of the partial thermal neutron capture cross section of 0.17(3) b from [MDH81]. Using these data the thermal neutron flux at the location of the HPGe detector can be estimated to be about $4.4(23) \times 10^{-5} \text{ cm}^{-2} \text{ s}^{-1}$ during the spectrum acquisition period. This value is quite low compared to the value of approximately $3 \times 10^{-3} \text{ cm}^{-2} \text{ s}^{-1}$ for a conventional shielding without a neutron moderator given in [ŠAK⁺92] and proves the effectiveness of the neutron shielding.

Besides the neutron capture γ lines given in Table 3.3 and partly discussed above, two possible peaks from $^{65}\text{Cu}(n, \gamma)$ reactions can be located in the spectrum. Since both peaks at 186.0 keV and 237.8 keV unfortunately interfere with

neighbouring peaks, their actual count rate remains unclear. Because both γ lines do not stem from metastable states, their peaks should be suppressed by the cosmics veto, unless the moderation of the muon induced neutrons take longer than the applied rejection time. As discussed already above a fit to the ~ 186 keV supports ^{235}U as its source although discrepancies to other ^{235}U lines remain. The β decay of ^{66}Cu , produced by the (n, γ) reaction, can as well not be detected, since in more than 90% of the decays the transition ends directly in the ground state of ^{66}Zn and the energy of the alternatively emitted γ ray is with 1039.2 keV relatively high leading to a FEP efficiency much smaller than for the two above mentioned γ ray peaks (compare decay scheme at [Fir96, NuD]).

In contrast to thermal neutrons, fast neutrons, which are produced by interactions of muons with lead to a large extend, interact by inelastic $(n, n'\gamma)$ reactions with the materials of the germanium detector and its surrounding shielding. As it is shown in [WMA⁺96] and [ŠAK⁺92] the interaction of fast neutrons with the different germanium isotopes lead to broadened and to higher energies asymmetric peaks due to the nuclear recoil of the target nucleus, which depends on the neutron scattering angle (compare [WMA⁺96]). In contrast to the spectrum of an above ground detector set-up without a neutron shielding shown by [WMA⁺96], which shows very prominent broadened peaks at 595.9 keV and 691.4 keV, in the DLB background spectrum none of these peaks are visible. Due to the absence of the asymmetric peaks their width is unknown and consequentially an estimation of a net peak area impossible. Therefore, Table 3.3 does not give upper limits for inelastic scattering peaks at germanium isotopes. In addition to the aforementioned peaks Wordel et al. [WMA⁺96] list three peaks at 68.8 keV, 562.9 keV and 834.0 keV, which are not visible in the background spectrum as well. Using the width of the peak at 691.4 keV from [ŠAK⁺92], one can calculate an upper limit on the count rate of this peak in the spectrum of $5.7 \times 10^{-5} \text{ s}^{-1}$. According to Škoro et al. [ŠAK⁺92] the flux of fast neutrons can be calculated from the count rate R_n of the 691.4 keV peak with the empirical formula

$$\Phi_{\text{fast}} \left(\frac{\text{n}}{\text{cm}^2 \text{ s}} \right) = k \frac{R_{n, 691.4 \text{ keV}}}{V} \quad , \quad (3.2)$$

where V is the volume of the detector in cm^3 and k an empirical factor of 900 ± 150 . According to [ŠAK⁺92] the 691.4 keV peak is used since it stems from a $0^+ - 0^+$ transition, which releases its energy in 100% of all cases by internal conversion (compare also [Fir96]) and the energy is therefore nearly always completely deposited within the detector crystal. Using Equation (3.2), $k = 900$, the detector volume of 234 cm^3 and the count rate given above, an upper limit on the flux of fast neutrons of $2.2 \times 10^{-4} \text{ cm}^{-2} \text{ s}^{-1}$ within the spectrum acquisition period can be determined, but it should be kept in mind that this value can vary nearly by 50% due to variations in the cosmic ray flux (compare [WMA⁺96, Fig. 3]). Also this calculated value is nearly two orders of magnitude smaller

3. Detector system

than the value of $1.7 \times 10^{-2} \text{ cm}^{-2} \text{ s}^{-1}$ given by [ŠAK⁺92] for a conventional system without integrated neutron shielding. It has to be denoted that the calculated upper limit is nearly equal to the upper limit of $2 \text{ m}^{-2} \text{ s}^{-1}$ given by [WMA⁺96] for a system with 500 mwe of overburden. This again impressively demonstrates the achieved background reduction with respect to neutrons.

In contrast to inelastic scattering in germanium the interaction in materials around the detector crystal lead to sharp peaks in the spectrum since the recoil energy of the target nucleus remains in the material and only the emitted γ ray has a certain chance to be detected in the germanium detector. Table 3.3 lists in total five $(n, n'\gamma)$ reactions in copper and lead, more for these two and other materials can be found in [Heu93], but were not seen in the spectrum. As can be seen in Table 3.3 for the peaks with energies of 669.3 keV, 1063.7 keV and 1115.6 keV only upper limits were determined. The peak at 569.7 keV belonging to the inelastic scattering at ^{207}Pb was calculated to have a small but yet significant count rate per day. Since the peak at 962.1 keV was not completely resolvable from the neighbouring peak of ^{228}Ac the peak count rate was calculated for the combined region. Nevertheless, it is visible by eye that the $^{63}\text{Cu}(n, n'\gamma)^{63}\text{Cu}$ contributes more to this region. This is also supported by the fact that another neighbouring ^{228}Ac peak at 969.0 keV with a more than three times higher emission probability than the 964.8 keV γ line shows an even smaller count rate than the one calculated for the combined region mentioned above.

As already discussed in Section 3.1.2 the neutron shielding is based on the moderation of neutrons by PE and the capture of thermal neutrons by the (n, α) at ^{10}B . Since in 93.7% of all reactions ^7Li is left in its first excited state, a 477.6 keV γ ray is released in this case with a probability of 100%. As one can see in Table 3.3 and Figure 3.11 a corresponding peak can not be seen in the spectrum and only an upper limit of 0.79 cts/d is given. Since the neutron flux is heavily suppressed (see discussion above) the two innermost shielding layers of 20 mm lead with less than 3 Bq/kg ^{210}Pb and 8 mm electrolyte copper, which are placed inside of the neutron shielding, effectively suppress the γ ray emitted in the capture process.

4. Software for data processing and analysis

The DAQ chain described in Section 3.4 ends with the up to now used conventional read out in the Ortec *TRUMP*[®]-*PCI-8K* multi channel buffer (MCB). The MCB itself is read out by the Ortec *Maestro*[®]-32 multi channel analyzer (MCA) emulation software, which allows only some simple operations on the acquired spectra. The software is able to calibrate the data but uses only a linear calibration function if specifying two or a quadratic function if specifying three calibration points. This is sufficient for an approximate assignment of peaks in the spectrum to common nuclides contained in the internal (limited) database of the MCA software. But, as the example of the unknown origin of the 186 keV line in Section 3.5.1 shows, often a more precise calibration is necessary, especially to fully exploit the superb energy resolution of a germanium detector. *Maestro*[®]-32 is able to store the acquired spectra in the binary CHN and ASCII SPE file format described in [Adv02]. Furthermore, the software is able to execute batch files allowing automated data acquisition and storage in certain time intervals. This feature was used before the DAQ system was equipped with a UPS ensuring that the acquired data are not lost due to a power failure. The spectrum acquisition in time intervals allows the check for a decreasing activity of radon at the beginning of the measurement (compare also Section 3.4).

The actual data processing and evaluation tools described in the following are all based on ROOT, a very powerful and sophisticated data analysis framework developed at CERN [BR97]. ROOT provides the interpreter CINT to do simple data processing tasks interactively and uses the programming language C++. Many different object classes can be used to store and manipulate histograms and graphs of different dimensions, find peaks in spectra, fit user defined functions to data and plot these in many different ways, to name but a few of the possibilities provided by ROOT.

4.1. Data conversion tool `ge-multi-convertingtool`

For historical reason attributable to the beginning of the development of the data converting tool `ge-convertingtool` by H. Gastrich [Gas09], the file format used to store the data within the *Maestro*[®]-32 software is the ASCII based, human readable SPE format. The old version could only convert single SPE files to a ROOT file and was using the simple calibration provided by the *Maestro*[®]-32 software.

4. Software for data processing and analysis

The conversion tool was completely reworked and extended so that it is able to convert many input files belonging to the same measurement into a single ROOT output file. The single spectra produced by the batch mode of the DAQ software are stored in a ROOT TTree structure. A TTree can be understood as a list containing several columns, called branches, which store different kind of values assigned to them. Each event or data set fills one row of the TTree structure and is therefore described by the set of variables stored in the different branches. In the output file format each entry of the tree (like a row in a table) contains all data related to a single short DAQ run of the MCA software. Each spectrum recorded during one run is stored as a vector within the entry and data like the life, real and start time as well as calibrations are stored parallel to it. In addition to the TTree structure that preserves the granularity of the taken spectra for a whole data taking period, the produced ROOT file contains also an uncalibrated and an energy calibrated histogram representing the sum spectrum of all runs. Furthermore, a calibrated and scaled histogram for quick comparisons with other data and the functions describing the energy and resolution calibration produced by the calibration software (see Section 4.2) are stored.

The `ge-multi-convertingtool` is a standalone command line executable file using the libraries of ROOT. Several options allow different conversion settings so that different data taking scenarios can be mapped. The option `“-noveto”` allows to switch off the reading of the externally recorded (relative) veto time, in case the veto system was not used to suppress background. `“-calib CALIBFILE”` specifies the calibration that should be used to convert the raw data and from that the calibration functions are copied to the ROOT output file. Before the latter was implemented, T. Köttig introduced two options `“-m SLOPE”` and `“-b INTERCEPT”` to specify the parameters for the calibration manually. These options also allow the usage of the tool for data stored in the SPE format but not related to the DLB DAQ system and calibration convention.

If the conversion tool is called without specifying a calibration file, the data are automatically calibrated with the function stored within the SPE file format. This is especially done for calibration measurements with a radioactive source, when there does not exist any valid calibration, for example after a shutdown of the system. The output ROOT file is then processed by the calibration software described in Section 4.2 to calculate valid calibration data. Afterwards, the formally uncalibrated data can be converted again using a valid calibration.

4.2. Calibration software GeCal

Based on `cal-event`, the calibration tool for COBRA CdZnTe data developed by T. Köttig in his diploma thesis [Köt08], Th. Quante programmed in his master’s thesis [Qua12] a C++ class called `GeCal` for calibration tasks related to high resolution γ ray spectra. This class can be used with the ROOT interpreter to produce

calibration functions from measurements containing known γ lines. It provides many methods (also called member functions) to load raw spectra, do automatic peak searches, associating these with γ ray energies, fitting the predefined functions to the calibration points and much more.

To locate peaks in the input spectrum the ROOT class `TSpectrum` is used. Several methods for the commonly used calibration nuclides are implemented in `GeCal`. If the user chooses the appropriate method, the algorithms are almost always able to automatically assign the associated γ ray energies to the found peaks. Afterwards, a function is fitted to each peak including also the background region next to it. Depending on the spectral shape and distance to found neighbouring peaks, different fit functions are used to describe the spectrum locally. The positions of the means and the widths are then extracted from the peak fits and stored for a following calibration. This procedure can be repeated for different calibration measurements (in case several radioactive source were measured one after the other), a linear function is fitted to the energy calibration points and one of the form

$$\sigma(E) = \sqrt{e^2 + p^2E + c^2E^2} \quad (4.1)$$

to the peak width data points. Equation (4.1) is recommended by G. Gilmore [Gil08] and Hurtado et al. [HGLGT06]. It is motivated by the three different components contributing to the detector resolution. Parameter e represents the electronic noise, which is energy independent, p is the statistical fluctuation of the charge production, which scales with \sqrt{E} , and c the charge collection parameter (for a detailed discussion and explanation see [Gil08]).

Afterwards all calibration data, graphs and the fit functions can be saved to a ROOT file that can be loaded by the data conversion tool described in Section 4.1. For a detailed description of the work flow within the calibration software see [Qua12].

4.3. Spectrum evaluation standards

γ ray spectra are, like all other kinds of spectra, showing a certain physical property in dependence of energy and are a composition of signal and background. In (high resolution) γ ray spectrometry the signals are (approximately) Gaussian shaped peaks on top of a background stemming from different sources. For low background spectrometry the main sources of background to the peaks of interest are signals induced by cosmic particles (and their progenies) and unshielded γ rays. The latter cause small peaks in the background spectrum (compare Section 3.5 and Figure 3.10) and increase the continuum by Compton scattering. Depending on the strength of unshielded γ rays, which can be contaminations within the materials used in the shielding or in the detector itself or high energetic γ rays from the systems environment, the background continuum can be

4. Software for data processing and analysis

dominated by the Compton continua of these γ rays.

The background to a certain peak of interest can also be caused by radioactive nuclides contained in the sample itself. In case these emit intense γ rays with energy higher than the one of interest, they increase the background due to Compton interactions and therefore lower the sensitivity for lower energetic γ rays. Additionally, nuclides emitting a high energetic β particle during their decay can be responsible for a background increase as well, since β particles emit bremsstrahlung when slowing down.

Peaks that can be found in the background spectrum (compare Section 3.5.1) are more problematic for the evaluation of signal peaks than the continuum, since their energy often matches the one of interest or is very close to it. The correction for peaks found in the background spectrum is called peaked background correction (PBC).

To determine the contribution of the background within a region of interest (ROI) of certain width around an energy of interest, the bin contents of the spectrum to the left and right of the ROI are used. The two German spectrum evaluation standards described in Section 4.3.1 and Section 4.3.2 use different methods to deduce the background under the peak of interest from the neighbouring bins.

Both standards have in common that the total number of counts within the ROI is determined by a simple sum over the bin contents belonging to it. In contrast to this method fitting a function to the peak together with the background under it would require an exact knowledge of the different contributions to the peak shape. Otherwise the used function would be not suitable to describe the peak shape and the retrieved parameters would be biased due to the inaccurate peak model. For a simple sum of the counts no exact knowledge of the peak shape except from its extent is required.

After a net area of a peak is calculated it has to be decided whether the determined value is with a certain probability compatible with a background fluctuation or not. Therefore, the determined value is compared to a pre-established threshold. In case the value does exceed the threshold, there is still a certain probability that it is caused by a background fluctuation (false positive, type I error). In the other case, it is decided that no contribution exist. This decision again can be wrong with a certain probability (false negative, type II error). Therefore, in both standards two characteristic values are defined to describe the probabilities of making type I and type II errors during the decision process whether a count within a peak is significant or not.

The first value is called decision threshold or critical limit (German: Erkennungsgrenze). In case the calculated net area of a peak is higher than that value, the null hypothesis of no contribution of the effect of interest to the spectrum ($R_b = R_0$, the gross rate is compatible with the background rate) is rejected and the alternative hypothesis that there is a contribution ($R_b > R_0$), accepted. In the other case, the null hypothesis is accepted and it is concluded that no contribu-

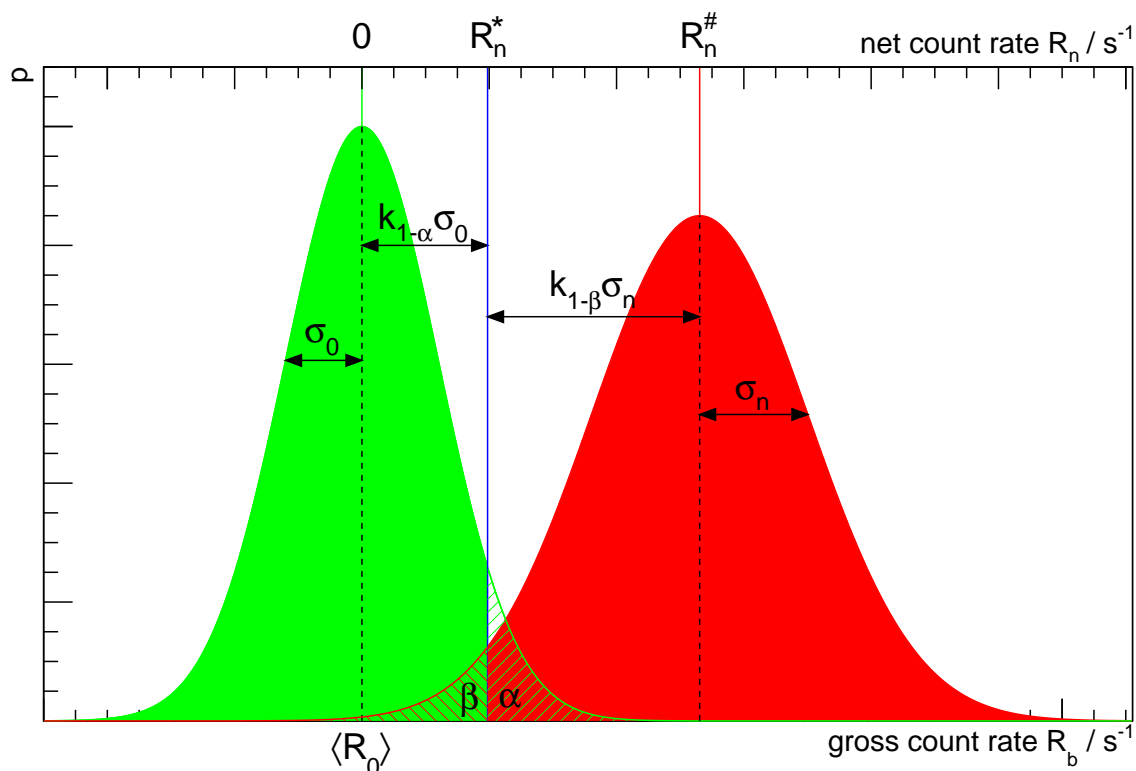


Figure 4.1.: Characteristic limits used for spectrum evaluation. $\langle R_0 \rangle$ is the expectation value of the background count rate. R_n^* is the decision threshold for the net count rate R_n calculated for a probability of α for incorrectly rejecting the null hypothesis $R_b = R_0$. The detection limit $R_n^{\#}$ is the smallest expectation value of the net count rate R_n that will be detected with a probability $(1 - \beta)$ as a net effect using the decision threshold R_n^* . The σ_i are the standard uncertainties of the values R_i with $i = 0, n$ and k_{1-j} the quantiles to the error probabilities $j = \alpha, \beta$. (Figure according to [Gil08])

tion exists. The decision threshold R_n^* (in general indicated with ‘*’), which is an a posteriori value (calculated after the acquisition of the spectrum), takes the variation of the background into account (compare Figure 4.1). The value is calculated in that way that the probability for a false positive decision (the null hypothesis is incorrectly rejected, ‘error of first kind’), is equal to the probability α , which has to be defined before the measurement. (Compare [DIN93, ISO00, Gil08].)

The second characteristic limit is called detection limit (German: Nachweisgrenze). It is in contrast to the decision threshold not used during the evaluation of an acquired spectrum. The detection limit $R_n^{\#}$ (in general indicated with ‘#’) is an a priori value, calculated from a spectrum acquired under similar conditions like the ones of interest. It is compared with a guide line value (German: Richtwert), which results from scientific, legal or other requirements and is therefore a measure for the suitability of the method or detector system. The value specifies the minimal expectation value of the net count rate R_n for which the (false) null hypothesis – that there is no net contribution of the effect of interest

4. Software for data processing and analysis

($R_b = R_0$) – is not rejected only with a probability β (false negative decision, ‘error of second kind’) using the decision threshold R_n^* (compare Figure 4.1). (Compare [DIN93, ISO00, Gil08].)

Both standards are described in the following, since they are applied in the evaluation of the simulations and measurements in Chapter 5 and Chapter 6. They are explained in detail, since it is, especially in DIN ISO 11929:2011, relatively complex to extract the relevant parts and understand the abstract descriptions of different measurement situations.

4.3.1. Standard DIN 25482-5:1993

The German standard DIN 25482-5, published in 1993, is equivalent to the international standard ISO 11929-3. It describes briefly the evaluation of high resolution γ ray spectrometry measurements. It is required that neighbouring γ lines are more than four times the full width at half maximum (FWHM) apart and the background around a peak can be described by a linear function, otherwise DIN 25482-2 has to be used. The standard neglects any influence of sample treatment, acquisition geometry, weighing, system instabilities and more. Furthermore, it is assumed that any factors needed to convert a measured count rate to a sample activity are known to a high precision, so that their uncertainties can be neglected. The data acquisition time has to be small in comparison to the (effective) half life of the nuclide of interest to fulfil the prerequisite of a constant activity. Moreover, it is implied that the detector signals, registered in the spectrum, are independent Poisson processes so that the sum of counts within a range of channels is Poisson distributed as well. Since only sums of channel contents are used, which are together usually in the order of at least 100, the Poisson distribution is approximated in the calculations of DIN 25482-2 by the Gaussian distribution. (Compare [DIN93, ISO00].) According to Blobel and Lohrmann [BL12] this approximation is sufficient for expectation values μ larger than 10, except far away from the maximum of the Poisson distribution. As a result, the approximation by a Gaussian distribution can be problematic in case of low statistics like short measuring periods in low background systems.

An ROI within a spectrum is denoted in DIN 25482-5 with B and has a width of b . The two regions to determine the background within the ROI are indicated with A_1 and A_2 , have a width of l and should be located next to the left and right edges of region B . Although it is recommended by the standard to choose the regions A_1 and A_2 next to the edges of the ROI B , DIN 25482-5, supplement 1 [DIN97] shows several options to shift both regions for background determination in case tails of neighbouring peaks reach into the regions, which is not allowed. The gross counts within the ROI are denoted with N_B (red area in Figure 4.2) and the background integrals with N_1 and N_2 (green areas). The calculated background within the ROI is denoted with N_0 (shaded area).

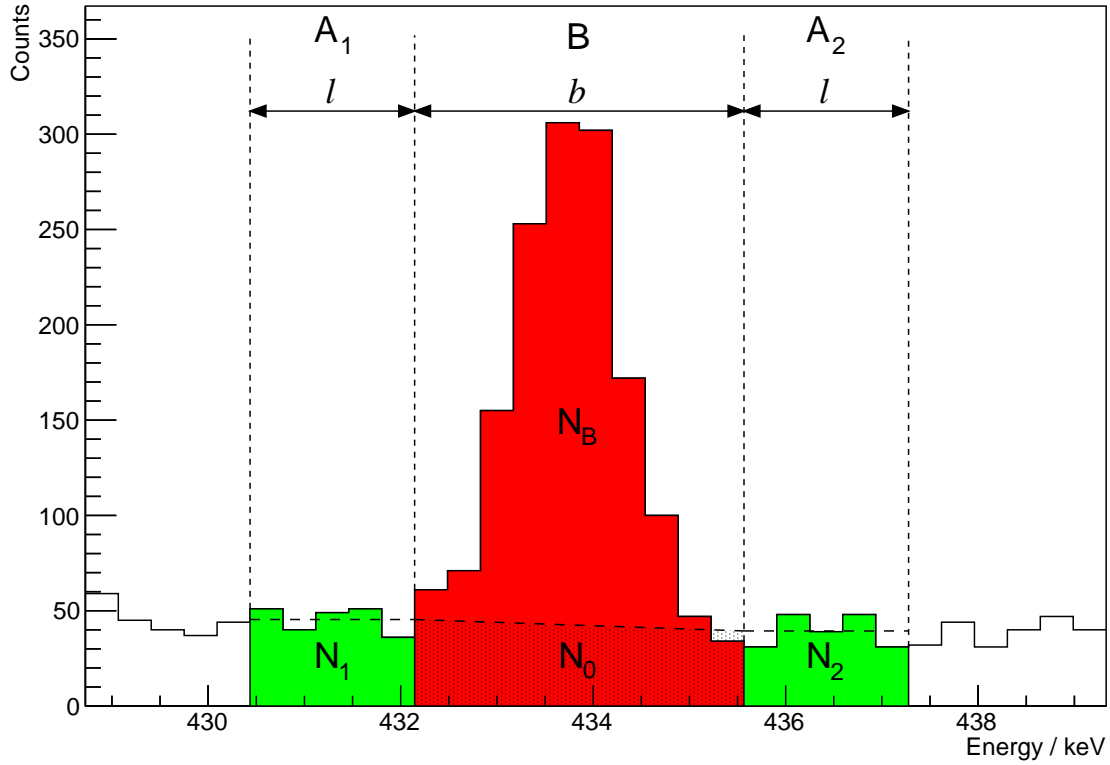


Figure 4.2.: Regions, widths and integrals used in DIN 25482-5 to determine the net peak area N_n . The gross counts N_B (red area) within the ROI, background integrals N_i with $i = 0, 1$ and background N_0 within the ROI (shaded area) are marked. (Spectrum shows the 433.94 keV peak of ^{108m}Ag found in a silver glue sample assayed for 496 h.)

According to DIN 25482-5 the conditions for the width b of an ROI are

$$\begin{aligned} 1 \times \text{FWHM} < b < 3 \times \text{FWHM} & \quad (4.2) \\ b & \geq 4 \text{ channels} \end{aligned}$$

and recommends $2.5 \times \text{FWHM}$ for non dominant background. The width of the background regions l can be defined under the boundary condition

$$\begin{aligned} b < 2l < 10b \\ \Leftrightarrow \frac{1}{10} < \frac{b}{2l} < 1 \quad . & \quad (4.3) \end{aligned}$$

The FWHM at the energy of the peak is taken from calibration data or neighbouring, well defined peaks. (Compare [DIN93].)

In the case the regions A_i can be chosen adjoining to the ROI, the background N_0 within region B can be simply calculated as

$$N_0 = (N_1 + N_2) \frac{b}{2l} \quad , \quad (4.4)$$

4. Software for data processing and analysis

which can be understood as the trapezoid shown in Figure 4.2 as the shaded area. The net area of the peak is then calculated as

$$N_n = N_B - N_0 \quad (4.5)$$

and its uncertainty

$$u(N_n) = \sqrt{N_B + N_0 \frac{b}{2l}} \quad (4.6)$$

In case the regions A_i have to be shifted, Equation (4.4) has to be modified to take the different distances to the ROI into account by introducing different weights for the two background integrals N_1 and N_2 . (Compare [DIN93].)

Based on these quantities, the acquisition time t and the quantile $k_{1-\alpha}$ of the Gaussian distribution for the type I error probability α , the decision threshold can be calculated according to DIN 25482-5 as

$$R_n^* = \frac{k_{1-\alpha}^2 b}{2t} \frac{b}{2l} \sqrt{1 + \frac{4N_0}{k_{1-\alpha}^2} \frac{2l}{b} \left(1 + \frac{2l}{b}\right)} \quad (4.7)$$

The detection limit is a priori calculated from a measurement similar to the one of interest according to DIN 25482-5 as

$$R_n^\# = (k_{1-\alpha} + k_{1-\beta}) \sqrt{\frac{N_0}{t^2} \left(1 + \frac{b}{2l}\right)} + \frac{1}{4t} (k_{1-\alpha} + k_{1-\beta})^2 \left(1 + \frac{b}{2l}\right) \quad (4.8)$$

with $k_{1-\beta}$ being the corresponding (single sided) quantile of a Normal distribution to the type II error probability β . The standard recommends to chose $\alpha = \beta = 0.025$, which means to correctly accept the null hypothesis $R_n = R_0$ in 97.5 % of all cases, if there is actually no contribution of the effect of interest in the spectrum. (Compare [DIN93].)

In case the measured count rate R_n is higher than the decision threshold R_n^* , a net effect is declared as detected and the result can be converted to an activity of the sample. Only in this case DIN 25482-5 lays down to calculate a confidence interval to the obtained value with the boundaries

$$R_n \pm k_{1-\gamma/2} \sqrt{\frac{N_b}{t^2} + \frac{N_0}{t^2} \frac{b}{2l}} \quad (4.9)$$

$k_{1-\gamma/2}$ is the (double sided) quantile to a confidence level of $1 - \gamma$. It is recommended to chose $\gamma = 0.05$. In case the measured count rate R_n does not exceed the decision threshold R_n^* , the effect of interest is just classified as not detected. (Compare [DIN93].) DIN 25482-5 does not include the calculation of upper limits.

Due to the approximation of the Poisson distribution by a Gaussian distribution, the standard does in addition define some conditions in that the real decision

error possibilities can differ from the desired probabilities α and β . In case the ratio $b/2l$ is chosen as 1 and low counts can be expected, Equations (4.7) and (4.8) are applicable to the widest input range.

A major drawback of DIN 25482-5 is that it does not define any methods to correct for peaks already present in the background spectrum. It is only possible to evaluate peaks in an acquired spectrum in case there is no peak found at the same energy in the background spectrum or the peak of interest is high in comparison to the corresponding background peak so that the latter is negligible.

4.3.2. Standard DIN ISO 11929:2011

In contrast to DIN 25482-5, which is based on conventional statistics, DIN ISO 11929:2011 [DIN11] is based on Bayesian statistics and is able to handle not only statistical uncertainties ('type A of uncertainty') but also type B uncertainties (based on other available information) according to the Guide to the Expression of Uncertainty in Measurement (also referred to as ISO/IEC Guide 98-3:2008 [ISO08b], JCGM 100:2008 or GUM). The new standard is the German version of the international standard ISO 11929:2010 and considers the uncertainties of the measurement as well as the one from weighing, sample treatment, efficiency calculations etc. DIN ISO 11929:2011 replaces the previous German standards DIN 25482-1 to -7 and -10 to -12 and therefore includes all special cases handled in the single standards before. Consequently, the standard discusses at first the general model and procedure common to all different cases and gives details of the special cases afterwards. A major difference of the Bayesian approach to conventional statistics is that the non negativity of the measurand, i.e. the area of a peak in a spectrum, is considered in the calculations. Physical quantities are denoted by capital letters and the corresponding values in lower case letters. (Compare [DIN11].)

DIN ISO 11929:2011 assigns an estimator Y to the measurand, which is also denoted by Y . Based on the measurements a primary result y and its corresponding standard uncertainty $u(y)$ can be obtained by applying a model describing the measurement process to the input values. It is possible that y is negative, especially if the true value \tilde{y} of the measurand is very close to 0. The best estimator \hat{y} is calculated from y and includes the information of non negativity of the measurand. $u(\hat{y})$ is the standard uncertainty belonging to \hat{y} and is always lower than the standard uncertainty $u(y)$ of the primary result. (Compare [DIN11].)

The measurand Y is regarded as a function G depending on several input quantities X_i like

$$Y = G(X_1, \dots, X_m) \quad , \quad (4.10)$$

which is the model of the data evaluation. By applying the model (4.10) to the input values x_i , the primary result y can be obtained. Depending on the input

4. Software for data processing and analysis

values x_i , the computation of a negative result y is possible, since the model does not include the non negativity of the measurand. The standard uncertainty $u(y)$ of the primary result is calculated from the standard uncertainties $u(x_i)$ of the input values by standard Gaussian error propagation

$$u^2(y) = \sum_{i=1}^m \left(\left. \frac{\partial G}{\partial X_i} \right|_{x_i} \right)^2 u^2(x_i) \quad . \quad (4.11)$$

(Compare [DIN11].)

The model Y , which is used in DIN ISO 11929:2011, can be written as

$$Y = (X_1 - X_2 X_3 - X_4) \frac{X_6 X_8 \cdots}{X_5 X_7 \cdots} = (X_1 - X_2 X_3 - X_4) \cdot W \quad (4.12)$$

with

$$W = \frac{X_6 X_8 \cdots}{X_5 X_7 \cdots} \quad . \quad (4.13)$$

X_1 denotes the gross count rate, X_2 the background count rate with a probably necessary attenuation factor X_3 (e.g. shielding by the sample) and X_4 an additional background correction. The factors X_i with $i > 4$ are scaling factors like – in case of γ ray spectrometry – the emission probability of the γ ray, the FEP efficiency, the sample mass (in case Y should be a specific activity), a decay correction (to a reference date), the dry-wet-ratio (needed for environmental samples), etc. (Compare [DIN11].)

X_1 and X_2 are the quantities that necessitate the calculation of the decision threshold y^* and the detection limit y^\sharp since the other input quantities have to be known a priori from other measurement, computer simulations, reference data, etc. Depending on the desired output quantity Y , the values of some factors x_i ($i = 3, i > 4$) can be set to 1 or 0 ($i = 4$) and their corresponding uncertainties $u(x_i)$ to 0. (Compare [DIN11].)

Using Equation (4.11) and Equation (4.12) with the values x_i , the standard uncertainty $u(y)$ can be expressed as

$$u(y) = \sqrt{w^2 [u^2(x_1) + x_3^2 u^2(x_2) + x_2^2 u^2(x_3) + u^2(x_4)] + y^2 u_{\text{rel}}^2(w)} \quad (4.14)$$

with

$$u_{\text{rel}}^2(w) = \sum_{i=5}^m \frac{u^2(x_i)}{x_i^2} \quad . \quad (4.15)$$

In case no scaling factors X_i ($i > 4$) are used, the value w is 1 and $u_{\text{rel}}^2(w) = 0$. (Compare [DIN11].)

To calculate the decision threshold y^* and the detection limit y^\sharp the probabilities α and β for false positive and false negative decision as well as the coverage probability $(1 - \gamma)$ have to be defined a priori. With the corresponding quantiles k of the normal distribution, the characteristic limits can be calculated.

If the (measured) value y of the quantity Y exceeds the decision threshold y^* , it is concluded that the effect of interest is seen (compare also Section 4.3). It is calculated by

$$y^* = k_{1-\alpha} \tilde{u}(0) \quad (4.16)$$

with $\tilde{u}(0)$ being the standard uncertainty of the true value \tilde{y} of the measurand for $\tilde{y} = 0$ (see below.).

The used method is only considered as suitable if the detection limit y^\sharp is smaller than the guide line value y_r , which describes the requirements concerning the measurement procedure. It is calculated by

$$y^\sharp = y^* + k_{1-\beta} \tilde{u}(y^\sharp) \quad (4.17)$$

so that y^\sharp is $\geq y^*$. Since the right side of Equation (4.17) depends on y^\sharp itself, y^\sharp can be calculated iteratively by

$$\tilde{y}_{i+1} = y^* + k_{1-\beta} \tilde{u}(\tilde{y}_i) \quad , \quad (4.18)$$

using a first value \tilde{y}_0 of for example $2y^*$. (Compare [DIN11].)

For the calculation of both characteristic limits y^* and y^\sharp the standard uncertainty of the measurand has to be known as a function of the true value \tilde{y} . In case $u(x_1)$ can be expressed as a function $h(x_1)$ of x_1 , an explicit function for $\tilde{u}(\tilde{y})$ exists. In the corresponding equation of Equation (4.12) containing the output value y and the input values x_i , y is replaced by \tilde{y} and the equation is solved for x_1 . x_1 is then replaced in Equation (4.14) and $u(x_1) = h(x_1)$ by $G^{-1}(\tilde{y}, x_2, \dots, x_m)$. (Compare [DIN11].)

The model of data evaluation (see Equation (4.12)) does not include the information of non negativity of the measurand. This constraint is taken into account by converting the primary result y and its standard uncertainty $u(y)$ (see Equation (4.13)) to the best estimator of the measurand

$$\hat{y} = y + \frac{u(y) \exp(-y^2 / [2u^2(y)])}{\Phi[y/u(y)] \sqrt{2\pi}} \quad , \quad (4.19)$$

with $\Phi(x)$ being the cumulative normal distribution, and its standard uncertainty

$$u(\hat{y}) = \sqrt{u^2(y) - (\hat{y} - y)\hat{y}} \quad . \quad (4.20)$$

According to DIN ISO 11929:2011 the coverage interval is computed by

$$y^\triangleleft = y - k_p u(y) \quad \text{with} \quad p = \Phi[y/u(y)] (1 - \gamma/2) \quad (4.21)$$

4. Software for data processing and analysis

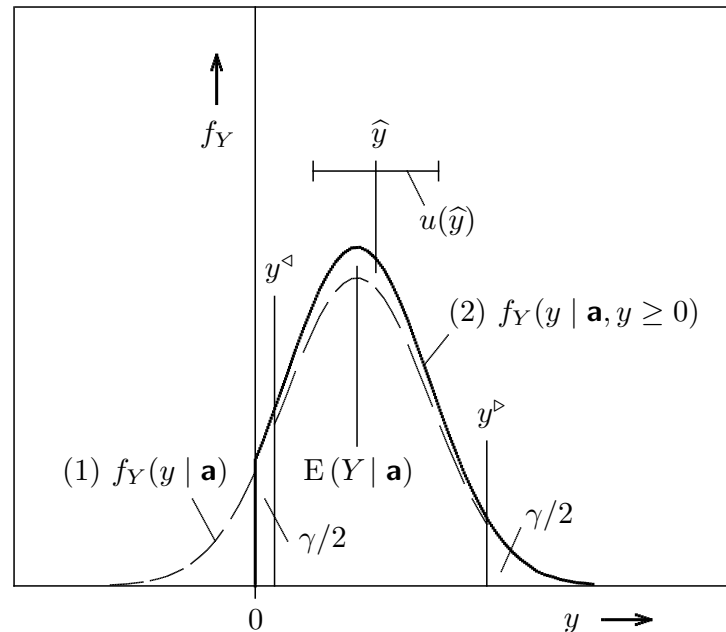


Figure 4.3.: Illustration of the best estimate \hat{y} (expectation of density (2)) of a non-negative measurand Y with the associated standard uncertainty $u(\hat{y})$ (...), and the limits y^\triangleleft and y^\triangleright of the probabilistically symmetric coverage interval that covers the true measurand value with the probability $1 - \gamma$. The dashed line represents the density (1) of the possible true measurand values y , based on the available information \mathbf{a} (from the measurement evaluated according to GUM (...)) ([ISO08b], author's note). By adding the condition $y \geq 0$ to \mathbf{a} , the density (1) is truncated at $y = 0$ and renormalized to form the bold-face density (2). (...) – Reprint of [WKM⁺13, Fig. 1] by courtesy of R. Michel and TÜV Media GmbH. (Author's note: [WKM⁺13] uses y as the true value of the measurand, not \tilde{y} like in [DIN11] and this document.)

and

$$y^\triangleright = y + k_q u(y) \quad \text{with} \quad q = 1 - \Phi[y/u(y)] \gamma/2 \quad . \quad (4.22)$$

The aforementioned quantities that describe the obtained measurement result are illustrated in Figure 4.3. (Compare [DIN11].)

The interval computed with Equation (4.21) and Equation (4.22) is *probabilistically symmetric* [ISO08a]. The two halves of the interval are neither symmetric to y nor to \hat{y} , but the probability that the true measurand \tilde{y} is smaller than the lower limit y^\triangleleft or greater than the upper limit y^\triangleright is the same and equal to $\gamma/2$. Therefore, the probabilistically symmetric interval does never extend to 0 at its lower end, even if y is 0 (see also Figure 4.4). In the following the *shortest coverage interval* [ISO08a] will be used, which is proposed by Weise et al. [WKM⁺13]. In the latter several demands to the coverage interval are defined. One of it is that the coverage interval “should cover the possible measurand value 0 if and only if this value is actually ‘highly probable’ ” [WKM⁺13]. This is fulfilled by the shortest

coverage interval defined by

$$y^{>,<} = y \pm k_p u(y) \quad \text{with} \quad p = (1 - \Phi[y/u(y)] (1 - \gamma))/2 \quad (4.23)$$

or, if a negative lower limit $y^<$ would result, by

$$y^< = 0 \quad \text{and} \quad y^> = y + k_q u(y) \quad \text{with} \quad q = 1 - \Phi[y/u(y)] \gamma \quad . \quad (4.24)$$

A graphical comparison of both coverage intervals and their properties can be found in Figure 4.4. It can be seen that both calculations lead to the same interval for large ratios $y/u(y)$, but its limits are different for small ratios. The shortest interval fulfils the demand of including the value 0 for values of y close to 0. By using the shortest coverage interval, there is a continuous transition of the result from being an upper limit to representing a detectable signal. This is important for low background γ ray spectrometry since it is always the goal to measure the activity of a sample to the highest achievable sensitivity. Since the coverage interval can also be calculated in case the obtained primary result y is lower than the decision threshold y^* , the comparison of y with y^* as a decision rule, whether an effect is quoted as seen or not, plays a minor role in our application.

According to DIN ISO 11929:2011 the results and input parameters of the measurement and its evaluation model should be summarised in a report that contains all information to retrace the results. Therefore, the version of the standard on which the evaluation is based, the physical effect of interest as well as the measurand and the model should be quoted. In addition, the a priori defined decision probabilities α , β and the coverage probability $(1 - \gamma)$ should be given. Furthermore, the primary result y and its uncertainty as well as the decision threshold y^* and the detection limit $y^\#$ should be quoted. Finally it should be stated if the effect of interest was detected and if so, the limits of the coverage interval as well as the best estimator of the result given. (Compare [DIN11].)

Application to spectroscopic measurements

The channels (or regions of channels combined) contain the values n_i with the corresponding, independent Poisson random variables N_i ($i = 1, \dots, M$ and $i = g$) assigned to it. The expectation values of N_i are then assigned to the input values X_i . The energy associated to the channels is denoted by ϑ . The lower and upper edge of channel (region) i is therefore denoted by ϑ_i and ϑ'_i respectively. For each channel i of width $\Delta\vartheta_i = \vartheta'_i - \vartheta_i$ and average spectral density ρ_i , it is $X_i = \rho_i \Delta\vartheta_i$. DIN ISO 11929:2011 denotes $\Delta\vartheta_i$ with t_i , which can cause confusion with the lifetime t_j of the measurement ($j = M$) or the background ($j = \text{Bg}$) needed for the following calculations as well. $x_i = n_i$ is the estimator for X_i with an uncertainty $u(x_i) = \sqrt{n_i}$. n_g ('g' for gross) and $X_g = \rho_g \Delta\vartheta_g$ describe the region of channels belonging to an ROI within the spectrum. (Compare [DIN11].)

For γ ray spectrometry usually a linear $H(\vartheta) = a_1 + a_2\vartheta$ ($m = 2$) or cubic $H(\vartheta) = a_1 + a_2\vartheta + a_3\vartheta^2 + a_4\vartheta^3$ ($m = 4$) parametrisation of the spectral density is chosen. (Compare [DIN11].)

The ROI is, as in DIN 25482-5, denoted by B with n_g gross counts in it and a width $\Delta\vartheta_g$. The latter will be denoted by b in the following for simplicity and as defined in DIN 25482-5 (see Section 4.3.1). It is recommended to choose a width b of approximately $2.5 \times \text{FWHM}$ in case the background is not dominant in comparison to the peak. Otherwise, a width of $1.2 \times \text{FWHM}$ is quoted as optimal. It has to be ensured that B spans an integer of channels, otherwise the width has to be enlarged to fulfil this requirement. (Compare [DIN11].) Unfortunately, the standard gives no clear definition of the term ‘dominant background’ and it is not easy to define either, since this strongly depends on peak width and relative ratios between peak and background.

Next to the left and right edges of region B in total m regions A_k of equal width l are chosen to calculate the background density $H(\vartheta)$. The total width $m \cdot l$ of m regions has to be maximised under the condition that the total number of used channels M is larger than m . If all channels have an equal width, which is the usual case, the total width $m \cdot l$ is equal to $M \cdot \Delta\vartheta_i$. To check whether the chosen background parametrisation $H(\vartheta)$ can describe the spectrum in the regions A_k , the value of Chi-square

$$\chi^2 = \sum_{i=1}^M \frac{[H(\bar{\vartheta}_i; a_k) \Delta\vartheta_i - n_i]^2}{n_i + 1} \quad (4.27)$$

is calculated, with $\bar{\vartheta}_i$ being the energy assigned to the centre of channel i . If, for a (recommended) probability δ of 0.05, the condition

$$\frac{|\chi^2 - (M - m)|}{\sqrt{2(M - m)}} \leq k_{1-\delta/2} \quad (4.28)$$

is fulfilled and M maximised under this condition, the parametrisation is taken to be valid. (Compare [DIN11].) The denominator $n_i + 1$ of Equation (4.27) is given in the standard to take care for the case that the content of a channel is 0. This case is avoided by adding 1, which does not change the value of χ^2 significantly for large channel contents. Since the algorithm implemented in the analysis software described in Section 4.4 is used to calculate the peak area in simulated spectra as well, the proposed increase of n_i by 1 can have a huge influence in the case of low statistics of the overall simulated continuum in the spectrum. To avoid this as well, the denominator is only set to 1 in case n_i is 0, otherwise the value n_i is used. This mainly avoids the huge influence for the case of small channel contents and uses an estimate for the uncertainty of an empty channel. Equation (4.28) can be derived with the central limit theorem and is an approximation of the χ^2 distribution for a large number of degrees of freedom ($M - m$) by the normal

4. Software for data processing and analysis

distribution. Therefore, $k_{1-\delta/2}$ is the quantile of the normal distribution. In case of two peaks in a spectrum that are situated close to each other, the degrees of freedom are limited and Equation (4.27) should be compared with the quantile of the χ^2 distribution instead, for which computer algorithms exist.

In the linear parametrisation $H(\vartheta)$ can be written as

$$H(\vartheta) = \underbrace{\frac{n_1 + n_2}{2l}}_{(a)} + \underbrace{\frac{n_2}{l} - \frac{n_1}{l}}_{(b)} (\vartheta - \bar{\vartheta}_g) \quad , \quad (4.29)$$

with $\bar{\vartheta}_g$ denoting the energy assigned to the centre of the ROI B , which is not necessarily identical to the energy of the evaluated γ ray peak due to the binning. n_1 and n_2 are the sum of counts of all channels belonging to the regions A_1 and A_2 respectively. (Compare [DIN11].) Part (a) in Equation (4.29) is the mean spectral density in the regions A_1 and A_2 assigned to the centre $\bar{\vartheta}_g$ of region B . Part (b) in Equation (4.29) is the slope between the mean spectral densities in each region A_k assigned to the centres of these regions. According to the standard the regions A_k and B have to be chosen next to each other. In case the width of B is chosen to be $1.2 \times \text{FWHM}$, it is questionable if this is appropriate, since the regions A_k then include a significant part of the peak. In the implementation described in Section 4.4 the distance between the inner edges of the regions A_k is always chosen to be at least $2.5 \times \text{FWHM}$ of the peak so that a gap between B and the regions A_k may occur. Under the restriction that the distances of B to A_1 and B to A_2 are equal, this can be taken into account in Equation (4.29) by replacing the denominator of part (b) by $\Delta(\bar{\vartheta}_2 - \bar{\vartheta}_1)$. The latter is the distance between the centres of region A_1 and A_2 , which is larger or equal to $b + l$. In case of unequal distances to the left and right side of B , weighing factors for n_1 and n_2 have to be included in the numerator of part (a) of Equation (4.29) as well.

If no valid linear parametrisation can be found, a cubic one has to be chosen. For that four background regions A_k with equal width l are necessary. Again the total width $4l$ has to be maximised. The functional relationship of the counts n_k in the regions, their widths and the assigned energies is much more complex than Equation (4.29) and is therefore not given here. For the case of adjacent regions A_1, A_2, B, A_3 and A_4 the formula can be found in [DIN11, p. 50].

By inserting the obtained function $H(\vartheta)$ into Equation (4.26), an estimate for the number of background counts z_0 in the ROI B can be calculated. From the obtained function $H(\vartheta)$ and the uncertainties of number of counts n_k in the regions A_k , the uncertainty $u(z_0)$ of the estimate z_0 can be deduced as well. If it is necessary to correct for a peak already present in the background spectrum, which is often the case for low background γ ray spectrometry, the procedure described above is repeated for the background spectrum as well and a set of values $n_{g,Bg}$, $z_{0,Bg}$ and their uncertainties u derived.

The primary result y for the specific activity A_{spec} of the sample can then be

calculated from the gross and background count rates by

$$y = \left[\underbrace{\frac{(n_{g,M} - z_{0,M})}{t_M}}_{=x_1} - \underbrace{\frac{(n_{g,Bg} - z_{0,Bg})}{t_{Bg}}}_{=x_2} \cdot \underbrace{\frac{f_{Bg}}{f_M}}_{=x_3} \right] \cdot w \quad (4.30)$$

with

$$w = \frac{1}{f_M M \varepsilon p F_{dw}} \cdot 2^{\frac{t_{Start} - t_{Ref}}{t_{1/2}}} \quad (4.31)$$

M denotes the mass of the sample during spectrum acquisition, p the emission probability of the analysed γ line and ε is the FEP efficiency, the probability that a γ ray with the energy of interest is detected in the full energy peak under the used conditions of sample to detector geometry and sample matrix (chemical composition and density). F_{dw} is the dry-to-wet ratio of the sample usually only used for environmental solid samples, where an activity per dry mass has to be specified. It is determined by drying an aliquot of the used sample in an oven. The width of the ROI B in the spectra $j = \{M, Bg\}$ (M for measurement, Bg for background) is chosen to be $b = \nu \times \text{FWHM}$. Hence, a correction factor $f_j = 2\Phi(\nu\sqrt{2\ln 2}) - 1$ is used to normalise the integrated peak area to unity, assuming that the distribution of counts of the peak follows a normal distribution. The second factor in Equation (4.31) corrects a decrease of the activity of the nuclide of interest with half life $t_{1/2}$ between the start of the measurement t_{Start} and a reference date t_{Ref} . It has to be denoted that strictly speaking the values $n_{g,Bg}$ and $z_{0,Bg}$ (see subtrahend of Equation (4.30)) for a peak already found in the background have to be extracted from background data that were acquired under exactly the same conditions as the sample measurement. Since the sample itself shields the detector from a part of the background radiation, the background spectrum is only valid if it was acquired with an absolutely radiopure sample, which is nearly impossible to find, of same chemical composition and density as the real sample placed on the HPGe detector. Since it is impossible to acquire a matching background spectrum for each geometry and impossible to correct for the attenuation by the sample as well (the location of the background sources is unknown), a slight overcompensation can be expected for very radiopure samples.

The different parts in Equation (4.30) are in addition annotated with the notation used in Equation (4.12), the general model of analysis in DIN ISO 11929:2011. In general, it is assumed that the uncertainties of the acquisition times t_j of the spectra $j = \{M, Bg\}$ as well as the correction factors f_j and the start and reference

4. Software for data processing and analysis

date can be neglected. The uncertainty of y can then be written as

$$\begin{aligned} u(y) &= \sqrt{w^2 [u^2(x_1) + x_3^2 u^2(x_2)] + y^2 u_{\text{rel}}^2(w)} \\ &= \sqrt{w^2 \left[\frac{1}{t_M^2} (n_{g,M} + u^2(z_{0,M})) + \frac{f_{Bg}}{t_{Bg}^2 f_M} (n_{g,Bg} + u^2(z_{0,Bg})) \right] + y^2 u_{\text{rel}}^2(w)} \end{aligned} \quad (4.32)$$

with

$$u_{\text{rel}}^2(w) = \frac{u^2(M)}{M^2} + \frac{u^2(\varepsilon)}{\varepsilon^2} + \frac{u^2(p)}{p^2} + \frac{u^2(F_{dw})}{F_{dw}^2} + \left(\frac{(t_{\text{Start}} - t_{\text{Ref}}) \ln 2}{T_{1/2}^2} \right)^2 u^2(T_{1/2}) \quad . \quad (4.33)$$

For the calculation of the characteristic limits y^* and $y^\#$ according to Equation (4.16) and Equation (4.17) the uncertainty $\tilde{u}(\tilde{y})$ in dependence of the true measurand value \tilde{y} is required. To derive this functional relationship Equation (4.30) is solved for $n_{g,M}$, $n_{g,M}$ replaced in Equation (4.32) and y finally substituted by \tilde{y} (compare procedure at page 67).

The information of non negativity of the measurand is included into the evaluation by converting the primary result y and its standard uncertainty $u(y)$ to the best estimator \hat{y} of the measurand and its standard uncertainty by applying Equation (4.19) and Equation (4.20). The lower and upper limit of the coverage interval can be calculated with Equation (4.21) and Equation (4.22) or Equation (4.23) respectively.

4.4. Analysis software GeAna

For the analysis of γ ray spectra acquired by HPGe detectors several commercially available software packages exist. Since most of them have some drawbacks and are, for example, not able to correctly apply peaked background correction (PBC) including the propagation of the uncertainties introduced by this correction or calculate upper limits for the activity of a nuclide of interest, a software tool was needed to evaluate the spectra acquired with the detector system described in Chapter 3.

At the beginning, a collection of functions was implemented using the programming language C++ and methods provided by the different classes of the ROOT data analysis framework. With these functions it is possible to calculate the net peak areas in a spectrum according to the former German standard DIN 25482-5, which is described in Section 4.3.1. In parts these functions have been extended by Th. Quante, who implemented for example the automatic shifting of the regions needed for the background estimation under a peak, in case

neighbouring peaks extend into these regions. Since it became more and more complex to handle the dependencies between the implemented functions and the obtained results, a class handling these dependencies was developed on the basis of the programmed collection of evaluation functions.

GeAna is a class for the use within the ROOT framework. To ease the usage and allow the simple finding within the huge amount of methods and functions provided by ROOT at its command line interface, all names of the member functions belonging to the class do start with 'GA'.

After creating a specific object of the class, a file has to be specified via `GAOpen`, which is used to store the results of the analysis. Simultaneously two data storage structures called `TTree` (see also Section 4.1) are created to save the information like the determined results in the one as well as the parameters and settings used to evaluate each peak in the other. In addition, the evaluation standard used is set, which defaults to 'ISO' denoting the new German standard DIN ISO 11929 described in Section 4.3.2, but can be set to 'DIN' likewise. Internally the method `GASetStandard` is executed that sets for example the decision error probabilities α and β (compare Section 4.3) and the used ROI width to the recommend values. `GASetStandard` can be used before the first evaluation of a γ line as well to change the evaluation standard.

Afterwards the user can load a data file via `GALoad` that was converted by the data conversion tool described in Section 4.1 containing the spectrum, its calibration data as well as the information about acquisition time and start of the measurement. By this method several internal variables are set, which hold the preceding quantities. The reference date is set to the start date of the measurement so that by default no decay correction (see Equation (4.31)) is done. The dates are handled in Unix time, a format specifying the number of elapsed seconds since 1970-01-01 00:00:00 UTC so that time spans can easily be calculated. In addition, the user can specify a description for the analysed sample. It can also be set by a separate method at a later time during the data evaluation process.

A reference date for decay correction can be set by the member function `GASetRefDate`, which requires the date as a text string of the form 'YYYY-MM-DD hh:mm:ss tz', where 'tz' is the time zone of the date and can be set to UTC, central European time (CET = UTC+1h) or central European summer time (CEST = UTC+2h). The date is converted to Unix time and stored internally as an integer number.

Usually the specific activity A_{spec} of a sample is of interest, since in material screening measurements it is either only possible to use a subset of the material for radio assaying or usually only a small amount of the material is used in the intended low background application and a huge amount of sample is used to increase the sensitivity to radioactive impurities. By default, when loading the input spectrum, a sample mass of (1 ± 0) kg is assumed. By this, the calculated results by default only have the unit Becquerel. If the user specifies a sample mass

4. Software for data processing and analysis

M , its uncertainty $u(M)$ (both in kilogram) and the dry-to-wet ratio F_{dw} (which is 1 as default) via the method `GASetSampleMass`, the results are scaled to the unit Bq/kg.

It is possible to load a background spectrum, which is then used for PBC, by calling the member function `GALoadBg`. In principle, the latter does the same as `GALoad` but sets the values of other variables that are intended for the background spectrum, like for example the corresponding life time. In this case an internal variable is set, which guarantees that the correct algorithms are used, and the program, in the other case, does not try to use unavailable data, which would result in memory access errors. After loading of the background spectrum, the usage of PBC can be toggled by the command `GASetBgPeakCorr`.

To determine the FEP efficiency ε for γ lines of interest for the sample geometry, a MC simulation with the program VENOM (see Section 4.5 and Chapter 5) is used. The file output from VENOM contains information about the energy depositions in the germanium detector for the simulated γ lines. Since mechanisms in VENOM and the underlying Geant4 do not contain a charge transport or electric field simulation, the MC simulation can not reproduce effects like detector resolution. The FEP efficiency can, in principle, also be obtained by measuring sources with well known activity and geometry, which would inevitably include the detector effects during the FEP determination. To be able to apply the same evaluation methods used for the acquired γ ray spectrum the simulation data that are loaded by the command `GALoadSim` are automatically convoluted with the energy dependent detector resolution, obtained from calibration measurements and given to the analysis software together with the input data. Since the MC simulations done with VENOM usually contain the decays of more than one type of nuclide, the user can specify a fraction that is used to calculate the number of simulated decays of one type of nuclide from the total number of simulated events. Furthermore, by default a general relative uncertainty of the calculated FEP efficiency of 5% is assumed. From the computer simulations alone it is not possible to determine the uncertainties, but since it makes no sense to overestimate the accuracy of a result, a general uncertainty is assumed. The default value is selected on the basis of the results of the simulation studies in Chapter 5. It can be modified by the user when calling `GALoadSim`, but can be changed later on by `GASetFEPUncertaintyRel` likewise. A further boolean parameter of `GALoadSim` specifies whether the MC simulation does already contain the emission probabilities p of the γ lines or not. If specified as 'true', which is default, it is assumed that the whole radioactive decay of the nuclide was simulated in VENOM. In this case, the FEP efficiency obtained is actually the product εp (compare Equation (4.31) and discussion in Section 5.3). Depending on the measurement situation modelled by the MC simulation, it can be much more efficient to store only simulated events that deposit energy within the detector (e.g. modelling background sources outside of the detector shielding). Since the information of the

total simulated events is lost in this case, another parameter can be given to the method `GALoadSim` to set this value, which is necessary to calculate the efficiency.

In case the user wants to change the recommended values for the decision error probabilities α and β or the confidence level (DIN 25482-5) or coverage probability γ (DIN ISO 11929:2011), the method `GASetErrorProb` can be used. As an alternative the corresponding quantiles can be set as well by `GASetQuantileLimits`. In evaluations according to DIN 25482-5 by default the values $\alpha = \beta = 0.05$ and $\gamma = 0.317$ are applied. DIN ISO 11929:2011 uses the defaults $\alpha = \beta = \gamma = 0.05$.

The width of an ROI used to evaluate the peak of a γ line is fixed in evaluations according to DIN ISO 11929:2011 to $2.5 \times \text{FWHM}$ and $1.2 \times \text{FWHM}$ respectively. In contrast to this, DIN 25482-5 only recommends $2.5 \times \text{FWHM}$, which is used as default, but all other widths under the restrictions expressed by Equation (4.2) can be set by `GASetPeakCoverage` as well.

In data evaluations according to DIN 25482-5 the regions A_1 and A_2 are used to estimate the background contribution in the ROI. Their single width l is calculated relative to the width b of the ROI B . The member function `GASetBto2L` can be used to change the default $\frac{b}{2l} = 1.0$ to a new value in the range allowed by Equation (4.3).

To evaluate a peak caused by γ ray emission during the decay or de-excitation of a certain nuclide the properties of this emission have to be provided to the evaluation class `GeAna`. Therefore, a method `GASetIsotope` is provided, which allows to set the name of the nuclide, its half life $t_{1/2}$ in seconds, the energy of the γ line of interest in keV and the relative emission probability p of this line. Furthermore, the uncertainties of the emission probability and the half life can be optionally set as well. By default the latter two are assumed to be 0. Since in some measurement constellations it is known that two γ lines contribute to the peak of interest in a certain ratio, a correction factor and its uncertainty, which are by default 1 and 0, can be given to the method as well.

Since it can be of interest to evaluate more than one γ line belonging to the decay of a certain nuclide, it is possible to add further γ ray emissions for evaluation to the already specified nuclide by using the method `GAAddIsotopeLine`. Analogue to `GASetIsotope` the energy of the γ line, its emission probability p and optionally the uncertainty of p as well as a correction factor and its uncertainty have to be specified.

The γ lines that have been defined by the two previous commands are then evaluated via `GAEvalIsotope`. Depending on the selected evaluation standard, different procedures are applied to the spectra. In general the former German standard DIN 25482-5 should only be used in special cases, where no PBC is necessary and a simplified evaluation is sufficient. In case DIN 25482-5 (compare Section 4.3.1) was selected, the ranges of the regions are calculated from the applied settings and the calibration data at first. Starting from the defined energy, the edges of the ROI are determined ensuring that the regions cover a

4. Software for data processing and analysis

whole-numbered amount of channels. By summing up the channel contents in the defined regions, the input parameters are fixed and the net count rate can be calculated. This result is then converted to a specific activity and further values like the uncertainty or confidence interval computed. In case the obtained result is below the decision threshold y^* an upper limit is calculated by a formula taken from the book by G. Gilmore [Gil08, p. 117].

By default the current German standard DIN ISO 11929:2011 (see Section 4.3.2) is selected. At the beginning of the evaluation of a γ line of interest the range of the ROI B is calculated for a coverage of $2.5 \times \text{FWHM}$ given by the resolution calibration. Again it is ensured that a whole-numbered amount of channels is used. At first it is tried to describe the shape of the background to the left and right of the peak by a linear model. Defined by the restrictions for the width of the regions A_k to estimate the background, a width of two channels is selected as a start. To secure that the peak of interest is completely covered by the defined ROI, a magnification of the spectrum around the ROI is presented to the user. At this point it is possible to apply different modifications to the defined regions (like enlarging, shifting, offset of the regions A_k , etc.) or even aborting the process via the command line. This was implemented since it can be possible that the user made a mistake during the setting of the values, which could then lead to wrong calculations of the channel content sums in the different regions. If the user confirms the usage of the plotted ranges, an iterative algorithm tries to find the maximum width l for the background estimation regions A_k . The check expressed by Equation (4.27), i.e. whether the estimated background function describes the spectrum correctly, becomes less sensitive to small peaks in the spectrum for increasing region widths l . Although these do not influence the estimated function much, by default a maximum width of one background region A_k of 200 channels is set. In case a valid setting for the widths is found, the estimated background z_0 in the ROI is calculated by Equation (4.26) and the net peak area is determined. If it is detected that the estimated background is dominant (for the used criterion see below), the above described procedure is repeated with an ROI width of $1.2 \times \text{FWHM}$. In case no matching linear background describing function $H(\vartheta)$ can be found, a cubic function is used. Again the procedure described above is applied and with an optimal background width the net peak area is calculated. If the user did load a background spectrum to correct for peaks already detected without a sample, the same algorithms are applied to the background spectrum as well. The FEP efficiency is calculated from a provided MC simulation likewise but only with an ROI width of $2.5 \times \text{FWHM}$, since the MC simulations should be set up in a way that there is a significant signal in the simulation spectrum to calculate the efficiency ε from. Together with the remaining input quantities like mass M and γ ray emission probability p the results from the different calculations are converted to a primary result A_{spec} and its uncertainty $u(A_{\text{spec}})$ by Equation (4.30) and Equation (4.32). Based on these primary results

the characteristic values like for example the decision threshold A_{spec}^* as well as the best estimator \hat{A}_{spec} of the true value of the measurand, its uncertainty and the coverage interval defined by $[A_{\text{spec}}^<, A_{\text{spec}}^>]$ are computed. The results for the defined nuclide are added to the TTree structure that was automatically created during the setting of an output file. In addition, a lot of information about the location of the different needed regions are stored to a second tree so that it is possible to check the results independently.

To ease the usage of the above described member functions `GASetIsotope`, `GAAddIsotopeLine` and `GAEvalIsotope`, an extensive set of methods for the evaluation of the usually needed, mostly natural occurring nuclides is implemented as well. These, with names like `GAEvalK40` or `GAEvalPb212`, already contain the decay and emission data of the specified nuclides. The decay data have been taken from the Decay Data Evaluation Project (DDEP) [Lab13] and the updated version of the Table of Isotopes [Fir96]. Based on the data referenced above and the book by G. Gilmore [Gil08] it was taken care to use preferably γ lines for evaluation that are not subject to TCS and do not interfere with γ ray emissions of other nuclides. An option can be specified so that the implemented data are only set but not evaluated. By this, it is possible to print the list of defined properties before the evaluation by `GAShowIsotope`, remove a single γ line by `GARemoveIsotopeLine` or even add further lines before an evaluation with the command `GAEvalIsotope`.

The exact behaviour of the evaluation algorithms according to DIN ISO 11929:2011 can be adjusted by two specialised methods. The maximum used width of one background region A_k (see discussion above) can be changed via `GASetIsoMaxBgWidth`. Since it is not defined in the standard what is regarded as dominant background (see remark in Section 4.3.2 at Equation 4.3.2), the method `GASetIsoBgDominanceFactor` is provided to be able to set a different value for the ratio between the calculated net peak area and the estimated background. By default the calculations are repeated with an ROI width of $1.2 \times \text{FWHM}$ if the ratio is lower than $\frac{1}{3}$.

In case several γ lines belonging to the decay of one nuclide have been analysed, the obtained results and their uncertainty can be plotted for a single nuclide in dependence of the γ energy by `GAPlotResults`. By this, it is possible to get an graphical overview of the calculated values and their differences.

Since it is inconvenient to view or extract the results stored in the ROOT TTree structure, a member function was implemented to generate an evaluation report containing all relevant data. Depending on the evaluation standard used, `GAExportResults` produces different output files. In case of DIN 25482-5 a simple plain text file is created containing the information like determined nuclide activities, lifetime of measurement, sample mass, decision error probabilities and so on. For DIN ISO 11929:2011 a \LaTeX file is produced since the notation of the output quantities is more complex and the standard requires a more extensive evaluation

4. Software for data processing and analysis

report. If a sample mass was set by the user, the units are automatically set to be 'per kilogram' and, as well as the symbols of the quantities, correctly printed to the evaluation report. Furthermore, the unit of the activity can be set by an option given to the export command to mBq (default), Bq, kBq or even counts per day. In case that several γ lines of one nuclide have been evaluated, a weighted mean and its uncertainty is calculated from the primary results and quoted as $A_{(\text{spec})}$. This value is then again converted to the best estimate and the coverage interval. It is possible to calculate all quantities even if the primary result should be negative. Therefore, the relevant values are automatically highlighted within the table of results. In case that the lower limit of the shortest coverage interval is equal to zero, only the upper limit of the coverage interval is highlighted. Otherwise the best estimator as well as the limits of the coverage interval are of relevance. The results are stored internally with the precision of the data type double. Since it does not make much sense to quote the results with a too high precision, the values are rounded for the evaluation report. To cover the requirements of correctly quoting a result (see JCGM 100:2008, Section 7.2.6 [ISO08b]) an internal function was implemented that rounds the uncertainties mainly upwards and prints out the value with two significant digits. The value of the quantity itself is rounded to the same precision as the corresponding uncertainty. The exported document contains as well the used decision error probabilities α and β and the coverage level $(1 - \gamma)$. Finally a remark about the different coverage intervals and their discussion in literature is included. An example of such an evaluation report of an analysis according to DIN ISO 11929:2011 can be found in Appendix C.

If all γ lines have been evaluated, the results can be stored with `GASave` to the `ROOT` output file and the different used files closed by `GAClose`. Depending on the specified option given to the command single files of the inputs can be closed. As an alternative both actions can be executed in combination via the method `GASaveClose`.

With the above mentioned commands it is possible to evaluate peaks in a γ ray spectrum in most cases. Nevertheless, it is necessary to extend the functionality of the class `GeAna` and implement the deconvolution of neighbouring peaks, since some of the γ lines occurring in spectra of materials containing the nuclides of the natural decay chains (see Section 2.2.2) do overlap or can not be separated at all. In many cases, like the 1460.8 keV γ line emitted during the decay of ^{40}K , the relevance of overlapping peaks varies widely with the ratios of activities of the different nuclides contained in a sample. Only 1.7 keV below the ^{40}K peak, a γ line of ^{228}Ac with a low emission probability can be found. Depending on the activity of ^{228}Ac contained in a sample, the γ line in the vicinity of the 1460.8 keV peak can be completely negligible or influencing the calculated peak area significantly. Another aspect that requires further effort is the sensible combination of results obtained from different γ lines belonging to the decay of one nuclide or even the combination of calculated activities of nuclides contained in parts of the natural

decay chains being in equilibrium. M. Heisel et al. [HKS09] present the statistical methods needed to combine several lines, but these have not been implemented in the scope of this work. The analysis class was especially designed to extract the information about the full peak efficiency for a certain γ line and geometry from MC simulations. If necessary, the class could be extended to be able to read-in efficiencies obtained by other methods or do comparative measurements with radioactive sources of (precisely) known activity. Overall with GeAna a software tool was developed that allows for a very fast, convenient and standardised work flow to evaluate γ ray spectra, including the correction of peaks already present in the background spectrum of the detector system. With all these features it is possible to reach very high sensitivities for radioactive impurities contained in different samples.

4.5. Simulation program VENOM

The full energy peak (FEP) or total efficiency (compare Section 2.3.1) for radiation emitted by a sample can often only be measured at great expenses. This holds especially for complex germanium detector systems like the DLB (described in Chapter 3). Due to the complexity of the physical processes of interaction of the different types of radiation with matter it is as well not possible to calculate these efficiencies analytically. Therefore, often computer programs are used that describe the different interactions by models and choose the types of interaction occurring at a certain point in the geometry by the parametrised probabilities for these.

The simulation program used in this work is called VENOM, since its development started in 2005 by scientists working at the COBRA experiment. It is based on the Geant4 MC framework [AAA⁺03] for the propagation of different types of particles through matter. Similar to the analysis software GeAna described in Section 4.4, which uses the classes and methods provided by ROOT, VENOM makes use of the many particles, geometry interfaces, interaction models, algorithms, etc. provided by Geant4. Geant4 was initially designed for high energy physics simulations. VENOM therefore uses the low energy extensions and provides many interfaces to generate different particles or decays at a certain location within the implemented geometries. Furthermore it handles the information produced during the tracking and interactions of particles by Geant4, extracts relevant data and allows to store these to structured ROOT files. By the different detector types provided by VENOM, for example only basic information like the energy deposited in a HPGe or CdZnTe crystal or more complex information like the hit voxel of a depth sensing pixel detector can be stored to the output files.

At the begin of this work VENOM was still designed for an old Geant4 version (~9.0), which did not support the usage of GDML geometries (see also Chapter 5). Together with T. Köttig, VENOM was adapted to the new methods and physics

4. Software for data processing and analysis

models provided by the newer Geant4 versions. VENOM was first adapted to function with Geant4 9.3 and during the time also upgraded to work with the releases 9.4 and 9.5. Geant4 does only provide methods for the import and export of GDML files but does not provide any methods to influence the data read-out from certain volumes of the geometry during the propagation of particles through it. T. Köttig extended the functionalities of VENOM and added many sophisticated methods for the adaptation of the system to many different simulation purposes. He implemented methods to assign a sensitivity (the Geant4 term for marking the information of interactions as relevant) to different volumes of an imported GDML geometry. As geometries of a detector set-up can be quite large, the precise tracking of particles in volumes far away from a sensitive volume (for example the detector) are usually only of limited relevance. Since the simulation of charged particles needs a lot of computing time, the reduction of the simulation mainly to regions close to the detector is desirable. In Geant4 it is possible to assign so called UserCuts in form of a remaining range or energy of a tracked particle to the different volumes of the geometry. T. Köttig therefore implemented several commands to set these values on a per volume basis and apply these to different selectable particles. These huge efforts, which are in detail described by him in [Köt12], made the simulation studies in Chapter 5 possible in the first place.

In case of complex geometries it can be inconvenient to set tracking cuts for every single volume. Therefore, an option was added to the already implemented commands to be able to apply a certain cut value to all volumes of the geometry. The cut value can then afterwards be lowered for important areas again. In addition, a command was added to set cuts for all volumes containing one material, which is useful to apply a certain cut value for example to the lead shielding of a detector but not to other components of the shield.

The simulation studies conducted by the users of VENOM cover a wide range of different processes of interest. For example in some cases the production of nuclides by cosmic particles or interaction of muons with the COBRA detectors are of interest, in others the appropriate shielding of neutrons and in others again the detection efficiency for double β decays is examined by MC studies. This wide field requires VENOM to handle many different tasks and leads to a certain size of the software package. Especially the database files of Geant4 describing the properties of many different particles, interactions and materials can have a remarkable size. The data files needed for all physics processes defined in the so called PhysicsList in VENOM are loaded to the memory of the executing PC. For the propagation of neutrons VENOM uses the high precision neutron data (NeutronHPElasticData, etc.). The amount of available neutron data did increase with the release of Geant4 9.5 tremendously so that the required memory rose by a factor of approximately 3. For analysis and simulation tasks the working group Physik EIV runs a small computing cluster managed by the Hadoop® framework

for distributed computing and load balancing. Since the single computing nodes fetch the required Geant4 libraries and data from the distributed files system AFS each time a job is started, this slows down the upstart of VENOM significantly. In addition, some computing nodes even ran out of memory with the more precise data so that simulation jobs failed. Since the propagation of neutrons is usually not necessary in simulations for the DLB, a compiler option was implemented in VENOM to switch off physics processes related to neutrons. If the option `VENOM_NO_NEUTRONS=true` is specified during the compilation of the VENOM application, the described problems can be circumvented and the single simulation jobs accelerated. The 'no neutrons' status is written to the log contained in the simulation output so that it is possible to track this setting also in the data.

VENOM uses the PhysicsList of the dark matter experiment (DMX) example of Geant4, which uses by default the Livermore physics models for processes like Compton scattering. Since some discrepancies were found in the simulation studies described in Chapter 5, an additional compiler option was implemented to be able to use alternative physics models from the PENELOPE [SFVS11] simulation package, also provided by Geant4, instead. Although it is in principle possible to implement an interface in VENOM to change the used physics models at runtime, this is of limited value, since a new simulation output file should be created anyway to separate the different results. The models used by default can be replaced by the PENELOPE models by specifying `VENOM_PENELOPE=true` during the compilation of VENOM. This is as well logged to the output files to be able to reconstruct the settings used for the production of a simulation data set.

4. Software for data processing and analysis

5. Monte Carlo simulation for full energy peak efficiency determination

In material assaying usually the absolute or specific activity of a sample is of interest. Since all decay products are emitted isotropically within the sample, already for geometrical reasons it is usually impossible for the detector to detect all of them. In addition, every detector has only a limited intrinsic detection efficiency for particles impinging on it due to the nature of the absorption characteristics of the particles. Even if a particle did deposit its whole energy within the detector, it is possible that the output signal does not correspond to a full energy deposition, since in turn the signal is influenced by imperfections such as impurities or an inhomogeneous electric field within the detection volume.

To determine the detection efficiency for a certain sample to detector geometry, two basically different approaches exist. The first is a comparative method in which the counting efficiency is determined by measuring a sample of precisely known activity emitting the particles of interest. The most precise approach is to have a standard with same matrix (chemical composition and density) and geometry containing exactly the radioactive nuclides of interest. In this case even complex effects like true coincidence summing (TCS) (see Section 2.3.2) in γ ray spectrometry are taken into account. This method to determine the efficiency can be extended by interpolating between calibration points at energies close to the ones of interest. Since it is impossible to have a standard for all counting geometries usually only some standardised sample geometries can be used. To a certain extent the obtained efficiency calibrations can be transferred to samples of different height or density by using corrections extracted from additional measurements. For a detailed discussion of different aspects of efficiency calibration in γ ray spectrometry with germanium detectors see the book by G. Gilmore [Gil08, Ch. 7.6].

The second approach can be called mathematical efficiency calculation and relies on the fact that the different mechanism of interactions of especially γ rays and β particles are well known and can be described by mathematical models. Even though analytical models do exist for special source to detector geometries, most of the mathematical efficiency calculations are Monte Carlo (MC) approaches modelling the emission of particles and tracking these through a geometry representing the actual detector set-up. At each tracking step it is randomly chosen according to the probabilities for different effects in the environment at that point whether an interaction occurs or not. Assuming that the used models can describe the real characteristics in the average, the reality can be reproduced

5. Monte Carlo simulation for full energy peak efficiency determination

by tracking a large number of particles through the geometry. Different so called MC frameworks like Geant4 or PENELOPE exist, which are in part only applicable to some types of particles. The simulation program used in this work is VENOM, which is developed by the COBRA collaboration and uses the libraries provided by Geant4 (for details see Section 4.5 and [Köt12]).

To describe the real experiment by computer simulations, it is necessary to model its geometry as precisely as possible. In older versions of VENOM it was necessary to implement the geometry in the source code of the application and, unless methods to change the geometry were implemented, rebuild the software whenever modifications were made. In addition, it is inconvenient to submit general modifications to the central VENOM repository if every VENOM user implements geometries that are not needed by other users. Due to this it was desired to decouple the simulation application and the geometry. Since the XML based Geometry Description Markup Language GDML is supported by the ROOT framework, the outer shielding has already been implemented in GDML for visualisation purposes as part of the authors diploma thesis (see Figure 3.1). With the implementation of GDML import and export modules in Geant4 starting with version 9.1, it was a logical consequence to use these as an interface for external geometries in VENOM. Due to the developments by T. Köttig described in [Köt12], VENOM does support the import and usage of GDML geometries for Geant4 9.4 and later. Within a short timespan GDML became the recommended and nearly exclusively used form to provide geometry information to simulations done with VENOM.

GDML allows to define constants, quantities, positions, rotations, etc. that are used for the modelling of a set-up. These can be used to describe the size and position of volumes representing the different parts of the geometry of an experiment. Simple solids like cuboids, spheres and cylinders and more complex ones, for example torus segments or tubes with hyperbolic profile, can be combined by boolean operations (unions and subtractions) to form even very complex solids. Materials can be defined by mass fraction of the constituents or by chemical composition of elements or other already defined materials. An aggregate state and a density is assigned to the materials as well. A volume is defined in its shape by one of the created solids and additional properties like the material or surface reflectance are associated with it. Furthermore, the defined volumes (often denoted as logical volumes) can contain auxiliary attributes, which can be used to mark special properties interpreted by the own simulation code like sensitivity of a detector. The volumes are finally placed as physical representations at certain positions in the 'world' volume defining the boundaries of the geometry. In case the geometry contains many identical objects also loops similar to the ones of other programming languages or matrices for dynamic positioning can be used. The geometries are defined hierarchical so that it is possible to first define a part of the geometry as a module in local coordinates and place this in the next higher

level of the geometry. If single parts are contained in own geometry files, it is quite simple to replace e.g. a modelled sample of a measurement by a different one without the need to change the other components of the geometry. This feature is extensively used in the simulation studies described in Section 5.2.

5.1. Geometry model

Based on the mechanical drawings prepared for the manufacturing of the inner shielding of the DLB, S. Schira implemented the geometry in GDML in his bachelor's thesis [Sch10]. It is split into four files for a separation of the different components. One file contains all definitions of materials, which is included by the other geometry files to ease necessary modifications to it. In the central file DLB.gdml the shielding against radiation from radioactivity in the vicinity of the germanium detector is implemented (compare Section 3.1.2). The plug, which can be lifted to access the measuring chamber (see Figure 3.4), is defined in a separate file to simplify the positioning at different heights for different measurements needed for the simulation studies in Section 5.2. The germanium detector is again implemented in a separate geometry file on the basis of mechanical drawings provided by the manufacturer [Can08b, Can10] and own measurements of some values.

The implemented geometry was modified by the author to correct several observed discrepancies and to make the visualisation of the whole geometry by the different visualisation systems provided by Geant4 possible. Depending on the order of boolean operations to create a complex solid, it is possible that after the geometry import the resulting solid is represented by a Geant4 internal solid type that can not be displayed by most visualisation systems. By rearranging the structure or avoiding some operations, the special cases can be displayed as well. Furthermore, several additional geometries like different radioactive sources, sample containers, sample holders and extenders to increase the height between detector and plug were modelled. By assigning colours to the materials used in the geometry, a better visibility and, depending on the used visualisation system, nearly photo-realistic graphics can be created (compare Figure 5.1).

The visualisation systems provided by Geant4 all have different advantages and drawbacks. The ASCII Tree module can be used to output details of the geometry parts like volume and mass in a text format. The HepRep file format allows to view the geometry with an external tool in wireframe presentation, hide different parts of the geometry tree or measure distances between elements so that it is easily possible to check the implementation of the detector set-up. Interactively rotatable semi-transparent views of the geometry including particle tracks can be visualised with the VRML file format. Photo-realistic graphics including surface reflectance can be created by the RayTracer module but no particle tracks or cuts through the geometry can be displayed. The latter can be shown by using

5. Monte Carlo simulation for full energy peak efficiency determination

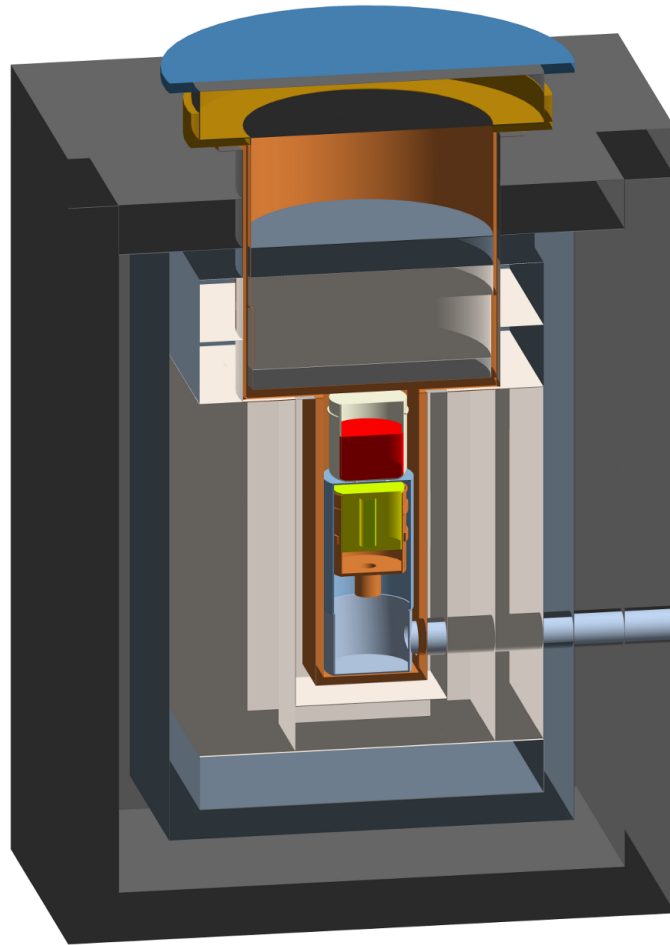


Figure 5.1.: Visualisation of the implemented geometry of the set-up. A sample container is placed on the detector endcap as well.

the OpenGL output of Geant4, which in turn can be exported to usual graphical file formats as well. During the simulation studies, the different visualisation managers were used to check and improve the implemented geometry and create graphics to display the used set-up (see Figure 5.1).

5.2. Geometry optimisation

The first simulations for the detector set-up of the DLB were performed by T. Köttig after the implementation of the GDML geometry parser in VENOM. For the comparison two calibrated radioactive sources by AEA Technologies QSA were measured by S. Schira with their lower tip in a distance of approximately 107 mm to the detector endcap. To make the placement of the source at this distance possible, the plug, usually closing the shielding, had to be placed at an elevated position. For this purpose an extender, made from a baseplate and four columns and

Table 5.1.: Deviations of simulated full energy peak count rates R relative to measurements for the sources placed at $z = 16$ mm (^{133}Ba , ^{60}Co and ^{137}Cs) above and directly on the detector endcap (^{40}K). Nominal detector parameters as given in Table 5.2. For details on the sources see Section 5.2.1 to Section 5.2.3. Emission probabilities p from [Lab13].

Energy / keV	Nuclide	p / %	Deviation $\frac{R_{\text{sim}} - R_{\text{meas}}}{R_{\text{meas}}}$ / %
53.2	^{133}Ba	2.14(3)	-27.9(15)
81.0	^{133}Ba	32.9(3)	0.8(16)
160.6	^{133}Ba	0.638(4)	9.2(21)
223.2	^{133}Ba	0.453(3)	18.2(25)
276.4	^{133}Ba	7.16(5)	16.6(18)
302.9	^{133}Ba	18.34(13)	18.1(18)
356.0	^{133}Ba	62.05(19)	14.8(18)
383.8	^{133}Ba	8.94(6)	16.4(18)
661.7	^{137}Cs	84.99(20)	14.2(18)
1173.2	^{60}Co	99.85(3)	16.1(18)
1332.5	^{60}Co	99.9826(6)	16.5(18)
1460.8	^{40}K	10.55(11)	11.96(32)

able to carry the weight of approximately 170 kg of the shielding plug, was designed by the author and build by the mechanical workshops. A distance further away from the detector than usual samples was chosen to reduce effects of the extensions of the radioactive sources and potential lateral misplacements. Although the overall shape of the spectra did agree quite well with the measurements (for details see [Köt12]), the results revealed deviations of the full peak count rates between simulation and measurement for the above mentioned source position of up to 14% (neglecting lines of low emission probability p). Based on several spectra of radioactive sources with known activities the deviations for close source to detector distances were calculated. The spectra, which were in the first place intended for the optimisation of the sensitive detector volume (for details see Section 5.2.3), were acquired with the sources at a distance of $z = 16$ mm (^{133}Ba , ^{60}Co and ^{137}Cs) and directly placed on the detector endcap (^{40}K) respectively. Table 5.1 shows a large underestimation of the FEP efficiency of low energy γ lines, whereas the efficiency for high energetic lines is overestimated by a nearly constant fraction. The discrepancies can be explained by the fact that the MC simulations performed with VENOM and Geant4 consider only the pure energy deposition by a tracked particle in a certain volume. Since no electrical field within the detector is simulated, effects like regions of weak field strength resulting in a lower contribution to the overall detector signal are neglected and a discrepancy between simulation and measurement can be expected.

Although it is possible to improve the simulation by feeding the results of the particle tracking into an external application capable of simulating the charge

5. Monte Carlo simulation for full energy peak efficiency determination

Table 5.2.: Nominal detector parameters used to optimise the agreement between simulation and measurement. Data from [Can10] and H.-J. Lange, Canberra Industries (compare Section 5.2.1).

Parameter	Value / mm
Outer dead layer thickness	0.7
Crystal to endcap distance	4.5
Core hole diameter	10
Core hole height	42

transport, the necessary effort is quite huge. Many publications have shown that the deviations between simulation and measurement can be reduced and a good agreement can be achieved by modifying several geometrical parameters of the used germanium crystal (see for example [BHMS09, HGLGT04, HHI⁺03, ALV99, CLPBC⁺10]). The nominal values of the parameters used in the following optimisation are given in Table 5.2.

The aim of the following optimisation of the MC model of the detector set-up is to reproduce the FEP efficiencies for different measurement geometries. This does not necessarily imply that the shape of the whole spectrum, especially the continuum, agrees with spectra obtained by measurements. To be able to apply the same evaluation algorithms to measured and simulated data, the latter is convoluted with the energy dependent detector resolution approximated by the function given in Equation (4.1). Since the calibration tool described in Section 4.2 approximates the peak shape by a Gaussian function, the convolution of the simulation data is done with a Gaussian function as well. Since there exist further contributions to the peak shape (see for example G. Gilmore [Gil08, p. 189f.]), which are neglected, this is taken into account by the simulation optimisation as well. For the following studies version 9.5 patch 01 of Geant4 was used. As a consequence, the derived optimised model is in the first place only valid for this Geant4 release, since it also includes the compensation of potential contained bugs in the Geant4 models or physics data.

In the following optimisation procedures the peaks in the spectra are evaluated according to DIN 25482-5 (see Section 4.3.1). From the net peak area N_n the net count rate is derived by normalising the spectrum to the acquisition time. The direct comparison of the measured rate to the simulation is only possible if a source with known activity A_0 is used. The simulated net count rate $R_{n,sim}$, needed in the following sections for several calculations, can then be calculated by

$$R_{n,sim} = \frac{N_{n,sim}}{N_{tot}} A_0 2^{-\frac{\Delta t}{T_{1/2}}} \quad (5.1)$$

and its uncertainty as

$$u(R_{n,\text{sim}}) = R_{n,\text{sim}} \left(\frac{u^2(N_{n,\text{sim}})}{N_{n,\text{sim}}^2} + \frac{u^2(A_0)}{A_0^2} + \left(u(T_{1/2}) \ln 2 \frac{\Delta t}{T_{1/2}^2} \right)^2 \right)^{\frac{1}{2}}$$

with $N_{n,\text{sim}}$ being the simulated net peak area and N_{tot} the total number of simulated events. The half life $T_{1/2}$ of the used nuclide is needed to correct the activity A_0 to the date T of measurement ($\Delta t = T - T_0$). In case of overlapping peaks in the spectrum (e.g. the 79.6 keV and 81.0 keV γ lines of ^{133}Ba) the FWHM of the line of higher emission probability was used and the ROI extended in that way that both peaks are completely covered.

5.2.1. Dead layer thickness

For the sensitivity of the detector to low energetic γ rays the thickness of the outer electrode as well as the detector endcap are crucial. Since the contact does not belong to the sensitive volume of the germanium crystal it is often also referred to as the outer dead layer. According to the detector data sheet [Can10] the outer dead layer has a thickness of 1.2 mm, but according to H.-J. Lange, Canberra Industries, a thickness of the outer contact of approximately 700 μm can be assumed. This value does fit to the data found in literature and is therefore taken as the nominal value. The thickness of the aluminium endcap of 1.5 mm [Can10] is fixed in this simulation study since the optimisation of two parameters at the same time is rather ambitious. In addition, the thickness of the outer contact has a stronger influence on the absorption characteristics due to the higher atomic number Z of germanium in comparison to aluminium.

The thickness of the contact can be determined by placing a radioactive γ ray source at a larger distance above the detector endcap. In case a source is used that emits at least two low energetic γ rays with a certain difference in energy, the activity of the source does not need to be known. The determination bases on the energy dependent absorption coefficients μ in the materials between the radioactive source and the sensitive volume of the detector. In the measured spectrum the ratio of the two peak areas is determined and represents the target value that has to be reproduced with the MC simulation.

The determination of the thickness by this procedure is common. D. Budjás et al. [BHMS09] for example use the 59.5 keV line as well as the region around the lines at 99 keV and 103 keV of ^{241}Am . This approach was at first used to optimise the dead layer of the detector used in this work. Nevertheless, some major problems arise from the characterisation with ^{241}Am . Since the emission probability of the two higher energetic γ lines is with approximately 0.02 % very low, a radioactive source of sufficient activity has to be used to keep the acquisition time in a time span of a few tens of hours. An ^{241}Am α source with an activity of

5. Monte Carlo simulation for full energy peak efficiency determination

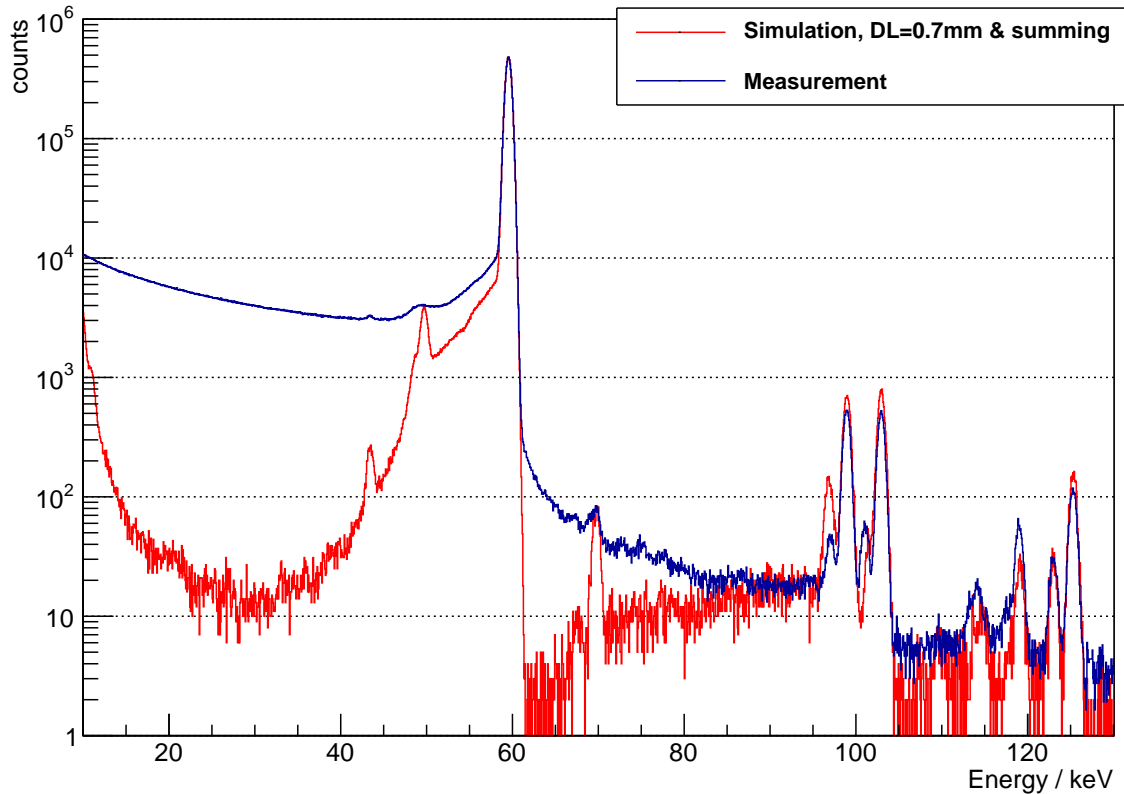


Figure 5.2.: Comparison of ^{241}Am measurement and simulation with nominal dead layer thickness. Since the summing peak at 119.1 keV is clearly visible, a summing of events was introduced. This was done by assuming a Poisson distribution for the number of events during the 500 ns after a first signal in which the PUR circuit is insensitive. It was assumed that the activity of the source has the specified value. The measurement was downscaled to match the simulation at the peak of the 59.5 keV γ line.

330 kBq produced by Amersham Buchler and Leybold was placed at a distance of approximately 198 mm above the endcap to reduce the influence of the source extensions as much as possible. The inner structure of the radioactive source was modelled according to the mechanical drawing provided by the manufacturer to be able to reproduce the primary particle spectrum emitted by the radioactive source as good as possible. The appropriate MC simulation is not simple, since a simulation of the decay of ^{241}Am by the Geant4 radioactive decay module (GRDM) would need a tremendous amount of events to reproduce the full energy hits in the very low emission γ ray peaks around 100 keV with a sufficient statistics ($p \approx 1/1800 p_{59\text{keV}}$ each). On the other hand, if the simple Geant4 General Particle Source (GPS) is used to simulate single γ rays, the correct reproduction of two X-ray peaks stemming from the ^{241}Am daughter, unfortunately lying in the upper ROI at 97.1 keV and 101.1 keV as well, is very complicated. On the other hand, GPS can be used to simulate only γ rays emitted in a narrow cone around the axis between source and detector and therefore safes a lot of com-

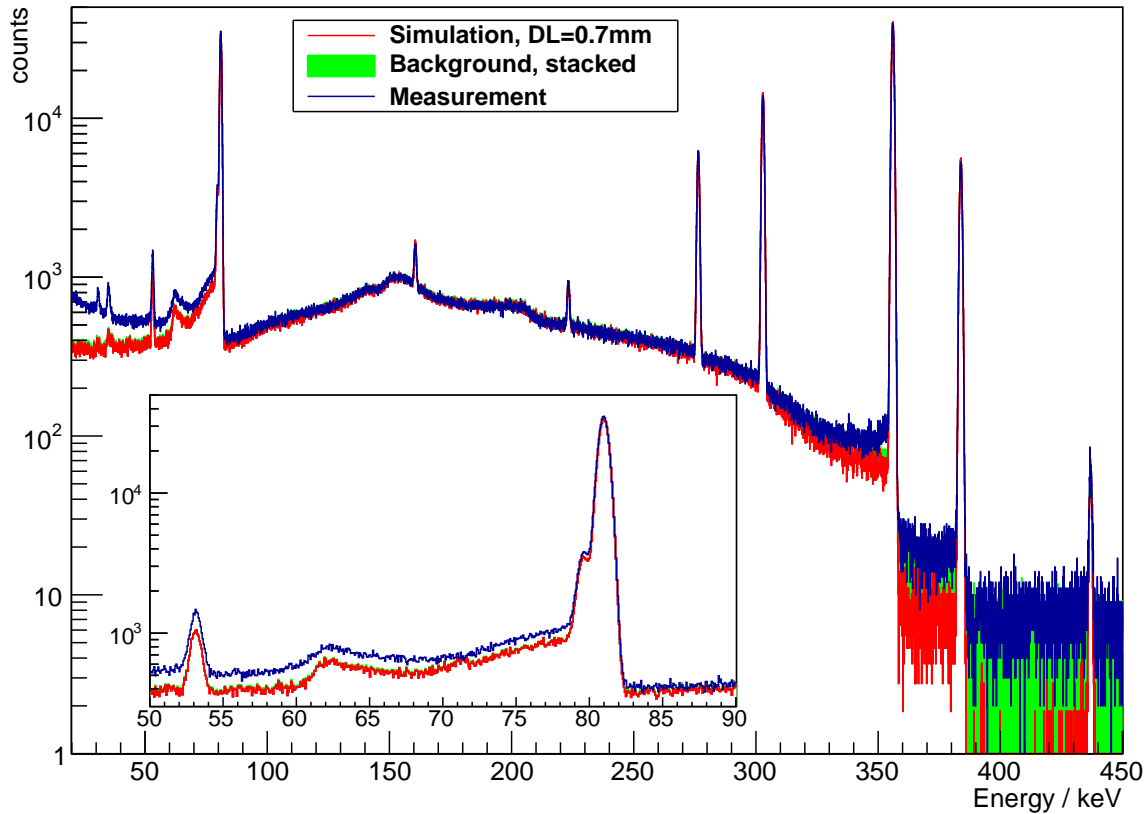


Figure 5.3.: Comparison of ^{133}Ba measurement and simulation with nominal dead layer thickness. In contrast to Figure 5.2 the deviations between simulated and measured spectrum are much smaller. The simulation was scaled to the number of decays during the measurement time since the radioactive source has a known activity. The background spectrum was acquired under the same general conditions, but in the absence of the radioactive source. It is added to the simulation but its contribution to the continuum is, except for the region above the 356 keV peak, negligible. The source was placed about 176 mm above the endcap to minimise the impact of positioning uncertainties.

puting time. After different tests the MC simulation was done by using GRDM. By applying user cuts to the geometry to stop electrons produced by interactions in the shielding as well as increasing the general lower range threshold for electrons to $1\ \mu\text{m}$, the simulation is accelerated by several orders of magnitude. In addition, the computing was split into parts by using the possibility to set ^{237}Np , the daughter of ^{241}Am , into its different excited states and using the capabilities of the Geant4 internal de-excitation module to simulate cascades with the correct transition probabilities. By this, a bias was introduced in the simulation to gain enough statistics for the low emission γ lines. As it can be seen in Figure 5.2 a slight summing peak at 119.1 keV is visible. Although summing was included into the evaluation of the simulation data, huge discrepancies between measurement and simulation are clearly visible. The shape of the simulated spectrum did change only in minor details by using the PENELOPE instead of the default Liv-

5. Monte Carlo simulation for full energy peak efficiency determination

ermore interaction models of Geant4 (see Section 4.5). Furthermore, a simulation with a simplified geometry using the standalone PENELOPE tool kit has been conducted to be able to exclude a general problem with Geant4. This short study led to an, in comparison to the Geant4 results, overall identical spectral shape. A general problem is that in the simulation the transition between the outer contact and the sensitive detector volume is assumed to be sharp. Keeping in mind that the outer contact is produced by diffusing lithium into the detector surface it is more probable that a certain doping profile exists. This would lead to a smooth transition in the contribution to the detector signal. Since no doping parameters are known, the overall impact of such a profile on the spectral shape was tested. Therefore, the detector front was modelled by implementing 20 layers of 100 μm thickness each, since VENOM is not designed to read out the coordinates of each energy deposition. For this the pixel detector data class of VENOM was used. The energy depositions in the different layers was weighted by a Fermi function with the origin at the centre of the dead layer. In case energy depositions were found in neighbouring layers, their vertical location was estimated by calculating a mean between the positions of the layers weighted by the amount of energy deposition, since it is likely that an electron did cross the boundary between the layers. Furthermore, the Fermi function was sampled at a randomized position within the thickness of each layer to avoid quantisation effects. Although this procedure did increase the continuum in the region between 10 keV and 50 keV notably, still huge discrepancies were found to the left and right of the 59.5 keV peak. Due to the inability to reproduce the overall spectral shape and the resulting wrong background estimation below the peaks of interest, the approach of using ^{241}Am for the optimisation of the dead layer thickness was discarded.

As an alternative to ^{241}Am ^{133}Ba can be used as well. The decay scheme of ^{133}Ba (see for example [Fir96]) reveals that there is a certain probability that true coincidence summing (TCS) (see Section 2.3.2) occurs. Therefore, it is important to use a primary particle generator like GRDM for the MC simulation to be able to reproduce the γ ray emission characteristics of the source. As it can be seen in Figure 5.3, the overall deviations of the simulated spectrum to the measurement are much smaller than in the case of ^{241}Am .

A weak but calibrated ^{133}Ba source by AEA Technologies QSA (formerly Amer-sham) with an activity of $4.15\text{ kBq} \pm 1.5\%$ (Oct. 2000) was placed in a distance of approximately 176 mm above the detector endcap by a holder fixed to the top of the extender carrying the shielding plug (for details on the extender see Figure B.2 and Figure D.1). The source consists of a closed plastic container shaped like a test tube containing the activity in a volume of approximately 13 mm height and 11 mm diameter in its lower end. The distance to the detector was chosen to minimise the impact of small misplacements in the x - y plane. At such a distance a vertical misplacement should have nearly no influence since just the ratio of peak count rates and not

absolute values are of interest. This was tested in the simulations of ^{241}Am , where no significant impact was found. To gather enough statistics a spectrum was acquired for nearly 50 h (see Figure 5.3). The same geometry was implemented in GDML for the MC simulation using the information of the mechanical drawings of the source and the shielding (compare Figure 5.4). The spectrum was simulated for dead layer thicknesses of 0.2 mm to 1.0 mm in steps of 100 μm . For the determination of the thickness of the outer contact three ratios η were used. These are calculated from the different combinations of the peak count rates of the γ lines at 53.2 keV, 79.6 keV, 81.0 keV and 160.6 keV. Due to the overlap of the second and third line (see inset in Figure 5.3) these lines were always evaluated as a pair denoted as the 80 keV region. The ratio η is calculated as

$$\eta_{(E1/E2)} = \frac{R_{n,E1}}{R_{n,E2}} \quad (5.2)$$

and the net peak count rate can be expressed as

$$R_{n,E} = A \cdot p_E \cdot \varepsilon_E e^{-\mu_{Al,E}d_{Al}} e^{-\mu_{Ge,E}d_{Ge}}$$

with the activity A of the source, the emission probability p of the γ line with energy E and the FEP efficiency ε . Furthermore, μ_x is the absorption coefficient in material x with a thickness d . Therefore, the dependence of the ratio η on the dead layer thickness d is again described by an exponential function. By evaluating the inverse of the functional dependence of the simulated ratio at the measured value, it is possible to derive the effective dead layer thickness of the used germanium crystal. In Figure 5.5 the simulated ratio of the 53.2 keV line and 80 keV region is plotted. The measured count rate ratio is propagated from the y axis to the fit function and down to the x axis, where it is possible to read off the effective dead layer thickness d_{dl} .

The same procedure was applied to the other two ratios $\eta_{(53\text{ keV}/160\text{ keV})}$ and $\eta_{(80\text{ keV}/160\text{ keV})}$ (see Appendix D, Figure D.2 and D.3). The resulting dead layer thicknesses are summarised in Table 5.3. It has to be noted that the three results are not completely uncorrelated, since a systematic error in the simulation would have an impact on all of them. The weighted result for the effective dead layer thickness, combining the three different values, was calculated to be

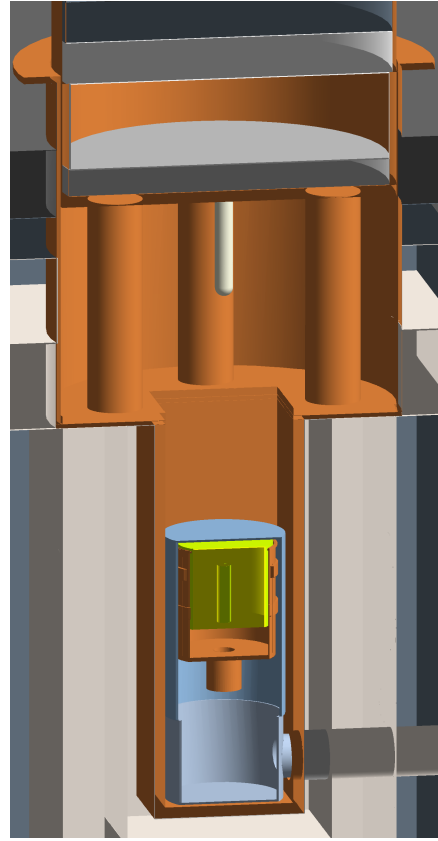


Figure 5.4.: Set-up used for tuning of dead layer thickness. The plastic structure, holding the source at its upper end, was not implemented. See Figure B.2 and Figure D.1 for details on the extender.

5. Monte Carlo simulation for full energy peak efficiency determination

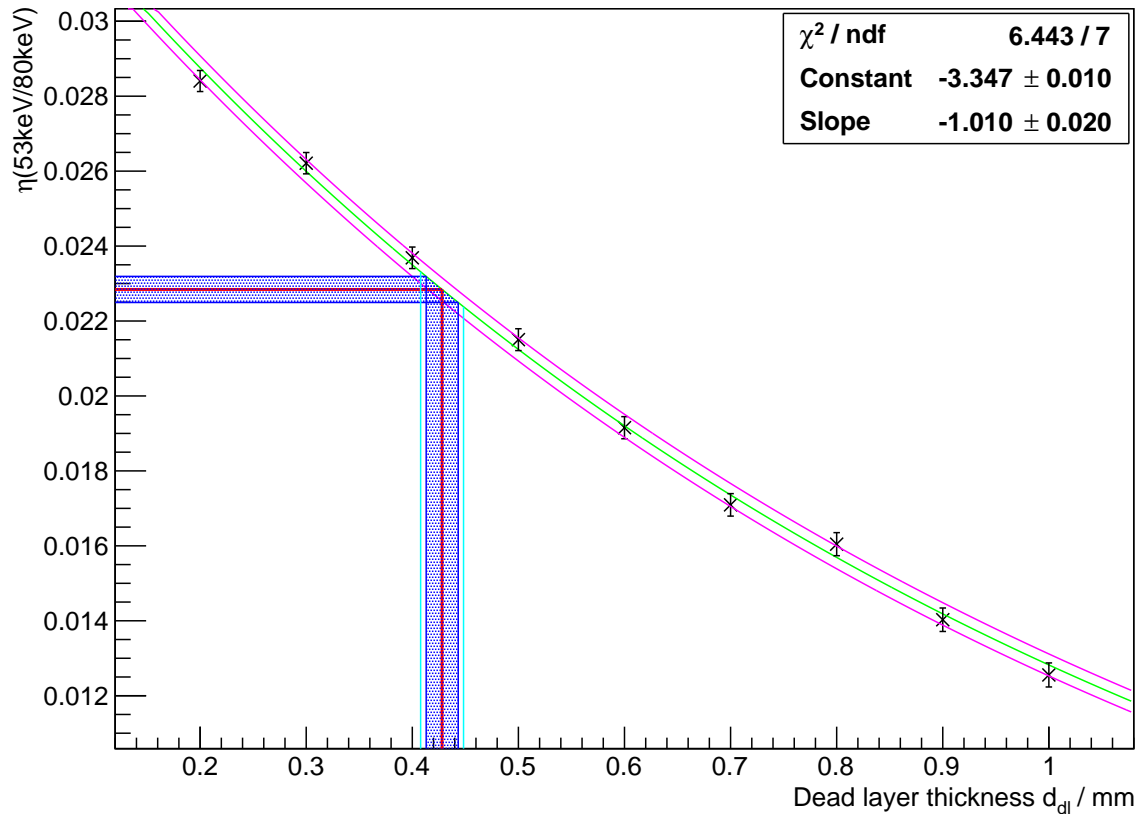


Figure 5.5.: Dead layer thickness optimisation with ^{133}Ba using the 53.2 keV line and 80 keV region. The simulated data and their statistical uncertainties are plotted. The fit to the data is shown in green (—) and its uncertainties in magenta (—). The measured peak ratio of 0.02284(35) is marked in red (—) with the uncertainty in blue (—). The uncertainty of the resulting dead layer thickness d_{dl} is derived from the measurement as well as the fit and is shown in cyan (—).

0.437(16) mm, which is used in the MC geometry in the following. Although the result is lower than the usual thickness of the outer contact of p-type HPGe detectors, which can be found in literature, the result seems to be plausible keeping in mind that the dead layer thickness is slowly growing if the detector is not stored at liquid nitrogen temperature. Since the detector was permanently cooled since its delivery in 2008, except for one thermal cycle of approximately 48 h duration, a relatively low dead layer thickness can be expected.

To obtain the thickness of the outer contact at the side of the germanium crystal it is necessary to place a radioactive source in a certain distance to the side. Since it is not possible to position a source in this direction inside of the inner shielding (compare Section 3.1.2) and the measurement was not done before surrounding the detector with the shielding, it is impossible to determine the thickness of the dead layer at the side of the crystal. It seems to be plausible that the diffusion of lithium into the crystal surface did occur more or less homogeneously, therefore the dead layer thickness determined for the detector front is used for the side as

Table 5.3.: Results of the dead layer optimisation and the combined value.

Ratio η	Thickness d_{dl} / mm
$\eta_{(53\text{ keV}/80\text{ keV})}$	0.428(21)
$\eta_{(53\text{ keV}/160\text{ keV})}$	0.447(26)
$\eta_{(80\text{ keV}/160\text{ keV})}$	0.503(87)
combined	0.437(16)

well. The influence of a not correct dead layer thickness at the side should be small, since the shielding design of the DLB does not allow to measure samples in Marinelli¹ geometry but only samples on top of the detector.

5.2.2. Crystal to endcap distance

If a sample or a radioactive source is placed on top of the detector endcap, the FEP efficiency strongly depends on the source distance to the crystal surface. Already small deviations can lead to huge variations in the efficiency since the crystal is usually mounted close to the detector endcap. Several groups (see for example [BÅJ08, GHJT08]) have found discrepancies between the nominal crystal position within the endcap as specified by the manufacturer and the actual values derived by different measurements. Bearing in mind that the crystal is mounted manually and the endcap is put over the crystal and its supporting structures, it is impossible to check the actual distance between crystal front and detector endcap without X-raying the whole detector. Several authors actually have done this (see [BÅJ08, BHMS09]), although strong X-ray devices are needed to penetrate the metal housing and supporting structures of a germanium detector.

One possibility to determine the vertical position of the HPGe crystal inside the endcap by using the germanium detector itself is to do a vertical scan with a low energetic collimated source pointing radially to the z axis of the cylindrical crystal and measuring the peak count rate of the emitted γ line in dependence of the vertical position. This has to be done carefully, since it is difficult to align the collimated beam exactly perpendicular to the z axis and geometrical properties of the crystal like the rounding of the upper edge (often referred to as ‘bulletisation’) influence the count rate profile in such a vertical scan as well. Nevertheless, several authors have used this method to deduce the vertical position of the crystal within the detector endcap (see [Key04, Sch07, CLPBC⁺10, BÅJ08, HHI⁺03]).

Unfortunately, such a vertical scan was not performed for the HPGe detector before it was placed inside of the inner shielding. It is as well not possible to take these data inside of the shielding due to the very limited space around the

¹A Marinelli beaker is a special container to place liquid or gaseous samples or bulk material around the sides and on top of a germanium detector.

5. Monte Carlo simulation for full energy peak efficiency determination

detector (compare Section 3.1.2). In case a radioactive source emitting low energetic γ rays with a very precisely known activity is available, the crystal to (the inside of the) endcap distance d_{cc} ('cc' for 'crystal to cap') can be determined by measuring the peak count rate and varying the distance in the MC simulation until the correct peak count rate can be reproduced. By extending this procedure, the distance d_{cc} can also be found out by using a source of unknown activity. In this case two spectra at different but precisely known distances to the detector endcap are acquired and the ratio of the peak count rates is calculated. By applying this method, the unknown activity of the source cancels out like in the dead layer thickness optimisation described in Section 5.2.1. The spectrum obtained with the radioactive source at a large distance to the endcap serves as a reference, since a small change in the distance does only lead to a very small change in the peak count rate. On the other hand, the peak count rate obtained with the source being in a close position to the detector endcap does change more in case the unknown vertical position of the germanium crystal is changed. A source emitting low energetic γ lines below 150 keV should be used for this procedure to secure that the γ rays are absorbed within the upper closed end of the germanium crystal. This way the parameter optimisation is as far as possible insensitive to the dimensions of the inner contact, which is optimised in the third stage of the geometry optimisation (see Section 5.2.3).

This method to determine the crystal to endcap thickness d_{cc} is for example applied by Hardy et al. [HISV⁺02], who use ^{57}Co because of its two low energetic γ lines at 122.1 keV and 136.5 keV. Although the decay scheme reveals that a certain probability exist that a 122.1 keV photon and the also emitted 14.4 keV γ ray are impinging the detector at the same time, the probability for TCS with the usage of a p-type detector is negligible due to the high lower energy threshold of approximately 40 keV for that type.

The procedure with a source of unknown activity was applied to the germanium detector of the DLB. For the precise positioning of the source, the shielding extender already used for the optimisation measurements in Section 5.2.1 together with an additional source holder was used again. For the spectrum acquisition with the source being in the large distance to the endcap, the upper end of the source was mounted between the upper end of the extender columns in a distance of ~ 222 mm to the endcap. The spectrum at the close position was acquired with the source attached to an additional inset placed into the holder shown in Figure B.2 (part 9), with the activity approximately 60 mm above the detector endcap. Since only an old and therefore due to its short half life of 271.8 d weak ^{57}Co source was available, the spectra had to be acquired for a relative long time of 71 h (far position) and 21 h (close) respectively to gather enough statistics. Due to the long acquisition times and the time span between the start times of the measurements the decrease of the activity was taken into account for the calculation of the peak count rate ratio. In the MC simulations the radioactive

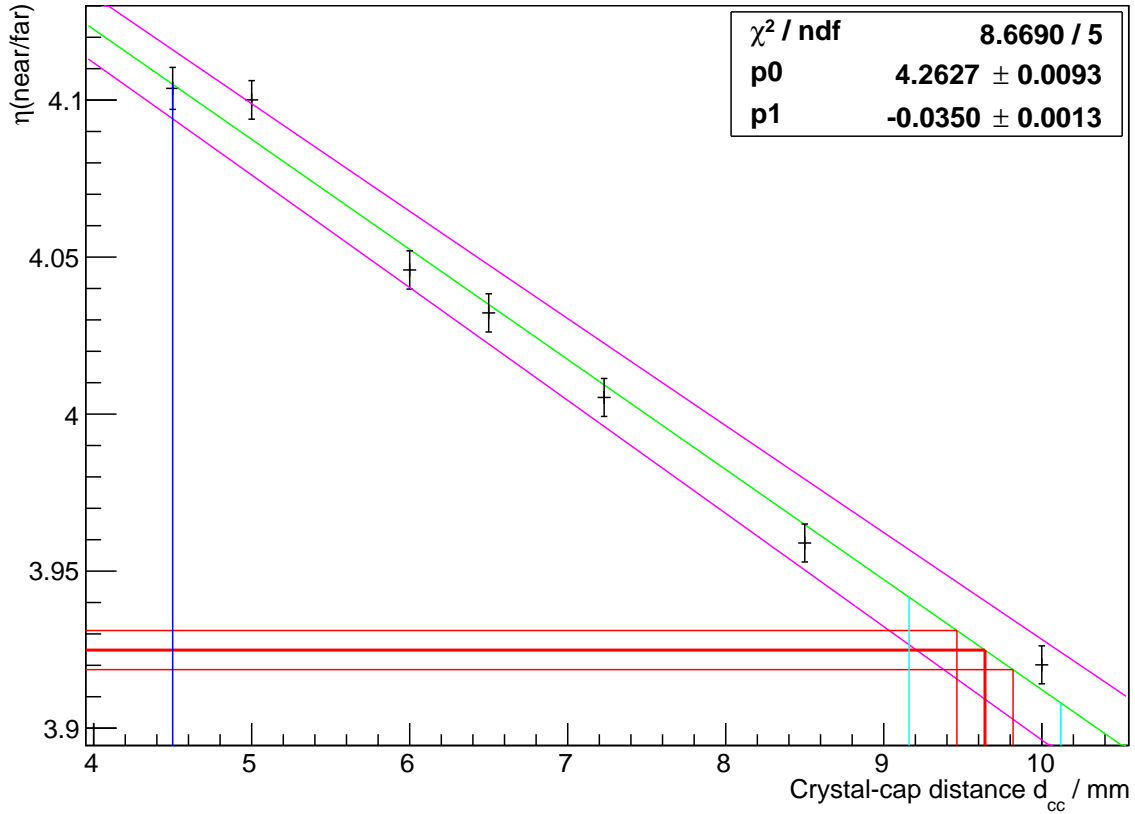


Figure 5.6.: Crystal to endcap distance optimisation with ^{133}Ba using the 80 keV region. The simulated data and their statistical uncertainties are plotted. The fit to the data is shown in green (—) and its uncertainties in magenta (—). The measured peak ratio and its uncertainty are marked in red (—). The uncertainty of the resulting crystal to endcap distance d_{cc} is derived from the measurement as well as the fit and is shown in cyan (—). For comparison the nominal value of d_{cc} is shown in blue (—).

source was placed at the measured distances above the detector endcap. The distance d_{cc} of the crystal surface to the inside of the detector endcap was varied between 3.5 mm and 8.5 mm in steps of 0.5 mm. To keep the statistical uncertainties for each setting at a negligible level a sufficient amount of events was simulated. By approximating the simulated data points, the effective distance d_{cc} can be derived from the measured ratio analogously to the method described in Section 5.2.1. The obtained results using the 122.1 keV and 136.5 keV γ lines are 7.22(18) mm and 7.30(54) mm. Comparing these to the nominal value of 4.5 mm, already a huge discrepancy became obvious.

For a cross-check of the results obtained from the ^{57}Co measurements, the same procedure was applied to a pair of ^{133}Ba spectra using the region of the γ lines at 79.6 keV and 81.0 keV. In addition to the measurement already used for the optimisation of the dead layer thickness in Section 5.2.1, a spectrum with the same source approximately 73.5 mm above the detector endcap was used, which was originally acquired for the optimisation of the detector volume described in

5. Monte Carlo simulation for full energy peak efficiency determination

Table 5.4.: Crystal to endcap distance optimisation check with ^{133}Ba at ~ 74 mm above endcap for the nominal value (4.5 mm), the combined value (7.50(16) mm), determined with ^{57}Co and ^{133}Ba , and the ^{133}Ba value (9.64(48) mm). The relative deviations $\frac{R_{n,\text{sim}} - R_{n,\text{meas}}}{R_{n,\text{meas}}}$ between the net count rates R_n in simulation and measurement for the different γ lines should in the optimum be compatible with zero. The uncertainties are predominantly due to the uncertainty of the source activity.

$d_{\text{cc}} / \text{mm}$	Deviation $\frac{R_{n,\text{sim}} - R_{n,\text{meas}}}{R_{n,\text{meas}}} / \%$			
	53.2 keV	79.6 keV&81.0 keV	160.6 keV	223.2 keV
4.5	10.8(21)	12.5(17)	8.8(24)	11.7(28)
7.50(16)	5.5(19)	6.4(16)	2.9(21)	6.5(24)
9.64(48)	4.7(20)	5.5(16)	1.2(22)	7.0(27)

Section 5.2.3. In the case of ^{133}Ba it is again advisable to use a primary particle generator in the MC simulations that can reproduce the cascading de-excitation to take TCS at the closer position into account. As one can see in Figure 5.6, MC simulations were conducted for seven different crystal to endcap distances. The resulting value for d_{cc} of 9.64(48) mm differs significantly from the values obtained with the ^{57}Co measurements.

Although the three results are not compatible, in a first attempt they were combined, since non of the measurements was more reliable than the other one. To ensure that the whole geometry optimisation does not lead to completely wrong results with the final complete parameter set due to a mistake in one of the first two optimisation steps, some simulations to check the determined crystal to endcap distance were conducted. Using the ^{133}Ba source and a similar ^{152}Eu source with $4.13 \text{ kBq} \pm 1.5\%$ activity (Oct. 2000) of the same manufacturer, the FEP efficiencies were calculated from the measurement as well as from the MC simulations for different source positions. Table 5.4 summarises the normalised deviations between simulation and measurement for three different crystal to endcap distances d_{cc} at the four ^{133}Ba γ lines lowest in energy. For the nominal value of 4.5 mm a systematic deviation is noticeable with the simulation overestimating the FEP efficiency. Using the combined value of the parameter optimisations with ^{57}Co and ^{133}Ba the deviations are approximately halved in comparison to the ones of the nominal value. Since the deviations of the simulation conducted with the value only determined from the ^{133}Ba spectra are slightly smaller (except for the deviation at 223.2 keV) than the ones for the combined parameter and the deviations of the ^{152}Eu spectrum support also a value of d_{cc} larger than the combined result, the value 9.64(48) mm obtained from the optimisation with ^{133}Ba is taken as the final result. Using the combined result the optimisation of the sensitive detector volume in Section 5.2.3 showed a larger deviation in the low energy region that could not be reduced, which supports the larger value of d_{cc} as well.

The result of 9.64(48) mm for the crystal to endcap distance is more than twice

as large as the nominal value. The determined value will not be the actual distance but it is the value that is necessary to reproduce the detection characteristics of the detector. It seems to be unlikely that the actual position of the crystal differs that much from the nominal one, since an uncertainty of less than 2 mm should be achievable.

5.2.3. Sensitive detector volume

Due to the absorption characteristics of γ rays with energies below 150 keV to 200 keV in germanium, their detection efficiency is dominated by the detector parameters discussed and optimised in Section 5.2.1 and Section 5.2.2. With rising energy the absorption length increases and also the probability that a γ ray interacts by Compton scattering exceeds the probability for photoelectric absorption. Consequently, the FEP detection efficiency at higher energies does not depend on a linear parameter like the dead layer thickness but on the effective volume of the detector crystal. Due to the fact that the MC simulation does not take the charge transport in the electric field within the detector into account and therefore assigns an unweighted sensitivity to probably existing regions of weak field strength, the detection efficiency obtained by MC simulation will inevitably be larger than the one observed in measurements.

To reproduce the FEP efficiencies of the measurements by the MC simulation, it is common to change the dimensions of the inner contact of the detector crystal (see [BHMS09, CLPBC⁺10, HGLGT04, ALV99]). According to Lépy et al. [LAA⁺01] the diameter of the inner contact is the more important parameter, which is obvious since a slight enlargement of the diameter leads to a larger decrease of the effective detector volume for high energetic γ rays than an enlargement of the height of the contact. The ratio of the influences of both dimensions depends on the effective ratio of them. If a radioactive source emitting γ rays with an energy in the order of 1 MeV is placed above the endcap, the density of interactions occurring in the crystal decreases much slower with the depth in germanium than in the case of a source emitting 200 keV γ rays so that – depending on the γ ray energy – only a part of the detector volume contributes to the signal (compare Appendix E). Therefore, the relevance of the contact height increases for the FEP efficiency with decreasing γ ray energy. Some authors correlate the FEP efficiency with the detector volume and determine the optimal volume for different radioactive nuclides (see for example [BHMS09]), but a certain detector volume can be achieved by choosing many different combinations of inner contact diameter and height, which do not have the same impact on the detection efficiency. Varying the inner contact dimensions by starting from the nominal values of the used detector, an increase of the diameter by 1 mm is equivalent to nearly 9 mm increase of the height regarding the detector volume but the latter has a much higher influence on the absorption of low energetic γ rays.

5. Monte Carlo simulation for full energy peak efficiency determination

To check whether the MC simulation can reproduce the FEP efficiencies for different radioactive sources at several positions above the detector, spectra were acquired using four radioactive sources by AEA Technologies QSA of identical geometry and calibrated regarding their activity. In addition to the ^{133}Ba and ^{152}Eu sources already described in Section 5.2.1 and Section 5.2.2, a ^{137}Cs source with an activity of $4.01 \text{ kBq} \pm 1.5\%$ (Oct. 2000) and a ^{60}Co source with $4.02 \text{ kBq} \pm 1.5\%$ (Oct. 2000) were used. They were placed approximately 16 mm, 40 mm and 74 mm (detector endcap to tip of source) above the detector and spectra were acquired. Additionally a volumetric ^{40}K source of 73 mm diameter and 45 mm height was used, which was prepared by the preparation laboratory of the Faculty of Physics by drying potassium chloride (KCl) and preparing gravimetrically a solution of known potassium content. By assuming the natural abundance of ^{40}K , the activity was calculated to be $326.1 \text{ Bq} \pm 0.1\%$. The low uncertainty of the value was assumed due to the high precision of the used scale, which would result in an even much lower uncertainty, but this value seemed to underestimate the uncertainty.

After the optimisation of the dead layer thickness d_{dl} and the crystal to endcap distance d_{cc} the MC simulations did deviate especially for γ ray energies above 400 keV from the measurement. However, the deviations also depended on the used calibrations source (compare Figure 5.7). To bring the FEP efficiencies determined from the MC simulations into accordance with the ones obtained from measurement, the dimensions of the inner contact were varied and for each parameter set the deviations between simulation and measurement calculated. The nominal diameter of 10 mm was increased in the range of 0 mm to 4 mm in steps of 1 mm. For each diameter value the nominal height of 42 mm was in addition increased by 2 mm, 4 mm and 6 mm. The simulation of all parameter combinations together with the different positions, radioactive sources and the necessary amount of simulated events was only possible due to the computing cluster operated by the working group, since with ~ 80 computing nodes the simulations did still took roughly two days.

The deviations were determined from the net count rates R_{n} obtained from measurement and simulation. The determination from the acquired spectrum is straightforward and the value for the simulation was obtained according to Equation (5.1) on page 90. The uncertainties of the relative deviations are mainly due to the uncertainty of the source activity and the low peak statistics in the measured spectrum in case of γ lines of low emission probability.

As it can be seen in Figure 5.7, the deviations for the γ lines of the different nuclides are randomly distributed and no obvious tendency or dependence can be recognised. The reader may assume that the simplest way to correlate the deviations for the γ lines to the used detector parameters is to calculate a weighted mean of all deviations, taking the uncertainties into account. The optimal detector parameters would then be derived by minimising the absolute value of the

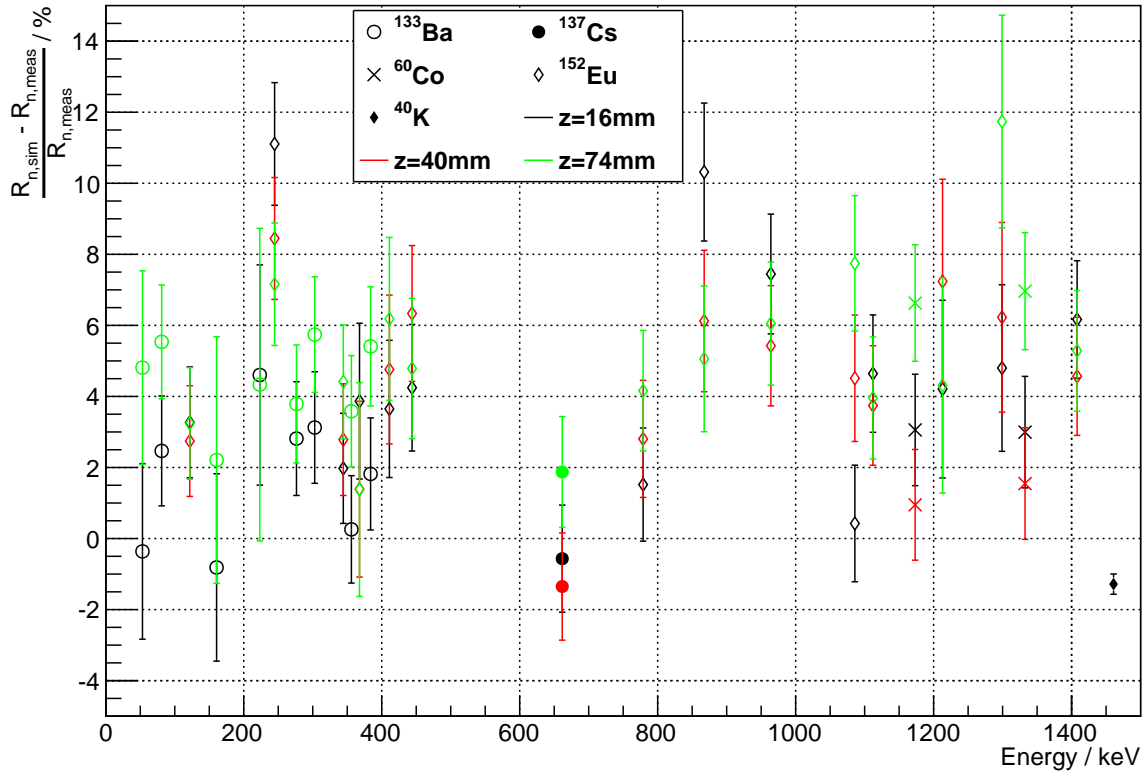


Figure 5.7.: Deviations between simulation and measurement with optimised dead layer thickness and crystal to endcap distance but nominal dimensions of the inner contact. Deviations of all major γ lines of ^{133}Ba , ^{152}Eu , ^{137}Cs and ^{60}Co for three source positions above the endcap. ^{133}Ba was not measured at $z = 40$ mm. ^{40}K as a volumetric source of 45 mm height was placed approximately 2.1 mm (sum of foot height and wall thickness of the used container) above the endcap.

mean. This method does not take into account that the nominal activities of the different sources can deviate from the true values to different extents. Combining all deviations at once neglects the different number of lines belonging to the different sources so that especially a deviation of the activity of ^{152}Eu would have the largest impact on the calculated mean due to the large number of γ lines. Apart from deviations due to probably incorrect γ ray emission probabilities and angular correlations in the MC simulation the deviations of all γ lines belonging to one nuclide should be describable by a single mean. Since the deviations for a single nuclide at different γ ray energies depend differently on the used detector parameters, the uncertainty of the mean would be minimal in case the optimal parameters are found and the aforementioned impacts are neglected. This corresponds to the situation that a functional fit through all deviations at the different γ ray energies of the nuclide requires only a constant component to minimise the fit uncertainties and all higher order parameters are negligible. The remaining deviation does then only depend on the difference between nominal and true activity of the source.

5. Monte Carlo simulation for full energy peak efficiency determination

The fact that the difference of the nominal and true activity varies for the different calibrated sources can already be seen in Figure 5.7. The deviations of the 661.7 keV γ line of ^{137}Cs as well as of the 1173.2 keV and 1332.5 keV lines of ^{60}Co vary only slightly for the two source positions $z = 16$ mm and $z = 40$ mm but have different means. Due to this it can be assumed that the distribution of the deviations of the ^{152}Eu lines is mainly due to inaccuracies of the MC decay generator GRDM. The emission probabilities for the γ lines in the MC simulation of ^{152}Eu were checked by simply creating a normalised spectrum of the emitted energies. Although some small deviations were found, these show a different pattern than the net peak count rate deviations between simulation and measurement, which could be due to the additional probability for TCS distorting the spectrum further. However, VENOM does allow the usage of a different primary particle generator. With the external generator DECAY0 [PTZ00] it is possible to produce primary particles for some radioactive nuclides used as calibration sources. Since the code was developed many years ago, no further developments are done and deviations to the data of the Decay Data Evaluation Project (DDEP) [Lab13] for e.g. ^{152}Eu are found as well, DECAY0 is no real alternative as a particle generator. Since the design and correct implementation of a primary particle generator goes beyond the scope of this work, the deviations in the primary particle properties have to be accepted. The optimisation of the detector parameters therefore also corrects for the deficiencies of the GRDM.

To avoid the problem of different weights due to the different numbers of γ lines, the optimisation of the dimensions of the inner contact was done by first averaging the relative net count rate deviations of each nuclide. Due to the height of 45 mm of the volumetric ^{40}K source, which was placed directly on top of the detector endcap (for the geometry see Figure 5.1), the means for each calibration source at the positions $z = 16$ mm and $z = 40$ mm were combined and afterwards the mean deviation of all used sources calculated. The additional measurements and MC simulations for the sources (except for ^{40}K) being placed approximately at 74 mm above the endcap were not taken into account, since larger deviations than for the closer positions were found, which could be due to inaccuracies in the positioning (compare Figure 5.7). Furthermore, for the 74 mm position the activity was located between $z = 74.5$ mm and $z = 87$ mm what is some distance above the usual sample height of at most 65 mm.

The MC simulation for each used nuclide and parameter set Δd and Δh were evaluated according to the procedure described at the beginning of Section 5.2 and the deviations between MC simulation and measurement were calculated. The deviations determined for the different γ lines of the used nuclides were combined according to the aforementioned method. Afterwards the means of the deviations for the different positions and nuclides were combined as well. This procedure was applied to the full energy range of γ lines (compare Figure 5.7) and to two smaller parts of the range to take the different impact of the varied

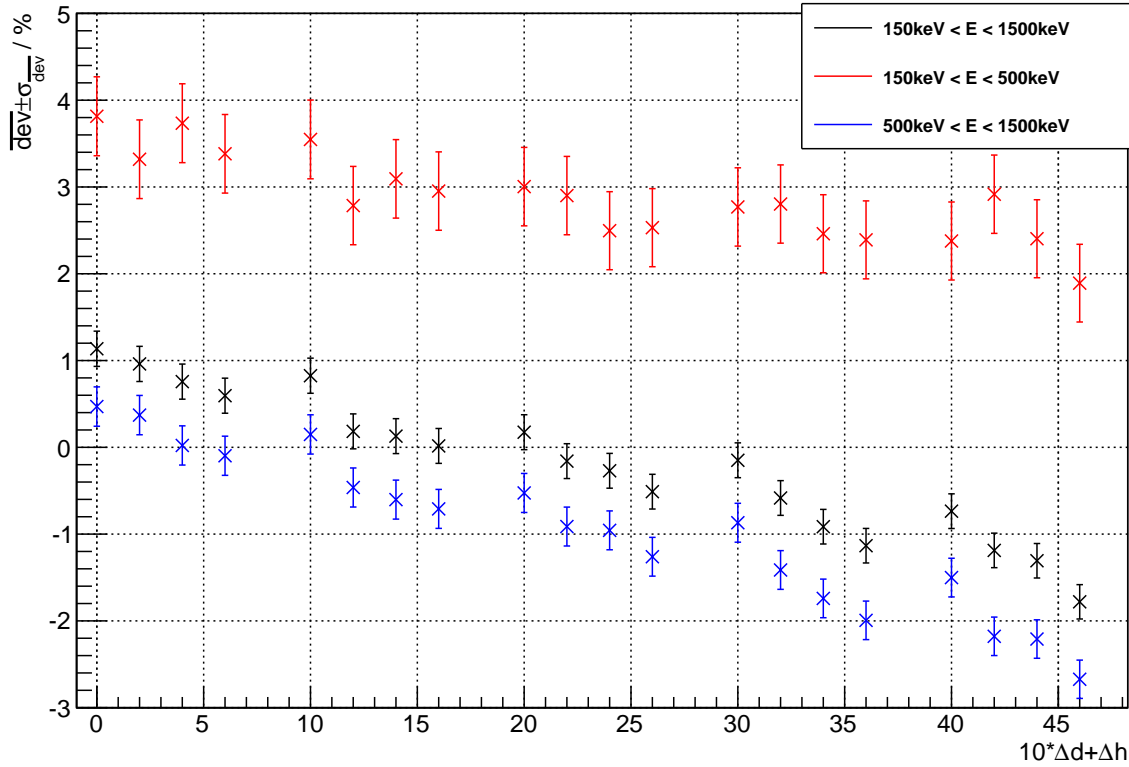


Figure 5.8.: Optimisation of sensitive detector volume. Mean of deviations of γ lines in three energy ranges for different changes of the dimensions of the inner contact Δd and Δh .

simulation parameters into account. As it can be seen in Figure 5.8, the impact of the chosen parameters Δd and Δh on the low energy deviation mean is small, but the impact rises for increasing γ ray energy. Furthermore, it is visible that the low energy deviation mean is systematically higher than the one for the high energy range, since the value of the first is strongly influenced by the high deviations of ^{152}Eu γ lines with energy smaller than 500 keV (compare Figure 5.9). Therefore, only the medium and high energy range deviations are used for optimisation. Since both before mentioned mean deviations do not vanish for the same parameter set, the values Δd and Δh are taken as a final result for which the absolute value of the sum of both means is minimal. This is the case for the values $\Delta d = 1 \text{ mm}$ and $\Delta h = 2 \text{ mm}$. Comparing the deviations of the net peak count rates of the different γ lines for the nominal (see Figure 5.7) and optimised detector parameters (see Figure 5.9) it becomes clear that the applicability of the MC model has been improved significantly. As it can be seen in Figure 5.9 as well, the remaining deviations of all γ lines lie in the range of $\pm 3\%$ (see also Table 5.5) if the deviations of ^{152}Eu are neglected, which are in general worse. As it is already discussed above, this could be due to a larger deviation between nominal and true activity of the radioactive source and a worse MC particle generator implementation for this nuclide.

5. Monte Carlo simulation for full energy peak efficiency determination

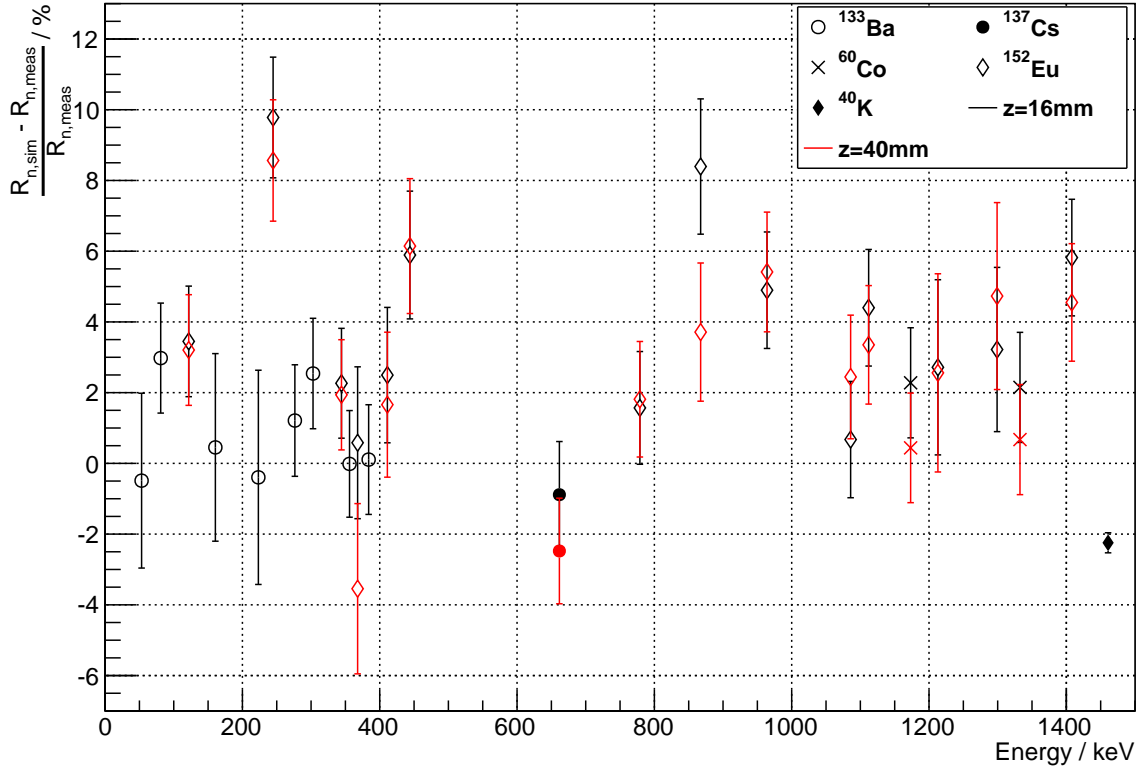


Figure 5.9.: Deviations between MC simulation and measurement with optimised detector parameters. For remarks see caption of Figure 5.7.

5.2.4. Discussion of results

Table 5.5 summarises the deviations found between MC simulation and measurement for the different stages of MC model optimisation. Especially the FEP efficiency for the 53.2 keV γ line is largely underestimated in the model with nominal detector parameters, since the dead layer thickness d_{dl} is much too large. On the other hand, the efficiencies (and with this also the net peak count rates) of γ lines with higher energies are largely overestimated.

By the optimisation of the thickness d_{dl} of the outer detector contact (see Section 5.2.1), the FEP efficiency for the 53.2 keV and 81.0 keV is corrected and the resulting deviations are similar to the ones of high energetic γ lines (compare Table 5.5). Reviewing the procedure for optimisation, it would have been advisable to use only the ratio of the net peak areas of the 53.2 keV γ line and the 80 keV region. Using the absorption coefficient for 161 keV γ rays in germanium, which can be taken from [BHS⁺10], the remaining intensity at a depth of 18 mm (the nominal distance between detector front and upper end of the inner contact) of 161 keV γ rays impinging perpendicular to the detector surface can be calculated to be still 11.9% of its original value. Hence, the dimensions of the inner contact have a certain impact on the two ratios using the 160.6 keV γ line and are therefore slightly dependent on the dimensions of the inner contact, which

Table 5.5.: Comparison of net peak count rate deviations for different stages of optimisation of the used MC model. The measurements are the ones used in Section 5.2.3 for the optimisation of the detector volume. The ^{133}Ba , ^{137}Cs and ^{60}Co sources were placed at $z = 16$ mm above, the volumetric ^{40}K source directly on the endcap.

Energy / keV	Nuclide	nominal	Deviation $\frac{R_{n,\text{sim}} - R_{n,\text{meas}}}{R_{n,\text{meas}}} / \%$		
			d_{dl} opt.	d_{cc} opt.	full opt.
53.2	^{133}Ba	-27.9(15)	13.3(22)	0.8(25)	-0.5(25)
81.0	^{133}Ba	0.8(16)	17.7(18)	2.5(16)	3.0(16)
160.6	^{133}Ba	9.2(21)	17.5(23)	-1.4(27)	0.5(27)
223.2	^{133}Ba	18.2(25)	17.9(25)	2.8(31)	-0.4(31)
276.4	^{133}Ba	16.6(18)	19.5(19)	2.8(16)	1.2(16)
302.9	^{133}Ba	18.1(18)	22.1(19)	3.1(16)	2.5(16)
356.0	^{133}Ba	14.8(18)	18.8(18)	0.3(16)	0.0(15)
383.8	^{133}Ba	16.4(18)	21.5(19)	1.8(16)	0.1(16)
661.7	^{137}Cs	14.2(18)	18.3(18)	-0.6(15)	-0.9(15)
1173.2	^{60}Co	16.1(18)	20.2(18)	3.1(16)	2.3(16)
1332.5	^{60}Co	16.5(18)	20.5(19)	3.0(16)	2.1(16)
1460.8	^{40}K	11.96(32)	15.73(33)	-1.29(29)	-2.25(29)

are only optimised in the third step of the optimisation process. Omitting both dead layer thickness determined using the 160.6 keV γ line as a reference, the resulting dead layer thickness d_{dl} would have been about 9 μm thinner (437 μm (combined) vs. 428 μm ($\eta_{(53\text{ keV}/80\text{ keV})}$ only), compare Table 5.3) leading to an approximately 1.3 % lower attenuation of 53 keV γ rays (using the coefficients given in [BHS⁺10]) and therefore a higher FEP efficiency. Considering the 46.5 keV γ line of ^{210}Pb used to determine the activity of this relatively long lived isotope, the deviation due to this possibly better result is even larger. The best way to check the determination of FEP efficiencies for low energies would be to determine the activity of a radioactive source or sample with a very precisely known activity and emitting those low energetic γ lines. In general it should be possible to change the value of the dead layer thickness after the whole optimisation process by the mentioned value of 9 μm without influencing the other optimised parameters significantly, although this should be checked by repeating the simulations for the final parameter set (see Figure 5.9 and Table 5.5) and comparing these results to the former ones. Since the deviations of the final detector model are acceptable and there is currently no possibility to cross-check the obtained result for the dead layer thickness, the originally determined value is used (see Table 5.6).

The influence of a small change of the dead layer thickness on the derived crystal to endcap distance d_{cc} (see Section 5.2.2) should be negligible, since the impact on the net peak count rates at both positions should be similar, although for the

5. Monte Carlo simulation for full energy peak efficiency determination

Table 5.6.: Comparison of nominal and optimised detector parameters. Nominal values from [Can10] and H.-J. Lange, Canberra Industries (compare Section 5.2.1).

Parameter	nominal / mm	optimised / mm
Outer dead layer thickness	0.7	0.437(16)
Crystal to endcap distance	4.5	9.64(48)
Core hole diameter	10	11
Core hole height	42	44

closer position a significant fraction of the γ rays does not traverse the dead layer vertically and therefore is stronger attenuated than for the far position. In case the dead layer thickness at the side of the detector crystal should be larger in reality than the value obtained for the detector front, the influence on the derived crystal to endcap distance d_{cc} should be very small since again both peak count rates are effected in the same way although the impact on the measurement acquired in the close position should be slightly larger.

The assumption that both dead layer thicknesses are the same or at least similar is as well supported by the fact that the optimisation of the inner contact dimensions (see Section 5.2.3 and the following paragraph) resulted in parameters deviating only slightly from the nominal parameters. The in comparison to the nominal value reduced dead layer thickness (see Table 5.6) increases the sensitive volume of the detector by nearly 2%. To reproduce the correct FEP efficiencies for high energy γ lines by using the nominal contact thickness at the crystal side, it would be necessary to even reduce the dimension of the inner contact, which is contrary to the assumption that regions of weak electric field in the crystal reduce the measured FEP efficiencies.

The optimisation of the dimensions of the inner detector contact unfortunately relies on the accuracy (or trueness) as well as the uncertainty of the known activity of the used sources. As it is already discussed in Section 5.2.3, especially the accuracy of the activity of the used ^{152}Eu source is questionable and has a certain influence on the obtained result. Since it seems to be questionable to exclude the source from the optimisation procedure without knowing whether the found deviations stem from a bias of the activity or are due to deficiencies of the detector model, this was not done. By using more nuclides, preferably not emitting γ ray cascades but single γ lines, different sources of the used ones, but with precisely known activities, and different source geometries and matrices it should be possible to improve the accuracy of the MC model even further if required. In general it could be possible to find a parameter set for which the mean deviations are even smaller. Since two parameters were optimised at the same time, the uncertainties of the deviations are relatively large, and the actual functional dependence between the parameters and the efficiency is unknown, it is very difficult to interpolate between the different simulated data points. Never-

theless, it should be noted that the derived MC model is sufficiently precise to determine the FEP efficiency of different γ rays and sample geometries within an uncertainty of 3 % to 5 % (compare Table 5.5) in case the emission characteristics of the nuclide are reproduced correctly by the used MC event generator.

Table 5.6 summarises the used detector parameters and compares the nominal to the optimised values. Especially the reduction of the dead layer thickness and the optimisation of the crystal to endcap distance lead to a large improvement of the accuracy of the FEP efficiencies obtained by MC simulation (compare also Table 5.5). While the corrected thickness of the outer contact seems to be plausible due to the history of the detector (compare Section 5.2.1), the optimised crystal to endcap distance is rather large and the source of this deviation remains unclear. The small changes to the dimensions of the inner contact seem to be plausible as well. In case the deviations of the γ lines belonging to ^{152}Eu would have been smaller and another source emitting low energetic γ lines would have been available, even smaller changes to the inner contact would certainly have been favoured.

5.3. Emission probabilities of γ rays in Geant4

Usually samples of interest are placed directly on top of the detector to increase the detection efficiency. Therefore, for a lot of nuclides a reasonable chance exists that two γ rays emitted in the decay of the same nucleus are hitting the detector simultaneously and the resulting detector signal corresponds to the sum of both energy depositions. Since this effect, called true coincidence summing (TCS) (see also Section 2.3.2), lowers the FEP of the single γ ray it is necessary to take this effect in the FEP efficiency determination into account. It is therefore desirable to use a MC primary particle generator that is able to reproduce the emission characteristics of a certain nuclide. This requirement is in general fulfilled by the Geant4 radioactive decay module (GRDM), which is usually used in the VENOM MC tool, although some problems of this generator like the identical simulated spectral shape of β decays independent of their transition classification are known.

As it was in part already discussed in Section 5.2, the usage of GRDM relies on the correctness of the underlying physical data. By using GRDM, actually the product of the FEP efficiency ε and the emission probability p (compare Equation (4.31)) of a certain γ line is determined from the MC simulation. Consequently, any bias of the emission probability in the MC simulation inevitably leads to the same (relative) bias of the determined nuclide activity but with the opposite sign (if TCS is unlikely). To allow for the correct determination of sample activities the emission probabilities used by GRDM of Geant4 9.5.p01 were checked. Since usually only some or even single γ lines are used as references for a certain nuclide (see also Section 4.4 and [Gil08, Wah07]) only these were

5. Monte Carlo simulation for full energy peak efficiency determination

checked as well. For this check 10^6 decays were generated per nuclide (for ^{133}Ba , ^{60}Co , ^{137}Cs and ^{152}Eu 5×10^6 each) and stored with a special option in VENOM to a ROOT output file. The simulated emission probabilities were calculated and compared to the DDEP data. For many γ lines the relative deviations between simulation and measurement were found to be compatible with 0, but some emission probabilities deviate significantly from the literature data. A compilation of the calculated data comparison can be found in Table F.1.

For example the emission data for the decay of ^{208}Tl , in which TCS is likely due to the complicated decay scheme, are completely compatible with the data given in [Lab13]. Other isotopes like ^{210}Pb and ^{226}Ra deviate significantly. The by far worst results were found for ^{235}U , which is unfortunately the only nuclide of the ^{235}U decay chain usually analysed. As one can see in Table F.1 for the original Geant4 data set deviations of up to 365% were calculated. A corrected so called 'PhotonEvaporation' data file, describing the de-excitation characteristics of a certain nuclide, in this case the daughter nuclide, was taken from the Geant4 users forum² and integrated into the used data set. Although the deviations were reduced, smaller ones still remain and originate probably from wrong data in the corresponding 'RadioactiveDecay' data file, describing the branching ratios and decay characteristics of the mother nuclide. Due to the complexity and correlation between both data sets it is nearly impossible to correct the data manually, although this was tried by the author with a certain success. Since at least in all checked cases the data set of the newer Geant4 version 9.6 did not differ from the used data set an improvement was not expected and the newer version therefore not tested. An updated physics data set is under development by the Geant4 developers at least since 2011³ but up to now (2013-06-01) unfortunately not yet released.

In case TCS is unlikely in the decay of a nuclide, which is obviously the case for nuclides emitting a single γ line or reference γ lines, since they are selected due to a low summing probability in the first place, it is possible to correct the result of the MC simulation using the factors given in Table F.1 as well. For nuclides with a decay scheme supporting TCS a correction after the MC simulation inevitably leads to still wrong results unless one knows the summing probabilities for the different combinations of emitted γ rays, which are dependent on the used measurement geometry. The probabilities can be in principle calculated from MC simulations using single γ ray emissions of the same energies but this is due to the complexity of the subsequent calculations beyond the scope of this work. Instead the as significant regarded correction factors given in Table F.1 are used in the calculations of Chapter 6. These are applied in cases where there is a certain chance for TCS as well unless the activity of a certain nuclide can be derived from

²<http://hypernews.slac.stanford.edu/HyperNews/geant4/cindex>, for the thread see <http://hypernews.slac.stanford.edu/HyperNews/geant4/get/hadronprocess/1270/1.html>

³<https://indico.fnal.gov/getFile.py/access?contribId=60&sessionId=7&resId=0&materialId=slides&confId=4535>, last accessed 2013-06-01

the activities of in the decay chains pre- or succeeding nuclides. Although the correction of peaks in the spectrum of a decay with TCS is not completely correct, it is likely that the results improve since the summing effect should be relatively small.

As an alternative, single γ lines emitted in decays of nuclides can be simulated by using the Geant4 General Particle Source (GPS) neglecting any X-ray or bremsstrahlung emission by β particles (see also discussion in Section 5.2.1). In this case, the result of the MC simulation does not contain the emission probability p of the γ line. As one major drawback for the usage of GPS one has to define a volume by its dimensions and position in the geometry in which vertices are generated. Although it is possible to confine the position generation additionally to a certain volume of the MC geometry there is no mechanism ensuring that the volume used as a confinement is completely included in the defined position generation volume. The definition of the volume used by GPS for vertices generation is complicated, since one has to calculate the position of a certain geometry part in global coordinates, which is usually hierarchical defined and only local coordinates are known. The sophisticated position generator used in VENOM was implemented by T. Köttig (for details see [Köt12]) but is only available for the generators in VENOM based on GRDM. With this extension it is sufficient to provide the decay generators with the name of the volume and the minimal dimensions of the bounding box including the volume are retrieved from Geant4 internal methods. Because of this, the decay generators based on GRDM are usually preferred to the Geant4 provided GPS generator, although the above discussed drawbacks remain.

5. Monte Carlo simulation for full energy peak efficiency determination

6. Radioassay of samples

The main purpose of the DLB is to screen samples of materials needed for the development and construction of the COBRA R&D set-up and the future major experiment for intrinsic radioactivity. The detector set-up described in Chapter 3 is used to acquire high resolution γ ray spectra of material samples in an environment with as low as reasonably achievable background radiation. Using the MC simulation described in Chapter 5, the efficiency of the detector system for γ radiation emitted by the samples of interest is individually determined. Using the software explained in Chapter 4 the acquired spectra can be analysed and activities of the samples can be determined.

Usually the radioactivity contained in the samples of interest is fairly low or even below the detection limits of the detector system so that often only upper limits on the activities can be provided. In the following the analysis of different samples is discussed. Since it is necessary to test the evaluation procedures on special samples against pre-established values, the results of the participation in two interlaboratory comparisons, also called intercomparison exercises or proficiency tests, are discussed as well.

In this chapter the notation of DIN ISO 11929:2011 is used (compare Section 4.3.2). \hat{A}_{spec} denotes the most probable value of the measurand. Its standard uncertainty is given with $k = 1$. $A_{\text{spec}}^<$ and $A_{\text{spec}}^>$ are the lower and upper limit of the coverage interval, which is here always calculated with $k_{1-\frac{\gamma}{2}} = 1.96$ what corresponds to a 95.0% coverage probability. In case the primary result of the measurement (compare Section 4.3.2) does not exceed the decision threshold A_{spec}^* , which is computed for $k_{1-\alpha} = 1.645$ and is equal to 5.0% false positive decision probability, the activity is usually declared as not detected. In case the lower limit of the coverage interval is 0 the upper limit is the relevant result instead of \hat{A}_{spec} . The detection limit $A_{\text{spec}}^{\#}$ is calculated for $k_{1-\beta} = 1.645$, which corresponds to a 5.0% false negative decision probability.

6.1. IAEA proficiency tests

Among others the Bundesamt für Strahlenschutz (Germany), the National Physical Laboratory (NPL, United Kingdom) and the IAEA organise proficiency tests for the determination of α , β and γ ray emitting radioactive nuclides in different sample matrices and activity ranges. After registration the participants receive the requested samples and have to submit the results within a certain time span.

6. Radioassay of samples

Afterwards each laboratory receives its own evaluation report and a summarising report of the whole intercomparison exercise is usually published later. The IAEA organises the proficiency test free of charge to support the knowledge in radiation measurement.

In both IAEA proficiency tests, in which the DLB participated (see Section 6.1.1 and 6.1.2), the reported activities X were evaluated according to several criteria. The relative bias is calculated as

$$\text{Rel. bias / \%} = \frac{X_{\text{Lab}} - X_{\text{IAEA}}}{X_{\text{IAEA}}} \times 100 \quad (6.1)$$

and compared to the maximum acceptable bias (MAB). The z-Score is defined as

$$z_{\text{Score}} = \frac{X_{\text{Lab}} - X_{\text{IAEA}}}{\sigma} \quad (6.2)$$

with a target value for the standard deviation σ of $0.1 \times X_{\text{IAEA}}$. If $|z_{\text{Score}}| \leq 2$ (relative deviation $\leq 20\%$), the performance of the laboratory is satisfactory, questionable for $2 < |z_{\text{Score}}| < 3$ and unsatisfactory for $|z_{\text{Score}}| \geq 3$. The trueness of the quoted result is fulfilled if

$$A1 \leq A2 \quad (6.3)$$

with

$$A1 = |X_{\text{IAEA}} - X_{\text{Lab}}| \quad ,$$
$$A2 = 2.58 \times \sqrt{u(X_{\text{IAEA}})^2 + u(X_{\text{Lab}})^2} \quad .$$

The estimator

$$P/\% = \sqrt{\left(\frac{u(X_{\text{IAEA}})}{X_{\text{IAEA}}}\right)^2 + \left(\frac{u(X_{\text{Lab}})}{X_{\text{Lab}}}\right)^2}$$

is calculated to score the precision and is accepted (A) in case the value is smaller than an in advance defined limit of acceptable precision (LAP). In case either trueness or precision are classified as 'not acceptable' (N), the final score will be a warning (W) only if the relative bias is smaller than the MAB value, otherwise it is not acceptable as well.

6.1.1. IAEA-CU-2010-03 World-wide open proficiency test

The intercomparison exercise IAEA-CU-2010-03 did include in total six samples, but only one was intended mainly for analysis by γ ray spectrometry. Since the work on the MC simulation of the detector system had started just shortly before the submission deadline April 15th 2011, only the soil sample was analysed. The sample stems from a Syrian oil field and is contaminated with ^{226}Ra due to contact to process water returning from the oil well containing high concentrations of natural occurring radioactive nuclides.

Table 6.1.: (Corrected) Intercomparison result for IAEA-CU-2010-03, Sample 6. Sample mass 15.0(5) g, live-time of measurement 35.7 h. Specific activity per dry mass. For denotation and coverage probabilities see introduction of Chapter 6.

Isotope	$\hat{A}_{\text{spec, Lab}}$ / Bq/g	$A_{\text{spec, IAEA}}$ / Bq/g	Rel. bias / %	z-Score	P / %	Trueness	Precision	Final
^{226}Ra	18.7(12)	19.05(26)	-1.70	-0.17	6.25	A	A	A
^{214}Pb	18.1(11)	-						
^{214}Bi	17.53(77)	-						
^{210}Pb	6.06(56)	-						
^{228}Ac	1.59(12)	-						
^{212}Pb	2.29(15)	-						
^{40}K	0.374(44)	-						

Due to a mistake in the sample placement within the MC geometry, the determined FEP efficiency was largely overestimated so that an unacceptable result was submitted. The specific activity of ^{226}Ra quoted in Table 6.1 was determined by using the correct MC geometry and is compared to the target values referenced by the IAEA. Although the soil sample does contain high activities of most of the natural occurring radioactive nuclides, only the analysis of ^{226}Ra was requested. Since the activity had to be expressed per dry sample mass, an aliquot of several gram mass was dried for approximately 16 h at 80 °C to determine the dry to wet ratio to 0.9695. For the evaluation by the IAEA both acceptance limits LAP and MAB were established to be 20 %.

The results of the first three evaluated nuclides show that ^{226}Ra and its daughters are in equilibrium, which is what one would expect due to the short half lives of ^{214}Pb and ^{214}Bi unless ^{222}Rn , which lies between ^{226}Ra and ^{214}Pb , as a noble gas is able to escape from the sample. ^{228}Ac and ^{212}Pb from the ^{232}Th decay chain differ. In this case the activity of the upper part of the decay chain is lower than the activity of the lower part (after ^{228}Th), which is unusual since a depletion of ^{232}Th would include the chemically identical ^{228}Th as well. The sample does contain a certain amount of ^{40}K , but its determined activity is well within usual ranges of environmental samples.

6.1.2. IAEA-TEL-2011-03 World-wide open proficiency test

The IAEA-TEL-2011-03 proficiency test did consist of four samples intended for analysis. The first three were prepared by spiking tap water gravimetrically with a known amount of a solution containing several γ ray emitting radionuclides. It was requested to determine the specific activities of the nuclides given in Table 6.2. The evaluation data of the water samples 1–3 can be found in Table 6.2

6. Radioassay of samples

Table 6.2.: Intercomparison results for IAEA-TEL-2011-03, Sample 1–3. Gravimetrically spiked tap water. Sample masses 233.9(10) g, 253.6(10) g and 253.6(10) g, live-time of measurements 55.1 h, 37.6 h and 103.3 h. Reference date November 15th 2011.

Isotope	submitted, non final geometry optimisation							final geometry optimisation							
	$A_{\text{spec,IAEA}}$ / Bq/kg	$\hat{A}_{\text{spec,Lab}}$ / Bq/kg	Bias / %	z-Score	P / %	Trueness	Precision	Final	$\hat{A}_{\text{spec,Lab}}$ / Bq/kg	Bias / %	z-Score	P / %	Trueness	Precision	Final
Sample 1															
^{241}Am	4.7(1)	4.97(22)	5.74	0.57	4.91	A	A	A	5.34(33)	13.62	1.36	6.54	A	A	A
^{133}Ba	5.0(1)	4.99(9)	-0.20	-0.02	2.69	A	A	A	5.19(22)	3.80	0.38	4.69	A	A	A
^{60}Co	15.3(2)	15.82(15)	3.40	0.34	1.61	A	A	A	15.72(58)	2.75	0.27	3.91	A	A	A
^{134}Cs	7.7(1)	7.61(12)	-1.17	-0.12	2.04	A	A	A	7.86(41)	2.08	0.21	5.38	A	A	A
^{137}Cs	6.2(1)	6.32(10)	1.94	0.19	2.26	A	A	A	6.57(35)	5.97	0.60	5.57	A	A	A
^{152}Eu	15.4(2)	14.76(15)	-4.16	-0.42	1.65	A	A	A	15.24(34)	-1.04	-0.10	2.58	A	A	A
Sample 2															
^{241}Am	2.4(1)	2.31(18)	-3.75	-0.38	8.84	A	A	A	2.36(19)	-1.67	-0.17	9.07	A	A	A
^{133}Ba	2.5(1)	2.42(7)	-3.20	-0.32	4.94	A	A	A	2.54(12)	1.60	0.16	6.19	A	A	A
^{60}Co	7.6(1)	7.63(11)	0.39	0.04	1.95	A	A	A	7.71(30)	1.45	0.14	4.11	A	A	A
^{134}Cs	3.8(1)	3.69(9)	-2.89	-0.29	3.59	A	A	A	3.79(21)	-0.26	-0.03	6.13	A	A	A
^{137}Cs	3.1(1)	3.09(8)	-0.32	-0.03	4.14	A	A	A	3.24(19)	4.52	0.45	6.69	A	A	A
^{152}Eu	7.7(1)	7.30(11)	-5.19	-0.52	1.99	N	A	W	7.82(20)	1.56	0.16	2.87	A	A	A
Sample 3															
^{241}Am	3.3(1)	3.22(13)	-2.42	-0.24	5.05	A	A	A	3.42(21)	3.64	0.36	6.85	A	A	A
^{133}Ba	3.5(1)	3.57(5)	2.00	0.20	3.18	A	A	A	3.72(15)	6.29	0.63	4.94	A	A	A
^{60}Co	10.7(2)	11.01(9)	2.90	0.29	2.04	A	A	A	11.09(40)	3.64	0.36	4.06	A	A	A
^{134}Cs	5.4(1)	5.25(7)	-2.78	-0.28	2.28	A	A	A	5.43(28)	0.56	0.06	5.48	A	A	A
^{137}Cs	4.4(1)	4.46(7)	1.36	0.14	2.76	A	A	A	4.74(25)	7.73	0.77	5.74	A	A	A
^{152}Eu	10.8(2)	10.38(10)	-3.89	-0.39	2.09	A	A	A	11.15(24)	3.24	0.32	2.84	A	A	A

Table 6.3.: Intercomparison results for IAEA-TEL-2011-03, Sample 4. Soil collected in 1990 on a farm. Results determined with optimised MC geometry compared to values provided by IAEA and M. Laubenstein, LNGS. Sample mass 42.2(5) g, live-time of measurement 58.1 h. Reference date November 15th 2011.

Isotope	$\hat{A}_{\text{spec, Lab}}$ / Bq/kg	Reference IAEA						Reference LNGS							
		$A_{\text{spec, IAEA}}$ / Bq/kg	Bias / %	z-Score	P / %	Trueness	Precision	Final	$A_{\text{spec, LNGS}}$ / Bq/kg	Bias / %	z-Score	P / %	Trueness	Precision	Final
^{228}Ac	39.5(27)	41.0(20)	-3.66	-0.37	8.40	A	A	36.6(21)	7.92	0.79	8.92	A	A	A	A
^{212}Pb	40.2(22)	36.5(16)	10.14	1.01	7.01	A	A	34.7(26)	15.85	1.59	9.28	A	A	A	A
^{208}Tl	13.87(51)	13.0(7)	6.69	0.67	6.52	A	A	12.9(9)	7.52	0.75	7.89	A	A	A	A
^{234}Th	21.5(41)	27.0(14)	-20.37	-2.04	19.76	A	A	31.2(27)	-31.09	-3.11	20.94	A	A	A	A
$^{234\text{m}}\text{Pa}$	21.7(43)	27.0(14)	-19.63	-1.96	20.48	A	N	31.2(27)	-30.45	-3.04	21.62	A	N	N	N
$^{226}\text{Ra}^{\text{a}}$	42.4(26)	50.2(20)	-15.54	-1.55	7.31	A	A	39.1(32)	8.44	0.84	10.23	A	A	A	A
^{214}Pb	41.0(23)	50.0(38)	-18.00	-1.80	9.45	A	A	36.6(21)	12.02	1.20	8.02	A	A	A	A
^{214}Bi	38.7(20)	50.0(28)	-22.60	-2.26	7.62	N	A	37.6(19)	2.93	0.29	7.23	A	A	A	A
^{210}Pb	42.3(99)	42.6(22)	-0.70	-0.07	23.97	A	N	-	-	-	-	N	A	N	N
$^{235}\text{U}^{\text{b}}$	1.441(86)	1.24(2)	16.21	1.62	6.18	A	A	1.99(16)	-27.59	-2.76	10.01	N	A	N	N
$^{235}\text{U}^{\text{c}}$	< 1.12	1.24(2)	-	-	-	-	-	1.99(16)	-	-	-	-	-	-	-
^{40}K	502(27)	485(11)	3.51	0.35	5.84	A	A	479(36)	4.80	0.48	9.24	A	A	A	A
^{137}Cs	14.77(80)	14.4(60)	2.57	0.26	6.83	A	A	14.1(11)	4.75	0.48	9.50	A	A	A	A

^a 186 keV peak assumed as ^{226}Ra only, ^{238}U chain in equilibrium and natural uranium abundances. Correction factor 0.5754(11)

^b 186 keV peak assumed as ^{226}Ra only, ^{238}U chain in equilibrium and natural uranium abundances. Correction factor 0.019547(52)

^c 163 keV peak, emission probability $p = 5.08(3)\%$ (185.72 keV line with $p = 57.0(3)\%$)

6. Radioassay of samples

and are based on the pre-established acceptance limits of each 20 % (15 % for ^{60}Co and ^{152}Eu). As one can see in Table 6.2, all values but one were classified as accepted in the evaluation process. The determined activity value of ^{152}Eu did receive a warning since the trueness was not accepted due to the criterion in Equation (6.3). Comparing the submitted values with the results determined using the fully optimised MC geometry, it has to be noted that in some cases the relative bias was reduced whereas in others like the results for ^{137}Cs the deviations did increase. Nevertheless, for most of the determined activities the target value lies well within the quoted standard uncertainty.

The fourth specimen has been a soil sample collected in 1990 by the IAEA Seibersdorf laboratories on a farm and prepared by milling and sieving so that a homogeneous fine powder with grain size smaller than 150 μm was produced. For this sample the specific activities of the nuclides of the natural decay chains as well as ^{40}K and ^{137}Cs had to be determined. For laboratories being able to apply also other analysis methods than γ ray spectrometry the activities of several α and β emitters had to be determined in addition to the above mentioned nuclides. The results submitted to the IAEA did deviate especially for ^{226}Ra , ^{214}Pb and ^{214}Bi systematically from the target values, but were consistent to each other. This consistency is expected due to their sequence and positions in the ^{238}U decay chain. According to the values provided by the IAEA, the activity of ^{238}U , which was determined via $^{234\text{m}}\text{Pa}$, did differ significantly from the other three results indicating that the decay chain is not in equilibrium. Additionally, the quoted activities did not match to the activity given for ^{210}Pb at the end of the ^{238}U decay chain. Due to the not optimal MC geometry and not correct emission probability of the 46.54 keV γ line, the efficiency was not correctly reproduced and the activity of ^{210}Pb largely overestimated so that a strongly deviating result for ^{210}Pb was submitted.

Because of the large discrepancies for the above mentioned nuclides between the determined values and the ones quoted by the IAEA, the obtained results were in addition compared to the activities determined by M. Laubenstein at LNGS. Surprisingly the deviations for ^{226}Ra , ^{214}Pb and ^{214}Bi did vanish in comparison to the LNGS data, what also shows a nearly equilibrium of the whole ^{238}U decay chain. As these discrepancies may hint to a mistake in the IAEA reference evaluation, an enquiry was written to the responsible officer at the IAEA. Although the receipt of the questions was acknowledged, up to now no answers were provided. Since the final summary report, usually scheduled for the end of the year in which the results are submitted, has not been published yet as well, the official results remain unfortunately unknown.

After the optimisation of the MC geometry (see Section 5.2) the evaluation of the data was repeated. The determined values are summarised in Table 6.3 and due to the above mentioned discrepancies compared to the results by the IAEA and the ones of the γ ray spectrometry facility at LNGS. As one can see, the ac-

tivity of the low energy γ ray emitter ^{210}Pb is now correctly determined and is consistent to the calculated activities of ^{226}Ra , ^{214}Pb and ^{214}Bi , showing that this part of the ^{238}U chain is in equilibrium. Although most of the results are accepted by the limits set by the IAEA, the still existing difference between the referenced IAEA values and the determined activities is obvious. The source of the deviation of the results for ^{234}Th and ^{234m}Pa reflecting the ^{238}U activity remains unclear. The activities determined for ^{235}U from the 186 keV composite peak (^{235}U 185.7 keV and ^{226}Ra 186.2 keV, compare Section 3.5.1) and from the 163 keV γ line, but with a more than ten times lower emission probability than the 185.7 keV line, are not compatible to each other. Also the first three nuclides referenced in Table 6.3 show an equilibrium of the ^{232}Th decay chain if one keeps in mind that ^{212}Bi decays only with a probability of 35.93(7) % to ^{208}Tl . Correcting for this branching a value of 38.6(15) Bq/kg for ^{212}Bi is determined showing that the ^{208}Tl activity is compatible with the first two results.

6.2. Material samples for COBRA

The main intention for the construction of the DLB has been to characterise materials needed for the development and operation of COBRA regarding their intrinsic radioactivity. In the following the results of a small selection of analysed materials is discussed and the obtained values presented.

In addition to the results discussed in Section 6.1, which prove the correct determination of activity values with the procedures described in Chapter 4 and Chapter 5, the results presented in the following sections confirm the very high sensitivities achievable with the DLB detector system.

6.2.1. Conductive silver Ferro LS200

The electrical contacting of the CdZnTe coplanar grid (CPG) detectors used by the COBRA experiment on the one hand has to be reliable to allow for a stable operation. On the other hand the contacting needs to be of very high radiopurity since due to the closeness of contacts to the sensitive detector volume any impurities have a large impact on the achievable background level. In addition to these requirements the CdZnTe detectors are fragile and can not be contacted by techniques like bonding. Furthermore, they are destroyed if they are heated to more than 80 °C so that soldering is not possible as well.

Due to these constraints, already several different approaches for detector contacting were tested by D. Münstermann [Mü07] and T. Köttig [Köt08]. Since other materials like copper filled glue lead to unreliable detector contacts, the currently applied technique uses conductive silver, a mixture of very small silver flakes and a chemical matrix that evaporates to a huge fraction after application.

6. Radioassay of samples

Table 6.4.: Radiopurity data of Ferro LS200 conductive silver used for electrical contacting of COBRA CdZnTe detectors. Sample mass 200.4(10) g, live-time of measurement 496.4 h. For denotation and coverage probabilities see introduction of Chapter 6 and Section 4.3.2.

Isotope	$A_{\text{spec}} / \text{mBq/kg}$	$A_{\text{spec}}^* / \text{mBq/kg}$	$A_{\text{spec}}^{\#} / \text{mBq/kg}$
^{108m}Ag	101.0 ± 3.9	3.2	6.7
^{110m}Ag	4.9 ± 2.2	3.5	7.5
^{234}Th	< 8.0	7.9	16.9
^{234m}Pa	< 600	520	1100
^{226}Ra	< 145	85	175
^{214}Pb	< 25.1	18.2	37.8
^{214}Bi	< 86	84	178
^{210}Pb	$< 16.1 \times 10^3$	24.1×10^3	49.7×10^3
^{228}Ac	< 39	29	62
^{212}Pb	< 13.7	9.5	19.6
^{212}Bi	< 259	224	494
^{208}Tl	< 4.0	5.4	11.2
^{235}U	< 97	91	188
^{40}K	< 71	79	165
^{137}Cs	< 4.4	3.0	6.4
^{60}Co	< 4.5	4.4	9.4

Silver has the drawback that both natural occurring isotopes ^{107}Ag and ^{109}Ag are subject to neutron activation. In the capture process of, for example, secondary neutrons induced by cosmic radiation the long-living nuclides ^{108m}Ag and ^{110m}Ag are produced. Especially the latter is of concern, since ^{110m}Ag decays to 1.36 % by isomeric transition (IT) to ^{110}Ag . ^{110}Ag itself decays to 99.7 % by β decay most of the time directly to the ground state of ^{110}Cd (compare [Fir96]). With $Q_{\beta^-} = 2892 \text{ keV}$ the decay reaches into the COBRA ROI for the $0\nu\beta\beta$ decay of ^{116}Cd at $Q_{\beta\beta} = 2813.5 \text{ keV}$ [REE⁺11]. ^{110m}Ag itself does only decay with a maximum β energy of 1510 keV and subsequent γ ray emissions so that deposition of the total decay energy within one detector crystal is very unlikely.

Due to the application of the conductive silver, a sample of 200.4 g mass was checked for its radiopurity. The activities determined after a measurement period of nearly four weeks are summarised in Table 6.4. Since the silver flakes within the mixture did settle during the measurement, the efficiencies obtained by MC simulations were calculated by assuming that all nuclides except for ^{108m}Ag and ^{110m}Ag are homogeneously distributed within the chemical matrix and the silver isotopes are concentrated in a layer at the bottom of the sample container. As one can see in Table 6.4, only for the silver nuclides significant activities were found.

The impact of the very small amounts of conductive silver used at each de-

Table 6.5.: Radiopurity data of OPERA lead sheets. Sample mass 182.5(10) g, live-time of measurement 558.5 h. All values in Bq/kg. For denotation and coverage probabilities see introduction of Chapter 6 and Section 4.3.2.

Isotope	\hat{A}_{spec}	$A_{\text{spec}}^{<}$	$A_{\text{spec}}^{>}$	A_{spec}^{*}	$A_{\text{spec}}^{\#}$	Remarks
^{210}Pb	62(11)	41	82	15	31	GRDM & Correction
^{210}Pb	57.5(98)	38.4	76.6	14.2	29.2	GPS
^{210}Pb	50.5(30)	44.7	56.3	1.5	3.0	^{210}Bi β^- ind. X-rays, GRDM

tector contact was investigated by B. Hillringhaus [Hil12]. Based on preliminary activity data, which deviate only slightly due to a non fully optimised MC model, she found that the contribution of ^{110m}Ag to the background of the COBRA experiment is several orders of magnitude below the necessary background level within the ROI.

6.2.2. OPERA lead sheets

The OPERA experiment is located, like the COBRA R&D set-up, at LNGS and uses bricks made of thin lead plates and emulsion sheets to track secondary particles induced by a neutrino beam send from CERN to LNGS. Due to the end of the data taking phase in 2012 the radiopurity of the lead plates was investigated for a possible re-usage of the about 1250 t tracking bricks. Due to the usually high radiopurity of lead with respect to all nuclides of the natural decay chains except for ^{210}Pb and its daughters (compare [HLN06, LHG⁺04]) only the specific activity of ^{210}Pb was determined, which is crucial due to the high energetic β emission ($Q_{\beta^-} = 1162 \text{ keV}$) of its daughter nuclide ^{210}Bi producing intense bremsstrahlung.

Table 6.5 summarises the results deduced in different ways. The values in the first two rows were determined from the ^{210}Pb 46.5 keV γ line, which unfortunately has a low emission probability p and due to the low energy value and strong self absorption in the lead plates a very low FEP efficiency. For the result given in the first row the FEP efficiency was determined by using the GRDM generator with the correction of the biased γ ray emission probability (see discussion in Section 5.3). For the results of the second row the GPS generator was used in the MC simulation. This result is slightly lower than the first one, since the MC simulation of the latter does not contain any bremsstrahlung and therefore underestimates the background of the γ ray peak. A too high FEP efficiency then inevitably leads to a too low activity result.

The result of the ^{210}Pb activity given in the last row of Table 6.5 was determined from the lead K_{α} X-ray peaks at 72.81 keV and 74.97 keV induced by the β particles emitted in the decay of the short lived daughter nuclide ^{210}Bi . The spectral shape of this first non-unique forbidden β decay deviates significantly from an

6. Radioassay of samples

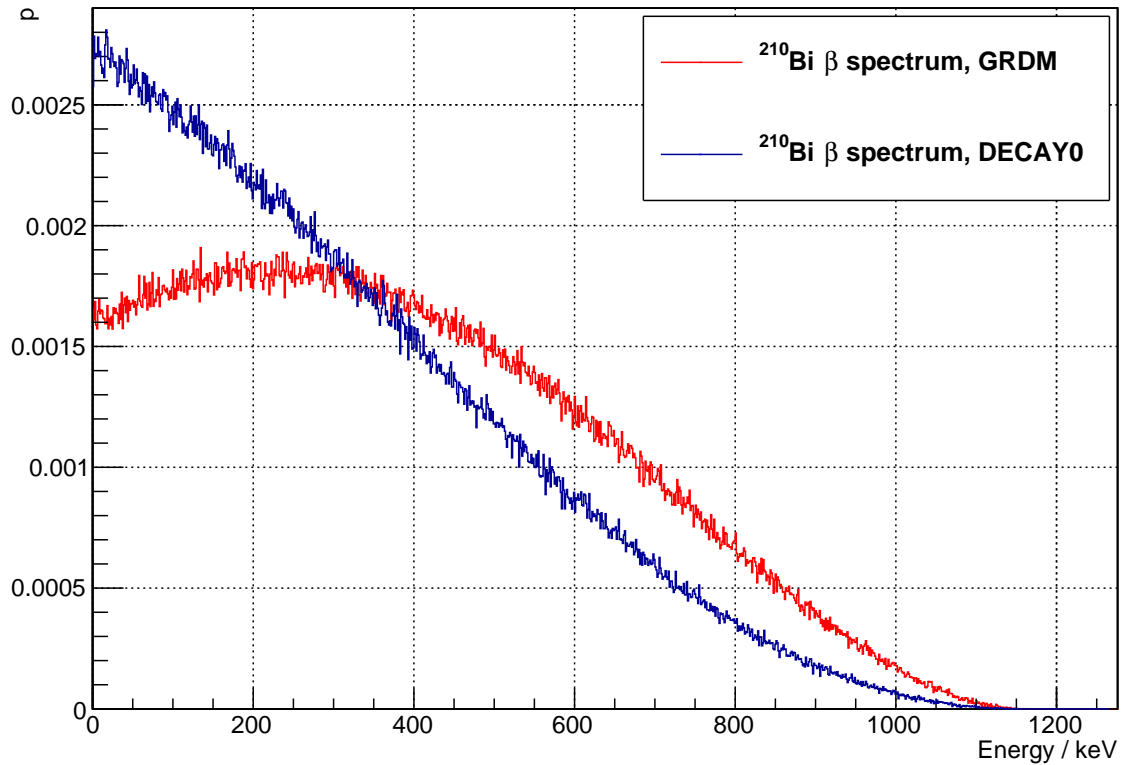


Figure 6.1.: Different spectral shape of ^{210}Bi β spectrum generated by GRDM and the external DECAY0 generator [PTZ00]. 10^6 generated primary particles per generator.

allowed transition, but GRDM currently treats all β transitions as that latter type (compare Figure 6.1). Since the mean of the spectrum generated by GRDM is higher than in the one generated by DECAY0 [PTZ00], more X-rays are emitted during the scattering of the β particles thus leading to a too high efficiency and a reduced activity. Due to the high self absorption of the X-rays, a huge amount of simulated β particle is necessary to gather sufficient statistics for the efficiency determination. Because of the available mechanism of providing DECAY0 events as an input to VENOM, it is not easily possible to carry out such a simulation at the computing cluster already described in Section 4.5. Therefore, an analysis based on a MC simulation using DECAY0 as a particle generator was not conducted as part of this work.

In case the β spectrum and the emission probabilities of the X-rays are correctly reproduced in the MC simulation the determination via the lead K_{α} X-ray peaks does allow for a much lower detection limit (compare Table 6.5, column $A_{\text{spec}}^{\#}$). Due to the higher energy of the X-ray peaks in comparison to the 46.5 keV γ line the detection efficiency is higher as well. In addition, the background spectrum does not already contain the X-ray peaks, which is in contrast to the ^{210}Pb 46.5 keV peak. On the other hand it is possible that lead X-rays are as well emitted due to the interaction of other particles like muons with the lead sample leading to

Table 6.6.: Radiopurity data of Timepix readout chips used for silicon and CdZnTe pixel detectors. In total 30 chips were measured, assumed as pure silicon with density 2.33 g/cm^3 . Live-time of measurement 551.3 h. For denotation and coverage probabilities see introduction of Chapter 6 and Section 4.3.2.

Isotope	$A_{\text{spec}} / \mu\text{Bq}/\text{chip}$	$A_{\text{spec}}^* / \mu\text{Bq}/\text{chip}$	$A_{\text{spec}}^{\#} / \mu\text{Bq}/\text{chip}$
^{234}Th	< 1.52	1.34	2.86
^{234m}Pa	< 1030	1720	3640
^{226}Ra	< 334	183	375
^{214}Pb	58 ± 29	50	104
^{214}Bi	< 313	300	630
^{210}Pb	< 2630	3130	6420
^{228}Ac	< 99	94	200
^{212}Pb	< 40	24	49
^{212}Bi	< 1330	790	1730
^{208}Tl	< 13.6	17.7	37.1
^{235}U	< 11.4	6.2	12.7
^{40}K	< 247	262	544
^{137}Cs	10.9 ± 5.6	9.4	20.1
^{60}Co	< 13.0	15.9	34.1

additionally enhanced X-ray peaks.

6.2.3. Pixel detector readout chips

As an alternative to CPG detectors the COBRA collaboration investigates the usage of different types of pixel detectors which, depending on the used pixel pitch, provide different possibilities for background reduction due to discrimination techniques. Due to the large amount of required readout channels, pixel detectors are usually mounted directly on top of a corresponding readout chip. Consequently, any radioimpurities contained in them or the supporting PCB and surrounding electronic components have a huge impact on the background seen by these systems.

Thin sensors with a thickness of about 1 mm and a pixel pitch in the order of $100 \mu\text{m}$ allow to track particles and distinguish between different particle types. For the readout of such sensors made of silicon or CdZnTe currently two different chips developed by the Medipix⁴ collaboration are in use namely the Timepix and the Medipix ASIC. 30 pieces of the Timepix and 44 of the Medipix ASICs were separately measured with the DLB for about four weeks each. Within the MC simulation for FEP efficiency determination the readout chips were assumed as

⁴<http://medipix.web.cern.ch/medipix/>

6. Radioassay of samples

pure silicon, neglecting all metallisations within the chips, which have unknown amounts. The density of the chips was adapted to the measured value that was derived from the outer dimensions of the stacked chips and their mass. In case of the Timepix chips the calculated density was compatible to the literature value of 2.3296 g/cm^3 whereas the value for the Medipix chips was more than 1 g/cm^3 higher. Unfortunately the source of this large deviation remains unclear.

The determined activities per readout chip are summarised in Table 6.6 and Table 6.7. The analysis of the measurements did derive only upper limits, except for in total four values for different nuclides. In case of the Timepix readout chips it was found that amounts of ^{214}Pb and ^{137}Cs are contained that are not compatible with the system background. Taking a closer look at the evaluation data and keeping in mind that the decision threshold A_{spec}^* is computed for a 5.0% false positive decision probability, it becomes obvious that the measured value exceeds the decision threshold in both cases only slightly and the coverage interval of 95% probability also nearly includes the value 0 at its lower end. Due to the decision rules (see Section 4.3.2) and the chosen conditions (see introduction of Chapter 6) the values are classified as significant. The same holds true for the data of the Medipix readout chips. In this case the values for ^{226}Ra and ^{235}U seem to be significant. Both values are correlated since they are derived from the combined peak at 186 keV. Under the assumption that the ^{238}U chain is in equilibrium and the isotopic composition of the contained uranium is the natural one, the peak can be divided by mathematical means into the contributions by ^{226}Ra and ^{235}U (see also remarks to Table 6.3).

Table 6.7.: Radiopurity data of Medipix readout chips used for silicon and CdZnTe pixel detectors. In total 44 chips were measured, assumed as pure silicon with density 3.2 g/cm³. Live-time of measurement 537.8 h. For denotation and coverage probabilities see introduction of Chapter 6 and Section 4.3.2.

Isotope	$A_{\text{spec}} / \mu\text{Bq}/\text{chip}$	$A_{\text{spec}}^* / \mu\text{Bq}/\text{chip}$	$A_{\text{spec}}^{\#} / \mu\text{Bq}/\text{chip}$
²³⁴ Th	< 0.75	0.88	1.89
^{234m} Pa	< 1320	1050	2220
²²⁶ Ra	132 ± 66	116	237
²¹⁴ Pb	< 51	33	69
²¹⁴ Bi	< 161	176	372
²¹⁰ Pb	< 960	1860	3840
²²⁸ Ac	< 45	61	130
²¹² Pb	< 25.9	15.7	32.4
²¹² Bi	< 960	550	1190
²⁰⁸ Tl	< 10.4	12.0	25.1
²³⁵ U	4.5 ± 2.3	3.9	8.1
⁴⁰ K	< 232	169	351
¹³⁷ Cs	< 7.0	6.1	13.2
⁶⁰ Co	< 9.5	10.4	22.2

6. Radioassay of samples

7. Shielding design for the COBRA R&D set-up

The R&D set-up of the COBRA experiment is situated in the Italian underground laboratory LNGS, which is located next to a highway tunnel through the Gran Sasso massif near L'Aquila in Abruzzo. Up to the year 2011 the set-up was installed inside a container next to the main tunnel through the underground laboratory. In 2011 the experiment was moved to a solid hut formerly used by the Heidelberg-Moscow experiment [GHH⁺97]. Due to the new possibilities offered by the larger available space and an installed crane, the shielding of the set-up was completely redesigned and reworked.

Because of the experience of the author in shielding design and his affinity to technical projects and mechanical designs by means of CAD, the modifications were planned by the author and constructed by the mechanical workshop of the faculty of Physics at TU Dortmund and external companies. The compliance with the tight schedule was only possible due to the close cooperation between the workshop and the author.

In the following the three major redesigned parts of the experiment's shielding are briefly described.

7.1. Neutron shielding

Due to the high overburden of the LNGS underground laboratory of 1400 m rock the flux of cosmic muons is reduced approximately by a factor 10^6 [Zan91]. In contrast to the shielding design of the DLB (see Section 3.1.2) the neutron shielding can therefore be placed outside of the shield against environmental γ radiation since the chance of neutron production by muon interactions in the lead is very low.

The former design of the neutron shielding did consist of a layer of Paraffin wax bricks for neutron moderation and boron loaded polyethylene (BPE) plates for further moderation and capturing of thermal neutrons by the reaction discussed in Section 3.1.2 on page 28. The design was developed as part of the thesis by S. Oehl [Oeh04], but in the last used configuration the layer of Paraffin wax was not installed. This was done, since the bricks are brittle and use much space and the BPE plates were regarded to be a sufficient neutron shielding for the background level achievable with the R&D set-up. In principle, the shielding was a cuboid made of BPE with inner dimensions of 88 cm \times 102 cm \times 186 cm and a

7. Shielding design for the COBRA R&D set-up

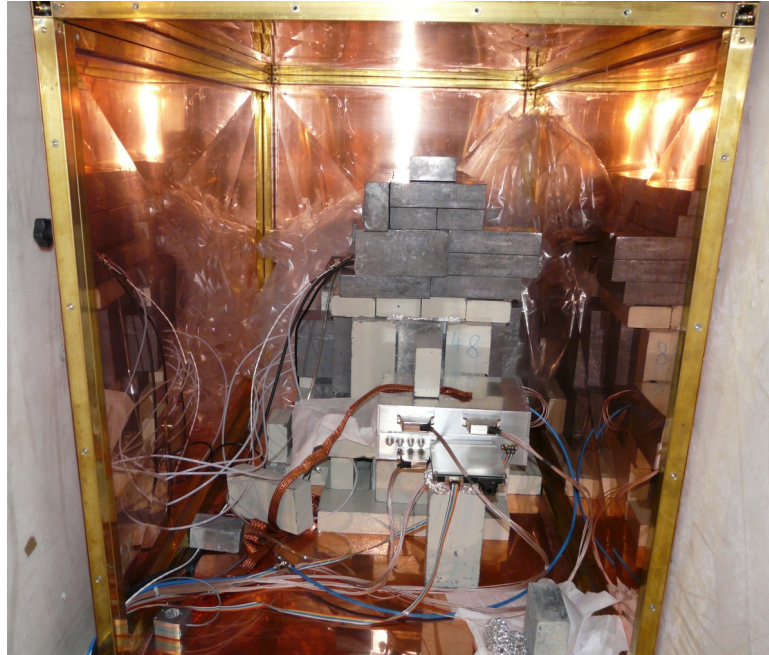


Figure 7.1.: View into the former COBRA set-up. At the sides the neutron shielding made of BPE plates is visible. The EMI shielding did consist of copper plates screwed to a brass frame. In the centre the lead castle with the pre-amplifiers in front of it can be seen.

wall thickness of approximately 7 cm. Due to the proximity to the surrounding rock the bottom of this box was reinforced by a second BPE plate, to gain a higher attenuation for neutrons impinging from below. The shielding was placed on top of rubber blocks, which in turn were put on lead bricks inside a bed of sand for vibration damping. The neutron shielding did contain the whole detector set-up including the electromagnetic interference (EMI) shielding made of copper sheets and the lead shielding against γ radiation. The access to the interior was possible by opening one of the short ends of the cuboid shaped shielding, since it is impossible to handle the large BPE plates of approximately 200 kg weight by hand. Due to this limited access it was complicated to reach certain parts of the experimental set-up.

Since in the new location a crane is installed, the neutron shielding was re-designed in that way that the main access to the set-up is possible from one of the long sides. Therefore, a rectangular steel tube was attached to the upper edge of the front BPE plate and an eyelet screwed to it so that an easy upright lifting of the plate is possible to access the set-up (compare Figure 7.2). Furthermore, all plates were rearranged to increase the depth of the inside of the shielding by 7 cm and to reduce the less important height. To allow for a possibly necessary access from above, the top BPE plate was reinforced by two L-sections and four bars (compare Figure 7.2) so that it is possible to easily lift this plate with the installed crane as well.

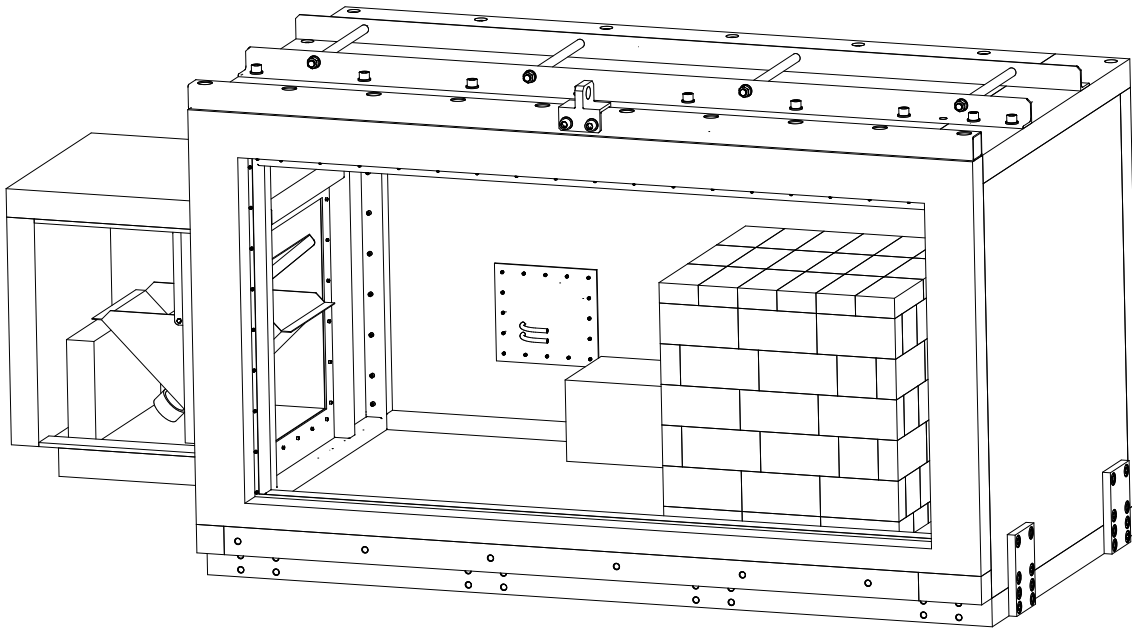


Figure 7.2.: Mechanical CAD drawing of the new neutron and EMI shielding for the COBRA R&D set-up. Cut-away view through the front door and the shielding extension at the left. In the centre one of the two feedthroughs, which are used for calibration tubes guiding radioactive sources mounted to a wire, is visible in the back wall. The box in the centre symbolises the preamplifier electronics used to read out the detectors hidden in the centre of the lead and copper shielding (right half of the interior). Drawing by the author using VariCAD [Var13]. Design of all parts by the author except for the BPE lifting support.

At the left side of the neutron shielding an extension is installed that surrounds the copper granule bath of the EMI shielding (see Section 7.2) used to feed necessary electrical connections and different media like cooling agent and nitrogen gas into the set-up. This extension includes a chicane preventing any line of sight pointing towards the lead shielding and the installed CdZnTe detectors so that all neutrons entering through the opening for cables have to be reflected at least once to reach the inner shielding. The extension shown in Figure 7.2 was only the first draft and is in the realised design supported by a three wheeled chassis on a rail to allow for an easy access to the copper granule bath. The basic plans for the machining of the BPE building blocks used for the extension were drawn by the author but the supporting structures were designed by the design office of the Faculty of Physics at TU Dortmund.

7.2. EMI shielding

The amount of charge induced by interaction of radiation in CdZnTe detectors is very small so that the signals have to be amplified by a high factor. Since

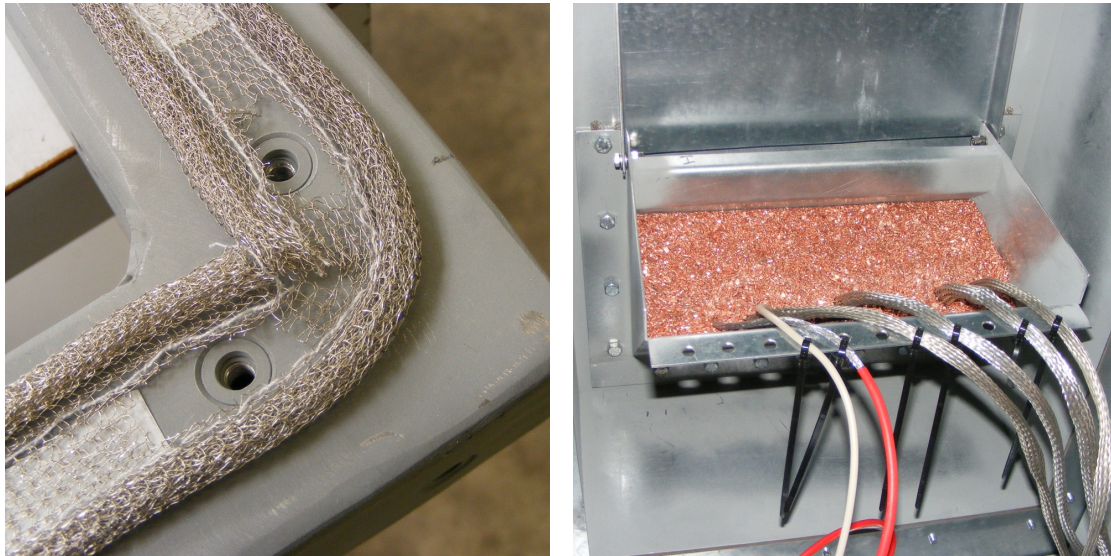
7. Shielding design for the COBRA R&D set-up

electronic components are usually not very radiopure, the preamplifiers used in the COBRA set-up are located outside of the lead shielding. Due to the large amount of connections needed to read out the 64 detector array, this is done with thin copper traces on Kapton®, a polyimide film. Because of the undesirable high capacity, these signal cables are not shielded so that the risk of picking up external signals between detector and preamplifier is very high.

To prevent disturbances by any electromagnetic signals from the surroundings, in the old set-up an EMI shielding made of 1 mm thick copper sheets mounted to a brass frame was installed (compare [Mü07]). During a discussion with M. Obholz, professorship for high voltage engineering, TU Dortmund and the following study of the books by Wolfsperger [Wol08] and Schwab and Kürner [SK11] it became clear that an EMI shielding made of copper has some drawbacks for the application in the COBRA R&D set-up. Especially for low frequency disturbances the thickness of a copper shielding has to be much higher than a shield made from iron to gain the same high (≥ 60 dB) suppression factor (compare [Wol08, Table 4.4–4.11]). Due to the inevitable corrosion of iron it is usually desired to use other materials. Stainless steel can not be used since it is amagnetic and therefore not suitable as a shielding against the magnetic component of electromagnetic waves. Consequently, often galvanised steel is used, but the protective zinc layer has to be destroyed to provide a good electrical contact between the shielding parts. The formerly used shielding was put together without using any type of conductive gasket to ensure a good electrical contact between the metal sheets at all edges. According to [SK11] this is especially important for a shielding against the magnetic component of electromagnetic waves.

Based on these information a new EMI shielding made of galvanised steel sheets and rectangular steel tubes was constructed by the author (compare Figure 7.2). Due to the limited space and transportation possibilities to LNGS in Italy, it was not feasible to weld the different sides to each other and a solution for a stable but dispersible EMI shielding had to be found. Therefore, different steel frames were constructed that are fixated to each other with screws and wire mesh gaskets in between to ensure a good electrical contact. These frames form the shape of a box fitting with only a small gap into the neutron shielding. The structure is surrounded by 2 mm thick galvanised steel sheets screwed to it using different types of wire mesh gaskets (see Figure 7.3a). Depending on whether a certain steel sheet is often opened (like the front door) or not, gaskets with or without a rubber core have been used, since the ones without a core are for single use only. The gaskets were purchased from Germania Elektronik, Germany, and consist of wires made of tin plated copper clad steel. When the wire mesh is compressed, it penetrates the zinc layer of the steel sheets and frames. This secures a good electrical contact along all edges.

To operate devices like the preamplifiers inside an EMI shielding, usually special feedthroughs for cables are used that connect the outer shield of a cable to



(a) Wire mesh gasket for good electrical contact between shielding parts. (b) Copper granule bath used for cable feedthrough.

Figure 7.3.: Components of EMI shielding.

the shielding. Due to the large amount of cables necessary to read out the detectors, to supply different voltages and to control the preamplifiers, the usage of feedthroughs would have been rather inconvenient. As an alternative a copper granule bath was constructed, which allows the flexible installation of different amounts and types of cables (see Figure 7.3b, principle taken from [Wol08]). If the outer insulation of a cable is (partly) removed and it is put through the emptied copper bath, the shield of the cable can be connected to the EMI shielding by filling the chute with copper granule made for example from recycled electrical cables.

Since the radioactive sources used for the calibration of the CdZnTe detectors are permanently attached to wires of limited length, it was not possible to guide these by tubes through the granule bath as well. Therefore, additional feedthrough tubes were installed in the back wall of the EMI shielding (see Figure 7.2). According to the equations given in [Wol08, Section 3.1.4.3] one can calculate the critical wavelength of the feedthrough functioning as a waveguide and furthermore the necessary length to attenuate waves to a negligible level. For the chosen inner diameter of 6 mm a length of less than 1.5 cm should be sufficient. Nevertheless, the feedthroughs were build with a length of more than 10 cm so that the impact of the feedthroughs on the shielding effectiveness should be negligible. If the radioactive source is put through one of the tubes into the detector set-up, its wire acts up to now as an antenna guiding disturbances into the shielding, since the wire is not connected to the EMI shield. This problem has to be solved at some time to lower the noise level during detector calibrations as well.

7. Shielding design for the COBRA R&D set-up

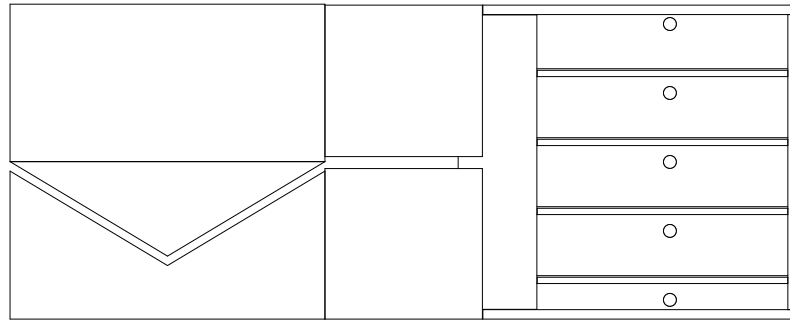
Although it was planned to measure the effectiveness of the constructed EMI shielding in a facility operated at the TU Dortmund, this had to be cancelled due to the lack of time. Nevertheless, for the experimental test set-up of COBRA at the TU Dortmund a similar EMI shielding was constructed and tested for its effectiveness. Y. Bernau measured in [Ber13] the attenuation of an EMI shielding with in all dimensions half the size of the one constructed for the COBRA set-up at LNGS. In a special electromagnetically shielded, anechoic room (see [Ber13]) an attenuation higher than 60 dB for frequencies above 3 MHz was determined, which is a very remarkable value in comparison to much more expensive industrial shieldings. Since the attenuation of a shielding increases with its size, at least a similar value can be expected for the EMI shielding at LNGS.

7.3. Shielding against environmental background

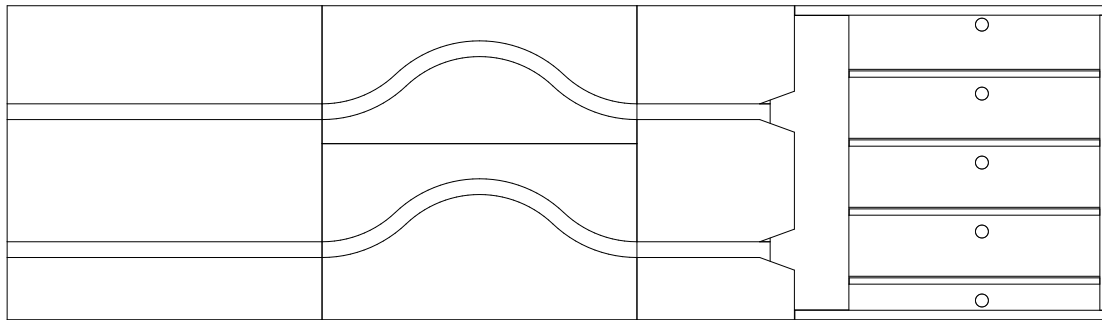
To shield the CdZnTe detectors operated in the R&D set-up at LNGS from environmental radiation these are surrounded by layers of copper and lead. Depending on the configuration up to 16 CdZnTe detectors of approximately $(10 \times 10 \times 10) \text{ mm}^3$ size are assembled in a supporting structure made of laser cut POM sheets. Up to four of these layers can be installed above each other inside a copper structure usually referred to as the NEST (compare [Mü07]). The NEST furthermore is designed to be equipped with five calibration tubes made of PTFE above, below and between the four detector layers. The NEST has a dimension of $(10 \times 10 \times 10) \text{ cm}^3$ and its front was in the old design closed by two 5 cm thick copper bricks leaving a small horizontal gap in between to run cables to the preamplifiers. The structure holding the detector layers is surrounded by 5 cm thick copper bricks so that in total outer dimensions of $(20 \times 20 \times 20) \text{ cm}^3$ are reached. In the old design the copper was surrounded by at least 15 cm of lead of unknown quality to shield the detectors from γ radiation from the environment. The cables were run through a special lead brick with a V-shaped gap to prevent any lines of sight to the detectors (compare Figure 7.4a).

The old design of the cable feedthroughs in the copper and lead layers aimed at the usage of thin flat cables made of Kapton® for the signal read out as well as the supply with HV. Due to discharges the usage of Kapton® for the HV side was not suitable and had to be changed to single cables. Since usual cables require larger bending radii than the ones necessary for cables made from foil, the design of the feedthroughs in copper and lead had to be modified (compare Figure 7.4). Furthermore, it was decided to surround the copper shielding layer, which is very radiopure, with lead bricks of an intrinsic activity of ^{210}Pb of less than 3 Bq/kg to reduce the intensity of bremsstrahlung of high energetic β particles emitted in the decay of the ^{210}Pb daughter nuclide ^{210}Bi .

The cables used for the supply of the high voltage are glued to the bottom POM plates of each layer. To reduce the bending radii of the cables two feedthroughs



(a) Feedthrough and NEST before upgrade.



(b) Feedthrough and NEST after upgrade.

Figure 7.4.: Cross section through feedthrough and NEST before and after upgrade. Only the bottom POM plate of each detector layer is drawn, since the HV supplying cables are mounted to it. The holes for the calibration tubes are visible. The vertical positions of the new feedthroughs are centred to the lower edges of two layers each. Drawings not to scale.

were foreseen so that the cables of two layers each run through one of these. Since the Kapton® cables used for the signal read out are much more flexible than the HV cables the vertical position of the feedthroughs is centred to the distance between the lower edges of the upper and lower detector layer pair. The mechanical drawings for the different new and modifications to existing parts were done by the author. The machining of the copper blocks as well as the outer straight lead feedthrough was done by the mechanical workshop at LNGS to reduce the exposure of the copper parts to cosmic radiation and limit the activation to a minimum level. The lead feedthrough formed like a wave was machined according to the authors drawings from lead with less than 3 Bq/kg ^{210}Pb by Plombum, Poland, who provided the other high purity lead bricks as well.

Due to the additional layer of high purity lead the total thickness of the new lead shielding is 20 cm. To reduce lines of sight through the lead shielding, after a stock taking of all available parts the arrangement of the complete lead shielding was planned with CAD by the author. These drawings were prepared so that

7. Shielding design for the COBRA R&D set-up

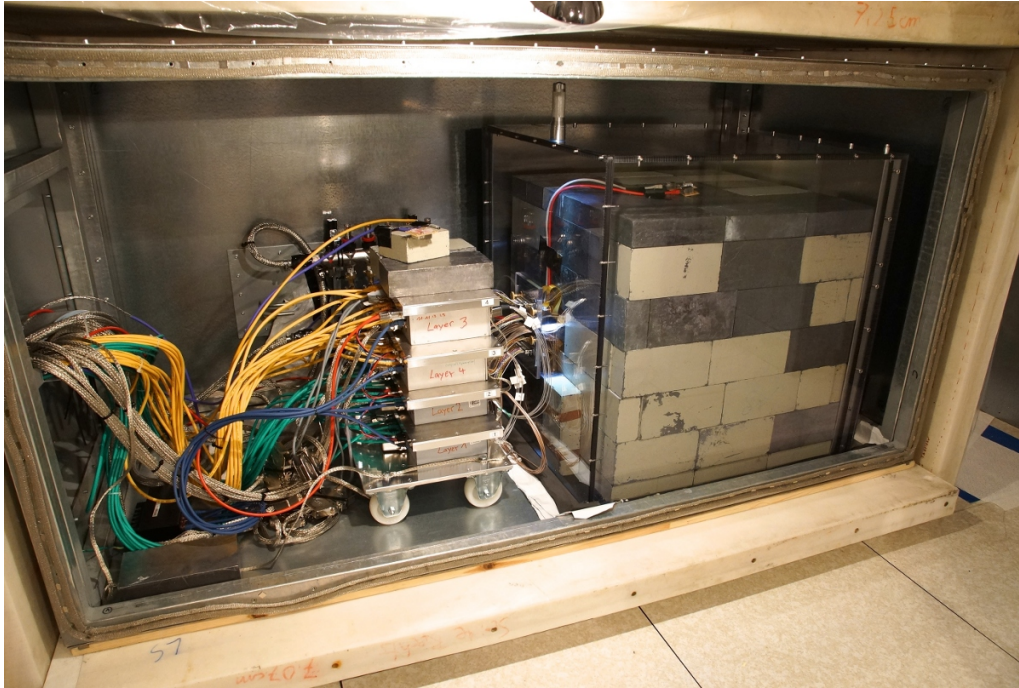


Figure 7.5.: View into the opened new COBRA set-up with the EMI shielding consisting of galvanised steel sheets. The radon shielding made of Tropic III foil has been replaced recently by a housing made of polycarbonate. In the back the additionally installed per-amplifier cooling system is visible. The cable feed trough in the EMI shielding can be seen at the left edge of picture.

they are readable for COBRA shifters installing new detectors in the R&D set-up without requiring knowledge of the used CAD software.

To prevent the diffusion of airborne ^{222}Rn into the NEST and reduce the background induced by it and its daughter nuclides a system for flushing with filtered gaseous nitrogen was designed in [Mü07] and improved in [Ale09, Sch11]. To increase the efficiency of the flushing it was planned to surround the lead and copper shielding with a special foil impermeable for diffusing radon gas. Based on the results of Mamedov et al. [MČSŠ11] Tropic III foil was chosen. The gas-tight enclosure for the lead shielding was constructed by J. Tebrügge [Teb11] by using aluminium sheets and the aforementioned foil so that it possible to keep the set-up under a slight overpressure.

8. Summary and outlook

In this work the two individual detector systems of the HPGe detector with its massive shielding and the anti cosmics veto have been combined to a low background γ ray spectrometry system. Furthermore, a data analysis chain was developed to allow for reliable low background material characterisation with respect to radioactivity.

An enormous background suppression was achieved reflecting the great efforts put into the construction of the DLB detector system. The already remarkable low background level of the γ ray spectrometry system without the active veto is even further reduced by nearly a factor of 6 by applying the anti coincidence system. By this means, a very low resulting integral count rate of 4.06 cts/(kg min) is achieved. Nevertheless, several small peaks caused by radioimpurities in the detector crystal and all surrounding materials can be identified in the spectrum. Their origin has been investigated by means of MC simulation and the determined activity values have been cross checked with other data. In addition to the peaks caused by radioimpurities, only three small peaks caused by neutron capture induced metastable states of germanium isotopes can be identified. Due to the integrated neutron shielding these peaks are much smaller than in the spectra of other γ ray spectrometry systems. Based on a formula given in [ŠAK⁺92], a remarkably low thermal neutron flux of $4.4(23) \times 10^{-5} \text{ cm}^{-2} \text{ s}^{-1}$ at the location of the HPGe detector was determined, which is nearly two orders of magnitude below the value of conventional detector systems and proves the effectiveness of the neutron shielding. The thermal neutron induced peaks can not effectively be suppressed further by the anti cosmics veto, since the lifetimes of the metastable states of germanium are longer than the applied rejection time of the veto. The similar determined upper limit on the flux of fast neutrons is with $2.2 \times 10^{-4} \text{ cm}^{-2} \text{ s}^{-1}$ nearly equal to the upper limit for a system with 500 mwe of overburden (compare [WMA⁺96]).

Based on the DIN ISO 11929:2011 [DIN11] standard a data analysis software was developed to allow the reliable determination of nuclide activities from the low background γ ray spectra acquired with the DLB. This software provides different methods to the analyst, including efficiency determination based on MC simulations, and allows to present the obtained results in a standardised evaluation report to the requesting user.

The MC simulations necessary for the efficiency determination rely on some extensions to the COBRA simulation framework VENOM allowing the read-in of externally defined GDML geometries. In the scope of the present work fur-

8. Summary and outlook

ther methods have been implemented to make the convenient modification of simulation cuts possible, which puts the focus on important regions within the simulated detector set-up as well as reduces the computational effort.

Using the MC geometry of the detector system based on the data sheet of the HPGe detector and other mechanical drawings, a comparison between measurements and simulations revealed discrepancies of up to 28 %. While the efficiency in the low energy region was vastly underestimated in the simulation, the efficiency for γ rays with energy higher than 200 keV was overestimated by a nearly constant fraction. Therefore, complex and detailed simulation studies have been carried out to determine modified detector parameters enabling the reliable reproduction of the measured detection characteristics. Based on the measured peak ratio of two low energetic γ ray peaks, it was possible to determine the thickness of the outer detector contact, which especially influences the efficiency in the energy region below 200 keV, by MC simulation. In this manner, a thickness of the outer contact was determined that is with 437 μm about 37 % smaller than the value given in the manufacturers data sheet. The vertical distance of the detector crystal to the inside of the endcap was deduced by comparing the ratio of the same low energetic γ ray peak in two spectra recorded with the same radioactive source placed at different, but precisely known heights above the detector endcap. From these spectra a distance more than twice as large as the nominal value was determined, which is necessary to adjust an overall bias of the detection efficiencies in the MC simulation to the ones seen in the measurements (compare Table 5.5). The detection efficiency in the high energy region does not depend significantly on the thickness of the outer contact, but the overall detector volume determines the probability for multi-site interactions, which dominate the full energy deposition in this energy region. By a slight adjustment of the dimensions of the inner contact, an overall good agreement with deviations in the range of $\pm 3\%$ between simulation and measurement has been obtained. Except from the γ lines from the used ^{152}Eu source, which was in general problematic, the range of deviations holds true for all γ lines used in the MC optimisation.

Based on the established MC model of the detector system, the analysis of different material samples was conducted. A comparison of the results determined for two IAEA proficiency tests using the new MC model reveals a general good agreement with the target values. Nevertheless, some values show significant deviations, but cross-checks with the results of M. Laubenstein, LNGS, suggest that the indicated target values could be biased. After proving the reliability of the developed analysis methods, several material samples were examined for the COBRA experiment. In the assessment of a conductive silver sample with a mass of 200 g upper limits as low as a few mBq/kg were determined for some radionuclides, what emphasises the detection potential of the constructed γ ray spectrometry system.

Besides the efforts put in the commissioning of the DLB detector system as well

as the development of the analysis chain, a huge contribution to the redesign and relocation of the COBRA R&D set-up at LNGS was made. In addition to the modification of the neutron shielding a completely new EMI shield was designed and its construction supervised. The new parts of the lead and copper shielding, necessary for the modification as well, were also designed. Only due to the in detail planned time schedule to coordinate the delivery of machined parts and ordered equipment, it was possible to relocate the whole detector set-up at LNGS within three weeks. In combination with the DAQ electronics developed by O. Schulz, T. Köttig and J. Tebrügge the value of the modifications is reflected by the high quality data taken with the COBRA set-up since then.

The discrepancies observed for the ^{152}Eu γ lines are most likely caused by an inaccurately calibrated activity of the radioactive source as well as a primary particle generator in Geant4 not able to correctly reproduce the decay characteristics of ^{152}Eu . The insufficiencies of the data that is used by the decay generator have also been seen in the comparison of the simulated decay characteristics with literature values for different nuclides of the decay chains. Since the decay databases have been updated to the ENSDF 2012 data set in Geant4 10.0, efforts should be put in the migration of VENOM to this new Geant4 release. To further increase the reliability of the MC model, the simulation should be compared to measurements of additional calibrated radioactive sources. As far as possible these sources should be voluminous and at least one nuclide with a low energetic γ ray emission should be contained for a check of the thickness of the outer contact. To a certain extent this could be realised by producing a source with a mixture of different chemicals containing known amounts of naturally occurring radioactive isotopes of lutetium, lanthanum and potassium (compare [IHM⁺97]).

The results of this work show that the DLB has already a remarkable high sensitivity for the detection of traces of radioactivity despite its location above ground. As it is recommended in this work, the extension of the anti cosmics veto detector is currently implemented. This will provide a further suppression of the remaining background and allow to achieve lower detection limits in the same acquisition time.

8. *Summary and outlook*

Acknowledgements / Danksagung

During the time I spend at Physik EIV, I met many brilliant and kind people working for different projects and experiments. Since the mother tongue of some of those people is not German, I would like to thank them first.

Many thanks to my COBRA colleagues for the interesting collaboration meetings and enjoyable stays at Dresden, Erlangen, Freiburg, Hamburg and Prague. With your hard work during the long and exhausting LNCS shifts you made the realisation of the time-consuming relocation of the R&D set-up and the resulting impressive improvements of the experiment possible in the first place.

Herrn Prof. Dr. Claus Gößling danke ich sehr, dass er mir die Möglichkeit zur Promotion gegeben hat. Zu dem stets sehr angenehmen und produktiven Arbeitsklima am Lehrstuhl Physik EIV haben vor allem sein großes Vertrauen in uns, sowie die Anerkennung unserer Arbeit beigetragen, welche er uns stets entgegengebracht hat.

Prof. Dr. Kai Zuber möchte ich dafür danken, dass er das COBRA Experiment vor einigen Jahren initiiert und mit seinem Herzblut den Grundstein für unsere Arbeit gelegt hat. Insbesondere möchte ich ihm dafür danken, dass er die Zweitkorrektur meiner Arbeit übernommen hat, obwohl sein Terminkalender immer lange im Voraus überfüllt ist.

Bei Frau Dr. Bärbel Siegmann möchte ich mich bedanken, dass sie sich bereit erklärt hat, als Vertreterin der wissenschaftlichen Mitarbeiter Teil der Prüfungskommission zu sein. Neben der guten Zusammenarbeit mit ihr während meiner Zeit als Assistent im Fortgeschrittenen-Praktikum hat sie mich häufig durch leihweises zur Verfügung stellen von Geräten und Materialien aus dem Praktikumsfundus unterstützt. Einige Messungen wären ohne dies überhaupt nicht möglich gewesen.

Dr. Oliver Schulz hat mich mit großem Engagement während meiner Diplomarbeit betreut. Ich durfte sehr viel von ihm lernen und möchte mich für die wirklich sehr gute und freundschaftliche Zusammenarbeit während unserer gemeinsamen Zeit am Lehrstuhl bedanken.

PD Dr. Reiner Klingenberg bin ich aufgrund der vielen kleinen und größeren Diskussionen und Ratschläge insbesondere in Bezug auf Statistik sowie der sehr guten Zusammenarbeit im Bereich des Strahlenschutzes bei Physik EIV dankbar.

Markus Alex hat mich als Techniker und IT-Beauftragter des Lehrstuhls auf vielfältigste Weise unterstützt. Danke für die vielen Diskussionen über zu lö-

Acknowledgements / Danksagung

sende technische Probleme und die schnellen Reaktionen auf auftretende IT-Probleme fern jeglicher Arbeitszeiten. Danke für die vielen zusätzlichen Stunden, die du für uns aufgebracht hast. Besonders geht hier mein Dank an das Team aus Oliver Schulz, Markus Alex und Reiner Klingenberg, die den Hadoop-Cluster aufgesetzt und stets am Laufen gehalten haben, wenn auch so einige Hürden zu nehmen waren. Erst dadurch konnten die aufwändigen MC-Simulationen in dieser Arbeit umgesetzt werden.

Meinen COBRA-Kollegen möchte ich für die gute Zusammenarbeit und das tolle Klima in der Gruppe danken. Mein Dank geht dabei auch an die Bachelor- und Master-Studenten, deren Arbeit ich während meiner Promotion begleiten durfte. Insbesondere danke ich dabei Christian Nitsch und Thomas Quante, die viel zur Verbesserung der DLB beigetragen haben und diese Arbeit fortführen.

Dr. Matthias Junker hat uns sehr bei den aufwändigen Arbeiten am LNGS unterstützt und stets bei Problemen weitergeholfen. Ohne seine Dolmetschertätigkeit in den Werkstätten hätten wir das COBRA Set-Up so nicht realisieren können.

Die mechanischen Werkstätten der Fakultät Physik an der TU Dortmund unter der Leitung von Susanne Kralemann haben diese Arbeit mit der exzellenten Fertigung von Bauteilen und Konstruktionen in vielen Punkten unterstützt. Ich habe einiges bezüglich mechanischen Konstruktionen und den dazu notwendigen Zeichnungen gelernt. Insbesondere habe ich mich für die Erfüllung von etlichen komplizierten und vor allem kurzfristigen Fertigungswünschen zu bedanken. Herr Rudloff als Leiter des Konstruktionsbüros hat mir häufig Fragen zu Konstruktionen, Metallbau und Materialverarbeitung beantwortet, sodass ich vieles von ihm gelernt habe.

Jan Tebrügge, meinem Bruder Paul Neddermann und ganz besonders Dr. Tobias Köttig möchte ich für die viele Zeit und den Einsatz danken, die sie für das Gegenlesen meiner Arbeit aufgebracht haben.

Bei Tobias Köttig bedanke ich mich für die tolle Zeit, die wir während des Studiums und der Promotion zusammen verbracht haben. Es war mir stets eine Ehre mit so einem engagierten Menschen bei COBRA zusammen arbeiten zu dürfen. Er hat mich insbesondere bei den Anfängen der Simulationsstudien mit seiner Hilfe unterstützt. Ich habe vieles von ihm gelernt, wofür ich ihm dankbar bin. Über die Zeit ist er ein sehr guter Freund geworden und ich bedauere sehr, dass wir uns nun eher selten treffen können.

Meinen Eltern möchte ich für die Unterstützung während meines gesamten Studiums danken, dass Sie mir immer geholfen haben, wenn ich es einmal brauchte und mich stets motivierten. Mein Dank geht auch an meinen Bruder für die vielen schönen Fachsimpeleien und Diskussionen.

Abschließend möchte ich einen sehr großen Dank an meine Frau Judith richten, die während des Verfassens dieser Arbeit jede Höhe und Tiefe miterlebt und mich, wo immer es ging, unterstützt hat. Sie hat stets an mein Ziel geglaubt und mich ermuntert, wenn ich es einmal nicht mehr gesehen habe.

A. Natural decay chains

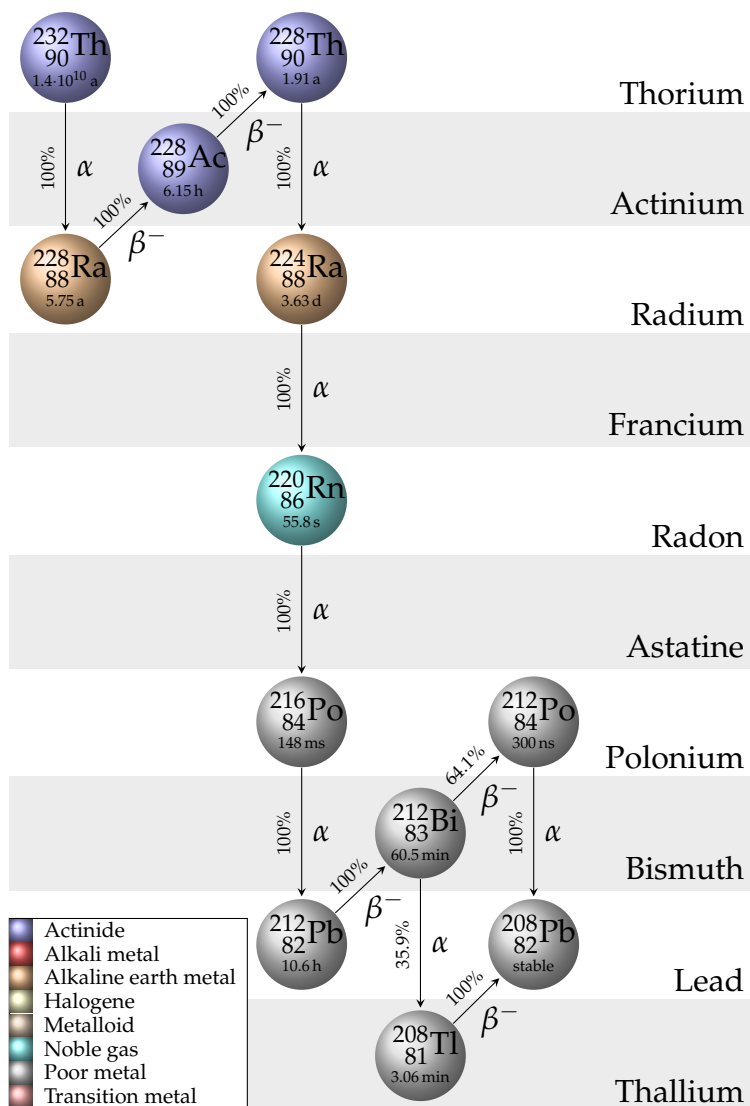


Figure A.1.: ^{232}Th decay chain. Data taken from [Lab13]. Decay channels with probability smaller than 0.1 % are omitted.

Design based on [Wik14]. Work released under CC-BY-SA-3.0¹.

¹This work is licensed under the Creative Commons Attribution-ShareAlike 3.0 Unported License. To view a copy of this license, visit <http://creativecommons.org/licenses/by-sa/3.0/> or send a letter to Creative Commons, 444 Castro Street, Suite 900, Mountain View, California, 94041, USA.

A. Natural decay chains

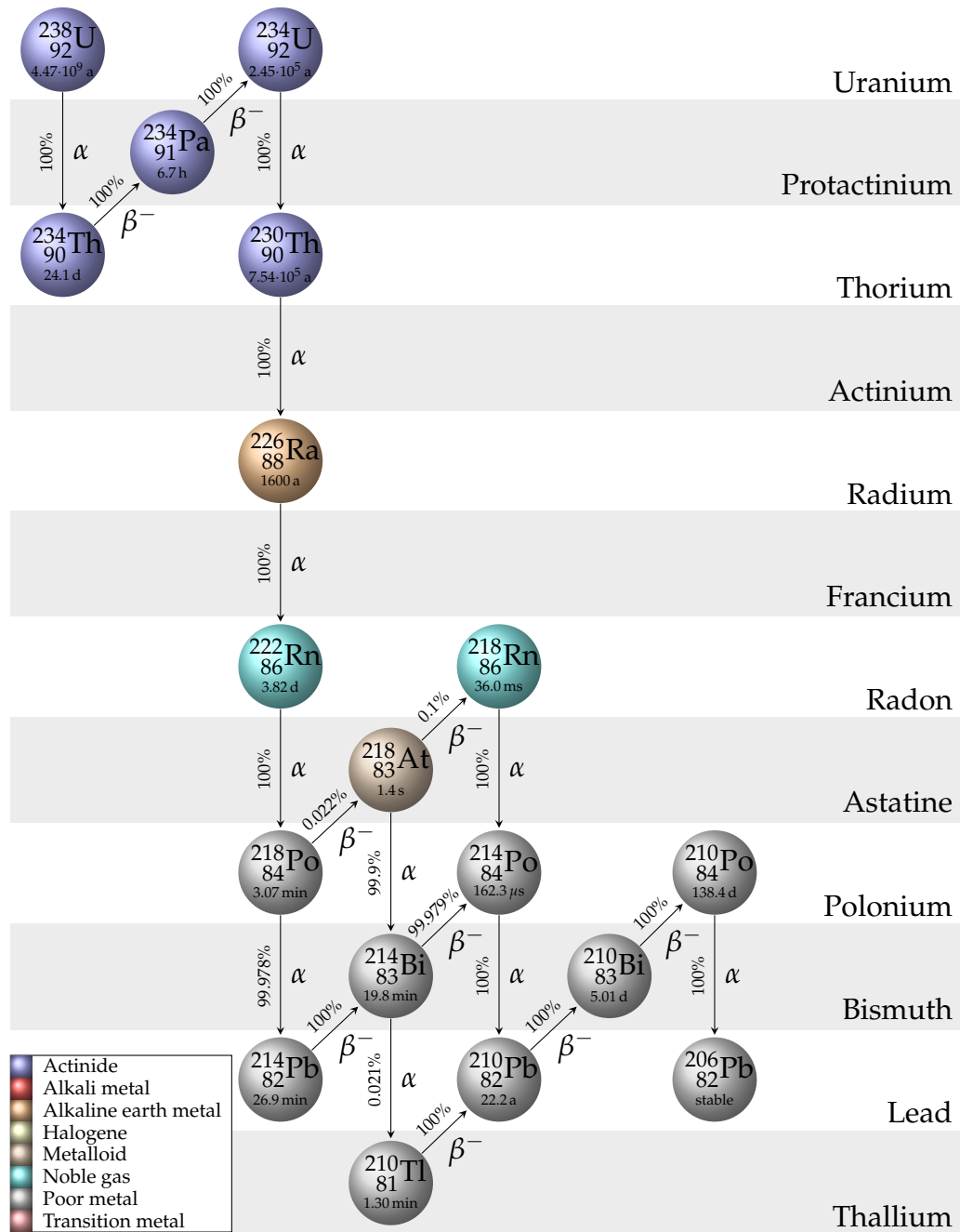


Figure A.2.: ^{238}U decay chain. Data taken from [Lab13]. Decay channels with probability smaller than 0.01 % are omitted.

^{234}Th actually decays to the metastable state of ^{234}Pa . ^{234m}Pa has a half life of 1.159 min, decaying to 0.15 % by IT to ^{234}Pa and to 99.85 % by β decay to ^{234}U . ^{234}Pa decays to 100 % by β decay to ^{234}U as well. This can not be displayed in this graphic scheme and is left out.

Design based on [Wik14]. Work released under CC-BY-SA-3.0¹.

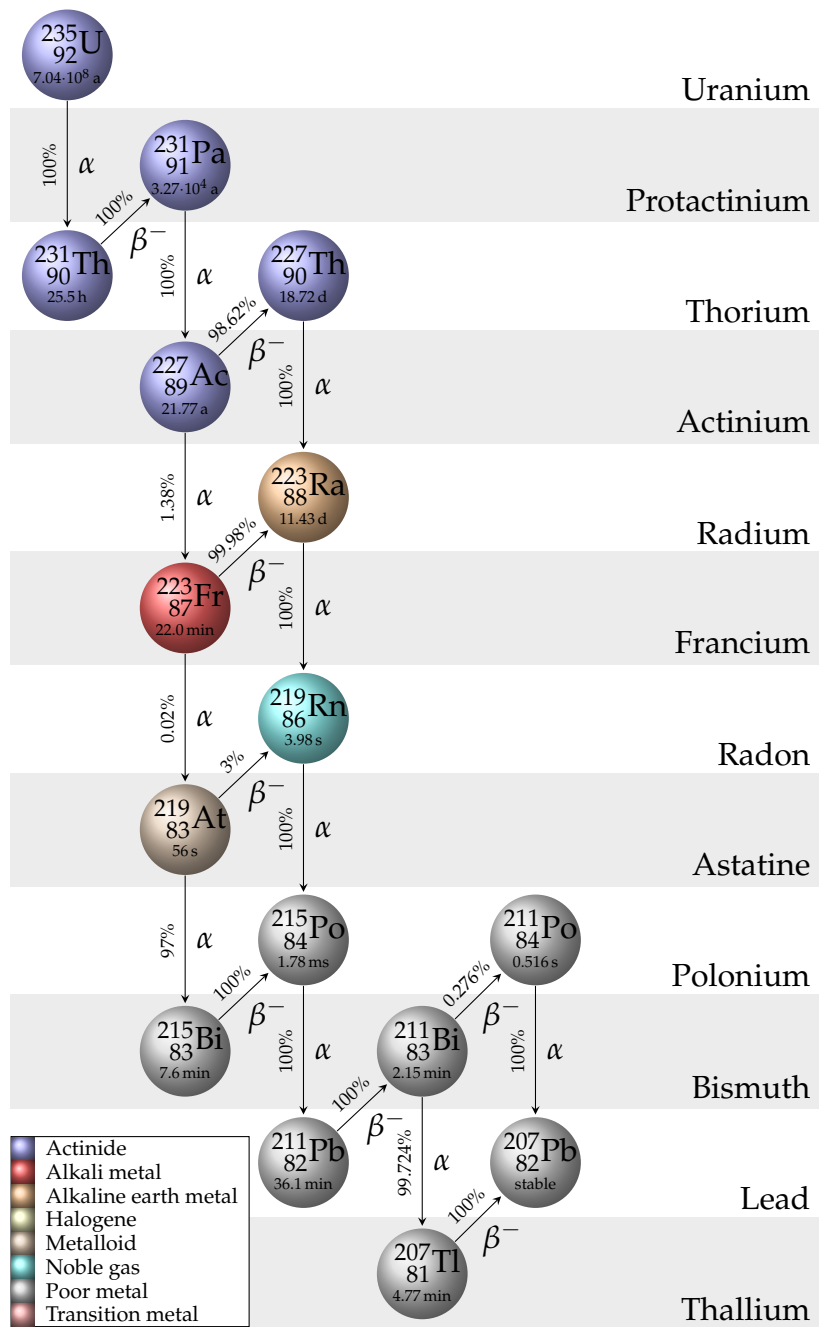
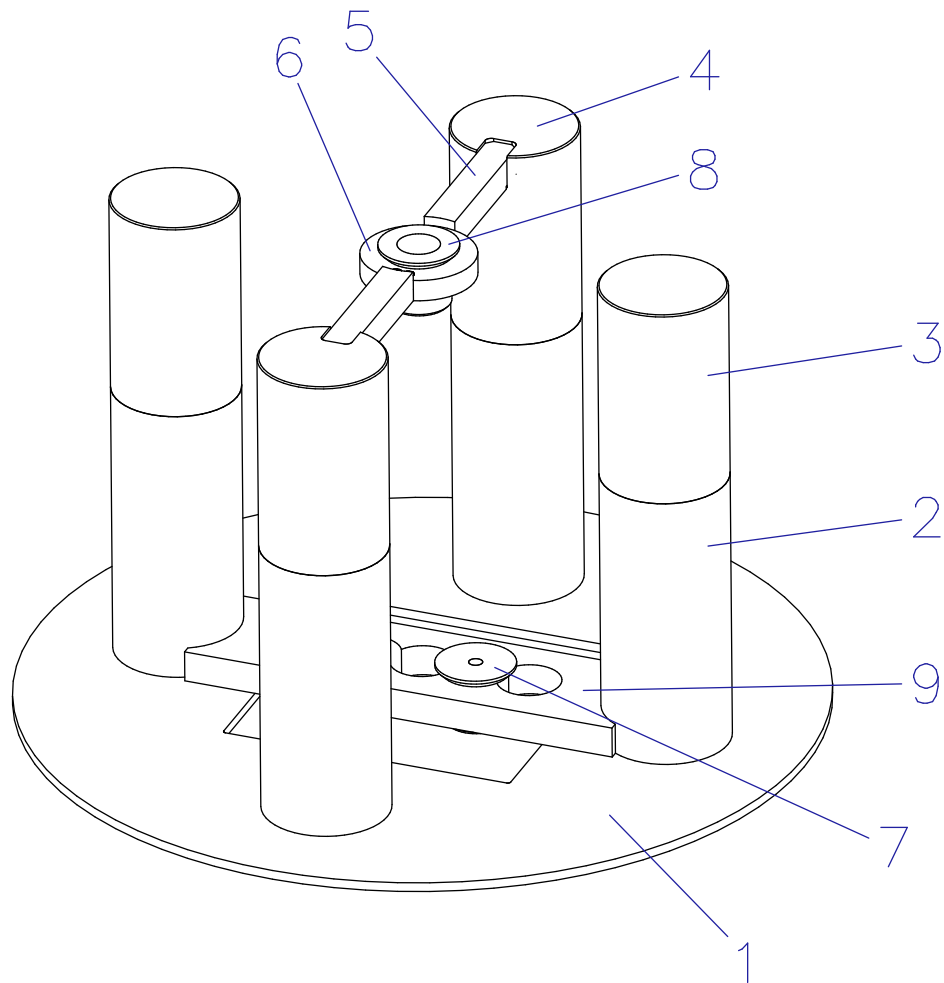


Figure A.3.: ^{235}U decay chain. Data taken from [Lab13], for ^{227}Th from [Fir96]. Decay channels with probability smaller than 0.01 % are omitted. Design based on [Wik14]. Work released under CC-BY-SA-3.0¹.

A. Natural decay chains

B. CAD drawings




Zeichnungsnr.			Beschreibung	
E4-DLB-CuExt			inkl. Quellen-Halterung	
Material		Serien-Nr.		
Masse		Baugruppen-Nr.		
Oberfläche		Datum		
Maßstab	Format	Menge		
1:2	A4			
			Bezeichnung	
			DLB-Cu-Extender	

Figure B.2.: Mechanical drawing of the shielding extender used for the measurements of the simulation studies in chapter 5. Part 5 and 6 as well as 9 are different removable source holder structures made of POM. 7 and 8 are insets for different radioactive sources. Drawing not to scale. Design of all parts by the author.

C. Exemplary data evaluation report

TU Dortmund

Experimentelle Physik IV

Evaluation report

Sample	Ferro conductive silver, silver settled
Mass	(0.2004 ± 0.0010) kg
Evaluation standard	DIN ISO 11929:2011
Measurement procedure	Low-level γ ray spectrometry
Measurand	Specific activity
Lifetime	1786872.1 s
Starttime	Fri Dec 2 17:53:17 2011 UTC

Isotope	A_{spec}	$u(A_{\text{spec}})$	\hat{A}_{spec}	$u(\hat{A}_{\text{spec}})$	$A_{\text{spec}}^<$	$A_{\text{spec}}^>$	A_{spec}^*	$A_{\text{spec}}^{\#}$	Remarks
Ag-108m	101.0	3.9	101.0	3.9	93.4	108.5	3.2	6.7	
Ag-110m	4.8	2.3	4.9	2.2	0.6	9.1	3.5	7.5	
Th-234	-2.3	4.8	3.1	2.5	0.0	8.0	7.9	16.9	
Pa-234m	-30	320	240	190	0	600	520	1100	
Ra-226	55	53	69	43	0	145	85	175	186keV & corr.
Pb-214	5	12	10.8	7.6	0.0	25.1	18.2	37.8	
Bi-214	-14	49	34	27	0	86	84	178	
Pb-210	-26000	15000	5800	5200	0	16100	24100	49700	
Ac-228	6	18	16	12	0	39	29	62	
Pb-212	3.2	5.9	6.0	4.2	0.0	13.7	9.5	19.6	
Bi-212	-10	140	105	80	0	259	224	494	
Tl-208	-2.7	2.8	1.5	1.3	0.0	4.0	5.4	11.2	
U-235	1.9	1.8	2.3	1.5	0.0	4.9	2.9	6.0	186keV & corr.
K-40	-39	48	27	23	0	71	79	165	
Cs-137	1.0	1.9	1.9	1.3	0.0	4.4	3.0	6.4	
Co-60	0.8	2.1	1.9	1.4	0.0	4.5	4.4	9.4	

Specific activity A_{spec} in mBq/kg

\hat{A}_{spec} \leftrightarrow most probable value

$A_{\text{spec}}^<$ \leftrightarrow lower limit of coverage interval

$A_{\text{spec}}^>$ \leftrightarrow upper limit of coverage interval

$u(x)$ \leftrightarrow (standard) uncertainty of x with $k = 1$

A_{spec}^* \leftrightarrow decision threshold / critical limit

$A_{\text{spec}}^{\#}$ \leftrightarrow detection limit

C. Exemplary data evaluation report

Coverage interval & upper limit with $k_{1-\frac{\gamma}{2}} = 1.96 \leftrightarrow 95.0\%$ coverage probability

Decision threshold / critical limit with $k_{1-\alpha} = 1.645 \leftrightarrow 5.0\%$ false positive decision probability

Detection limit with $k_{1-\beta} = 1.645 \leftrightarrow 5.0\%$ false negative decision probability

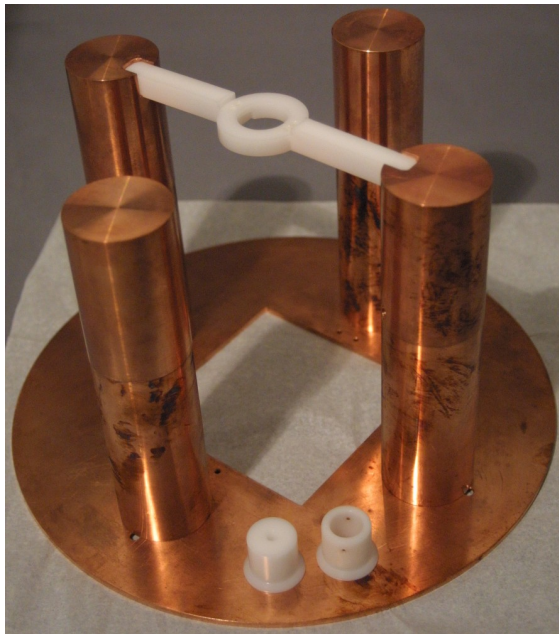
Lower and upper limit not according to DIN ISO 11929:2011 (probabilistically symmetric coverage interval, notation y^{\triangleleft} and y^{\triangleright}) but as proposed by K. Weise et al. / PROGRESS IN RADIATION PROTECTION FS-2013-167-AKSIGMA (Fachverband für Strahlenschutz e. V.) (shortest coverage interval, notation $y^<$ and $y^>$).

T. Neddermann
till.neddermann@tu-dortmund.de

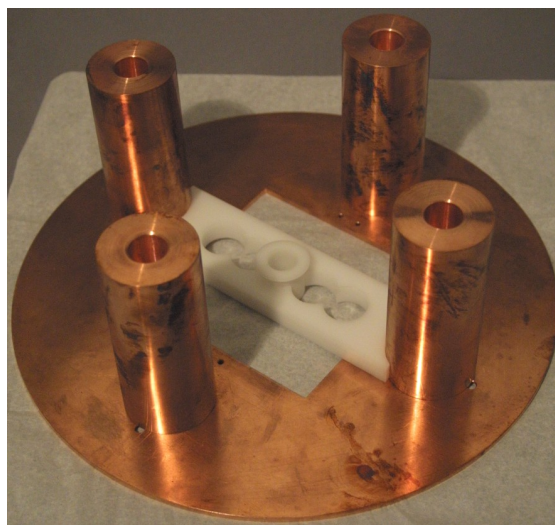
June 10, 2013

1

D. MC geometry optimisation



(a) High shielding extender.



(b) Low shielding extender.

Figure D.1.: Shielding extender and source holders used in the different geometry optimisation measurements. The upper part of the columns can be removed to reduce the height for measurements with the source placed between the columns at the base plate (Figure D.1b).

D. MC geometry optimisation

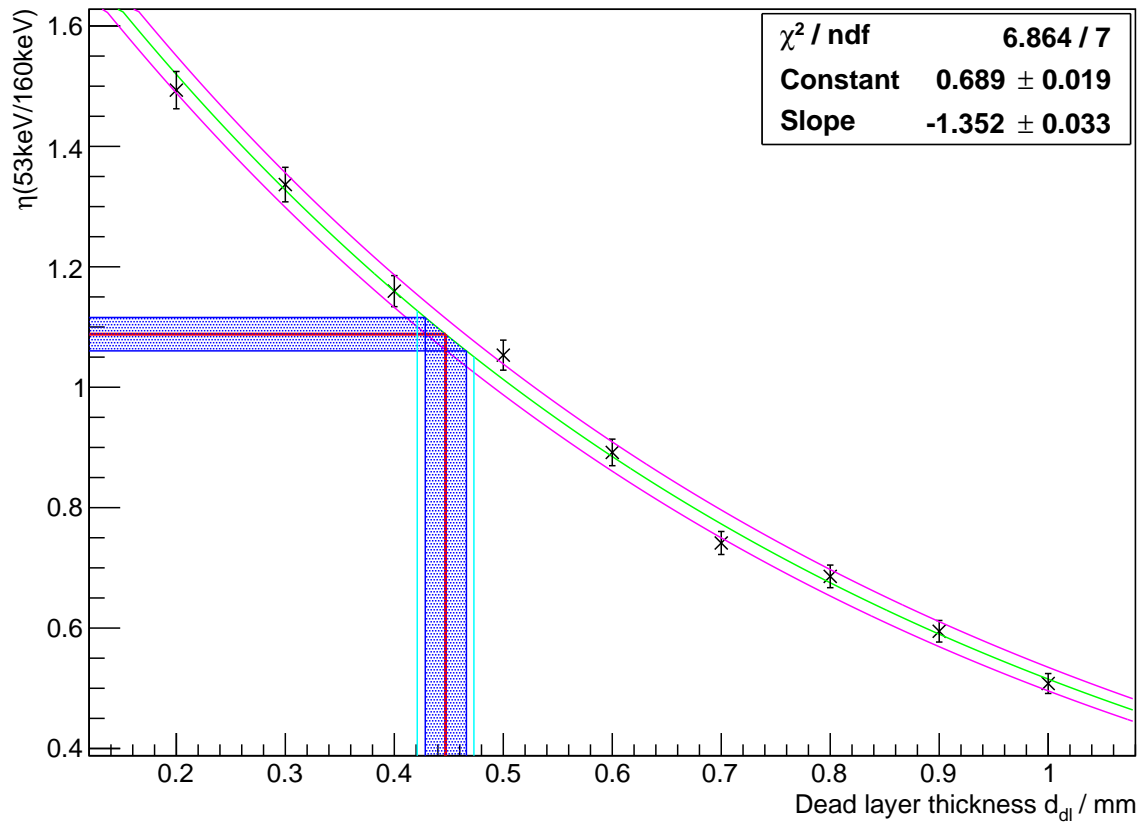


Figure D.2.: Dead layer thickness optimisation with ^{133}Ba using the 53.2 keV and 160.6 keV line. The simulated data and their statistical uncertainties are plotted. The fit to the data is shown in green (-) and its uncertainties in magenta (-). The measured peak ratio is marked in red (-) with the uncertainty in blue (-). The uncertainty of the resulting dead layer thickness d is derived from the measurement as well as the fit and is shown in cyan (-).

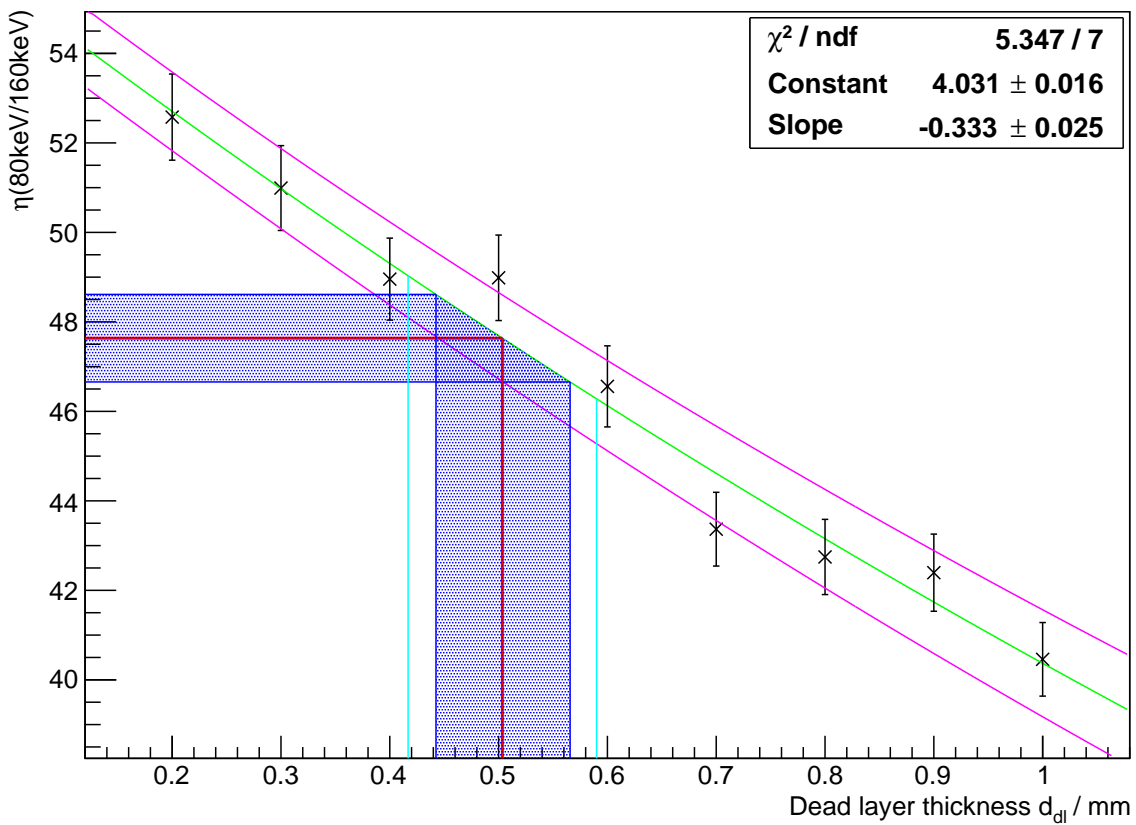
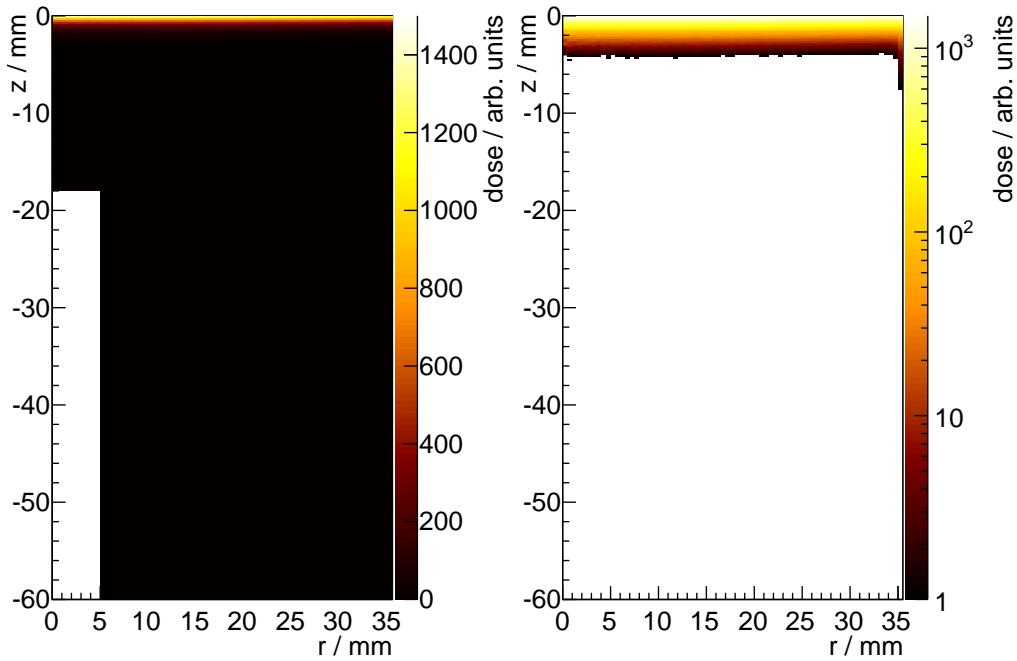


Figure D.3.: Dead layer thickness optimisation with ^{133}Ba using the 80 keV region and 160.6 keV line. For the legend see Figure D.2.

D. MC geometry optimisation

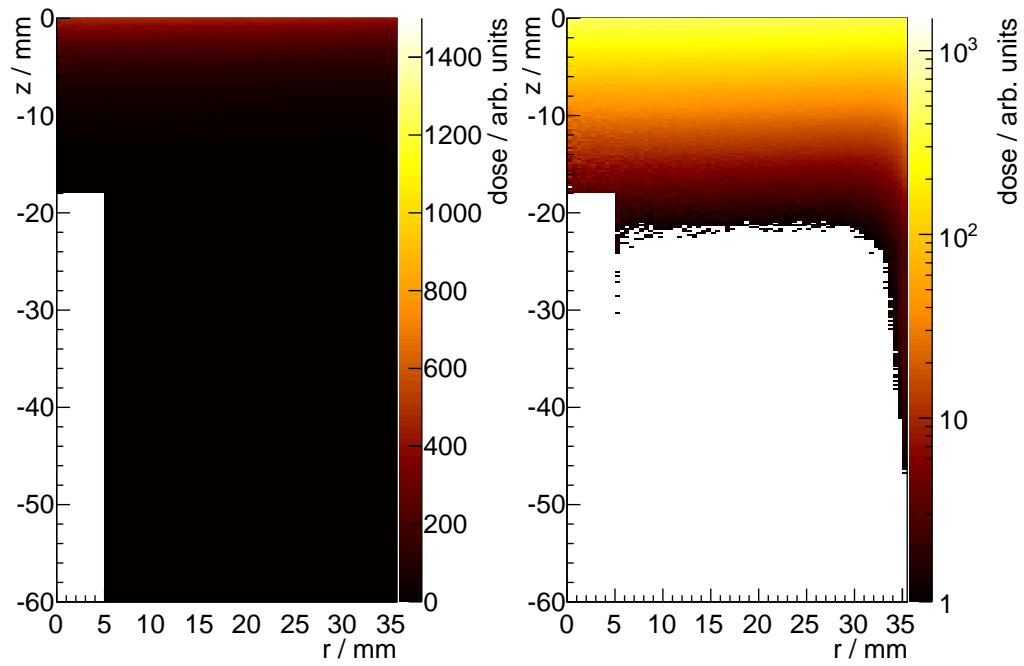
E. Dose distribution in HPGe detector



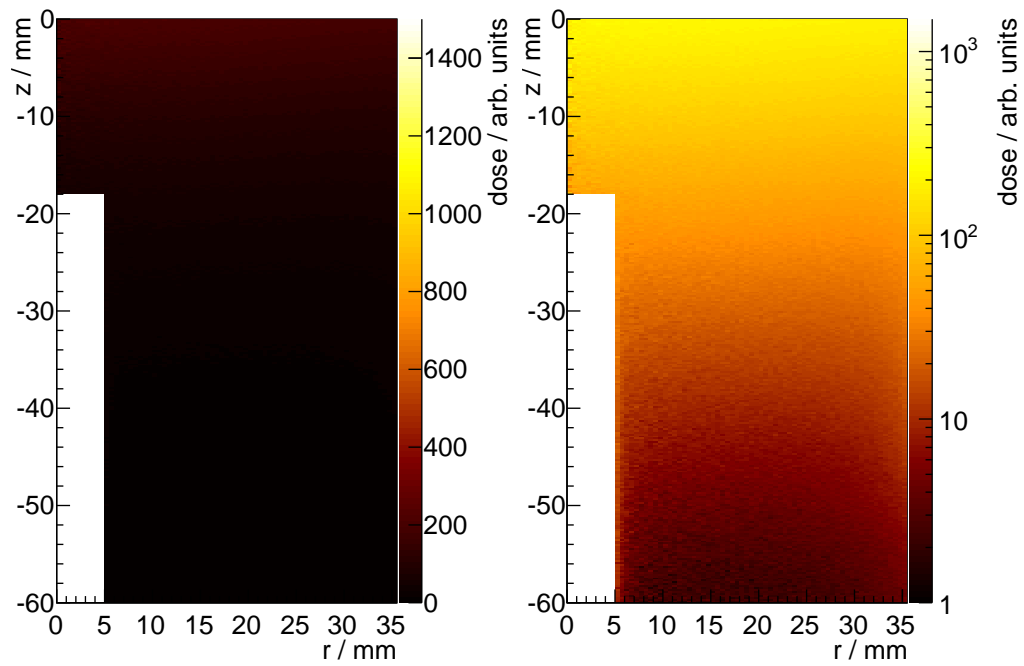
(a) 50 keV γ rays.

Figure E.1.: Simulated dose distributions within the used HPGe crystal for different γ ray energies. Radial cross section displayed. Computed by PENELOPE, visualised using ROOT. The complete detector (endcap, holder, etc.) was implemented, the cross section of the copper shielding layer was assumed as circular. Calibration source placed 74 mm above the detector endcap. γ rays simulated only within a cone towards the detector. In Figure E.1b scattering of γ rays at the holder structure and detector shielding is clearly visible.

E. Dose distribution in HPGe detector

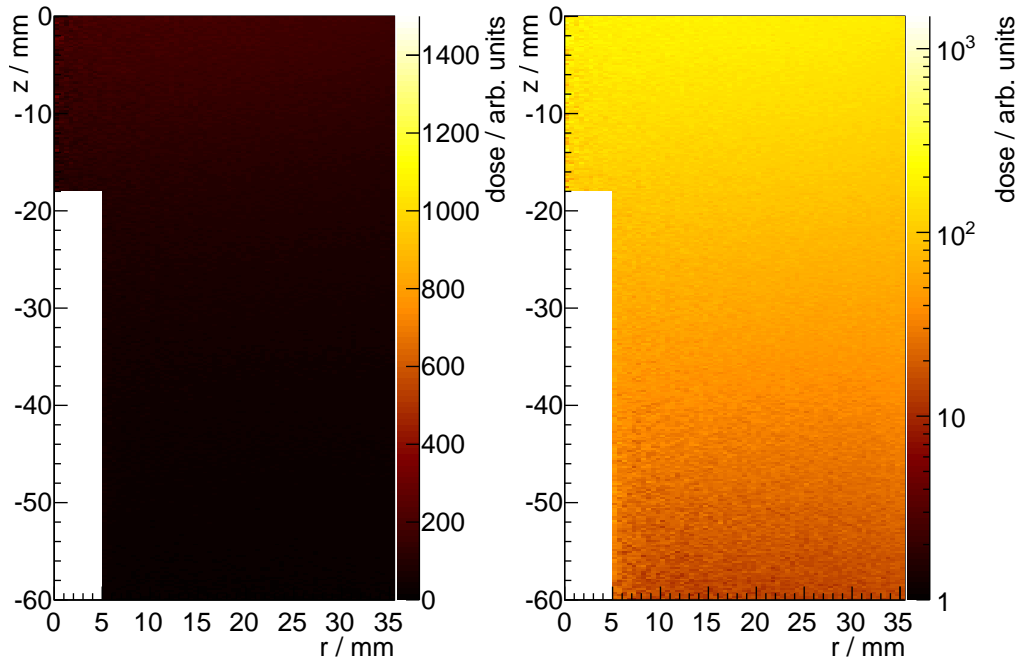


(b) 100 keV γ rays.

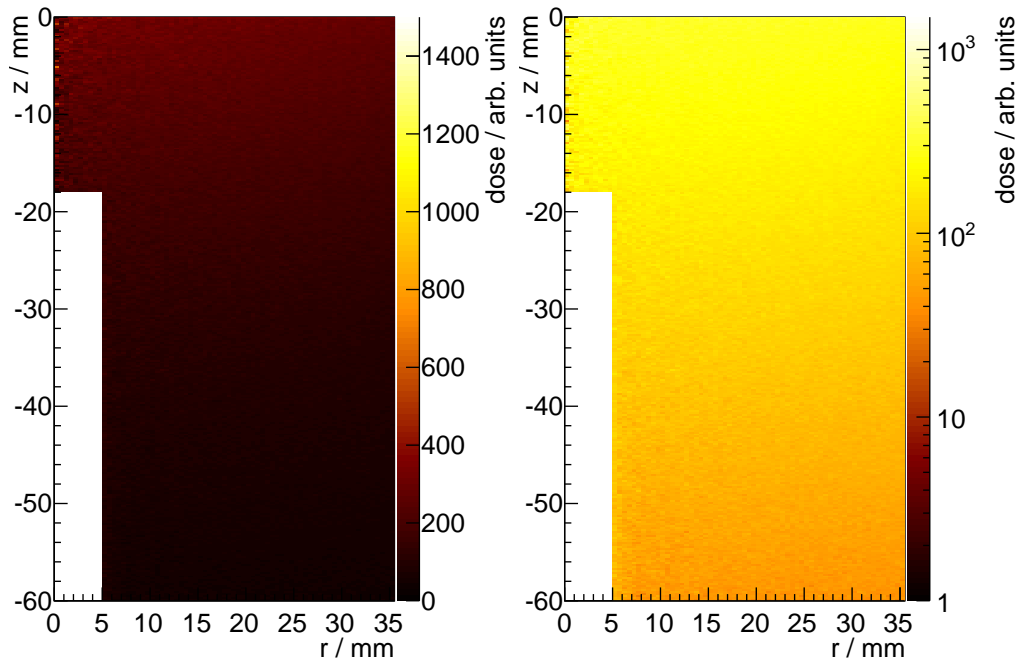


(c) 200 keV γ rays.

Figure E.1.: Simulated dose distributions in the HPGe detector. (Continued)



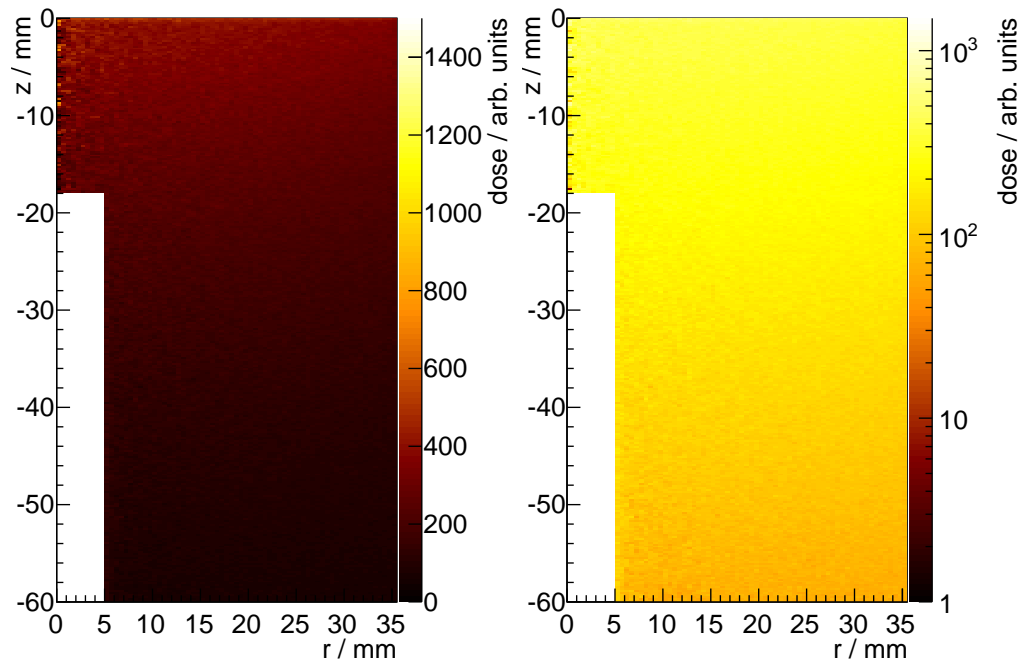
(d) 400 keV γ rays.



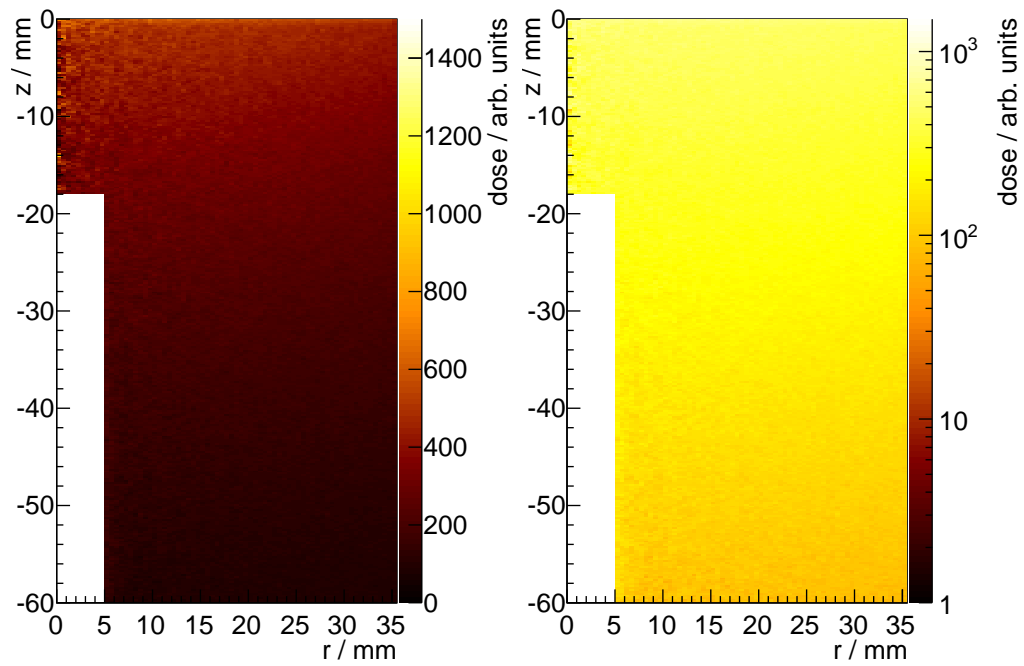
(e) 1000 keV γ rays.

Figure E.1.: Simulated dose distributions in the HPGe detector. (Continued)

E. Dose distribution in HPGe detector



(f) 1500 keV γ rays.



(g) 2000 keV γ rays.

Figure E.1.: Simulated dose distributions in the HPGe detector. (Continued)

F. GRDM γ ray emission probabilities

Table F.1.: GRDM γ ray emission probabilities in Geant4 9.5.p01 and deviations to literature. Energies E and literature data from [Lab13]. Uncertainties given with $k = 1$. Highlighted if correction factor is not compatible with 1 (95 % CL, $k = 2$). Deviation calculated as $\frac{p_{\text{lit}} - p_{\text{sim}}}{p_{\text{lit}}} \times 100$. Correction factor f_{corr} calculated as $\frac{p_{\text{sim}}}{p_{\text{lit}}}$ can be used for GASetIsotope in GeAna (compare section 4.4).

Nuclide	E / keV	p_{sim} / %	p_{lit} / %	dev. / %	f_{corr}
^{228}Ac	911.20	24.934(50)	26.2(8)	-4.8(30)	0.952(30)
^{228}Ac	964.79	5.132(23)	4.99(17)	2.8(36)	1.028(36)
^{228}Ac	968.96	15.257(39)	15.9(5)	-4.0(31)	0.960(31)
^{108m}Ag	433.94	90.496(96)	90.1(6)	0.44(68)	1.0044(68)
^{108m}Ag	614.28	90.972(96)	90.5(16)	0.5(18)	1.005(18)
^{108m}Ag	722.91	91.077(96)	90.8(16)	0.3(18)	1.003(18)
^{110m}Ag	657.76	94.446(98)	94.38(8)	0.07(14)	1.0007(14)
^{241}Am	59.54	35.899(60)	35.92(17)	-0.06(51)	0.9994(51)
^{133}Ba	53.16	2.1175(65)	2.14(3)	-1.1(15)	0.989(15)
^{133}Ba	79.61	2.5847(72)	2.65(5)	-2.5(19)	0.975(19)
^{133}Ba	81.00	33.326(26)	32.9(3)	1.29(93)	1.0129(93)
^{133}Ba	160.61	0.6113(35)	0.638(4)	-4.18(82)	0.9582(82)
^{133}Ba	223.24	0.4354(30)	0.453(3)	-3.88(91)	0.9612(91)
^{133}Ba	276.40	6.857(12)	7.16(5)	-4.24(69)	0.9576(69)
^{133}Ba	302.85	18.015(19)	18.34(13)	-1.77(71)	0.9823(71)
^{133}Ba	356.01	59.773(35)	62.05(19)	-3.67(30)	0.9633(30)
^{133}Ba	383.85	8.794(14)	8.94(6)	-1.64(68)	0.9836(68)
^{212}Bi	1620.74	1.490(13)	1.51(3)	-1.3(22)	0.987(22)
^{214}Bi	1764.49	15.421(40)	15.31(5)	0.73(42)	1.0073(42)
^{214}Bi	2204.21	5.103(23)	4.913(23)	3.86(67)	1.0386(67)
^{57}Co	122.06	85.942(93)	85.51(6)	0.50(13)	1.0050(13)
^{57}Co	136.47	10.325(33)	10.71(15)	-3.6(14)	0.964(14)
^{60}Co	1173.23	99.856(45)	99.85(3)	0.006(54)	1.00006(54)
^{60}Co	1332.49	99.986(45)	99.9826(6)	0.004(45)	1.00004(45)
^{134}Cs	604.72	97.621(99)	97.63(8)	-0.01(13)	0.9999(13)
^{137}Cs	661.66	84.852(42)	84.99(20)	-0.16(24)	0.9984(24)
^{152}Eu	121.78	28.240(24)	28.41(13)	-0.60(47)	0.9940(47)
^{152}Eu	244.70	7.701(13)	7.55(4)	2.01(57)	1.0201(57)
^{152}Eu	295.94	0.4447(30)	0.442(3)	0.61(96)	1.0061(96)
^{152}Eu	344.28	26.559(23)	26.59(12)	-0.11(46)	0.9989(46)

Continued on next page.

F. GRDM γ ray emission probabilities

Table F.1.: (Continued.)

Nuclide	E / keV	p_{sim} / %	p_{lit} / %	dev. / %	f_{corr}	
^{152}Eu	367.79	0.8703(42)	0.862(5)	0.97(76)	1.0097(76)	
^{152}Eu	411.12	2.2392(67)	2.238(10)	0.06(54)	1.0006(54)	
^{152}Eu	443.96	3.1658(80)	3.120(28)	1.47(95)	1.0147(95)	
^{152}Eu	778.90	12.944(16)	12.97(6)	-0.20(48)	0.9980(48)	
^{152}Eu	867.38	4.2567(93)	4.243(23)	0.32(59)	1.0032(59)	
^{152}Eu	964.08	14.644(18)	14.50(6)	0.99(44)	1.0099(44)	
^{152}Eu	1085.84	10.212(15)	10.13(6)	0.81(62)	1.0081(62)	
^{152}Eu	1089.74	1.7363(59)	1.73(1)	0.36(68)	1.0036(68)	
^{152}Eu	1112.08	13.644(17)	13.41(6)	1.74(48)	1.0174(48)	
^{152}Eu	1212.95	1.4228(54)	1.416(9)	0.48(75)	1.0048(75)	
^{152}Eu	1299.14	1.6237(57)	1.633(9)	-0.57(65)	0.9943(65)	
^{152}Eu	1408.01	21.006(21)	20.85(8)	0.75(40)	1.0075(40)	
^{40}K	1460.82	10.498(33)	10.55(11)	-0.5(11)	0.995(11)	
^{234m}Pa	1001.03	0.9180(96)	0.847(8)	8.4(16)	1.084(16)	
^{210}Pb	46.54	3.944(20)	4.252(40)	-7.24(99)	0.9276(99)	
^{212}Pb	238.63	42.739(66)	43.6(5)	-2.0(12)	0.980(12)	
^{214}Pb	295.22	18.786(44)	18.414(36)	2.02(31)	1.0202(31)	
^{226}Ra	186.21	3.212(18)	3.555(19)	-9.65(70)	0.9035(70)	
^{234}Th	63.30	4.882(22)	3.75(8)	30.2(29)	1.302(29)	
^{234}Th	92.38	2.666(17)	2.18(19)	22(11)	1.22(11)	
^{234}Th	92.80	2.748(17)	2.15(19)	28(12)	1.28(12)	
^{208}Tl	583.19	84.930(93)	85.0(3)	-0.08(37)	0.9992(37)	
^{208}Tl	860.53	12.520(36)	12.4(1)	0.97(87)	1.0097(87)	
^{208}Tl	2614.51	99.84(10)	99.755(4)	0.09(10)	1.0009(10)	
^{235}U	143.77	0.9332(97)	10.94(6)	-91.47(10)	0.0853(10)	} original
^{235}U	163.36	23.522(49)	5.08(3)	363.0(29)	4.630(29)	
^{235}U	185.72	4.971(23)	57.0(3)	-91.278(61)	0.087 22(61)	
^{235}U	205.32	23.349(49)	5.02(3)	365.1(30)	4.651(30)	
^{235}U	143.77	10.299(32)	10.94(6)	-5.86(60)	0.9414(60)	} corrected
^{235}U	163.36	4.923(23)	5.08(3)	-3.10(72)	0.9690(72)	
^{235}U	185.72	53.800(74)	57.0(3)	-5.61(52)	0.9439(52)	
^{235}U	205.32	4.896(23)	5.02(3)	-2.47(73)	0.9753(73)	

Publications

Articles

M. Fritts, J. Tebrügge, ..., T. Neddermann, ...

Pulse-shape discrimination of surface events in CdZnTe detectors for the COBRA experiment

Nuclear Instruments and Methods in Physics Research Section A

2014

<http://dx.doi.org/10.1016/j.nima.2014.02.038>

J. Ebert, M. Fritts, ..., T. Neddermann, ...

Current Status and Future Perspectives of the COBRA Experiment

Advances in High Energy Physics

Volume 2013 (2013), Article ID 703572

<http://dx.doi.org/10.1155/2013/703572>

Conference Talks

T. Neddermann on behalf of the COBRA collaboration

Status des COBRA-Experiments

Particle Physics DPG Spring Meeting

February 27 – March 02 2012, Göttingen (Germany)

T. Neddermann

A Low Background Germanium Facility under Heavy Shielding located at the Surface

IEEE Nuclear Science Symposium (NSS)

October 24 – 28 2011, Valencia (Spain)

T. Neddermann

Die DLB: Eine oberirdische Low Background Germanium Facility mit großer Überdeckung

Canberra Fachgespräch

October 05 – 07 2011, Gelsenkirchen (Germany)

Publications

T. Neddermann

The DLB: A non-underground low background germanium facility under heavy shielding

10th CELLAR Meeting

October 14 – 15 2010, Dresden (Germany)

T. Neddermann

Die Dortmund-Low-Background-HPGe-Facility - Material Screening für das COBRA-Experiment

Particle Physics DPG Spring Meeting

March 15 – 19 2010, Bonn (Germany)

Conference Poster

T. Neddermann

A Heavy Shielded Low Background Germanium Facility Located Above-ground

Advanced WE-Heraeus Physics School on Ionising Radiation and Protection of Man

August 10 – 19 2012, Bad Honnef (Germany)

T. Neddermann

A non-underground Low Background Germanium Facility under Heavy Shielding

International School for Astroparticle Physics (ISAPP)

July 13 – 22 2010, Zaragoza (Spain)

T. Neddermann

Set-up of an Overground Low Background Germanium Facility under Heavy Shielding

IEEE Nuclear Science Symposium (NSS)

October 19 – 25 2008, Dresden (Germany)

Bibliography

- [AAA⁺03] AGOSTINELLI, S. ; ALLISON, J. ; AMAKO, K. et al.: Geant4 — a simulation toolkit. In: *Nuclear Instruments and Methods in Physics Research Section A: Accelerators, Spectrometers, Detectors and Associated Equipment* 506 (2003), No. 3, 250–303. [http://dx.doi.org/10.1016/S0168-9002\(03\)01368-8](http://dx.doi.org/10.1016/S0168-9002(03)01368-8). – DOI 10.1016/S0168-9002(03)01368-8. – ISSN 0168-9002
- [AAA⁺12] APRILE, E. ; ARISAKA, K. ; ARNEODO, F. et al.: The XENON100 dark matter experiment. In: *Astroparticle Physics* 35 (2012), No. 9, 573 - 590. <http://dx.doi.org/10.1016/j.astropartphys.2012.01.003>. – DOI 10.1016/j.astropartphys.2012.01.003. – ISSN 0927-6505
- [AAA⁺13] ACKERMANN, K.-H. ; AGOSTINI, M. ; ALLARDT, M. et al.: The Gerda experiment for the search of $0\nu\beta\beta$ decay in ^{76}Ge . In: *The European Physical Journal C* 73 (2013), No. 3, 1-29. <http://dx.doi.org/10.1140/epjc/s10052-013-2330-0>. – DOI 10.1140/epjc/s10052-013-2330-0. – ISSN 1434-6044
- [AAB⁺09] ALIMONTI, G. ; ARPESELLA, C. ; BACK, H. et al.: The Borexino detector at the Laboratori Nazionali del Gran Sasso. In: *Nuclear Instruments and Methods in Physics Research Section A: Accelerators, Spectrometers, Detectors and Associated Equipment* 600 (2009), No. 3, 568 - 593. <http://dx.doi.org/10.1016/j.nima.2008.11.076>. – DOI 10.1016/j.nima.2008.11.076. – ISSN 0168-9002
- [AAB⁺12] AUGER, M. ; AUTY, D. J. ; BARBEAU, P. S. et al.: The EXO-200 detector, part I: detector design and construction. In: *Journal of Instrumentation* 7 (2012), No. 05, P05010. <http://dx.doi.org/10.1088/1748-0221/7/05/P05010>. – DOI 10.1088/1748-0221/7/05/P05010
- [ABB⁺02] ARPESELLA, C. ; BACK, H. O. ; BALATA, M. et al.: Measurements of extremely low radioactivity levels in BOREXINO. In: *Astroparticle Physics* 18 (2002), No. 1, 1 - 25. [http://dx.doi.org/10.1016/S0927-6505\(01\)00179-7](http://dx.doi.org/10.1016/S0927-6505(01)00179-7). – DOI 10.1016/S0927-6505(01)00179-7. – ISSN 0927-6505
- [ABB⁺09] ANGLOHER, G. ; BAUER, M. ; BAVYKINA, I. et al.: Commissioning run of the CRESST-II dark matter search. In:

BIBLIOGRAPHY

- Astroparticle Physics* 31 (2009), No. 4, 270 - 276. <http://dx.doi.org/10.1016/j.astropartphys.2009.02.007>. – DOI 10.1016/j.astropartphys.2009.02.007. – ISSN 0927–6505
- [ABC⁺92] AVIGNONE III, F. T. ; BRODZINSKI, R. L. ; COLLAR, J. I. et al.: Theoretical and experimental investigation of cosmogenic radioisotope production in germanium. In: *Nuclear Physics B - Proceedings Supplements* 28 (1992), No. 1, 280 - 285. [http://dx.doi.org/10.1016/0920-5632\(92\)90184-T](http://dx.doi.org/10.1016/0920-5632(92)90184-T). – DOI 10.1016/0920–5632(92)90184–T. – ISSN 0920–5632
- [Adv02] ADVANCED MEASUREMENT TECHNOLOGY, INC.: *ORTEC Software File Structure Manual for DOS and Windows® Systems*. Rev. E, 2002. www.ortec-online.com/download/ortec-software-file-structure-manual.pdf
- [Ale09] ALEX, Markus: *A microcontroller based solution for remote laboratory data acquisition and control*, TU Dortmund, Diploma thesis, 2009
- [ALV99] ASHRAFI, S. ; LIKAR, A. ; VIDMAR, T.: Precise modeling of a coaxial HPGe detector. In: *Nuclear Instruments and Methods in Physics Research Section A: Accelerators, Spectrometers, Detectors and Associated Equipment* 438 (1999), December, No. 2-3, 421–428. [http://dx.doi.org/10.1016/S0168-9002\(99\)00862-1](http://dx.doi.org/10.1016/S0168-9002(99)00862-1). – DOI 10.1016/S0168–9002(99)00862–1. – ISSN 01689002
- [BÅJ08] BOSON, Jonas ; ÅGREN, Göran ; JOHANSSON, Lennart: A detailed investigation of HPGe detector response for improved Monte Carlo efficiency calculations. In: *Nuclear Instruments and Methods in Physics Research Section A: Accelerators, Spectrometers, Detectors and Associated Equipment* 587 (2008), No. 2-3, 304 - 314. <http://dx.doi.org/10.1016/j.nima.2008.01.062>. – DOI 10.1016/j.nima.2008.01.062. – ISSN 0168–9002
- [BCK⁺03] BYUN, Jong I. ; CHOI, Yun H. ; KWAK, Seung I. et al.: An anticoincidence-shielded gamma-ray spectrometer for analysis of low level environmental radionuclides. In: *Applied Radiation and Isotopes* 58 (2003), No. 5, 579 - 583. [http://dx.doi.org/10.1016/S0969-8043\(03\)00023-X](http://dx.doi.org/10.1016/S0969-8043(03)00023-X). – DOI 10.1016/S0969–8043(03)00023–X. – ISSN 0969–8043
- [BDA⁺09] BRONIATOWSKI, A. ; DEFAY, X. ; ARMENGAUD, E. et al.: A new high-background-rejection dark matter Ge cryogenic detector. In: *Physics Letters B* 681 (2009), No. 4, 305 - 309. <http://dx.doi.org/10.1016/j.physletb.2009.10.036>. – DOI 10.1016/j.physletb.2009.10.036. – ISSN 0370–2693

- [Ber13] BERNAU, Yvonne: *Untersuchung der elektromagnetischen Abschirmung für das COBRA Experiment*, TU Dortmund, Bachelor's thesis, September 2013
- [Bet11] BETTINI, A.: Underground laboratories. In: *Nuclear Instruments and Methods in Physics Research Section A: Accelerators, Spectrometers, Detectors and Associated Equipment* 626-627, Supplement (2011), January, S64 - S68. <http://dx.doi.org/10.1016/j.nima.2010.05.017>. – DOI 10.1016/j.nima.2010.05.017. – ISSN 0168-9002
- [BHMS09] BUDJÁS, D. ; HEISEL, M. ; MANESCHG, W. et al.: Optimisation of the MC-model of a p-type Ge-spectrometer for the purpose of efficiency determination. In: *Applied Radiation and Isotopes* 67 (2009), No. 5, 706 - 710. <http://dx.doi.org/10.1016/j.apradiso.2009.01.015>. – DOI 10.1016/j.apradiso.2009.01.015. – ISSN 1872-9800. – 5th International Conference on Radionuclide Metrology - Low-Level Radioactivity Measurement Techniques ICRM-LLRMT'08
- [BHS⁺10] BERGER, M. J. ; HUBBELL, J. H. ; SELTZER, S. M. et al.: XCOM: *Photon Cross Section Database (version 1.5)*. Version: November 2010. <http://physics.nist.gov/xcom>, Accessed 2013-01-08. Website
- [BK74] BUNTING, R. L. ; KRAUSHAAR, J. J.: Short-lived radioactivity induced in Ge(Li) gamma-ray detectors by neutrons. In: *Nuclear Instruments and Methods* 118 (1974), No. 2, 565 - 572. [http://dx.doi.org/10.1016/0029-554X\(74\)90667-3](http://dx.doi.org/10.1016/0029-554X(74)90667-3). – DOI 10.1016/0029-554X(74)90667-3. – ISSN 0029-554X
- [BL12] BLOBEL, Volker ; LOHRMANN, Erich: *Statistische und numerische Methoden der Datenanalyse*. 2012 <http://www-library.desy.de/elbook.html>. – ISBN 978-3-935702-66-9
- [BLB⁺05] BÖHLKE, J. K. ; LAETER, J. R. ; BIEVRE, P. D. et al.: Isotopic Compositions of the Elements, 2001. In: *Journal of Physical and Chemical Reference Data* 34 (2005), No. 1, 57-67. <http://dx.doi.org/10.1063/1.1836764>. – DOI 10.1063/1.1836764
- [BMLA94] BOURLAT, Y. ; MILLIES-LACROIX, J-C. ; ABT, D.: Measurement of low-level radioactivity in the Modane underground laboratory. In: *Nuclear Instruments and Methods in Physics Research Section A: Accelerators, Spectrometers, Detectors and Associated Equipment* 339 (1994), January, No. 1-2, 309-317. [http://dx.doi.org/10.1016/0168-9002\(94\)91823-6](http://dx.doi.org/10.1016/0168-9002(94)91823-6). – DOI 10.1016/0168-9002(94)91823-6. – ISSN 01689002

BIBLIOGRAPHY

- [BR97] BRUN, Rene ; RADEMAKERS, Fons: ROOT — An object oriented data analysis framework. In: *Nuclear Instruments and Methods in Physics Research Section A: Accelerators, Spectrometers, Detectors and Associated Equipment* 389 (1997), No. 1–2, 81–86. [http://dx.doi.org/10.1016/S0168-9002\(97\)00048-X](http://dx.doi.org/10.1016/S0168-9002(97)00048-X). – DOI 10.1016/S0168-9002(97)00048-X. – ISSN 0168-9002. – See also <http://root.cern.ch/>
- [Can04] CANBERRA INDUSTRIES, INC.: *Model 2002 Spectroscopy Preamplifier - User's Manual*, 2004
- [Can08a] CANBERRA INDUSTRIES, INC.: *Ultra Low-Background Cryostats (ULB)*. Version: 2008. <http://www.canberra.com/products/detectors/pdf/Ultra-LowBkgrnd-Cryo-SS-CSP0173.pdf>, Accessed 2013-01-20. Website
- [Can08b] CANBERRA INDUSTRIES N.V.: Outline drawing, Model 7915-30, U-style intrgral. 2008. – Data sheet
- [Can09] CANBERRA INDUSTRIES, INC.: *Standard Electrode Coaxial Ge Detectors (SEGe)*. Version: 2009. <http://www.canberra.com/products/detectors/pdf/SEGe-SS-C37419.pdf>, Accessed 2013-01-18. Website
- [Can10] CANBERRA INDUSTRIES, INC.: Inner drawing p-type, S/N 07064. 2010. – Data sheet
- [CGL⁺10] CEBRIÁN, S. ; GÓMEZ, H. ; LUZÓN, G. et al.: Cosmogenic activation in germanium and copper for rare event searches. In: *Astroparticle Physics* 33 (2010), No. 5-6, 316–329. <http://dx.doi.org/10.1016/j.astropartphys.2010.03.002>. – DOI 10.1016/j.astropartphys.2010.03.002. – ISSN 0927-6505
- [CHO⁺11] CHADWICK, M. B. ; HERMAN, M. ; OBLOŽINSKÝ, P. et al.: ENDF/B-VII.1 Nuclear Data for Science and Technology: Cross Sections, Covariances, Fission Product Yields and Decay Data. In: *Nuclear Data Sheets* 112 (2011), No. 12, 2887–2996. <http://dx.doi.org/10.1016/j.nds.2011.11.002>. – DOI 10.1016/j.nds.2011.11.002. – ISSN 0090-3752. – Special Issue on ENDF/B-VII.1 Library
- [CLPBC⁺10] CABAL, Fatima P. ; LOPEZ-PINO, Neivy ; BERNAL-CASTILLO, Jose L. et al.: Monte Carlo based geometrical model for efficiency calculation of an n-type HPGe detector. In: *Applied Radiation and Isotopes* 68 (2010), No. 12, 2403 - 2408. <http://dx.doi.org/10.1016/j.apradiso.2010.06.018>. – DOI 10.1016/j.apradiso.2010.06.018. – ISSN 0969-8043

- [CMPS06] CHYTRACEK, Radovan ; MCCORMICK, J. ; POKORSKI, W. et al.: Geometry Description Markup Language for Physics Simulation and Analysis Applications. In: *Nuclear Science, IEEE Transactions on* 53 (2006), No. 5, p. 2892–2896. <http://dx.doi.org/10.1109/TNS.2006.881062>. – DOI 10.1109/TNS.2006.881062. – ISSN 0018–9499
- [DIN93] Standard DIN 25482-5 June 1993. *Nachweisgrenze und Erkennungsgrenze bei Kernstrahlungsmessungen - Teil 5: Zählende hochauflösende gammaspektrometrische Messungen ohne Berücksichtigung des Probenbehandlungseinflusses*
- [DIN97] Standard DIN 25482-5, Supplement 1 December 1997. *Nachweisgrenze und Erkennungsgrenze bei Kernstrahlungsmessungen - Teil 5: Zählende hochauflösende gammaspektrometrische Messungen ohne Berücksichtigung des Probenbehandlungseinflusses - Beispiele und Erläuterungen*
- [DIN11] Standard DIN ISO 11929 January 2011. *Bestimmung der charakteristischen Grenzen (Erkennungsgrenze, Nachweisgrenze und Grenzen des Vertrauensbereichs) bei Messungen ionisierender Strahlung – Grundlagen und Anwendungen*
- [DRW⁺09] DAWSON, J.V. ; REEVE, C. ; WILSON, J.R. et al.: An Investigation into the ¹¹³Cd Beta Decay Spectrum using a CdZnTe Array. In: *Nuclear Physics A* 818 (2009), No. 3–4, 264–278. <http://dx.doi.org/10.1016/j.nuclphysa.2008.12.010>. – DOI 10.1016/j.nuclphysa.2008.12.010. – ISSN 0375–9474
- [EFG⁺13] EBERT, J. ; FRITTS, M. ; GÖSSLING, C. et al.: Current Status and Future Perspectives of the COBRA Experiment. In: *Advances in High Energy Physics* 2013 (2013), 6. <http://dx.doi.org/10.1155/2013/703572>. – DOI 10.1155/2013/703572
- [Fir96] FIRESTONE, Richard B. ; SHIRLEY, Virginia S. (Pub.): *Table of Isotopes*. Vol. I & II. 8th Ed. New York, Chichester, Brisbane, Toronto, Singapore : John Wiley & Sons, 1996. – 2877 pages. <http://ie.lbl.gov/toi/>. – ISBN 978–0–471–14918–7. – 1999 Update to the 8th Edition: <http://www.wiley-vch.de/books/info/0-471-35633-6/toi99/toi.htm>
- [FS99] FARHAN, Ameenah R. ; SINGH, Balraj: Nuclear Data Sheets for A = 75. In: *Nuclear Data Sheets* 86 (1999), No. 4, 785 - 954. <http://dx.doi.org/10.1006/ndsh.1999.0012>. – DOI 10.1006/ndsh.1999.0012. – ISSN 0090–3752

BIBLIOGRAPHY

- [Gas09] GASTRICH, Holger: *Die Dortmund Low Background Facility - Aufbau einer inneren Abschirmung und Inbetriebnahme des HPGe-Detektors*, TU Dortmund, Diploma thesis, May 2009
- [GHH⁺97] GÜNTHER, M. ; HELLMIG, J. ; HEUSSER, G. et al.: Heidelberg-Moscow $\beta\beta$ experiment with ^{76}Ge : Full setup with five detectors. In: *Phys. Rev. D* D55 (1997), January, 54–67. <http://dx.doi.org/10.1103/PhysRevD.55.54>. – DOI 10.1103/PhysRevD.55.54
- [GHJT08] GASPARRO, Joel ; HULT, Mikael ; JOHNSTON, Peter N. et al.: Monte Carlo modelling of germanium crystals that are tilted and have rounded front edges. In: *Nuclear Instruments and Methods in Physics Research Section A: Accelerators, Spectrometers, Detectors and Associated Equipment* 594 (2008), No. 2, 196 - 201. <http://dx.doi.org/10.1016/j.nima.2008.06.022>. – DOI 10.1016/j.nima.2008.06.022. – ISSN 0168–9002
- [Gil08] GILMORE, Gordon R.: *Practical gamma-ray spectrometry*. 2. ed., reprint. with corr. Chichester, West Sussex : John Wiley & Sons, Ltd, 2008. <http://dx.doi.org/10.1002/9780470861981>. – ISBN 978-0-470-86196-7
- [GMS01] GROOM, Donald E. ; MOKHOV, Nikolai V. ; STRIGANOV, Sergei I.: Muon stopping power and range tables 10 MeV–100 TeV. In: *Atomic Data and Nuclear Data Tables* 78 (2001), No. 2, 183–356. <http://dx.doi.org/10.1006/adnd.2001.0861>. – DOI 10.1006/adnd.2001.0861. – ISSN 0092–640X. – <http://pdg.lbl.gov/2012/AtomicNuclearProperties/adndt.pdf>
- [GSZT⁺00] GÜLER, M. ; SERIN-ZEYREK, M. ; TOLUN, P. et al.: An appearance experiment to search for $\nu_\mu \rightarrow \nu_\tau$ oscillations in the CNGS beam: experimental proposal / CERN. Geneva, July 2000 (CERN-SPSC-2000-028. LNGS-2000-25. SPSC-P-318). – Research report
- [GZX⁺11] GE, Z. G. ; ZHAO, Z. X. ; XIA, H. H. et al.: The Updated Version of Chinese Evaluated Nuclear Data Library (CENDL-3.1). In: *Journal of the Korean Physical Society* 59 (2011), August, No. 23. <http://dx.doi.org/10.3938/jkps.59.1052>. – DOI 10.3938/jkps.59.1052
- [Heu91] HEUSSER, G.: Studies of γ -ray background with a low level germanium spectrometer. In: *Nuclear Instruments and Methods in Physics Research Section B: Beam Interactions with Materials and Atoms* 58 (1991), No. 1, 79 - 84. [http://dx.doi.org/10.1016/0168-583X\(91\)95680-C](http://dx.doi.org/10.1016/0168-583X(91)95680-C). – DOI 10.1016/0168-583X(91)95680-C. – ISSN 0168–583X

- [Heu93] HEUSSER, G.: Cosmic ray-induced background in Ge-spectrometry. In: *Nuclear Instruments and Methods in Physics Research Section B: Beam Interactions with Materials and Atoms* 83 (1993), October, No. 1-2, 223–228. [http://dx.doi.org/10.1016/0168-583X\(93\)95931-T](http://dx.doi.org/10.1016/0168-583X(93)95931-T). – DOI 10.1016/0168-583X(93)95931-T. – ISSN 0168583X
- [Heu96] HEUSSER, G.: Cosmic ray interaction study with low-level Ge-spectrometry. In: *Nuclear Instruments and Methods in Physics Research Section A: Accelerators, Spectrometers, Detectors and Associated Equipment* 369 (1996), February, No. 2-3, 539–543. [http://dx.doi.org/10.1016/S0168-9002\(96\)80046-5](http://dx.doi.org/10.1016/S0168-9002(96)80046-5). – DOI 10.1016/S0168-9002(96)80046-5. – ISSN 01689002
- [HGLGT04] HURTADO, S. ; GARCÍA-LEÓN, M. ; GARCÍA-TENORIO, R.: Monte Carlo simulation of the response of a germanium detector for low-level spectrometry measurements using GEANT4. In: *Applied Radiation and Isotopes* 61 (2004), No. 2-3, 139 - 143. <http://dx.doi.org/10.1016/j.apradiso.2004.03.035>. – DOI 10.1016/j.apradiso.2004.03.035. – ISSN 0969-8043. – Low Level Radionuclide Measurement Techniques - ICRM
- [HGLGT06] HURTADO, S. ; GARCÍA-LEÓN, M. ; GARCÍA-TENORIO, R.: A revision of energy and resolution calibration method of Ge detectors. In: *Nuclear Instruments and Methods in Physics Research Section A: Accelerators, Spectrometers, Detectors and Associated Equipment* 564 (2006), No. 1, 295 - 299. <http://dx.doi.org/10.1016/j.nima.2006.03.018>. – DOI 10.1016/j.nima.2006.03.018. – ISSN 0168-9002
- [HHI⁺03] HELMER, R. G. ; HARDY, J. C. ; IACOB, V. E. et al.: The use of Monte Carlo calculations in the determination of a Ge detector efficiency curve. In: *Nuclear Instruments and Methods in Physics Research Section A: Accelerators, Spectrometers, Detectors and Associated Equipment* 511 (2003), No. 3, 360 - 381. [http://dx.doi.org/10.1016/S0168-9002\(03\)01942-9](http://dx.doi.org/10.1016/S0168-9002(03)01942-9). – DOI 10.1016/S0168-9002(03)01942-9. – ISSN 0168-9002
- [Hil12] HILLRINGHAUS, Bettina: *Betrieb von CdZnTe-Detektoren unter variablen Operationsbedingungen*, TU Dortmund, Bachelor's thesis, September 2012
- [HISV⁺02] HARDY, J. C. ; IACOB, V. E. ; SANCHEZ-VEGA, M. et al.: Precise efficiency calibration of an HPGe detector: source measurements and Monte Carlo calculations with sub-percent precision.

BIBLIOGRAPHY

- In: *Applied Radiation and Isotopes* 56 (2002), February, No. 1-2, 65–69. [http://dx.doi.org/10.1016/S0969-8043\(01\)00168-3](http://dx.doi.org/10.1016/S0969-8043(01)00168-3). – DOI 10.1016/S0969-8043(01)00168-3. – ISSN 09698043
- [HKS09] HEISEL, M. ; KAETHER, F. ; SIMGEN, H.: Statistical analysis of low-level material screening measurements via gamma-spectroscopy. In: *Applied Radiation and Isotopes* 67 (2009), No. 5, 741 - 745. <http://dx.doi.org/10.1016/j.apradiso.2009.01.028>. – DOI 10.1016/j.apradiso.2009.01.028. – ISSN 0969-8043. – 5th International Conference on Radionuclide Metrology - Low-Level Radioactivity Measurement Techniques ICRM-LLRMT'08
- [HLN06] HEUSSER, G. ; LAUBENSTEIN, M. ; NEDER, H.: Low-level germanium gamma-ray spectrometry at the $\mu\text{Bq/kg}$ level and future developments towards higher sensitivity. Version:2006. [http://dx.doi.org/10.1016/S1569-4860\(05\)08039-3](http://dx.doi.org/10.1016/S1569-4860(05)08039-3). In: POVINEC, P. (Pub.) ; SANCHEZ-CABEZA, J.A. (Pub.): *Radionuclides in the Environment - Int. Conf. On Isotopes in Env. Studies* Vol. 8. Elsevier, 2006. – DOI 10.1016/S1569-4860(05)08039-3. – ISSN 1569-4860, 495 - 510
- [IEE97] Standard IEEE 325-1996 1997. *IEEE Standard Test Procedures for Germanium Gamma-Ray Detectors*
- [IHM⁺97] ISAAC, M. C. P. ; HURLEY, D. ; MCDONALD, R. J. et al.: A natural calibration source for determining germanium detector efficiencies. In: *Nuclear Instruments and Methods in Physics Research Section A: Accelerators, Spectrometers, Detectors and Associated Equipment* 397 (1997), No. 2-3, 310 - 316. [http://dx.doi.org/10.1016/S0168-9002\(97\)00754-7](http://dx.doi.org/10.1016/S0168-9002(97)00754-7). – DOI 10.1016/S0168-9002(97)00754-7. – ISSN 0168-9002
- [ISO00] Standard ISO 11929-3 July 2000. *Determination of detection limit and decision threshold for ionizing radiation measurements - Part 3: Fundamentals and application to counting measurements by high resolution gamma spectrometry, without the influence of sample treatment*
- [ISO08a] Standard ISO/IEC Guide 98-3/Suppl.1 2008. *Propagation of distributions using a Monte Carlo method*. – Also published as JCGM 101:2008 by the Bureau International des Poids et Mesures (BIPM), Sèvres, France, <http://www.bipm.org/en/publications/guides/gum.html>
- [ISO08b] Standard ISO/IEC Guide 98-3 2008. *Uncertainty of measurement – Part 3: Guide to the expression of uncertainty in measurement*. – Also published as JCGM 100:2008 by the Bureau International des

Poids et Mesures (BIPM), Sèvres, France, <http://www.bipm.org/en/publications/guides/gum.html>

- [Key04] KEYSER, Ronald M.: Resolution and sensitivity as a function of energy and incident geometry for germanium detectors. In: *Nuclear Instruments and Methods in Physics Research Section B: Beam Interactions with Materials and Atoms* 213 (2004), 236 - 240. [http://dx.doi.org/10.1016/S0168-583X\(03\)01594-5](http://dx.doi.org/10.1016/S0168-583X(03)01594-5). – DOI 10.1016/S0168-583X(03)01594-5. – ISSN 0168-583X. – 5th Topical Meeting on Industrial Radiation and Radioisotope Measurement Applications
- [KKDHK01] KLAPDOR-KLEINGROTHAUS, H. V. ; DIETZ, A. ; HARNEY, H. L. et al.: Evidence for Neutrinoless Double Beta Decay. In: *Modern Physics Letters A* 16 (2001), No. 37, 2409-2420. <http://dx.doi.org/10.1142/S0217732301005825>. – DOI 10.1142/S0217732301005825
- [KKK06] KLAPDOR-KLEINGROTHAUS, H. V. ; KRIVOSHEINA, I. V.: The evidence for the observation of $0\nu\beta\beta$ DECAY: decay: The identification of $0\nu\beta\beta$ events from the full spectra. In: *Modern Physics Letters A* 21 (2006), No. 20, 1547-1566. <http://dx.doi.org/10.1142/S0217732306020937>. – DOI 10.1142/S0217732306020937
- [Köt08] KÖTTIG, Tobias: *Optimisation of Contacting and Energy Resolution of CdZnTe Detectors with Respect to Low Background Application*, TU Dortmund, Diploma thesis, November 2008
- [Köt12] KÖTTIG, Tobias: *Sensitivity Studies of CdZnTe Semiconductor Detectors for the COBRA Experiment*, TU Dortmund, PhD. thesis, September 2012. <http://hdl.handle.net/2003/29752>
- [LAA⁺01] LÉPY, M. C. ; ALTITZOGLOU, T. ; ARNOLD, D. et al.: Inter-comparison of efficiency transfer software for gamma-ray spectrometry. In: *Applied Radiation and Isotopes* 55 (2001), No. 4, 493 - 503. [http://dx.doi.org/10.1016/S0969-8043\(01\)00101-4](http://dx.doi.org/10.1016/S0969-8043(01)00101-4). – DOI 10.1016/S0969-8043(01)00101-4. – ISSN 0969-8043
- [Lab13] LABORATOIRE NATIONAL DE MÉTROLOGIE ET D'ESSAIS - LABORATOIRE NATIONAL HENRI BECQUEREL (LNE-LNHB): *Decay Data Evaluation Project*. Version: 2013. http://www.nucleide.org/DDEP_WG/DDEPdata.htm, Accessed 2013-04-22. Website. – Also published as a monograph (Vol. 1-7) by the Bureau International des Poids et Mesures (BIPM), Sèvres, France, <http://www.bipm.org/en/publications/monographie-ri-5.html>

BIBLIOGRAPHY

- [LBPA96] LAUREC, J. ; BLANCHARD, X. ; POINTURIER, F. et al.: A new low background gamma spectrometer equipped with an anti-cosmic device. In: *Nuclear Instruments and Methods in Physics Research Section A: Accelerators, Spectrometers, Detectors and Associated Equipment* 369 (1996), February, No. 2-3, 566–571. [http://dx.doi.org/10.1016/S0168-9002\(96\)80052-0](http://dx.doi.org/10.1016/S0168-9002(96)80052-0). – DOI 10.1016/S0168-9002(96)80052-0. – ISSN 01689002
- [Leo94] LEO, William R.: *Techniques for Nuclear and Particle Physics Experiments - A How-To Approach*. 2nd Rev. Berlin Heidelberg New York : Springer-Verlag, 1994. – ISBN 978-0-387-57280-2
- [LH09] LAUBENSTEIN, M. ; HEUSSER, G.: Cosmogenic radionuclides in metals as indicator for sea level exposure history. In: *Applied Radiation and Isotopes* 67 (2009), No. 5, 750 - 754. <http://dx.doi.org/10.1016/j.apradiso.2009.01.029>. – DOI 10.1016/j.apradiso.2009.01.029. – ISSN 0969–8043. – 5th International Conference on Radionuclide Metrology - Low-Level Radioactivity Measurement Techniques ICRM-LLRMT'08
- [LHG⁺04] LAUBENSTEIN, M. ; HULT, M. ; GASPARRO, J. et al.: Underground measurements of radioactivity. In: *Applied Radiation and Isotopes* 61 (2004), No. 2-3, 167 - 172. <http://dx.doi.org/10.1016/j.apradiso.2004.03.039>. – DOI 10.1016/j.apradiso.2004.03.039. – ISSN 0969–8043. – Low Level Radionuclide Measurement Techniques - ICRM
- [Lid98] LIDE, David R. (Pub.): *CRC Handbook of Chemistry and Physics*. 79th ed. Boca Raton : CRC Press LLC, 1998. – ISBN 978-0-849-30479-8
- [Lid05] LIDE, David R. (Pub.): *CRC Handbook of Chemistry and Physics, Internet Version 2005*. Boca Raton : CRC Press, 2005 <http://www.hbcernetbase.com>. – Section 14: Geophysics, Astronomy, and Acoustics - Abundance of Elements in the Earth's Crust and in the Sea.
- [LPL⁺08] LEE, K.B. ; PARK, Tae S. ; LEE, Jong M. et al.: Development of a low-level background gamma-ray spectrometer by KRISS. In: *Applied Radiation and Isotopes* 66 (2008), No. 6-7, 845 - 849. <http://dx.doi.org/10.1016/j.apradiso.2008.02.083>. – DOI 10.1016/j.apradiso.2008.02.083. – ISSN 0969–8043. – Proceedings of the 16th International Conference on Radionuclide Metrology and its Applications

- [Maß01] MASS, Martin: *Testmessungen, Aufbau und Inbetriebnahme des Halo-Zählers für das HARP-Experiment*, Universität Dortmund, Diploma thesis, October 2001
- [MČSŠ11] MAMEDOV, F. ; ČERMÁK, P. ; SMOLEK, K. et al.: Measurement of radon diffusion through shielding foils for the SuperNEMO experiment. In: *Journal of Instrumentation* 6 (2011), No. 01, C01068. <http://stacks.iop.org/1748-0221/6/i=01/a=C01068>
- [MDH81] MUGHABGHAB, S. F. ; DIVADEENAM, M. ; HOLDEN, N. E.: *Neutron Cross Sections from Neutron Resonance Parameters and Thermal Cross Sections*. Academic Press, 1981 (Neutron cross sections series). <http://ie.lbl.gov/ngdata/sig.htm>. – ISBN 0125097018. – Data taken from website. Last accessed 2013-05-30.
- [MLB⁺08] MANESCHG, Werner ; LAUBENSTEIN, Matthias ; BUDJÁŠ, Dušan et al.: Measurements of extremely low radioactivity levels in stainless steel for GERDA. In: *Nuclear Instruments and Methods in Physics Research Section A: Accelerators, Spectrometers, Detectors and Associated Equipment* 593 (2008), August, No. 3, 448–453. <http://dx.doi.org/10.1016/j.nima.2008.05.036>. – DOI 10.1016/j.nima.2008.05.036. – ISSN 01689002
- [Mü07] MÜNSTERMANN, Daniel: *Construction of a Low Background Facility for the COBRA Experiment and its Performance*, TU Dortmund, PhD. thesis, 2007. <http://hdl.handle.net/2003/25942>
- [Ned09] NEDDERMANN, Till: *Äußere Abschirmung und aktives Myon-Veto der Dortmund-Low-Background-HPGe-Facility*, TU Dortmund, Diploma thesis, April 2009
- [Nit12] NITSCH, Christian: *Entwicklung einer alternativen Methode zur Szintillatorauslese für das Myon-Veto der DLB*, TU Dortmund, Bachelor's thesis, September 2012
- [NuD] *NuDat 2*. <http://www.nndc.bnl.gov/nudat2/>, Accessed 2013-05-30. Website
- [Oeh04] OEHL, Sandra: *A Shielding System against Neutrons for the COBRA-Experiment and Characterisation of CdZnTe Detectors with the Transient Current Technique*, Universität Dortmund, Diploma thesis, November 2004
- [Pan11] PANDOLA, L.: Overview of the European Underground Facilities. In: *AIP Conference Proceedings* 1338 (2011), p. 12–19. <http://dx.doi.org/10.1063/1.3598888>

BIBLIOGRAPHY

- doi.org/10.1063/1.3579554. – DOI 10.1063/1.3579554. – Topical Workshop in Low Radioactivity Techniques (Sudbury, Canada), August 28-29, 2010m (LRT2010)
- [Pau71] PAUL, J. M.: The density effect and rate of energy loss in common plastic scintillators. In: *Nuclear Instruments and Methods* 96 (1971), September, No. 1, 51–59. [http://dx.doi.org/10.1016/0029-554X\(71\)90436-8](http://dx.doi.org/10.1016/0029-554X(71)90436-8). – DOI 10.1016/0029-554X(71)90436-8. – ISSN 0029554X
- [PDG12] BERINGER, J. ; ARGUIN, J. F. ; BARNETT, R. M. et al. (Particle Data Group): Review of Particle Physics. In: *Phys. Rev. D* 86 (2012), July, 010001. <http://dx.doi.org/10.1103/PhysRevD.86.010001>. – DOI 10.1103/PhysRevD.86.010001
- [Per00] PERKINELMER INSTRUMENTS: *TRUMP®-PCI-8K - Multichannel Buffer Card - Hardware Manual*. Rev. C, 2000
- [Per01] PERKINELMER INSTRUMENTS: *Model 672 Spectroscopy Amplifier - Operating and Service Manual*. Rev. G, 2001
- [PLBA96] POINTURIER, F. ; LAUREC, J. ; BLANCHARD, X. et al.: Cosmic-ray induced background reduction by means of an anticoincidence shield. In: *Applied Radiation and Isotopes* 47 (1996), No. 9-10, 1043–1048. [http://dx.doi.org/10.1016/S0969-8043\(96\)00103-0](http://dx.doi.org/10.1016/S0969-8043(96)00103-0). – DOI 10.1016/S0969-8043(96)00103-0. – ISSN 0969-8043. – Proceedings of the International Committee for Radionuclide Metrology Conference on Low-level Measurement Techniques
- [PTZ00] PONKRATENKO, O. A. ; TRETYAK, V. I. ; ZDESENKO, Yu. G.: Event generator DECAY4 for simulating double-beta processes and decays of radioactive nuclei. In: *Physics of Atomic Nuclei* 63 (2000), No. 7, p. 1282–1287. <http://dx.doi.org/10.1134/1.855784>. – DOI 10.1134/1.855784. – ISSN 1063-7788
- [Qua12] QUANTE, Thomas: *Upgrade of the Active Muon Veto and Software Development for the Dortmund Low Background Facility*, TU Dortmund, Master's thesis, September 2012
- [RA88] REEVES, J. H. ; ARTHUR, R. J.: Antic cosmic-shielded ultralow-background germanium detector systems for analysis of bulk environmental samples. In: *Journal of Radioanalytical and Nuclear Chemistry* 124 (1988), No. 2, 435–447. <http://www.springerlink.com/index/U242R15076614014.pdf>

- [REE⁺11] RAHAMAN, S. ; ELOMAA, V.-V. ; ERONEN, T. et al.: Double-beta decay Q values of ¹¹⁶Cd and ¹³⁰Te. In: *Physics Letters B* 703 (2011), No. 4, 412 - 416. <http://dx.doi.org/10.1016/j.physletb.2011.07.078>. – DOI 10.1016/j.physletb.2011.07.078. – ISSN 0370–2693
- [Rib08] RIBBONSOFT GMBH: QCAD 2.2.2.0. Version: August 2008. <http://www.qcad.org/>. Software
- [ŠAK⁺92] ŠKORO, G. P. ; ANIČIN, I. V. ; KUKOČ, A. H. et al.: Environmental neutrons as seen by a germanium gamma-ray spectrometer. In: *Nuclear Instruments and Methods in Physics Research Section A: Accelerators, Spectrometers, Detectors and Associated Equipment* 316 (1992), No. 2–3, 333 - 336. [http://dx.doi.org/10.1016/0168-9002\(92\)90918-T](http://dx.doi.org/10.1016/0168-9002(92)90918-T). – DOI 10.1016/0168–9002(92)90918–T. – ISSN 0168–9002
- [Sca] *The Scala Programming Language*. <http://www.scala-lang.org/>, Accessed 2013-02-15. Website
- [Sch07] SCHLÄGER, Martin: Precise modelling of coaxial germanium detectors in preparation for a mathematical calibration. In: *Nuclear Instruments and Methods in Physics Research Section A: Accelerators, Spectrometers, Detectors and Associated Equipment* 580 (2007), No. 1, 137 - 140. <http://dx.doi.org/10.1016/j.nima.2007.05.053>. – DOI 10.1016/j.nima.2007.05.053. – ISSN 0168–9002. – Proceedings of the 10th International Symposium on Radiation Physics – ISRP 10
- [Sch10] SCHIRA, Simon: *Charakterisierung des Detektorsystems der Dortmund-Low-Background-Facility*, TU Dortmund, Bachelor's thesis, 2010
- [Sch11] SCHULZ, Oliver: *Exploration of new Data Acquisition and Background Reduction Techniques for the COBRA Experiment*, TU Dortmund, PhD. thesis, August 2011. <http://hdl.handle.net/2003/29108>
- [SFVS11] SALVAT, F. ; FERNÁNDEZ-VAREA, J. M. ; SEMPAU, J. ; OECD NUCLEAR ENERGY AGENCY (Pub.): *PENELOPE–2011: A Code System for Monte Carlo Simulation of Electron and Photon Transport*. Issy-les-Moulineaux, France: OECD Nuclear Energy Agency, 2011. <http://www.oecd-nea.org/science/docs/2011/nsc-doc2011-5.pdf>
- [SK11] SCHWAB, Adolf J. ; KÜRNER, Wolfgang: *Elektromagnetische Verträglichkeit (VDI-Buch)*. Springer, 2011. <http://dx.doi.org/10.1007/978-3-642-16610-5>. – ISBN 3642166091
- [SSK04] SCHROETTNER, T. ; SCHWAIGER, M. ; KINDL, P.: Optimization of an active anti cosmic veto shielding. In: *Applied Radiation and*

BIBLIOGRAPHY

- Isotopes* 61 (2004), No. 2-3, 133–138. <http://dx.doi.org/10.1016/j.apradiso.2004.03.034>. – DOI 10.1016/j.apradiso.2004.03.034. – ISSN 0969–8043. – Low Level Radionuclide Measurement Techniques - ICRM
- [Teb11] TEBRÜGGE, Jan: *New read-out electronics and pulse shape analysis for the COBRA experiment*, TU Dortmund, Diploma thesis, 2011
- [TH91] THEODÓRSSON, Páll ; HEUSSER, Gerd: External guard counters for low-level counting systems. In: *Nuclear Instruments and Methods in Physics Research Section B: Beam Interactions with Materials and Atoms* 53 (1991), January, No. 1, 97–100. [http://dx.doi.org/10.1016/0168-583X\(91\)95450-R](http://dx.doi.org/10.1016/0168-583X(91)95450-R). – DOI 10.1016/0168–583X(91)95450–R. – ISSN 0168583X
- [The96] THEODÓRSSON, Páll: *Measurement of weak radioactivity*. Singapore : World Scientific, 1996 <http://www.worldscientific.com/worldscibooks/10.1142/2800>. – ISBN 978–9–810–22315–1
- [Var13] VARICAD S.R.O.: *VariCAD – 3D/2D CAD software for mechanical engineering*. Version: 2013. <http://www.varicad.com>, Accessed 2013-06-14. Website
- [Wah07] WAHL, Wolfgang: *$\alpha\beta\gamma$ -Table*. Version: 4.3, 2007. <http://www.isus.de/english/table.htm>. Handbook
- [Wah08] WAHL, Wolfgang: *Institute for Spectrometry and Radiation Protection*. Version: 2008. http://www.isus.de/english/system_details_e1.htm, Accessed 2013-01-03. Website
- [WB09] WIESER, Michael E. ; BERGLUND, Michael: Atomic weights of the elements 2007 (IUPAC Technical Report). In: *Pure and Applied Chemistry* 81 (2009), September, No. 11, 2131–2156. <http://dx.doi.org/10.1351/PAC-REP-09-08-03>. – DOI 10.1351/PAC-REP-09-08-03
- [Wik14] WIKIMEDIA COMMONS: *File:Decay Chain of Thorium.svg - Wikimedia Commons*. Version: 2014. http://commons.wikimedia.org/w/index.php?title=File:Decay_Chain_of_Thorium.svg&oldid=54396310, Accessed 2014-01-12. Website. – This work is licensed under the Creative Commons Attribution-ShareAlike 3.0 Unported License. To view a copy of this license, visit <http://creativecommons.org/licenses/by-sa/3.0/> or send a letter to Creative Commons, 444 Castro Street, Suite 900, Mountain View, California, 94041, USA.

- [WKM⁺13] WEISE, K. ; KANISCH, G. ; MICHEL, R. et al.: Characteristic values in radiation measurement – Material for a critical discussion on fundamentals and alternatives / Fachverband für Strahlenschutz e. V. TÜV Media GmbH, TÜV Rheinland Group, Köln, April 2013 (PROGRESS IN RADIATION PROTECTION FS-2013-167-AKSIGMA). – Research report. – ISSN 1013–4506
- [WMA⁺96] WORDEL, R. ; MOUCHEL, D. ; ALTZITZOGLU, T. et al.: Study of neutron and muon background in low-level germanium gamma-ray spectrometry. In: *Nuclear Instruments and Methods in Physics Research Section A: Accelerators, Spectrometers, Detectors and Associated Equipment* 369 (1996), February, No. 2-3, 557–562. [http://dx.doi.org/10.1016/S0168-9002\(96\)80050-7](http://dx.doi.org/10.1016/S0168-9002(96)80050-7). – DOI 10.1016/S0168-9002(96)80050-7. – ISSN 01689002
- [Wol08] WOLFSPERGER, Hans A.: *Elektromagnetische Schirmung: Theorie und Praxisbeispiele (VDI-Buch)*. Springer, 2008. <http://dx.doi.org/10.1007/978-3-540-76913-2>. – ISBN 3540769129
- [Zan91] ZANOTTI, L.: Experiments at the Gran Sasso underground laboratory. In: *Journal of Physics G: Nuclear and Particle Physics* 17, Supplement (1991), S373-S392. <http://dx.doi.org/10.1088/0954-3899/17/S/039>. – DOI 10.1088/0954-3899/17/S/039

BIBLIOGRAPHY

List of Figures

2.1. Decay scheme of ^{133}Ba	20
3.1. The set-up of the DLB.	23
3.2. Flux of primary and secondary cosmic rays	24
3.3. Angular distribution of overburden.	25
3.4. Different layers of the inner shielding.	26
3.5. Background count rate vs. applied rejection time.	33
3.6. Dead layer scanning position grid.	36
3.7. Position dependent detector front-side sensitivity.	38
3.8. Cross section through the detector front-side sensitivity.	39
3.9. DAQ system, conventional read out.	40
3.10. Evolution of detector background.	43
3.11. Final background spectrum.	47
4.1. Characteristic limits used for spectrum evaluation.	61
4.2. Regions used in DIN 25482-5	63
4.3. Probability distribution of true measurand and the corresponding characterising quantities.	68
4.4. Best estimate \hat{z} and coverage interval in dependence of primary measurement result $z_0 = y_0/u(y_0)$	70
5.1. Model of detector set-up	88
5.2. Spectrum comparison of ^{241}Am for nominal detector parameters.	92
5.3. Spectrum comparison of ^{133}Ba for nominal detector parameters.	93
5.4. Set-up used for tuning of dead layer thickness.	95
5.5. Dead layer thickness optimisation with ^{133}Ba using the 53.2 keV line and 80 keV region.	96
5.6. Crystal to endcap distance optimisation with ^{133}Ba	99
5.7. Deviations between simulation and measurement, d_{dl} and d_{cc} op- timised, inner contact dimensions nominal.	103
5.8. Optimisation of sensitive detector volume.	105
5.9. Deviations between simulation and measurement, optimised de- tector parameters.	106
6.1. Shape of ^{210}Bi β spectrum.	122
7.1. View into the former COBRA set-up.	128

LIST OF FIGURES

7.2.	CAD drawing of the new COBRA shielding.	129
7.3.	Components of EMI shielding.	131
7.4.	Cross section through feedthrough and NEST before and after upgrade.	133
7.5.	View into the current COBRA set-up.	134
A.1.	^{232}Th decay chain	141
A.2.	^{238}U decay chain	142
A.3.	^{235}U decay chain	143
B.1.	^{241}Am collimator	145
B.2.	Mechanical drawing of the shielding extender.	146
D.1.	Shielding extender and source holders.	149
D.2.	Dead layer thickness optimisation with ^{133}Ba using the 53.2 keV and 160.6 keV line.	150
D.3.	Dead layer thickness optimisation with ^{133}Ba using the 80 keV region and 160.6 keV line.	151
E.1.	Simulated dose distributions in the HPGe detector.	153

List of Tables

3.1. Radiopurity data of boron loaded polyethylene.	28
3.2. Background characteristics	45
3.3. Peaks in the background spectrum.	47
3.4. Activities of activation products in the germanium detector.	52
5.1. Deviations of MC simulation with nominal detector parameters.	89
5.2. Nominal detector parameters.	90
5.3. Dead layer optimisation results.	97
5.4. Crystal to endcap distance optimisation check.	100
5.5. Comparison of deviations for different stages of optimisation of the MC model.	107
5.6. Optimised detector parameters.	108
6.1. Results for IAEA-CU-2010-03.	115
6.2. Results for IAEA-TEL-2011-03, Sample 1–3.	116
6.3. Results for IAEA-TEL-2011-03, Sample 4.	117
6.4. Radiopurity data of conductive silver.	120
6.5. Radiopurity data of OPERA lead sheets.	121
6.6. Radiopurity data of Timepix readout chips.	123
6.7. Radiopurity data of Medipix readout chips.	125
F.1. GRDM γ ray emission probabilities and correction factors.	157

LIST OF TABLES

Acronyms

$0\nu\beta\beta$ decay neutrinoless double beta decay. 9, 120, 182

AFS Andrew file system, see <http://www.openafs.org/> for the used implementation OpenAFS. 42, 83

AMANDA Antarctic Muon And Neutrino Detection Array, pilot project of the IceCube experiment, see <http://icecube.wisc.edu>. 33, 42

ASCII American Standard Code for Information Interchange. 57

ASIC Application-specific integrated circuit. 123

BLR baseline restorer. 40

BOREXINO Borexino experiment to measure the ${}^7\text{Be}$ neutrino flux from the sun [AAB⁺09], located at LNGS, see <http://borex.lngs.infn.it/>. 15

BPE boron loaded polyethylene. 27–29, 51, 54, 127–129

CAD computer aided design. 36, 127, 129, 133, 134, 145

CdZnTe Cadmium Zinc Telluride, a room temperature semiconductor material. 29, 58, 81, 119, 120, 123, 125, 129, 131, 132

CERN Conseil Européen pour la Recherche Nucléaire, Particle physics laboratory at Geneva, Switzerland, homepage <http://cern.ch>. 30, 41, 57, 121

CL confidence level. 28, 51, 157

COBRA CdZnTe 0 ν β β Research Apparatus [EFG⁺13]. 9–11, 16, 17, 27, 33, 42, 58, 81, 82, 86, 113, 119–121, 123, 127–130, 132, 134–137, 139, 140, 185

CPG coplanar grid. 119, 123

CRESST Cryogenic Rare Event Search with Superconducting Thermometers [ABB⁺09], located at LNGS, see also <http://www.cresst.de>. 9

CSDA continuous-slowing-down-approximation (CSDA), “which neglect(s) multiple scattering and range straggling” [GMS01]. 31

DAQ data acquisition. 25, 33, 39–42, 57, 58, 137

Acronyms

- DAQCorE** Data-Acquisition and Control Environment. 42
- DDEP** Decay Data Evaluation Project [Lab13], see http://www.nucleide.org/DDEP_WG/DDEPdata.htm and <http://laraweb.free.fr/>. 11, 79, 104, 110
- DL** detection limit. 34
- DLB** Dortmund Low Background Facility. 10, 11, 23–25, 28, 30, 33, 34, 40, 41, 43–46, 55, 58, 81, 83, 87, 88, 97, 98, 113, 114, 119, 123, 127, 135–137, 140
- EDELWEISS** *Expérience pour Detecter les WIMPs en Site Souterrain*, an experiment searching for dark matter with germanium bolometers [BDA⁺09] at the Modane underground facility, France, see also <http://edelweiss2.in2p3.fr/>. 9
- EMI** electromagnetic interference. 128–132, 134, 137
- ENSDF** Evaluated nuclear structure data file, for database see for example <http://www.nndc.bnl.gov/ensdf/>. 20, 137
- EXO** *Enriched Xenon Observatory* [AAB⁺12] for the search of $0\nu\beta\beta$ decay in ^{136}Xe located in New Mexico, USA, see also <http://www-project.slac.stanford.edu/exo/>. 9
- FADC** flash analogue to digital converter. 33, 42
- FEP** full energy peak. 19, 21, 54, 55, 66, 73, 76, 78, 81, 89, 90, 95, 97, 100–102, 106–109, 115, 121, 123
- FET** field effect transistor. 39
- FWHM** full width at half maximum. 62, 63, 71–73, 77–79, 91
- GDML** Geometry Description Markup Language [CMPS06], <http://gdml.web.cern.ch/GDML/>. 23, 81, 82, 86–88, 95, 135
- Geant4** GEometry ANd Tracking, C++ based software framework for the simulation of particles through matter [AAA⁺03], see also <http://geant4.cern.ch>. 11, 76, 81–83, 86–90, 92–94, 109–111, 137, 157, 182, 183, 185
- GERDA** *Germanium Detector Array* [AAA⁺13] for the search of $0\nu\beta\beta$ decay in ^{76}Ge at LNGS, see also <http://www.mpi-hd.mpg.de/gerda/>. 9
- GPS** Geant4 General Particle Source, see <http://reat.space.qinetiq.com/gps/>. 92, 111, 121

- GRDM** Geant4 radioactive decay module, see Physics Reference Manual at <http://geant4.web.cern.ch/geant4/support/userdocuments.shtml>. 92–94, 104, 109, 111, 121, 122, 157
- HPGe** high purity germanium. 10, 11, 13, 14, 18–20, 23, 25, 27–29, 31, 34, 39, 42, 43, 54, 73, 74, 81, 96, 97, 135, 136, 153
- HV** high voltage. 39, 132, 133
- IAEA** International Atomic Energy Agency, Vienna, Austria, <http://www.iaea.org>. 11, 113–119, 136
- ICP-MS** inductively coupled plasma mass spectrometry. 13
- IP** Internet Protocol. 42
- IT** Isomeric Transition, γ transition from an isomeric state of a nucleus [Gil08]. 120, 142
- JVM** Java Virtual Machine. 42
- LN₂** liquid nitrogen. 35, 39
- LNGS** Laboratori Nazionali del Gran Sasso, underground physics laboratory close to l’Aquila, Italy, see also <http://www.lngs.infn.it>. 9, 11, 27–29, 51, 117, 118, 121, 127, 130, 132, 133, 136, 137, 139, 140, 181, 182, 185
- MANTiCORE** Multiple-Analysis Toolkit for the COBRA Experiment. 42
- MC** Monte Carlo. 11, 19, 21, 38, 46, 50–54, 76, 78, 81, 82, 85, 86, 89–96, 98, 100–111, 113–115, 117, 118, 120–123, 135–137, 140, 149
- MCA** multi channel analyzer. 32, 33, 41, 42, 57, 58
- MCB** multi channel buffer. 41, 42, 57
- mwe** meters of water equivalent. 24, 25, 44–46, 56, 135
- NA** neutron activation. 14, 41
- NAA** neutron activation analysis. 14, 18
- NaI(Tl)** sodium iodine. 19
- NIM** Nuclear Instrumentation Module, a standard for laboratory electronics in modules. 30, 39–41

Acronyms

- NORM** natural occurring radioactive material. 16, 17
- OPERA** Oscillation Project with Emulsion-tracking Apparatus [GSZT⁺00], see <http://operaweb.lngs.infn.it/?lang=en>. 121
- PBC** peaked background correction. 60, 74, 76, 77
- PC** Personal computer. 41, 42, 51, 82
- PCB** printed circuit board. 34, 123
- PCI** Peripheral Component Interconnect. 41
- PE** polyethylene. 27, 29, 56
- PENELOPE** PENetration and Energy LOss of Positrons and Electrons (photon simulation was introduced later), [SFVS11]. 83, 86, 93, 94, 153
- PMMA** Poly(methyl methacrylate), a transparent thermoplastic, sometimes called “acrylic glass”. 30, 37
- PMT** photomultiplier tube. 23, 30–32, 40
- POM** Polyoxymethylene, a thermoplastic. 132, 133, 146
- ppb** parts per billion. 34, 49
- PTFE** Polytetrafluoroethylene, a synthetic fluoropolymer. 132
- PUR** pile-up rejection. 40, 41, 92
- PZ** pole-zero. 40
- R&D** Research and Development. 9, 11, 113, 121, 127, 129, 130, 132, 134, 137, 139
- RCS** random coincidence summing. 20
- ROI** region of interest. 60, 62–64, 69, 71–73, 75, 77–79, 91, 92, 120, 121
- ROOT** Object orientated analysis framework developed at CERN [BR97], see also <http://root.cern.ch>. 11, 42, 57–59, 74, 75, 79–81, 86, 110, 153
- SCALA** Programming language, see <http://www.scala-lang.org> [Sca]. 42
- SE** single ended. 40
- SE** single escape. 44
- TAC** time to amplitude converter. 32

- TCP** Transmission Control Protocol. 42
- TCS** true coincidence summing. 17, 20, 21, 79, 85, 94, 98, 100, 104, 109–111
- TTL** Transistor-transistor logic. 41
- ULB** ultra low background. 34
- UPS** uninterruptible power supply. 43, 57
- UTC** Coordinated universal time. 75
- VENOM** Vicious Evil Network Of Mayhem, Geant4 based simulation program for COBRA. 11, 46, 76, 81–83, 86, 88, 89, 94, 104, 109–111, 122, 135, 137
- VME** Versa Module Eurocard (Bus), IEEE 1014-1987. 33, 42
- WIMP** Weakly interacting massive particle. 9
- XENON100** XENON Dark Matter Project [AAA⁺12] at LNGS, see also <http://xenon.astro.columbia.edu/>. 9
- XML** Extensible Markup Language, data format for encoding documents both human- and machine readable. 86